



Terms and Conditions of Use of Digitised Theses from Trinity College Library Dublin

Copyright statement

All material supplied by Trinity College Library is protected by copyright (under the Copyright and Related Rights Act, 2000 as amended) and other relevant Intellectual Property Rights. By accessing and using a Digitised Thesis from Trinity College Library you acknowledge that all Intellectual Property Rights in any Works supplied are the sole and exclusive property of the copyright and/or other IPR holder. Specific copyright holders may not be explicitly identified. Use of materials from other sources within a thesis should not be construed as a claim over them.

A non-exclusive, non-transferable licence is hereby granted to those using or reproducing, in whole or in part, the material for valid purposes, providing the copyright owners are acknowledged using the normal conventions. Where specific permission to use material is required, this is identified and such permission must be sought from the copyright holder or agency cited.

Liability statement

By using a Digitised Thesis, I accept that Trinity College Dublin bears no legal responsibility for the accuracy, legality or comprehensiveness of materials contained within the thesis, and that Trinity College Dublin accepts no liability for indirect, consequential, or incidental, damages or losses arising from use of the thesis for whatever reason. Information located in a thesis may be subject to specific use constraints, details of which may not be explicitly described. It is the responsibility of potential and actual users to be aware of such constraints and to abide by them. By making use of material from a digitised thesis, you accept these copyright and disclaimer provisions. Where it is brought to the attention of Trinity College Library that there may be a breach of copyright or other restraint, it is the policy to withdraw or take down access to a thesis while the issue is being resolved.

Access Agreement

By using a Digitised Thesis from Trinity College Library you are bound by the following Terms & Conditions. Please read them carefully.

I have read and I understand the following statement: All material supplied via a Digitised Thesis from Trinity College Library is protected by copyright and other intellectual property rights, and duplication or sale of all or part of any of a thesis is not permitted, except that material may be duplicated by you for your research use or for educational purposes in electronic or print form providing the copyright owners are acknowledged using the normal conventions. You must obtain permission for any other use. Electronic or print copies may not be offered, whether for sale or otherwise to anyone. This copy has been supplied on the understanding that it is copyright material and that no quotation from the thesis may be published without proper acknowledgement.

Ligand design for controlling dimensionality and chirality in novel lanthanide-organic hybrid materials with tuneable optoelectronic properties

Adam Ross Patterson

MChem (Hons.)

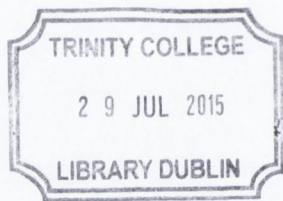


A thesis submitted to the University of Dublin, Trinity College
for the degree of Doctor of Philosophy.

Under the supervision of Dr. Rachel Evans and Dr. Wolfgang Schmitt

School of Chemistry
Trinity College Dublin

May 2015



Thesis 10659

Declaration

I declare that this thesis has not been submitted as an exercise for a degree at this or any other university and it is entirely my own work, except where otherwise cited, referenced, acknowledged or accredited.

I agree to deposit this thesis in the University's open access institutional repository or allow the library to do so on my behalf, subject to Irish Copyright Legislation and Trinity College Library conditions of use and acknowledgement.



.....

Adam Ross Patterson MChem (Hons.)

Acknowledgements

I wish to express my thanks for all the support my supervisors, Dr. Rachel Evans and Dr. Wolfgang Schmitt, have given over the last few years; a few instances come to mind... Rachel for her guidance through the Mike Lyons incident, and Wolfgang for his mute lack of judgement after meeting me while I was locked outside the Old Chemistry building in that black dress! In the years they have come to be like a pair of foster parents, and of the highest calibre, beautifully exemplified by their nonchalance upon my calling up to The Dean of the College with some members (cough, ALL) of the Evans group and one undergrad student in tow... In all seriousness though, I am genuinely grateful for their uncompromising patience, energetic enthusiasm and guidance through my research that has kept me trucking this whole time, thank you!

I have received help in many forms, especially from the academic, technical (Patsy Greene, you always turn a bad day round!) and administrative (Love you Helen and Tess!) staff within the Department. For measurements and training in crystallography required to complete this thesis I am in debt to Dr. Brendan Twamley and Dr. Tom McCabe. My special thanks are also extended to staff for other techniques: Dr. John O'Brien, Dr. Manuel Ruether, Dr. Martin Feeney and Dr. Gary Hessman for their measurements in the NMR and mass spectrometry services. I also owe my thanks to Dr. Clive Downing for his training and advice in SEM microscopy.

With my fingers firmly in the two pies I had the joy of knowing and working with people from both the Evans and Schmitt groups. Big up to the Evans crew Niamh, Jude,* Barry, Ilaria, Camille, Adarsh, Lauren and Steve and not to mention all past and visiting students (I am NOT going to name them all again, Niamh :s). For those newer to the group I hope I get to know you better over a few drinks or maybe a few climbing sessions! As to the Schmitt group, a heads up to Ian, Dave, Giuseppe, Camilia,* Bartosz, Ger, Anne-Marie, Lukas, Theresa, Colm, Kevin, Adam the Dentist :p, past students and the post-Docs for the chats and advice over the years. In particular, I would like to pay some thanks to Tania, one of my students who helped carry out some of the research that led to some of the results in this thesis. Best of luck to you in the future!

A young dumb fella from the Isle of Man couldn't make it through the years without a few close friends. From those early years I send my cheers to Ian, Ger, Gearoid, Kalle, Paddy and Dave for all the beers, rugby, banter, climbing and random encounters with ladies of the night! You know how to keep me on my toes.

In the later years how could I forget to mention the addition of Niamh, Jude and Beth to my life... damn you can be a pain in the ass, but it's good to know that my arts and crafts skills have been honed since meeting you guys, I also have you to thank for my sweet crimbo jumper :p Love you all :D and I'm sure you won't be getting rid of me any time soon, two big thumbs up to you for the last three years.

I would also like to extend my thanks to Joan, my landlord of the last four years. Not only did she welcome me into her home but became my very own Irish mammy! And was kind enough

to lend a listening ear in my times of woe as every PhD student no doubt experiences in their time!
Thanks for being so awesome and so patient.

To finish I would like to say thanks to my parents, never judging, never pushing me but always loving and supporting along the way whichever way I needed it. Love you guys...

To all, later dudes and, dare I say, enjoy...

(* - Proof-reading lifelines!)

Summary

The research presented in this thesis looks into the development of novel inorganic-organic hybrid materials with a particular focus on exploiting lanthanide(III) ions. The project considers the synthesis and structural characterisation of these materials and investigates their photoluminescence properties.

Chapter 1 introduces the reader to the area of research described in this thesis, introducing the Cheetham and Rao description for inorganic-organic materials. The discussion relates specifically to lanthanide-organic hybrid materials and discusses how inherent photoluminescence and magnetic properties of the lanthanide (III) centre are developed for applications in some of the contemporary materials reported to date. This chapter closes with a look at the aims for this thesis.

Chapter 2 provides an account of the experimental details for this work.

Chapter 3 discusses the synthesis of three novel lanthanide phosphonate series using the ligands *tert*-butyl-(**Bu'**-PO₃H₂), 1-naphthalene (**Naph**-PO₃H₂) and 4-biphenyl (**Biphen**-PO₃H₂) phosphonic acid. The **Ln-Bu'** series, [Eu(HO₃PC(CH₃)₃)₃]·H₂O was shown to be a 1D coordination polymer that packs into a *pseudo*-2D layer through hydrogen bonding. The **Ln-Naph** series, [Ln(O₃PC₁₀H₇)₂(H₂O)₂], is a 2D structure with two additional water molecules in the lanthanide coordination sphere and has a structure related to a reported lanthanide benzyl phosphonate. The **Ln-Biphen**, [Ln(O₃PC₁₂H₉)₂], series displays a 2D structure that is different from both **Ln-Bu'** and **Ln-Naph**. The nano-morphology of the resulting materials was studied to understand the effect of ligand size and shape and the effects of previously known crystal habit modifier, sodium *para*-toluenesulfonate. It was found that these materials can display 1D nanorods and 2D plates and the possible driving forces for the morphology are discussed. The photoluminescence (PL) properties for the three series of compounds, when Ln = Eu^{III}, Tb^{III}, Nd^{III} and Yb^{III}, were studied to investigate the ability to sensitise lanthanide luminescence through the aromatic ligand. In this respect, we report the first room temperature near-infrared (NIR) photoluminescence of an Yb^{III}-phosphonate, and discuss the absence of room-temperature Tb^{III} photoluminescence when excited through 1-naphthalene phosphonic acid.

Chapter 4 reports the isolation of mononuclear Na₂[Eu₂(Hheidi)₄(H₂O)(MeOH)]·3MeOH, **2**, and binuclear Na₂[Eu(Hheidi)(heidi)(H₂O)₂]·H₂O, **3**, lanthanide complexes from reaction with *N*-(2-hydroxyethyl)iminodiacetic acid, H₃heidi. By changing the type of base (NaN₃→NaOH) and pressure (atmospheric→high pressure) in the reaction conditions, additional μ₂-hydroxo interactions form that allow the binuclear complex of **3** to be isolated instead of mononuclear complex of **2**. A study of the steady-state and solution properties indicates that PL can be observed from Eu^{III}- and Tb^{III}- in the visible region, and from Nd^{III}- in the NIR region of the spectrum. We further show that in solution the mononuclear complex is stable and represents a potential solution species from which we can synthesise new hybrid materials using additional ligands.

In **Chapter 5** we discuss the chemistry of 2,2'-((3-carboxy-2-hydroxynaphthalen-1-yl)methylazanediyl)diacetic acid (H₄C₃hnida) and 2,2'-((6-carboxy-2-hydroxynaphthalen-1-

yl)methylazanediy)diacetic acid ($\text{H}_4\text{C6hnida}$) with lanthanide ions. We find that under solvothermal conditions the ligand $\text{H}_4\text{C6hnida}$ yields the structure 5,5'-methylenebis(6-hydroxy-2-naphthoic acid), **4**, and we discuss the relevance of the structure in relation to pamoic acid, an important reagent in isolating pharmaceutical products through lowering the product solubility. Reacting the alternative ligand, $\text{H}_4\text{C3hnida}$, with lanthanide ions can yield the chiral 3D structure $[\text{Ln}_5(\text{HC3hnida})(\text{C3hnida})_3(\text{H}_2\text{O})_{10}] \cdot 25\text{H}_2\text{O}$, **5**, that displays chiral blade-like channels along the c -axis and separate hydrophobic and hydrophilic channels along the a - and b -axes. The dimensionality of the material can be altered as a function of temperature towards the 1D coordination polymer $[\text{Nd}_{17}(\text{C3hnida})_{12}(\mu_3\text{-OH})_4(\text{H}_2\text{O})_{30}] \cdot x\text{H}_2\text{O}$, **6**, forming at higher temperature. We have investigated the optical properties of these materials and discuss the potential applications that these materials could be developed for.

The work presented in **Chapter 6** considers 3D chiral networks, $\text{Na}[\text{Ln}(\text{C}_6\text{H}_5\text{CO}_2)_4]$, **7**, derived from the achiral ligand, benzoic acid. The structure is discussed and identifies the origin of the chirality which manifests along the c -axis. Circular dichroism spectroscopy reveals a band centred at 240 nm assigned to the ligand absorption and shows that one enantiomer crystallises in excess. The photoluminescence of **7-Eu** was investigated and a high emission quantum yield, $\Phi_{\text{PL}} = 23.8\%$ measured. The potential isolation of an enantio-pure material and reasonably high emission quantum yield, make these promising materials for chiral security tags.

Chapter 7 looks into the synthesis of lanthanide networks using the sulphate ion. Particular emphasis is placed on the influence of organic templating agents for the isolation of higher order lanthanide sulphates. The 2D structure of $[\text{Ln}_2(\text{SO}_4)_3(\text{H}_2\text{O})_8]$, **8**, forms in the absence of an organic template. By comparison, the crystal structures of $(\text{C}_2\text{NH}_8)_9[\text{Nd}_5(\text{SO}_4)_{12}]$, **9**, $\text{NH}_4[\text{Dy}(\text{SO}_4)_2(\text{H}_2\text{O})]$, **10**, and $(\text{NH}_4)_3[\text{Dy}(\text{SO}_4)_3]$, **11**, show the progress made in determining new network materials that are 2D and 3D in their architecture and reveal a new approach to the use of the organic template through the *in-situ* formation of the template by decomposition of the solvent. The sulphate ion as a ligand is identified as potentially useful for creating materials for magnetic cooling, and the magnetic properties of **9** are currently under investigation.

Chapter 8 looks to provide some brief conclusions and outlines the future prospects for the research performed in this thesis.

List of publications

- (1) A. R. Patterson, W. Schmitt and R. C. Evans, *J. Phys. Chem. C*, 2014, **118**, 10291-10301.
- (2) J. E. Houston, A. R. Patterson, A. C. Jayasundera, W. Schmitt and R. C. Evans, *Chem. Commun.*, 2014, **50**, 5233-5235.

Table of Contents

Declaration.....	i
Acknowledgements.....	iii
Summary.....	v
List of publications.....	vi
Table of contents.....	vii
List of ligands.....	xii
List of compounds.....	xiii
Abbreviations.....	xiv
List of symbols.....	xvi
Chapter 1 - Introduction	1
1.1 Functional inorganic-organic materials.....	2
1.1 Classification of hybrid inorganic-organic materials.....	2
1.1.1 Hybrid structures built from inorganic connectivity, I^mO^0	3
1.1.2 Hybrid structures built from organic connectivity, I^0O^n	4
1.1.3 Hybrid structures built from mixed connectivity, I^mO^n	5
1.2 Lanthanide coordination.....	6
1.3 Optical transitions in lanthanide ions.....	7
1.3.1 Origin of lanthanide photoluminescence.....	7
1.3.2 Quenching by high frequency oscillators.....	9
1.3.3 Quantitative analysis of lanthanide luminescence.....	10
1.3.4 Magnetic properties of the lanthanide ions.....	13
1.4 Applications of hybrid inorganic-organic materials.....	14
1.4.1 White-lighting.....	14
1.4.2 Sensing applications.....	18
1.4.3 Imaging and non-linear optics.....	25
1.4.4 Magnetic properties and the magnetocaloric effect (MCE).....	28
1.5 Aims and objectives.....	29
1.6 References.....	30

Chapter 2 - Experimental	35
2.1 Materials and methods.....	36
2.1.1 Reagents	36
2.1.2 Nuclear magnetic resonance (NMR)	36
2.1.3 Fourier transform-infrared spectroscopy (FT-IR)	36
2.1.4 Mass Spectrometry	36
2.1.5 Thermogravimetric analysis (TGA)	36
2.1.6 Elemental analysis	36
2.1.7 Single crystal X-ray diffraction	37
2.1.8 Powder X-ray diffraction (PXRD).....	37
2.1.9 UV/Vis absorption spectroscopy	37
2.1.10 Photoluminescence spectroscopy	38
2.1.11 Circular Dichroism	39
2.1.12 Scanning electron microscopy (SEM).....	40
2.1.13 Solvothermal synthesis	40
2.2 Ligand Synthesis	40
2.2.1 Synthesis of 1-naphthalene phosphonic acid (Naph-PO₃H₂)	40
2.2.2 Synthesis of 1-biphenyl phosphonic acid (Biphen-PO₃H₂).....	41
2.2.3 Synthesis of 2,2'-((3-carboxy-2-hydroxynaphthalen-1-yl)methylazanediy)diacetic acid (H₄C₃hnida).....	41
2.2.4 Synthesis of 2,2'-((6-carboxy-2-hydroxynaphthalen-1-yl)methylazanediy)diacetic acid (H₄C₆hnida).....	41
2.3 Synthesis of lanthanide-organic hybrid compounds.....	42
2.3.1 Synthesis of lanthanide <i>tert</i> -butyl phosphonates (Ln-Bu^t), (1).....	42
2.3.2 Synthesis of lanthanide naphthalene phosphonates (Ln-Naph).....	42
2.3.3 Synthesis of lanthanide biphenyl phosphonates (Ln-Biphen)	43
2.3.4 Synthesis of Na ₂ [Eu ₂ (Hheidi) ₄ (H ₂ O)(MeOH)], (2)	43
2.3.5 Synthesis of Na ₂ [Eu(Hheidi)(heidi)(H ₂ O) ₂]·H ₂ O, (3)	43
2.3.6 Synthesis of 5,5'-methylenebis(6-hydroxy-2-naphthoic acid), C ₂₃ H ₁₆ O ₆ ·3DMF, (4)	44
2.3.7 Synthesis of [Nd ₅ (HC ₃ hnida)(C ₃ hnida) ₃ (H ₂ O) ₁₀]·25H ₂ O, (5)	44

2.3.8	Synthesis of $[\text{Nd}_{17}(\text{C3hnida})_{12}(\mu_3\text{-OH})_4(\text{H}_2\text{O})_{30}] \cdot x\text{H}_2\text{O}$, (6).....	45
2.3.9	Synthesis of $\text{Na}[\text{Ho}(\text{C}_6\text{H}_5\text{CO}_2)_4]$, (7).....	45
2.3.10	Synthesis of $[\text{Nd}_2(\text{SO}_4)_3(\text{H}_2\text{O})_8]$, (8).....	45
2.3.11	Synthesis of $(\text{C}_2\text{NH}_8)_9[\text{Nd}_5(\text{SO}_4)_{12}]$, (9).....	46
2.3.12	Synthesis of $(\text{NH}_4)[\text{Dy}(\text{SO}_4)_2(\text{H}_2\text{O})]$, (10).....	46
2.3.13	Synthesis of $(\text{NH}_4)_3[\text{Dy}(\text{SO}_4)_3]$, (11).....	46
2.4	References.....	46

Chapter 3 - Shedding light on two-dimensional lanthanide phosphonates: Understanding the structure-property relationships in developing visible and near-infra-red emitters 47

3.1	Introduction.....	48
3.2	Synthesis and characterisation of aromatic phosphonic acids.....	49
3.2.1	1-naphthalene phosphonic acid (Naph-PO₃H₂).....	50
3.2.2	4-biphenyl phosphonic acid (Biphen-PO₃H₂).....	50
3.3	Synthesis and characterisation of lanthanide phosphonates.....	51
3.3.1	Synthesis and crystal structure of $[\text{Eu}(\text{HO}_3\text{PC}(\text{CH}_3)_3)_3] \cdot \text{H}_2\text{O}$, Eu-Bu' , (1).....	51
3.3.2	Synthesis and structural characterisation of $[\text{Ln}(\text{O}_3\text{PC}_6\text{H}_5)_2(\text{H}_2\text{O})_2]$ and $[\text{Ln}(\text{O}_3\text{PC}_{12}\text{H}_9)_2]$	55
3.3.3	Physicochemical characterisation of Ln-phosphonates.....	56
3.4	Controlling crystal morphology in Ln-phosphonates.....	58
3.5	Steady-state and time-resolved photoluminescence studies of Ln-phosphonates.....	60
3.5.1	Eu^{III} - and Tb^{III} -phosphonates: Emission in the visible spectral region.....	60
3.5.2	Nd^{III} - and Yb^{III} -phosphonates: Emission in the Near-Infrared spectral region.....	67
3.6	Conclusion and Outlook.....	69
3.7	References.....	70

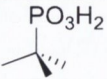
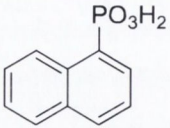
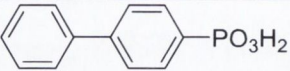
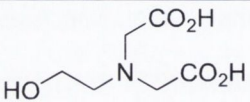
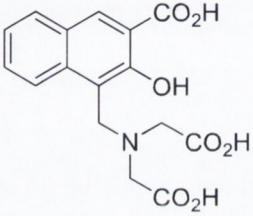
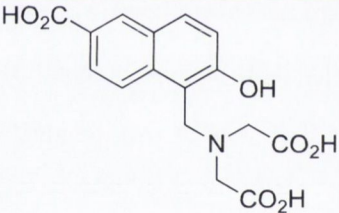
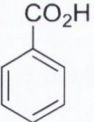
Chapter 4 - Building bridges: Lanthanide complexes derived from the ligand N-(2-hydroxyethyliminodiacetic acid, H₃heidi)..... 73

4.1	Introduction.....	74
4.2	Cluster chemistry of 2-hydroxyethyliminodiacetic acid, H ₃ heidi.....	75
4.2.1	Crystal structure of $\text{Na}_2[\text{Eu}_2(\text{Hheidi})_4(\text{H}_2\text{O})(\text{MeOH})]$, (2).....	75
4.2.2	Physicochemical characterisation of 2	79
4.2.3	Crystal structure of $\text{Na}_2[\text{Eu}(\text{Hheidi})(\text{heidi})(\text{H}_2\text{O})_2] \cdot \text{H}_2\text{O}$, (3).....	80

4.2.4	Physicochemical characterisation of 3	84
4.3	Solid-state and solution emission studies of lanthanide-heidi complexes: Understanding complex stability in solution	85
4.4	Conclusions and Outlook.....	90
4.5	References	91
Chapter 5 - Synthesis and characterisation of novel lanthanide-organic hybrid materials using iminodiacetic acid substituted aromatic ligands.....		93
5.1	Introduction	94
5.2	Synthesis and characterisation of the ligands	95
5.2.1	Synthetic mechanism for naphthol substituted iminodiacetic acids	95
5.2.2	Optical properties of H₄C3hnida and H₄C6hnida	96
5.3	The ligand chemistry of H ₄ C6hnida	99
5.3.1	Crystal structure of 5,5'-methylenebis(6-hydroxy-2-naphthoic acid), C ₂₃ H ₁₆ O ₆ ·3DMF, (4).....	100
5.3.2	Mechanism for the decomposition of H ₄ C6hnida.....	103
5.4	Lanthanide hybrid networks using the ligand H ₄ C3hnida	105
5.4.1	[Nd ₅ (HC3hnida)(C3hnida) ₃ (H ₂ O) ₁₀]-25H ₂ O, (5).....	105
5.4.2	[Nd ₁₇ (C3hnida) ₁₂ (μ ₃ -OH) ₄ (H ₂ O) ₃₀]:xH ₂ O, (6)	117
5.5	Conclusions	126
5.6	References	127
Chapter 6 - Probing the optical activity of chiral lanthanide networks derived from achiral ligands.....		129
6.1	Introduction	130
6.2	Crystal structure of Na[Ho(C ₆ H ₅ CO ₂) ₄], (7).....	131
6.3	Physicochemical characterisation of 7	135
6.4	Investigating the optical activity and emission properties of 7-Eu	136
6.4.1	UV/Vis Diffuse Reflectance and Circular Dichroism of 7-Eu	136
6.4.2	The emission properties of 7-Eu in the visible spectral range	138
6.5	Conclusions and Outlook.....	139
6.6	References	140

Chapter 7 - Exploiting organic templates to develop novel lanthanide sulphate frameworks.....	143
7.1 Introduction.....	144
7.2 Crystal structure of $[\text{Nd}_2(\text{SO}_4)_3(\text{H}_2\text{O})_8]$, (8).....	145
7.3 The crystal structure of $(\text{C}_2\text{NH}_8)_9[\text{Nd}_5(\text{SO}_4)_{12}]$, (9).	150
7.4 The crystal structure of $(\text{NH}_4)[\text{Dy}(\text{SO}_4)_2(\text{H}_2\text{O})]$, (10).	158
7.5 Crystal structure of $(\text{NH}_4)_3[\text{Dy}(\text{SO}_4)_3]$, (11)	162
7.6 Physicochemical characterisation of compounds 8-11	167
7.7 The effect of organic templates on the resulting structure.....	170
7.8 Conclusions and Outlook.....	170
7.9 References.....	171
Chapter 8 - Conclusions and future work	173
8.1 References.....	176

List of ligands

Abbreviation	Structure	Compound Name
'Bu-PO₃H₂		<i>tert</i> -butyl phosphonic acid
Naph-PO₃H₂		1-naphthalene phosphonic acid
Biphen-PO₃H₂		4-biphenyl phosphonic acid
H₃heidi		<i>N</i> -(2-hydroxyethyl)iminodiacetic acid
H₄C3hnida		2,2'-(((3-carboxy-2-hydroxynaphthalen-1-yl)methyl)azanediyl)diacetic acid
H₄C6hnida		2,2'-(((6-carboxy-2-hydroxynaphthalen-1-yl)methyl)azanediyl)diacetic acid
Benzoic acid		Benzoic acid

List of compounds

Ln-Bu'	$[\text{Ln}(\text{HO}_3\text{PC}(\text{CH}_3)_3) \cdot \text{H}_2\text{O}]$	$\text{Ln} = \text{Eu}^{\text{III}} \text{ (1)}, \text{Tb}^{\text{III}}, \text{Nd}^{\text{III}}, \text{Yb}^{\text{III}}$
Ln-Naph	$[\text{Ln}((\text{O}_3\text{PC}_{10}\text{H}_7)_2(\text{H}_2\text{O})_2)]$	$\text{Ln} = \text{Eu}^{\text{III}}, \text{Tb}^{\text{III}}, \text{Nd}^{\text{III}}, \text{Yb}^{\text{III}}$
Ln-Biphen	$[\text{Ln}((\text{O}_3\text{PC}_{12}\text{H}_9)_2)]$	$\text{Ln} = \text{Eu}^{\text{III}}, \text{Tb}^{\text{III}}, \text{Nd}^{\text{III}}, \text{Yb}^{\text{III}}$
2	$\text{Na}_2[\text{Ln}_2(\text{Hheidi})_4(\text{H}_2\text{O})(\text{MeOH})] \cdot 3\text{MeOH}$	$\text{Ln} = \text{Eu}^{\text{III}}, \text{Tb}^{\text{III}}$
3	$\text{Na}_2[\text{Ln}(\text{Hheidi})(\text{heidi})(\text{H}_2\text{O})_2] \cdot \text{H}_2\text{O}$	$\text{Ln} = \text{Eu}^{\text{III}}, \text{Nd}^{\text{III}}$
4	5,5'-methylenebis(6-hydroxy-2-naphthoic acid)	
5	$[\text{Ln}_5(\text{HC3hnida})(\text{C3hnida})_3(\text{H}_2\text{O})_{10}] \cdot 25\text{H}_2\text{O}$	$\text{Ln} = \text{Nd}^{\text{III}}, \text{Eu}^{\text{III}}, \text{Yb}^{\text{III}}$
6	$[\text{Nd}_{17}(\text{C3hnida})_{12}(\mu_3\text{-OH})_4(\text{H}_2\text{O})_{30}] \cdot x\text{H}_2\text{O}$	
7	$\text{Na}[\text{Ln}(\text{C}_6\text{H}_5\text{CO}_2)_4]$,	$\text{Ln} = \text{Ho}^{\text{III}}, \text{Eu}^{\text{III}}$
8	$[\text{Nd}_2(\text{SO}_4)_3(\text{H}_2\text{O})_8]$	
9	$(\text{Me}_2\text{NH}_2)_9[\text{Ln}_5(\text{SO}_4)_{12}]$	$\text{Ln} = \text{Nd}^{\text{III}}, \text{Gd}^{\text{III}}, \text{Dy}^{\text{III}}$
10	$\text{NH}_4[\text{Dy}(\text{SO}_4)_2(\text{H}_2\text{O})]$	
11	$(\text{NH}_4)_3[\text{Dy}(\text{SO}_4)_3]$	

Abbreviations

1D:	one-dimensional
2D:	two-dimensional
3D:	three-dimensional
2,5-H ₂ pydc:	pyridine-2,5-dicarboxylic acid
3-SBA:	3-sulfobenzoic acid
4-SBA:	4-sulfobenzoic acid
BET:	Brunauer-Emmett-Teller
bidc:	benzimidazole-5,6-dicarboxylic acid
Biphen-PO₃H₂ :	4-biphenyl phosphonic acid
bqdc:	2,2'-biquinoline-4,4'-dicarboxylic acid
BTB:	1,3,5-benzenetrisbenzoic acid
BTPCA:	1,1',1''(benzene-1,3,5-triyl)tripiperidine-4-carboxylic acid
Bu^t-PO₃H₂ :	<i>tert</i> -butyl phosphonic acid
CH ₃ CN:	acetonitrile
C ₆ H ₁₂ O:	cyclohexanol
CIE:	Commission Internationale de l'Eclairage
DABCO:	1,4-diazabicyclo[2.2.2]octane
DCM:	dichloromethane
DMF:	<i>N,N'</i> -dimethylformamide
DPA:	dipicolinic acid
ED:	electric dipole
EDTA:	ethylenediaminetetraacetic acid
EQ:	electric quadrupole
GGG:	gadolinium gallium garnet
H ₂ BDC:	1,4-benzenedicarboxylic acid
H ₂ BPDC:	2,2'-dipyridine-3,3'-dicarboxylic acid
H ₂ BPDCA:	biphenyl-4,4'-dicarboxylic acid
H ₃ BTC:	1,3,5-benzenetricarboxylic acid
H ₄ C3hnida:	2,2'-((3-carboxy-2-hydroxynaphthalen-1-yl)methylazanediy)diacetic acid
H ₄ C6hnida:	2,2'-((6-carboxy-2-hydroxynaphthalen-1-yl)methylazanediy)diacetic acid
H ₄ cit:	citrate
H ₃ heidi:	<i>N</i> -(2-hydroxyethyl)iminodiacetic acid
H ₃ hpdt:	hydroxypropane-1,3-diamine- <i>N,N,N',N'</i> -tetraacetic acid
H ₂ jda:	iminodiacetic acid
H ₆ Mell:	mellitic acid
H ₆ muc:	mucic acid

H ₂ ndc:	1,4-naphthalenedicarboxylic acid
H ₄ NDP:	naphthalene-1,4-diphosphonic acid
H ₂ oba:	4,4'-oxybis(benzoic acid)
H ₂ ox:	oxalic acid
H ₂ pvlc:	4,4-[2,5-dimethoxy-1,4-phenylene- <i>di</i> -2,1,ethenediyl]bisbenzoic acid
H ₂ pdic:	pyridine-2,6-dicarboxylic acid
H ₂ pza:	2,3-pyrazinedicarboxylic acid
H ₃ TCM:	(4,4',4''-(((2,4,6-trimethylbenzene-1,3,5-triyl)- <i>tris</i> (methylene))- <i>tris</i> (oxy)))tribenzoic acid
H ₂ tip:	5- <i>tert</i> -butylisophthalic acid
IP:	1 <i>H</i> -imidazo[4,5- <i>f</i>][1,10]-phenanthroline
ITO:	indium-tin-oxide
Ln ^{III} :	lanthanide (III) ion
<i>m</i> -BDC:	1,3-benzenedicarboxylic acid
MCE:	magentocaloric effect
MD:	magnetic dipole
MOF:	metal-organic frameworks
MRI:	magnetic resonance imaging
N-H ₂ BDC:	2-aminoterephthalic acid
Na-DMPS:	sodium dimercaptopropane sulfonate
Na(cda):	sodium carbamylidicyanomethanide
Naph-PO₃H₂ :	1-naphthalene phosphonic acid
NIR:	Near-Infrared
phen:	1,10-phenanthroline
PL:	photoluminescence
SMM:	single molecule magnet
STS:	sodium <i>p</i> -toluene sulfonate
SBU	secondary building unit
'Bubpy:	4,4'- <i>di-tert</i> -butyl-2,2'-bipyridine
TC:	tetracycline
UC:	Up-conversion

List of symbols

A_{MD} :	spontaneous emission probability
I_{tot} :	integrated area for the Eu^{III} emission spectrum
I_{MD} :	integrated area for the magnetic dipole transition, ${}^5\text{D}_0 \rightarrow {}^7\text{F}_1$, of the Eu^{III} ion
I_{tot}/I_{MD} :	ratio of the integrated areas for Eu^{III} emission spectrum to the ${}^5\text{D}_0 \rightarrow {}^7\text{F}_1$
J :	total angular momentum
k_r :	radiative rate constant
k_{nr} :	non-radiative rate constant
l_i :	orbital angular momentum
L :	total orbital angular momentum
n :	refractive index
n_w :	number of coordinated water molecules (in the first coordination sphere)
R :	gas constant
S_i :	spin angular momentum
S :	total spin angular momentum
S_n :	the n th excited singlet state
SS_{reg} :	sum of the squares
SS_{tot} :	total sum of the squares
T_n :	the n th excited triplet state
α_i :	pre-exponential factor
ΔS_m :	magnetic entropy change
ε :	molar absorption coefficient
$\hat{\varepsilon}$:	residual
η_{sens} :	efficiency of ligand sensitisation
λ :	wavelength
λ_{abs} :	wavelength of maximum absorption
λ_{ex} :	excitation wavelength
λ_{em} :	emission wavelength
ν_{XH} :	energy of the X-H bond vibration (in cm^{-1})
σ^2 :	variance of the data
$\tau(\text{H}_2\text{O})$:	observed photoluminescence lifetime in H_2O
$\tau(\text{D}_2\text{O})$:	observed photoluminescence lifetime in deuterated water, D_2O
τ_{obs} :	observed emission lifetime
τ_r :	radiative lifetime
Φ_{LS} :	ligand sensitised emission quantum yield
Φ_{PL} :	emission quantum yield
χ^2 :	the chi-square statistic

Chapter One



Introduction

1.1 Functional inorganic-organic materials

In the 1990s, inorganic-organic hybrid materials came to the forefront of research science with the development of metal organic frameworks (MOFs) that consist of inorganic cluster units which are connected through rigid polyfunctional ligands to produce extended structures that are often two-dimensional (2D) and three-dimensional (3D) in nature. These materials have largely been developed for creating porosity,¹⁻⁵ with applications designed towards gas storage⁶⁻⁸ and separation⁹ and heterogeneous catalysis.¹⁰ The definition for metal-organic frameworks is often confused with coordination polymers and inorganic-organic hybrid materials.¹¹ Metal-organic frameworks are now largely considered as 3D materials, where the rigid linkers impart porosity. These materials are a sub-group of the wider definition of inorganic-organic hybrids which are compounds that contain organic and inorganic components as part of their structure and whose bonding extends infinitely in at least one dimension of space.¹² The focus of this thesis is the synthesis and characterisation of hybrid lanthanide-organic materials. In particular, the incorporation of lanthanide (III) ions (Ln^{III}) to produce new functional materials that exploit the optical and magnetic properties of the lanthanide ion will be undertaken.

1.1 Classification of hybrid inorganic-organic materials

The classification outlined by Cheetham and Rao considers the dimensionality of hybrid materials to be broken into two types of connectivity; extended inorganic bridging (I) and bridging through an organic ligand (O).¹² This leads to a description of the overall dimensionality as $I^n O^m$, where n is the dimensionality of the inorganic bridging mode and m is the dimensionality imparted by the bridging ligand, where the sum of the exponents is the overall dimensionality in the structure.¹³

Table 1.1 summarises how the mixing of the two different bridging modes results in different inorganic-organic networks. The following paragraphs aim to highlight the structural features that differ between these structures. The description, $I^0 O^0$, describes molecular cluster based complexes, which go beyond the scope of the present work.

Table 1.1: Classification of hybrid inorganic-organic materials.

		Dimensionality of inorganic connectivity, I^n ($n = 0-3$)			
		0	1	2	3
Metal-organic-metal connectivity, O^m ($m = 0-3$)	0	Molecular complexes I^0O^0	Hybrid inorganic chains I^1O^0	Hybrid inorganic layers I^2O^0	3D inorganic hybrids I^3O^0
	1	Chain coordination polymers I^0O^1	Mixed inorganic-organic layers I^1O^1	Mixed inorganic-organic 3D framework I^2O^1	
	2	Layered coordination polymers I^0O^2	Mixed inorganic-organic 3D framework I^1O^2		
	3	3D coordination polymers I^0O^3			

1.1.1 Hybrid structures built from inorganic connectivity, I^mO^0

The first row in **Table 1.1** describes hybrid materials that have inorganic dimensionality varying from one-dimensional (1D) inorganic chains, to layers (2D) and 3D networks (**Figure 1.1**). A unique example of one-dimensional I^1O^0 Ln^{III} chains is observed in $[\text{Ln}_2(\text{H}_2\text{O})_2(\text{C}_{14}\text{H}_8\text{O}_4)_3]$ where $\text{Ln}^{\text{III}} = \text{Nd}^{\text{III}}$ or Dy^{III} and $(\text{C}_{14}\text{H}_8\text{O}_4) =$ biphenyl-2,2'-dicarboxylic acid.¹⁴ The structure contains two unique Ln^{III} centres in a distorted dodecahedral geometry and coordinated through two ligands, one that binds in a monodentate fashion and a second ligand that bonds through two monodentate oxygen centres and one bis-bidentate carboxylate group. Bridging through the carboxylate groups to further lanthanide centres results in the growth of a 1D chain that closely resembles the natural mineral, tancoite, of composition $[\text{M}(\text{TO}_4)_2\text{L}]_n$, where M and T are cations with different coordination geometry and L = small anionic ligand (*e.g.* O^{2-} , OH^-).

Metal phosphonates are excellent examples of hybrid inorganic layers with connectivity I^2O^0 .¹⁵ In the lanthanide phenyl phosphonate, $[\text{Ln}(\text{O}_3\text{PC}_6\text{H}_5)(\text{HO}_3\text{PC}_6\text{H}_5)]$, inorganic $\{\text{Ln}^{\text{III}}\text{-O}\}$ based regions extend in two dimensions forming a layered motif from the bridging P-O centres. The organic moieties are found to extend into the interlamellar spacings. We consider lanthanide phosphonate systems more extensively in **Chapter 3**.

Using the simple ligand, pyridine-2,5-dicarboxylic acid (2,5- H_2pydc) under hydrothermal conditions, the 3D inorganic network $[\text{Ln}_3(\mu\text{-OH})_4(2,5\text{-pydc})(2,5\text{-Hpydc})_3(\text{H}_2\text{O})_4]_n$ is isolated.¹⁶ The presence of four adjacent helical dodecahedral chains that connect further through edge-sharing polyhedra results in the generation of a 3D framework built from corrugated $\{\text{Ln}_{12}\}$ membered-wheels. The above examples are visualised in **Figure 1.1**.

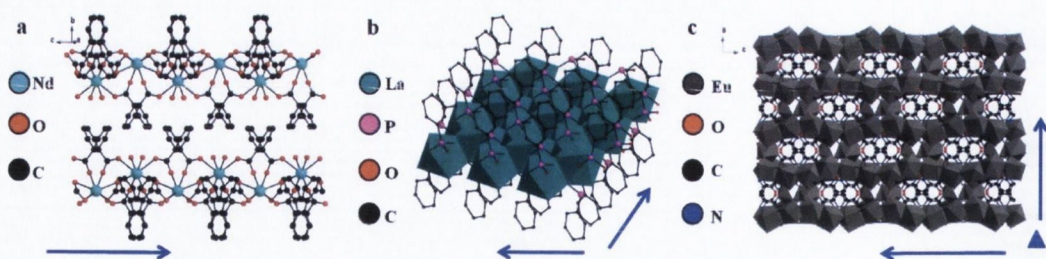


Figure 1.1: Representative crystal structures of (a) 1D chains of $[\text{Ln}_2(\text{H}_2\text{O})_2(\text{C}_{14}\text{H}_8\text{O}_4)_3]$, $I^1\text{O}^{14}$, (b) 2D layers of $[\text{Ln}(\text{O}_3\text{PC}_6\text{H}_5)(\text{HO}_3\text{PC}_6\text{H}_5)]$, $I^2\text{O}^{15}$ and (c) network structure of $[\text{Ln}_3(\mu\text{-OH})_4(2,5\text{-pydc})(2,5\text{-Hpydc})_3(\text{H}_2\text{O})_4]_n$, $I^3\text{O}^{16}$ whose bonding originates through inorganic M-O-M interactions. Blue arrows denote the direction of inorganic connectivity.

1.1.2 Hybrid structures built from organic connectivity, $I^0\text{O}^n$

The first column in **Table 1.1** represents materials that are solely constructed from bridging organic ligands and are shown in **Figure 1.2**. One-dimensional Ln^{III} chains are isolated in $[\text{Dy}(\text{BTC})(\text{H}_2\text{O})]\cdot\text{DMF}$, where $\text{H}_3\text{BTC} = 1,3,5\text{-benzenetricarboxylic acid}$ and $\text{DMF} = N,N\text{-dimethylformamide}$.¹⁷ Crystallising in the chiral space group $P4_322$, the chiral chains pack to form a porous framework that was shown to remain stable upon removal of coordinated H_2O , leading to a high surface area of $655 \text{ m}^2 \text{ g}^{-1}$, with potential for H_2 and CO_2 storage capabilities due to the free Lewis acidic site obtained from dehydration.

A layered $I^0\text{O}^2$ material based on a two-ligand system that was developed for white lighting is shown in **Figure 1.2b**.¹⁸ The reaction of $\text{Ln}(\text{NO}_3)_3$ with 4-sulfobenzoic acid (4-SBA) and 1*H*-imidazo[4,5-*f*][1,10]-phenanthroline (IP) yields the compound $[\text{Ln}(4\text{-SBA})(\text{IP})\text{OH}]\cdot 1.5\text{H}_2\text{O}$. The structure is built from a Ln^{III} binuclear unit that is bridged through the $\mu\text{-OH}$ groups to give the building unit, $[\text{Ln}_2(\mu_2\text{-OH})_2(\text{IP})_2]^{4+}$. These $[\text{Ln}_2(\mu_2\text{-OH})_2(\text{IP})_2]^{4+}$ units are further coordinated by the 4-SBA molecules. The 4-SBA bridges through the carboxylate and sulfo-moieties along the *a*-axis and the sulfo-moieties further link $[\text{Ln}_2(\mu_2\text{-OH})_2(\text{IP})_2]^{4+}$ moieties along the *b*-axis to form the layered structure.

The complexity of these building blocks can be extended to the formation of porous 3D framework materials with $I^0\text{O}^3$ connectivity.¹⁹ In the compound, $[\text{H}_2\text{NMe}_2][\text{Ln}_2(m\text{-BDC})_3(\text{phen})_2]$ where *m*-BDC is 1,3-benzenedicarboxylic acid and phen is 1,10-phenanthroline, an octahedral building unit of $[\text{Eu}_2(\text{COO})_6]$ is formed *in-situ*. These units are constructed from four bridging and two chelating carboxylates. This leads to two types of coordination modes of the *m*-BDC²⁻ ligand. The first type coordinates in a $\eta^1:\eta^1:\eta^1:\eta^1:\mu_2$ fashion linking the $[\text{Ln}_2(\text{COO})_6]$ units into a layer in the *bc*-plane. The second type coordinates in a $\eta^2:\eta^1:\eta^2:\mu_3$ mode and links these layers further in the *c*-direction to produce a pillared 3D framework.

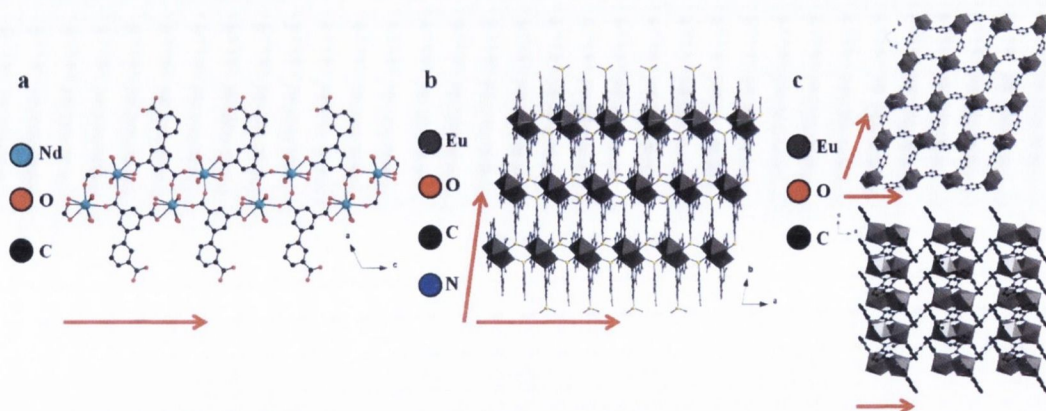


Figure 1.2: Representative crystal structures of (a) 1D chains of [Dy(BTC)(H₂O)]·DMF, I^0O' ,¹⁷ (b) 2D layers of [Ln(4-SBA)(IP)OH]·1.5H₂O, I^0O^2 ¹⁸ and (c) the network structure of [H₂NMe₂][Ln₂(m-BDC)₃(phen)₂], I^0O^3 ,¹⁹ where lanthanide centres are bridged through the ligands. Red arrows denote the projection along which connectivity extends through the bridging ligand molecules.

1.1.3 Hybrid structures built from mixed connectivity, I^mO^n

In **Figure 1.3**, examples of mixed inorganic-organic layered materials, I^lO^l , and mixed inorganic-organic 3D framework materials of connectivity I^lO^2 and I^2O^l are given. The I^lO^l connectivity is rare, with the lanthanum phosphonate, [La(H₂NDP(1,4))(H₃NDP(1,4))(H₂O)₂]_n (H₄NDP(1,4) = naphthalene-1,4-diphosphonic acid) being one of the few cases.²⁰ A number of 3D frameworks are based on the I^lO^2 connectivity. One such example is [Tb(BTB)(H₂O)]·2C₆H₁₂O, where BTB=1,3,5-benzenetrisbenzoic acid and C₆H₁₂O = cyclohexanol.²¹ The Tb^{III} centre is 9-coordinate and bound by eight carboxylate oxygen atoms and one water molecule. A chain of edge-sharing TbO₉ polyhedra extends along the *c*-axis that are connected *via* the tritopic ligand resulting in a 3D-framework with hexagonal 1D pores. Upon removal of the cyclohexanol, pore diameters of *ca.* 10 Å are observed and large surface areas of 730-930 m² g⁻¹ (Brunauer-Emmett-Teller (BET) model) could be obtained. In comparison, the lanthanide phosphonate, Ln(O₃PC₆H₅PO₃) based on I^2O^l connectivity, is a 3D framework constructed from the pillaring effect of the ligand of the inorganic layer formed through the coordinating phosphonate oxygen donor atoms.²² Each phosphonate on a ligand coordinates in a $\eta^2:\eta^1:\eta^1:\mu_3$ bonding mode. This coordination leads to the formation of edge-sharing inorganic chains parallel to the [101] direction, which is further connected through the phosphonate oxygen atoms into an inorganic layer. The organic moiety of the ligand bridges and pillars these layers along the *b*-axis. The low surface area (29 m² g⁻¹ (BET model) using N₂ at 77 K) shows that the channels created by the pillaring ligand are small and not accessible to the adsorbing gas.

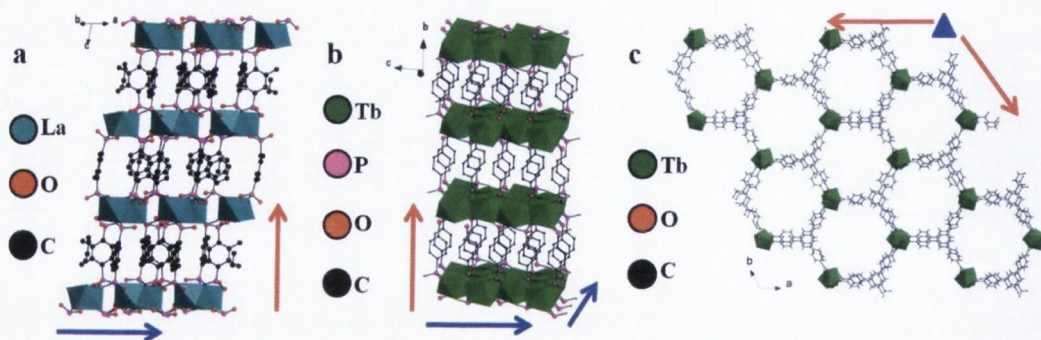


Figure 1.3: Crystal structures of discrete layers of (a) $[\text{La}(\text{H}_2\text{NDP}(1,4))(\text{H}_3\text{NDP}(1,4))(\text{H}_2\text{O})_2]_n$ in the plane of the page, $I^{\prime}O^{\prime}$.²⁰ (b) Mixed inorganic-organic framework $[\text{Tb}(\text{BTB})(\text{H}_2\text{O})] \cdot 2\text{C}_6\text{H}_{12}\text{O}$, $I^{\prime}O^{\prime}$.²¹ and (c) mixed inorganic-organic framework $\text{Ln}(\text{O}_3\text{PC}_6\text{H}_5\text{PO}_3)$, $I^{\prime}O^{\prime}$.²² Red arrows denote connectivity through organic ligands and blue arrows denote inorganic connectivity. The blue triangle denotes the inorganic chain in (c) that runs into the page along the *c*-axis.

The examples given here demonstrate the variety in the structures that are accessible for lanthanide-based materials. By tuning the amount of inorganic connectivity to organic connectivity in the hybrid, the density of the material can be tuned. Inorganic M-O-M bonding favours edge-sharing interactions between lanthanide centres and results in dense hybrid materials where the lanthanide centres are in close proximity. The higher density of lanthanide centres in these materials may favour applications that utilise the electronic and magnetic properties of the lanthanide. The result of organic connectivity can lead to larger voids between lanthanide centres or clusters of lanthanide centres. This often results in more open structures where the inherent porosity may be used for gas storage, small molecule sensing and catalytic purposes. This thesis focuses on the optical properties of the lanthanide and, where materials seemed interesting, considers the magnetic properties. The following section introduces some of the theoretical background behind the physical properties that will be discussed.

1.2 Lanthanide coordination

The lanthanides are characterised by the occupation of electrons in the *4f* orbitals. The radial distribution function of the *4f* orbitals shows the maximum charge density to be inside the outermost electrons of the *5d* and *5s* orbitals and is considered to be shielded. As a result the coordination nature is found to be largely due to electrostatic interactions with the ligands. Due to the large ionic radii of the lanthanide series (116.0-98.5 pm [La^{III} - Yb^{III} (coordination number = 8)]),²³ larger coordination numbers are possible and structures with coordination numbers from 3-12 are known, although 8 and 9 are considered the most common.²⁴ Focussing on coordination numbers of 8 and 9, a number of common coordination polyhedra appear, including dodecahedra and square antiprism for eight coordinate centres, while the capped square antiprism and the tricapped trigonal prism are common for 9-coordinate geometries. The geometry adopted by the lanthanide centres is difficult to predict and is a balance between the electrostatic interaction of the ion and ligand, and the steric demands originating from the ligand.

1.3 Optical transitions in lanthanide ions

1.3.1 Origin of lanthanide photoluminescence

Many of the lanthanide ions are known to display photoluminescence (PL) and this phenomenon arises from intra- $4f$ transitions. Depending on the lanthanide centre it is possible to observe visible (Ce^{III} ($4f$ - $5d$)-blue, Tm^{III} -blue, Sm^{III} -orange-red, Eu^{III} -red and Tb^{III} -green) and Near-Infrared (NIR) (Nd^{III} , Er^{III} and Yb^{III}) PL responses. Emission may also be observed from Pr^{III} , Dy^{III} , and Ho^{III} in both the visible and NIR regions, albeit much weaker than the former lanthanides. As the $4f$ electrons are shielded by the $5s$ and $5p$ orbitals, the resulting emission bands are narrow which leads to the high colour purity that the lanthanides are known for.

The splitting of the energy levels of the $4f$ orbitals is a consequence of electronic repulsion, spin-orbit coupling and ligand field effects, as shown in **Figure 1.4**. The strength of these interactions varies, resulting in the observed splitting of the energy levels. Electronic repulsion between electrons is the strongest interaction and splits the energy levels on the order of 10^4 cm^{-1} into term states of different energy. Spin-orbit coupling is the interaction between the spin angular momentum and the orbital angular momentum of the electrons and splits the energy levels on the order of 10^3 cm^{-1} , resulting in the J -states of the $4f$ levels. When placed in a ligand field, the degeneracy of the J -states is removed with splitting on the order of 10^2 cm^{-1} . The small nature of this splitting is a result of the shielded nature of the electrons.

The splitting of the energy levels into different J -states is summarised within a term symbol, $^{2S+1}L_J$, which can be described according to the Russell-Saunders coupling scheme.²⁵ This describes the spin multiplicity, $2S+1$, where S is the total spin angular momentum of the system. The total orbital angular momentum, L , is the combination from coupling of the individual orbital angular momenta, l_i , where $L = \sum_i l_i$. The value of L is given by the symbols S ($L = 0$), P ($L = 1$), D ($L = 2$), F ($L = 3$), G ($L = 4$) *etc.* Finally, J describes the total angular momentum and accounts for the spin-orbit coupling of the electrons and determined as $J = \sum_i (l_i + s_i)$. To determine the ground state term for the lanthanide ion, if the $4f$ electronic configuration is more than half-filled then $J = J_{\text{max}}$ and when the electronic configuration is less than half-filled, $J = J_{\text{min}}$.

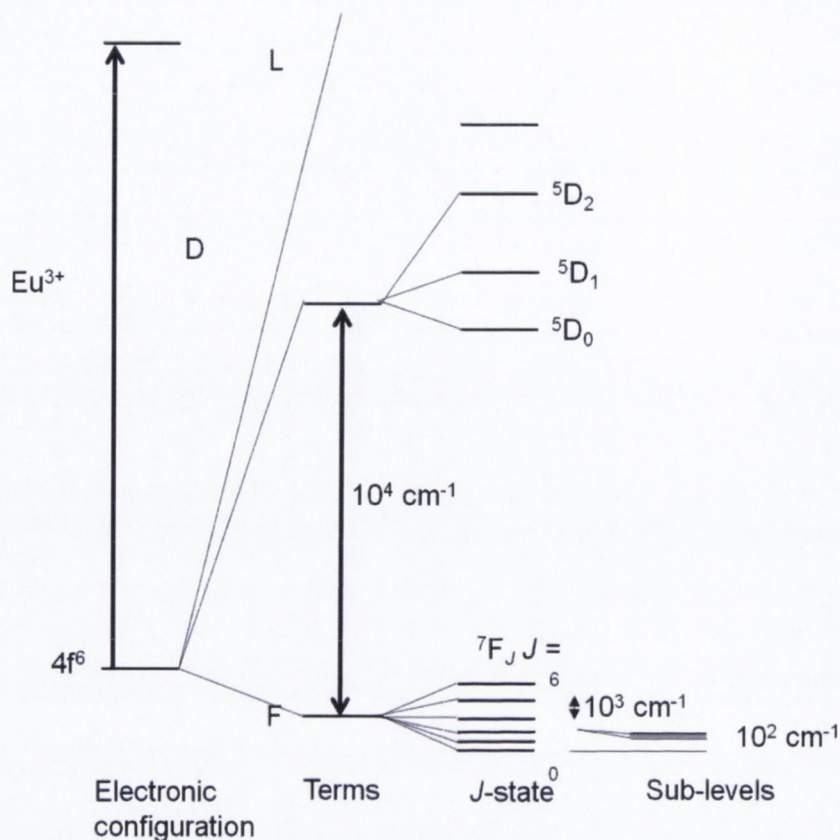


Figure 1.4: Schematic representation of the splitting of the $4f$ energy levels due to electronic repulsion, spin-orbit-coupling and ligand-field effects. The example presented is for a Eu^{III} ion.

Electron transitions occur between these energy levels *via* the absorption of light. For this to happen there are three operators that are related to the nature of light; the odd-parity electric dipole (ED), the even-parity magnetic dipole (MD) and the electric quadrupole operator (EQ). Transitions between electrons must obey certain selection rules related to these operators and are summarised in **Table 1.2**.²⁶ The Laporte (parity) rule also requires that the angular momentum of the electrons between the initial and final state must change by an odd integer. This restricts transitions from occurring within the same shell, *i.e.* $d-d$ transition and $f-f$ transitions.

Table 1.2: Selection rules for $f-f$ transitions between different energy levels.²⁶

Operator	Parity	ΔS	ΔL	ΔJ
ED	Opposite	0	≤ 6	≤ 6
MD	Same	0	0	$0, \pm 1$
EQ	Same	0	$0, \pm 1, \pm 2$	$0, \pm 1, \pm 2$

By considering the Laporte rule, electric dipole transitions within $f-f$ transitions are forbidden. Magnetic transitions are allowed, although they are observed with weak intensity due to low oscillator strengths. The Laporte rule and electric dipole transitions can be relaxed through a number of mechanisms. When the lanthanide centre experiences a ligand field, coupling between vibrational states reduces the symmetry around the lanthanide and increases the probability for the

transition to occur. Other mechanisms involve J -mixing and mixing with opposite-parity wavefunctions, largely the $5d$ orbitals, and through these mechanisms the electric dipole transitions become partially allowed. The result of these selection rules is that the molar absorption coefficients (ϵ) of these transitions are very low, with $\epsilon \leq 5 \text{ mol}^{-1} \text{ dm}^3 \text{ cm}^{-1}$.

Due to the core-like nature of the $4f$ electrons, the PL spectra for the lanthanides do not vary strongly with coordination environment. The emission lines arise from transitions between $4f$ energy levels and only small shifts in the wavelength of the bands in different ligand environments are observed. As such, the typical emission lines for certain lanthanides in this thesis are summarised in **Table 1.3**.

Table 1.3: Typical emission bands observed for Eu^{III} , Tb^{III} , Nd^{III} and Yb^{III} in the solid-state.

Ln^{III}	Transition	λ / nm	Ln^{III}	Transition	λ / nm
Eu	$^5\text{D}_0 \rightarrow ^7\text{F}_0$	580	Nd	$^4\text{F}_{3/2} \rightarrow ^4\text{I}_{9/2}$	880
	$^5\text{D}_0 \rightarrow ^7\text{F}_1$	590		$^4\text{F}_{3/2} \rightarrow ^4\text{I}_{11/2}$	1060
	$^5\text{D}_0 \rightarrow ^7\text{F}_2$	614		$^4\text{F}_{3/2} \rightarrow ^4\text{I}_{13/2}$	1330
	$^5\text{D}_0 \rightarrow ^7\text{F}_3$	650	Yb	$^2\text{F}_{5/2} \rightarrow ^2\text{F}_{7/2}$	980
	$^5\text{D}_0 \rightarrow ^7\text{F}_4$	700			
Tb	$^5\text{D}_4 \rightarrow ^7\text{F}_6$	490			
	$^5\text{D}_4 \rightarrow ^7\text{F}_5$	550			
	$^5\text{D}_4 \rightarrow ^7\text{F}_4$	590			
	$^5\text{D}_4 \rightarrow ^7\text{F}_3$	620			
	$^5\text{D}_4 \rightarrow ^7\text{F}_2$	650			

1.3.2 Quenching by high frequency oscillators

There are a number of non-radiative processes that compete with the radiative luminescence pathway and in particular, O-H ($\nu_{\text{OH}} \sim 3300\text{-}3500 \text{ cm}^{-1}$), C-H ($\nu_{\text{CH}} \sim 2950\text{-}3050 \text{ cm}^{-1}$) and N-H ($\nu_{\text{NH}} \sim 3300 \text{ cm}^{-1}$) vibrations can play a significant role in the quenching of energy from the excited state.²⁷ Quenching occurs through vibronic coupling with the $4f$ excited electronic states and a harmonic level of the vibration. As such, the quenching is more significant when a smaller number of harmonic vibrational quanta matches the lanthanide energy gap. This results in the O-H vibration showing significant quenching of the Eu^{III} and Tb^{III} luminescence by the fourth harmonic of the O-H vibration. The lanthanides Nd^{III} , Er^{III} and Yb^{III} have smaller energy gaps between the excited and ground states and so can be more efficiently quenched by the second harmonic of C-H and N-H oscillators. The relationship between the fundamental and harmonic energies of the different oscillators with the energy of the lanthanide excited states is summarised in the **Figure 1.5**. The extent to which the different lanthanide centres are quenched significantly

affects the emission lifetime and quantum yields of the lanthanide. The lanthanides, Eu^{III} and Tb^{III} , with a larger energy gap, are significantly quenched by the O-H oscillator and have lifetimes in the millisecond (ms) range, and the resulting quantum yields are often higher. By comparison, the NIR emitters are also prone to quenching from the C-H and N-H oscillators, which is reflected by their shorter lifetimes in the range of μs -ns, and much smaller emission quantum yields.

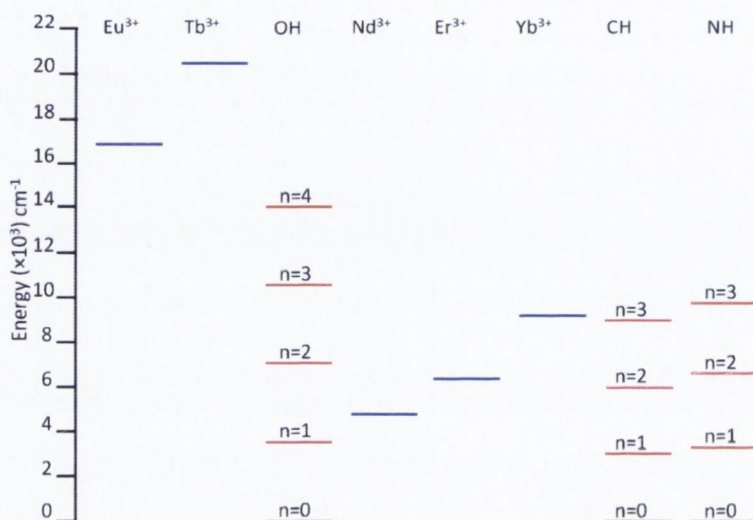


Figure 1.5: Schematic diagram showing the energy of the main excited state transitions for emission from Eu^{III} , Tb^{III} , Nd^{III} , Er^{III} and Yb^{III} and the energy of the harmonic levels of the vibrational oscillators of OH, CH and NH.

1.3.3 Quantitative analysis of lanthanide luminescence

In addition to measuring the steady-state PL spectrum of Ln^{III} materials, the observed emission lifetime, τ_{obs} , and the emission quantum yield, Φ_{PL} can be measured. When the excited and emissive state is formed *via* only light absorption or is formed with unitary efficiency, the emission quantum yield can be considered as the ratio of the number of emitted photons to the number of photons absorbed and may be measured directly using an integrating sphere, or through determination against a known standard. This property is a balance between the radiative rate constant, k_r , and the non-radiative rate constant, k_{nr} , which accounts for all pathways that result in relaxation of the excited state without emission of a photon. This can be expressed as:

$$\Phi_{\text{PL}} = \frac{k_r}{k_{\text{nr}} + k_r} = \frac{\tau_{\text{obs}}}{\tau_r} \quad \text{Eqn. 1.1}$$

where Φ_{PL} is the emission quantum yield, k_{nr} includes all non-radiative processes such as internal conversion, intersystem crossing and vibrational relaxation and τ_r is the radiative lifetime. The observed emission lifetime, τ_{obs} , is the average time that an electron spends in the excited state before spontaneous emission to the ground state and given by:

$$\tau_{\text{obs}} = \frac{1}{k_r + k_{\text{nr}}} = \frac{1}{k_{\text{obs}}} \quad \text{Eqn. 1.2}$$

where k_{obs} is the rate constant for the de-population of the excited state by both radiative and non-radiative pathways. In lanthanide-based materials, the observed emission lifetime, τ_{obs} , provides

information on the number of unique lanthanide centres within the complex/network structure. This may be obtained through fitting multi-exponential functions to the luminescence decay, where each exponential decay component relates to a unique lanthanide centre. However, caution must be taken in these measurements to (i) ensure no artefacts from the initial lamp excitation pulse are present at the start of the decay, (ii) the decay lasts up to five or six lifetimes and (iii) the signal returns to the background value at the end of the decay. The emission lifetimes can also be used for more in-depth analysis that will be discussed further below.

The Eu^{III} ion is a particularly good example where additional information can be extracted from the steady-state (**Figure 1.6**) and time-resolved PL. If the emission quantum yield cannot be measured directly, we can see from **Eqn. 1.1** that if the radiative lifetime, τ_r , is known, in addition to τ_{obs} , then the efficiency of emission from the lanthanide centre, we shall denote as η_{Ln} , can be estimated. In the case of Eu^{III} , the radiative lifetime, τ_r , can be determined using the corrected emission spectrum and by noting that the ${}^5\text{D}_0 \rightarrow {}^7\text{F}_1$ (**Figure 1.6**) is purely magnetic dipole in nature. By assuming that the energy and dipole strength of this transition is constant it is possible to estimate τ_r using the equation below:

$$\frac{1}{\tau_r} = A_{\text{MD}} n^3 \left(\frac{I_{\text{tot}}}{I_{\text{MD}}} \right) \quad \text{Eqn. 1.3}$$

where A_{MD} is a constant (14.65 s^{-1})²⁸ and is the spontaneous emission probability for the ${}^5\text{D}_0 \rightarrow {}^7\text{F}_1$ transition *in-vacuo*, n , is the refractive index of the medium and $(I_{\text{tot}}/I_{\text{MD}})$ is the ratio of the integrated area for the Eu^{III} emission spectrum, I_{tot} , to the integrated area for the ${}^5\text{D}_0 \rightarrow {}^7\text{F}_1$ transition, I_{MD} .

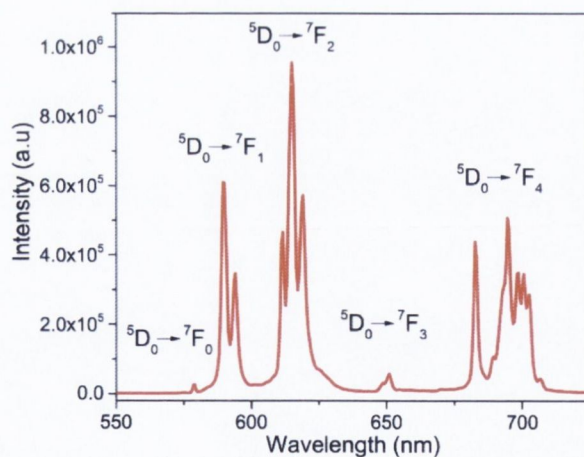


Figure 1.6: A typical steady-state PL spectrum for a Eu^{III} compound (**3-Eu** from **Chapter 4**) measured in the solid-state. The transitions have been identified for clarity with the text.

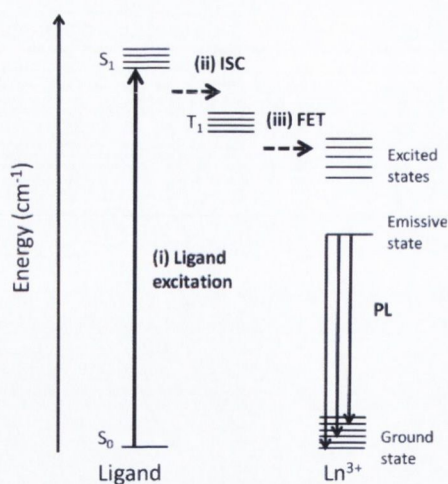


Figure 1.7: Schematic Jablonski diagram identifying the three main steps considered important in the role of the *antenna effect* in sensitising Ln^{III} emission. ISC – intersystem crossing, FET – forward energy transfer.

The low molar absorption coefficient exhibited by Ln^{III} ions typically leads to poor excitation of the centre and consequently weak emission. To overcome this drawback, the *antenna effect* has been established as an alternative route to excite the Ln^{III} centre.²⁹ The mechanism for sensitisation of Ln^{III} luminescence through an antenna ligand is often described by a three step process (**Figure 1.7**) involving (i) ligand excitation to the excited singlet state, S_n (often $n = 1$), (ii) intersystem crossing to an ligand excited triplet state, T_n (often $n = 1$) and (iii) energy transfer from the excited ligand triplet state to the excited state in the higher excited states of the Ln^{III} centre, followed by emission. Although this is accepted as the primary mechanism, other sensitisation routes involving energy transfer from excited S_1 states are known^{30, 31} and it is believed that up to 30 different rate constants are involved within the sensitisation pathway.³² By considering the simplified three step model, a few empirical guidelines to ligand design have surfaced:

- (i) The molar absorption coefficient of the ligand is to be as high as possible.
- (ii) For Eu^{III} and Tb^{III} , a T_n -Ln energy gap between 2500-3500 cm^{-1} is recommended. Below this range the probability of back energy transfer from the lanthanide to the ligand triplet state increases,³³⁻³⁵
- (iii) The ligand should fully fill the first coordination sphere of the lanthanide. Through this approach, coordinated water molecules are minimised, which reduces quenching through O-H oscillators.

Taking the above simple model for the antenna effect, the emission quantum yield upon ligand sensitisation, Φ_{LS} , can be considered by the following relation:

$$\Phi_{\text{LS}} = \eta_{\text{sens}} \Phi_{\text{PL}} \quad \text{Eqn. 1.4}$$

where η_{sens} is the efficiency of sensitisation from the organic ligand and takes into account the efficiency of ligand absorption, intersystem crossing in the ligand and energy transfer to the Ln^{III} centre. The closer to unity the value of η_{sens} , the greater the sensitisation from the ligand and as a result the stronger the emission from the Ln^{III} centre.

Additional analysis of the steady-state PL spectrum of the Eu^{III} ion provides information on the number of unique Eu^{III} sites and site symmetry of the centre. The ${}^5\text{D}_0 \rightarrow {}^7\text{F}_0$ transition is strictly forbidden, however, in the presence of a ligand field this transition may be weakly observed in the PL spectrum (**Figure 1.6**). As the excited and ground states of the transition are both non-degenerate, there is a one-to-one relationship between unique lanthanide centres and the composition of the band. By utilising Gaussian deconvolution of the emission line, the number of components required to fit the transition will directly relate to the number of Eu^{III} centres.

The Stark splitting patterns of the emission lines provide site symmetry information.³⁶ The number of Stark splitting components of the ${}^5\text{D}_0 \rightarrow {}^7\text{F}_1$ transition indicates the crystal system that the compound is in. A single component relates to the cubic crystal system, two components for a tetragonal, trigonal or hexagonal crystal system, while three components are due to the lower symmetry orthorhombic, monoclinic and triclinic crystal systems. The hypersensitive transition ${}^5\text{D}_0 \rightarrow {}^7\text{F}_2$ can be used to help determine the possible point group symmetry of the Eu^{III} centre based on the number of splitting components.

Lanthanide emission is sensitive to quenching by non-radiative pathways typically from O-H, C-H and N-H vibrations (**Section 1.3.2**) which decreases the observed emission lifetime. It is possible to determine the number of coordinated water molecules, n_w , to the lanthanide centre from the measured lifetime values in hydrated and deuterated solution. From a large series of lanthanide complexes, the following equation has been determined that can reliably determine n_w for lanthanide compounds:

$$n_w = A \left[\frac{1}{\tau(\text{H}_2\text{O})} - \frac{1}{\tau(\text{D}_2\text{O})} - B \right] \quad \text{Eqn. 1.5}$$

where $\tau(\text{H}_2\text{O})$ and $\tau(\text{D}_2\text{O})$ are the observed lifetimes in milliseconds in water and D_2O , respectively, and A and B are pre-determined constants that depend on the lanthanide ($A = 1.11$ - Eu^{III} , 5.0 - Tb^{III} , $B = 0.31$ - Eu^{III} , 0.06 - Tb^{III})^{37, 38}. In the case of the Eu^{III} ion, this can be modified to determine n_w in solid-state media, through substitution of τ_r for $\tau(\text{D}_2\text{O})$ and τ_{obs} , for $\tau(\text{H}_2\text{O})$ we obtain:³⁹

$$n_w = 1.11 \left[\frac{1}{\tau_{\text{obs}}} - k_r - 0.31 \right] \quad \text{Eqn. 1.6}$$

1.3.4 Magnetic properties of the lanthanide ions

The high spin value, $S = 7/2$, for the Gd^{III} ion has resulted in it being exploited for the successful development of magnetic resonance imaging (MRI) contrast agents in the medical field.^{40, 41} Since the discovery of the $\{\text{Mn}_{12}\}$ cluster, which led to the characterisation of single molecule magnets (SMMs),⁴² there has been a growth of interest in this research area with hundreds of SMMs now known. As a sub-set of this area, some groups moved towards the use of lanthanides and their high spin state, S , to develop new SMMs.⁴³ The properties that have favoured the use of lanthanide ions for magnetic studies include the high magnetic anisotropy and the slow relaxation of magnetisation.⁴⁴ However, while the focus of SMMs is on individual clusters, in

recent years there has been a shift towards investigating higher order coordination polymers and the magnetocaloric effect (MCE) that some of these polymers exhibit.⁴⁵

The magnetocaloric effect is the heating or cooling of a magnetic material as an external magnetic field is applied. This property allows the use of magnets for cooling and refrigeration, particularly in cryogenic magnetic cooling for temperatures sub-4 K. This property arises from coupling between the magnetic moment with the temperature of the lattice, as a consequence of entropy changes as an external magnetic field is varied. When a magnetic field is applied, the spins will align with respect to the field, producing a more ordered state with lower entropy. When the magnetic field is removed, the spins no longer align in the same direction and disorder increases. To account for this increase in entropy, energy must be removed from the lattice leading to cooling of the material. This is measured in terms of the magnetic entropy change, ΔS_m , and is given by:

$$\Delta S_m = -R \ln(2s + 1) \quad \text{Eqn. 1.7}$$

where R is the gas constant and s is the spin state. The magnitude of ΔS_m is found to be inversely proportional to the molecular weight and is measured in units, $\text{J kg}^{-1} \text{K}^{-1}$.⁴⁵ Based on these assumptions, focus to increase the magnetic entropy has been directed at ions with high spin states using f^7 and d^5 electronic configurations and selecting those elements with larger relative atomic weights, namely Gd^{III} , Mn^{II} and Fe^{III} .

1.4 Applications of hybrid inorganic-organic materials

1.4.1 White-lighting

The narrow bands and high colour purity in the visible region of certain ions (Eu^{III} -red, Sm^{III} -red/orange, Tb^{III} -green) make the lanthanides excellent candidates for developing warm white-light, solid-state lighting devices. In recent years, this has been achieved with some success using lanthanide hybrid inorganic-organic materials where white-light emission may be achieved through a number of routes.

The most common approach to achieving white-light is through a three-component system with appropriate contributions of blue, green and red light emitters. One example is the 1D I^1O^0 coordination polymer, $[\text{Ln}_3(\text{bidc})_4(\text{phen})_2(\text{NO}_3)] \cdot 2\text{H}_2\text{O}$, where bidc = benzimidazole-5,6-dicarboxylic acid.⁴⁶ The Eu^{III} and Tb^{III} polymers displayed characteristic emission bands in the red and green spectral regions with quantum yields of 13.2 and 2.08%, respectively. The Gd^{III} -analogue has broad blue ligand-centred emission band when excited in the UV. By doping the Gd-matrix with Eu^{III} and Tb^{III} , white-light could be obtained by careful variation of the doping ratios. When the $\text{Gd}^{\text{III}}:\text{Eu}^{\text{III}}:\text{Tb}^{\text{III}}$ ratio is 98.5:0.5:1 the Commission Internationale de l'Eclairage (CIE) colour coordinates were calculated to be (0.322, 0.328) which are very close to those required for pure white-light (0.333,0.333) (**Figure 1.8**). Although white-light emission was obtained, no quantitative data in terms of emission lifetimes and quantum yields were reported. This is still

absent in many publications, though it is often noted when determined that improving low quantum yields is the next challenge to overcome.

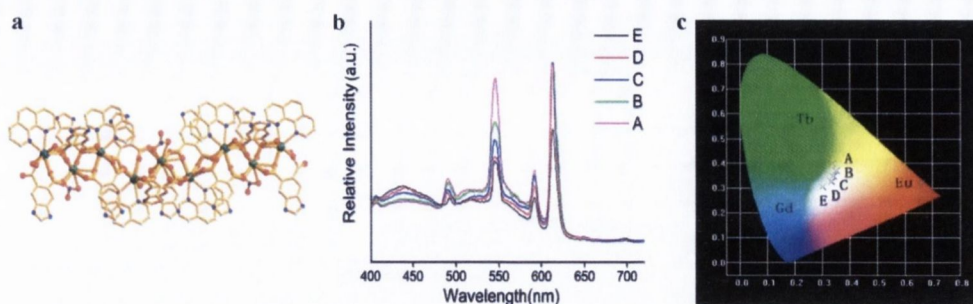


Figure 1.8: (a) Structure of the 1D coordination polymer $[\text{Ln}_3(\text{bidc})_4(\text{phen})_2(\text{NO}_3)_2] \cdot 2\text{H}_2\text{O}$, (b) emission spectra of doped Gd-matrix while exciting the ligand ($\lambda_{\text{ex}} = 376 \text{ nm}$) after varying the weight % of Gd^{III} , Tb^{III} and Eu^{III} in the compound and (c) the corresponding CIE chromaticity diagram for A-E displaying the human response to the emission spectrum.⁴⁶

By varying the coordinating ligand, the emission quantum yields of the resulting hybrid material can be improved. With the coordination of 4-(dipyridin-2-yl)aminobenzoate (L) to lanthanides, another $I'O^0$ 1D coordination polymer of formula $[\text{Ln}(\text{L})_3(\text{H}_2\text{O})_2]$ ($\text{Ln}^{\text{III}} = \text{Eu}^{\text{III}}$, Tb^{III} and Gd^{III}) is isolated.⁴⁷ While the Gd^{III} -polymer displays a broad violet-blue emission band under ligand excitation, the Eu^{III} and Tb^{III} polymers display their characteristic emission bands. The energy of the ligand excited triplet state is $23,697 \text{ cm}^{-1}$ and is a strong sensitizer of the Tb^{III} emission, resulting in a high emission quantum yield of 64%. Due to the larger energy mismatch with Eu^{III} , a lower quantum yield of 7% is obtained. The three component $\text{Gd}^{\text{III}}:\text{Tb}^{\text{III}}:\text{Eu}^{\text{III}}$ system produces white-light emission (CIE coordinates (0.32,0.34)) by tuning the Ln^{III} ratios and the excitation wavelength (λ_{ex}). When λ_{ex} is varied across the ligand absorption band, the resulting ligand emission can be controlled to give a blue to yellow response, depending on the efficiency of intersystem crossing for sensitization of Eu^{III} or Tb^{III} . The emission properties are greatly improved in the 3D $I'O^2$ framework of $[\text{Ln}(\text{BTPCA})\text{H}_2\text{O}] \cdot 2\text{DMF}$ (BTPCA = 1,1',1''(benzene-1,3,5-triyl)tripiperidine-4-carboxylic acid).⁴⁸ The La^{III} -analogue displays a broad blue emission band ascribed to the $\pi\text{-}\pi^*$ electronic transition of the ligand and the isostructural Eu^{III} - and Tb^{III} - analogues display the typical emission bands of the Ln^{III} centre. When the framework is doped so that the $\text{La}^{\text{III}}:\text{Eu}^{\text{III}}:\text{Tb}^{\text{III}}$ ratio is 0.6:0.1:0.3, white-light with the CIE coordinates (0.326, 0.330) is obtained, with a high emission quantum yield of 47.3% (**Figure 1.9**). Effective tuning of the white-light properties was found to be a balance of the energy transfer pathways between the ligand to Ln^{III} and between Tb^{III} to Eu^{III} , as revealed through emission lifetime analysis.

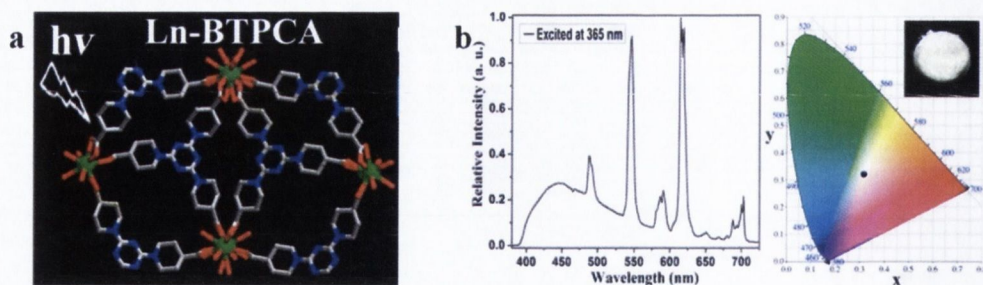


Figure 1.9: (a) Structure of $[\text{Ln}(\text{BTPCA})\text{H}_2\text{O}] \cdot 2\text{DMF}$ and (b) the emission response of the La-doped matrix, La, Eu, Tb ratio of 0.6,0.1,0.4. **Inset:** optical photograph of powder sample of La-doped matrix under UV (365 nm) excitation.⁴⁸

The above discussion has demonstrated some of the problems with formulating white-light emitters and how they have been overcome. However, other strategies are also available. A few reports have demonstrated the possibility of white-light emission in two-component systems. A 1D $\text{I}^0\text{O}'$ chain is obtained through reaction of $\text{Ln}(\text{NO}_3)_3$ ($\text{Ln} = \text{Gd}^{\text{III}}, \text{Eu}^{\text{III}}$) with 3-sulfobenzoic acid (3-SBA) and 1*H*-imidazo[4,5-*f*][1,10]-phenanthroline (IP).⁴⁹ The broad band emission of the IP ligand covers the range 400–580 nm and by doping small quantities of Eu^{III} (0.12–0.77%) into the Gd^{III} -matrix, white light can be obtained upon ligand excitation, with reasonable emission quantum yields up to 9.8%. It is also possible to use different lanthanides. One example is the doping of Dy^{III} into the Bi-Cd framework.⁵⁰ The 2D I^0O^2 framework of $[\text{Bi}_2\text{Cd}(\text{pdc})_4(\text{H}_2\text{O})_2] \cdot \text{H}_2\text{O}$ ($\text{H}_2\text{pdc} =$ pyridine-2,6-dicarboxylic acid) exhibits a broad blue emission band with a maximum at 471 nm. When 5% Dy^{III} is doped into the framework, the Dy^{III} emission bands centred at 479 nm (blue) and 571 nm (yellow) are sensitised by the framework leading to white-light with the CIE coordinates (0.32,0.37).

The compound $[\text{Ln}_2(\text{N-BDC})_3(\text{DMF})_4]$ ($\text{N-H}_2\text{BDC} =$ 2-aminoterephthalic acid, $\text{Ln}^{\text{III}} =$ $\text{Gd}^{\text{III}}, \text{Eu}^{\text{III}}, \text{Tb}^{\text{III}}$ and Sm^{III}) is the first single-component hybrid material reported to produce white-light.⁵¹ The ligand is able to sensitise the photoluminescence of $\text{Eu}^{\text{III}}, \text{Tb}^{\text{III}}$ and Sm^{III} centres. However, when the excitation wavelength of the Sm^{III} -analogue is varied between 300–400 nm, the intensity of the Sm^{III} bands can be tuned. Harnessing the concomitant broad blue band emission of the ligand (400 – 500 nm), the system can be tuned to produce light in the white region with CIE coordinates (0.309, 0.232).

As an alternative approach to the doping of lanthanide ions into a host matrix, some reports have demonstrated the ability of a 3D framework to encapsulate the lanthanide ions and engineer white-light through framework sensitisation. This approach was realised using the aluminium MOF, MIL-53, as the host matrix.⁵² The uptake of lanthanide ions into the pores was achieved by soaking nanocrystals of the MOF in an ethanolic solution of lanthanide salt and could be monitored using inductively-coupled mass spectrometry (ICP-MS). By utilising the broad blue emission of the ligand of the MOF, white-light could be obtained by varying the concentration of Eu^{III} in the pores or by varying the excitation wavelength in the UV range. As the energy moves to the lower range of the UV, the intensity of the broad blue band grows with a concomitant reduction in the Eu^{III} bands. This novel approach of encapsulation has numerous positive attributes. The first is the

demonstration of sensitised Eu^{III} emission through the *antenna effect* of the MOF-based ligand. Secondly, they were able to demonstrate that strong photoluminescence from Eu^{III} could be obtained in water, which was attributed to protection of the Ln^{III} centre from O-H oscillators by the MOF scaffold. To further show the novelty of this approach for practical applications, a colloidal suspension of Ln-encapsulated MOF was used to prepare continuous homogenous thin films that were studied by scanning electron microscopy (SEM). Of particular interest is that the thin films still show white-light under the correct excitation (**Figure 1.10**). Ma *et al.* showed separately that Ln^{III} ions can be encapsulated into a zinc-based MOF using a similar approach resulting in reasonable emission quantum yields up to 8% for white-light emission.⁵³

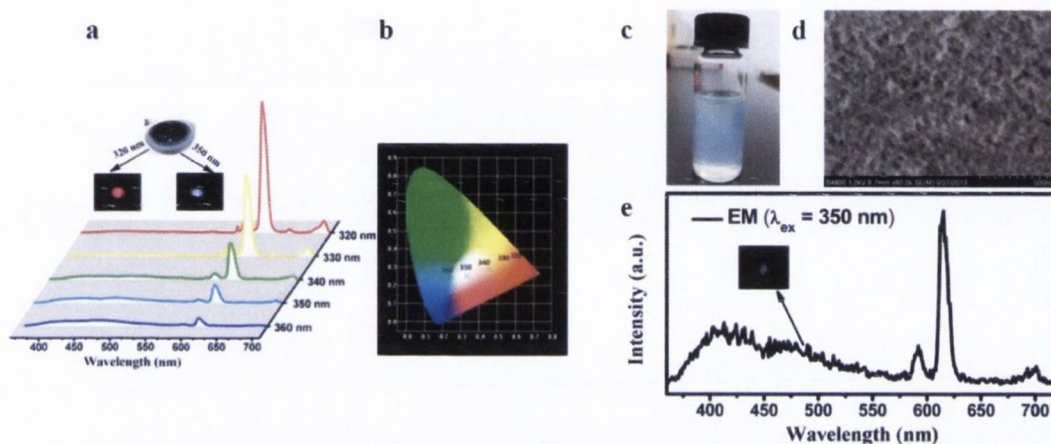


Figure 1.10: (a) The spectral response of Eu^{III} encapsulated MOF as a function of excitation wavelength, (b) the spectral response on a CIE diagram and (c) the prepared colloidal solutions of nanocrystals used to prepare (d) homogenous thin films and (e) the corresponding white-light response.⁵²

White-light emission can also be achieved through materials built from layer-by-layer epitaxial growth mechanisms.⁵⁴ Using the 3D lanthanide MOF, $[\text{Ln}_2(\text{Mell})(\text{H}_2\text{O})_8]$ (H_6Mell = mellitic acid), sequential layers of the isostructural MOFs, using Eu^{III} (red), Gd^{III} (blue - ligand emission) and Tb^{III} (green) were grown (**Figure 1.11**). By producing a material where the blue-green-red (BGR) layers were isolated in separate crystalline phases, it was possible to reduce and avoid the effects of energy transfer experienced by the more conventional doping approach, that can make optimisation of white-light emission difficult.

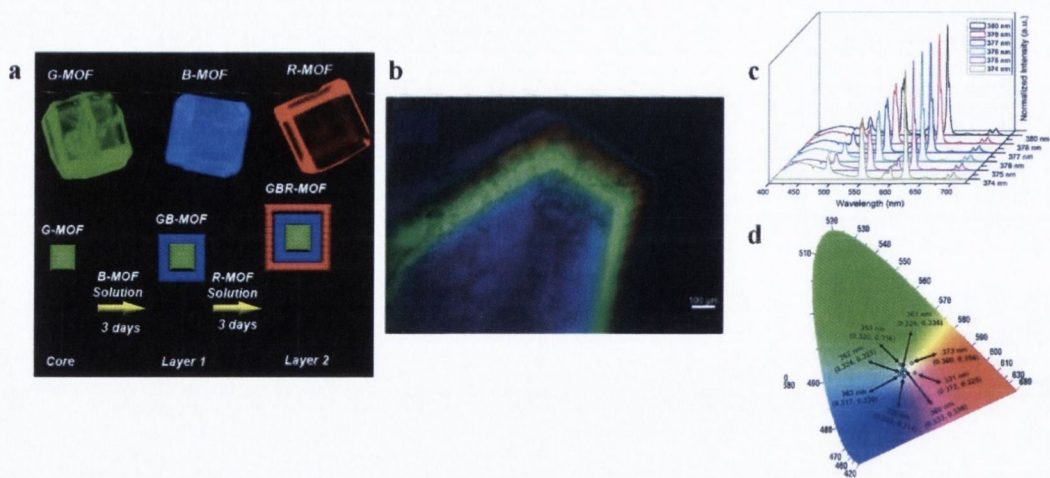


Figure 1.11: (a) Optical micrographs of $[\text{Tb}_2(\text{Mell})(\text{H}_2\text{O})_8]$ (green), $[\text{Gd}_2(\text{Mell})(\text{H}_2\text{O})_8]$ (blue) and $[\text{Eu}_2(\text{Mell})(\text{H}_2\text{O})_8]$ (red) MOFs and schematic for layer-by-layer epitaxial growth of blue-green-red (BGR) prepared material. (b) Fluorescence microscope image of the BGR-MOF material. (c) Corresponding emission spectra of the BGR-material at different excitation wavelengths and (d) the respective CIE coordinates.⁵⁴

1.4.2 Sensing applications

The ability of lanthanide systems to act as sensing platforms has been extensively researched in aqueous media and often exploits the use of supramolecular interactions in the system.^{55, 56} As the field of hybrid inorganic-organic materials has developed, so has the motivation to sense analytes through a heterogeneous system where the hybrid material is in the solid-state. To date, the range of analytes has covered cations, anions and small organic molecules.

Significant advances have been made in the field of cation sensing. In particular, steps are being taken to extend these materials towards sensing in biological media. The selective sensing of Cu^{2+} ions using the 3D $\text{I}^{\text{O}}\text{O}^3$ hybrid, $[\text{H}_2\text{N}(\text{Me})_2][\text{Ln}_3(\text{L})_2(\text{HCOO})_2(\text{DMF})_2(\text{H}_2\text{O})]$ ($\text{H}_4\text{L} = 2,6$ -di(3',5'-dicarboxylphenyl)pyridine and $\text{Ln} = \text{Eu}^{\text{III}}$, Tb^{III} , Gd^{III} and Dy^{III}) is possible.⁵⁷ The ligand contains hard oxygen donors that coordinate the lanthanide centres and the central pyridine-N atoms remain uncoordinated, leaving them open to interaction with other cations. The 3D structure is constructed from three different nanocages with different diameters of 2.4, 1.1 and 1.1 nm, respectively, which are occupied by solvent molecules. From the transition metal cations investigated as analytes, it was found that only Cu^{2+} ions significantly quench the luminescence intensity of the Eu^{III} -framework. This was attributed to the smaller ionic radius of Cu^{2+} , that allows the ions to come in close enough contact with the free pyridine N-atom to coordinate. After the Cu^{2+} ion coordinates to the pyridine there is a reduced efficiency of energy transfer from the ligand to the Eu^{III} centre, resulting in quenching of the PL intensity. In contrast, alkali earth and other transition metals investigated produced a small or negligible increase in the luminescence intensity. This was believed to be due to the ions binding inside the nanocages, with a concomitant exclusion of quenching solvent molecules from the framework. The removal of solvent from the nanocages leads to a reduction in non-radiative quenching through the O-H vibration.

The 3D I^0O^3 cationic framework of $[Ln_4(\mu_3-OH)_4(BPDC)_3(BPDCa)_{0.5}(H_2O)_6]ClO_4 \cdot 5H_2O$ ($Ln^{III} = Tb^{III}$) and $H_2BPDC = 2,2'$ -dipyridine-3,3'-dicarboxylic acid and $H_2BPDCa =$ biphenyl-4,4'-dicarboxylic acid has been shown to selectively sense Cu^{2+} ions in aqueous conditions simulating a cellular environment.⁵⁸ The framework contains two types of micropores; one running along the b -axis with dimensions $3 \times 7 \text{ \AA}^2$ and the second with pore size $4.5 \times 5.5 \text{ \AA}^2$ running along the c -axis. When the hybrid material was treated in aqueous solution with a number of metal ions, a high selectivity towards Cu^{2+} was observed and detected through the quenching of Tb^{3+} luminescence. In buffered conditions at pH 7, the quenching ability of Cu^{2+} ions is still observed, demonstrating that hybrid inorganic-organic materials show potential in the sensing of specific ions in a biological environment.

The framework, $[Ln_2(N-BDC)_3(DMF)_4]$, described earlier as a white-light emitter, also displays a sensing ability towards metal cations, specifically Al^{3+} .⁵¹ By using the emission spectra of the Eu^{III} -analogue, the sensing of metal ions leads to different quenching responses (**Figure 1.12**). In the presence of $M^{n+} = Li^+, Mn^{2+}, Zn^{2+}, Cd^{2+}$ and Ni^{2+} , a small quenching effect of the Eu^{III} emission was observed, with a concomitant increase in the ligand emission between 450-550 nm. This created a red to pink colour change that could be observed by the eye. In contrast, for $M^{n+} = Cu^{2+}, Fe^{2+}$ and Fe^{3+} , the Eu^{III} - and ligand-based emission is significantly quenched, switching off the emission. When Al^{3+} is introduced, the emission of the Eu^{III} is fully quenched, but the ligand emission remains strong, producing bright blue-light. This method provided a distinct sensing approach with high selectivity towards Al^{3+} ions and a good indicator for other biologically-important $Fe^{2+/3+}$ and Cu^{2+} ions. Depending on the metal cation, three different mechanisms can explain the quenching process. For those cations that produce a red-to-pink PL response, the presence of the cation leads to less efficient ligand to Eu^{III} energy transfer. When $M^{n+} = Cu^{2+}, Fe^{2+}$ and Fe^{3+} , powder X-ray diffraction shows that the crystal structure changes or collapses completely. When the structure collapses, the Eu^{III} emission is quenched and in solution $M^{n+} = Cu^{2+}, Fe^{2+}$ and Fe^{3+} completely quench the ligand emission, causing the emission to switch off. In solution, the Al^{3+} does not quench the ligand emission resulting in the selective blue spectral response.

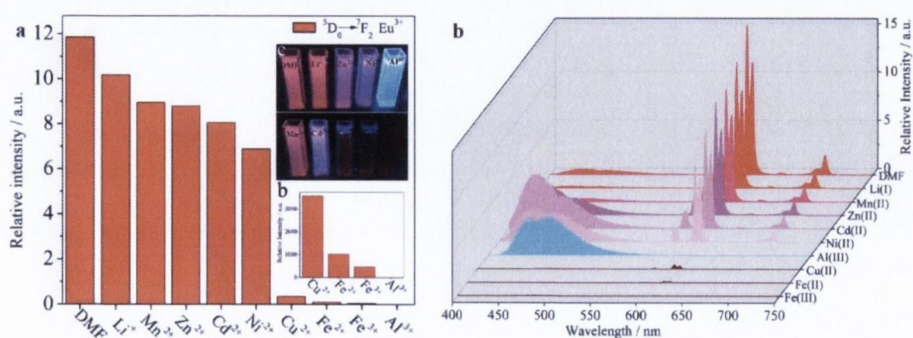


Figure 1.12: (a) Luminescence intensity of the ${}^5D_0 \rightarrow {}^7F_2$ transition of the $[Eu_2(N-BDC)_3(DMF)_4]$ in DMF solutions of different MCl_x ($\lambda_{exc} = 365 \text{ nm}$). Upper inset: optical images of the luminescence response at 365 nm excitation. Lower inset: Relative intensity of Eu-analogue through quenching from Cu^{2+} , $Fe^{2+/3+}$ and Al^{3+} . (b) Photoluminescence spectra of the responses to different M^{x+} .⁵¹

A highly sensitive, Hg^{2+} -sensing 2D framework based on $[\text{Eu}_2(\text{bqdc})_3(\text{H}_2\text{O})(\text{DMF})_3] \cdot 0.5\text{DMF} \cdot \text{H}_2\text{O}$, where bqdc = 2,2'-biquinoline-4,4'-dicarboxylic acid, has been characterised and successfully incorporated into a thin film sensor device.⁵⁹ The quenching mechanism is attributed to the coordination of the Hg^{2+} to the free N-pyridyl sites on the ligand and the resulting interference of the energy transfer from the ligand to the Eu^{III} centre. A thin film sensor was developed by film growth on a $\text{Eu}(\text{OH})_3$ support on an indium-tin-oxide (ITO) surface (**Figure 1.13**). Reproducible films could be made, as shown by SEM, and were able to sense Hg^{2+} ions with a red to UV-blue colour change detectable by the naked eye. Furthermore, the films were responsive within the range of U.S. permitted Hg^{2+} levels in drinking water, allowing identification down to dangerous levels.

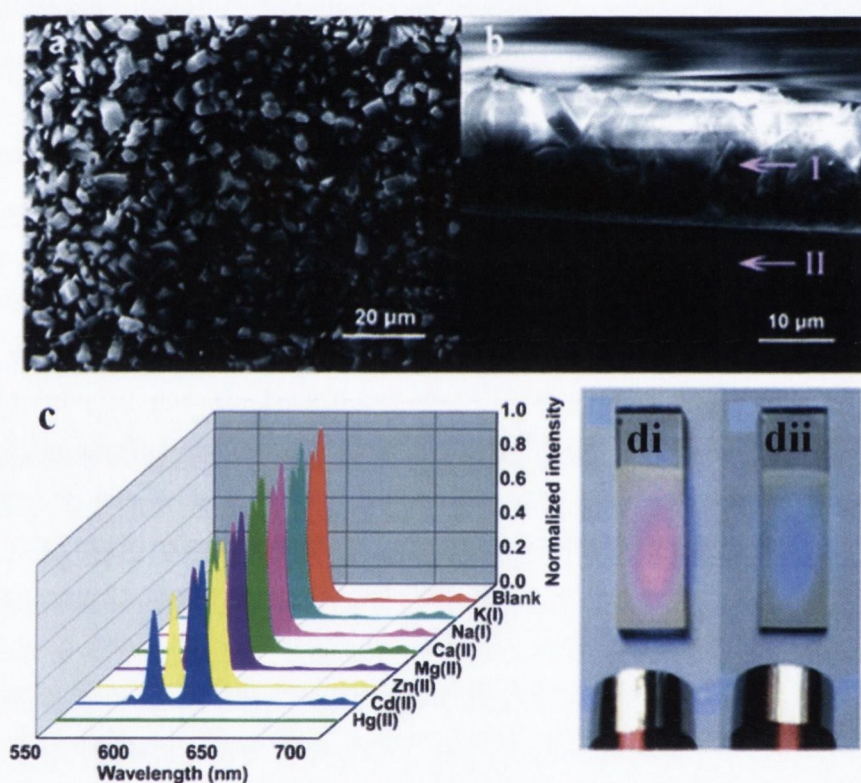


Figure 1.13: (a) Top-down SEM image of the coated film of the sensor hybrid material, $[\text{Eu}_2(\text{bqdc})_3(\text{H}_2\text{O})(\text{DMF})_3]$. (b) Side-on SEM image of sensor film (layer I: sensing film; layer II: ITO glass support). (c) Selective photoluminescence response of Hg^{2+} ions. (d) Optical images of thin film sensor using a small UV source (i) no Hg^{2+} (ii) Hg^{2+} detection.⁵⁹

Large metal clusters such as polyoxometalates (POMs) may also be sensed by lanthanide hybrid materials.⁶⁰ The 3D framework of $[\text{Ln}(\text{tip})_{1.5}]$ (H_2tip = 5-*tert*-butylisophthalic acid) forms hexagonal channels running along the *c*-axis with the hydrophobic *tert*-butyl groups located within. To act as a sensor, thin films of the crushed framework prepared on a quartz slide were immersed in aqueous solutions of different analytes. The common ions, sulphate, carbonate and phosphate, showed no quenching of the luminescence from the framework. However, detection of the POMs $(\text{NH}_4)_6\text{Mo}_7\text{O}_{24}$ and $\text{H}_3\text{PW}_{12}\text{O}_{40}$ was observed by a strong quenching of the red emission of the Eu^{III} centres. By washing the sample with water post-sensing, the material regained its luminescence

and could be re-used multiple times. It was proposed that the strong UV-induced photoelectron transfer processes of the POMs compete for the excitation light and so reduce the light absorbed by the ligand that can sensitise the lanthanide centre.

Alternative approaches to cation sensing have been demonstrated using nucleotide/ Ln^{3+} coordination polymers.⁶¹ SEM and FT-IR studies showed that an Ln^{3+} -ADP-phen coordination polymer could be synthesised whose luminescence was 32 times stronger than the weakly emissive Ln^{3+} -ADP polymer. The aqueous stability of the polymer was shown up to 30 days and the maximum luminescence intensity was obtained at pH 7.4, making it suitable for cell conditions. The coordination polymer was screened for sensing of several metal cations and significant quenching was observed for Fe^{2+} , Hg^{2+} and Cu^{2+} . By using the masking agents Sodium Dimercaptopropane Sulfonate (Na-DMPS) and $\text{NH}_2\text{OH}\cdot\text{HCl}$, the Hg^{2+} and Cu^{2+} responses could be removed to enable the selective sensing of Fe^{2+} . Time-resolved fluorimetry allowed detection of Fe^{2+} in human serum and a linear Stern-Volmer correlation was observed in the range 80 nM – 6 μM , typical for a healthy body.

A cation that is of biological importance, yet is less investigated using hybrid materials, is H^+ . One elegant example of pH sensing was performed using the layered material, ITQMOF-3, prepared from the reaction of Eu^{III} with 1,10-phenanthroline-2,9-dicarboxylic acid.⁶² The ligand was shown to strongly sensitise Eu^{III} emission, with a high emission quantum yield of 56%. There are two different layers within the structure, a negatively-charged layer of stoichiometry $[\text{Eu}(\text{L})_2]$ that contains the crystallographically unique Eu(1) centre and a positively-charged layer of $[\text{Eu}_2\text{L}_2(\text{OH})\text{H}_2\text{O}]_4$ that contains the crystallographically unique Eu(2) centre. These two different Eu^{III} environments can be identified from the $^5\text{D}_0 \rightarrow ^7\text{F}_0$ transition where two bands are observed, one band associated with each unique Eu^{III} centre. When the pH is varied in the range 5-7.5, the intensity of the $^5\text{D}_0 \rightarrow ^7\text{F}_0$ band for Eu(2) (positively charged layer) increases while the intensity of Eu(1) remains constant. Using the ratio of the two bands, an internal calibration for pH allows a linear response in the pH range 5-7.5 (Figure 1.14). A prototype pH sensor was made using a commercial fibre optic with a rapid response between the PL and pH showing potential as a sensor for biological cells.

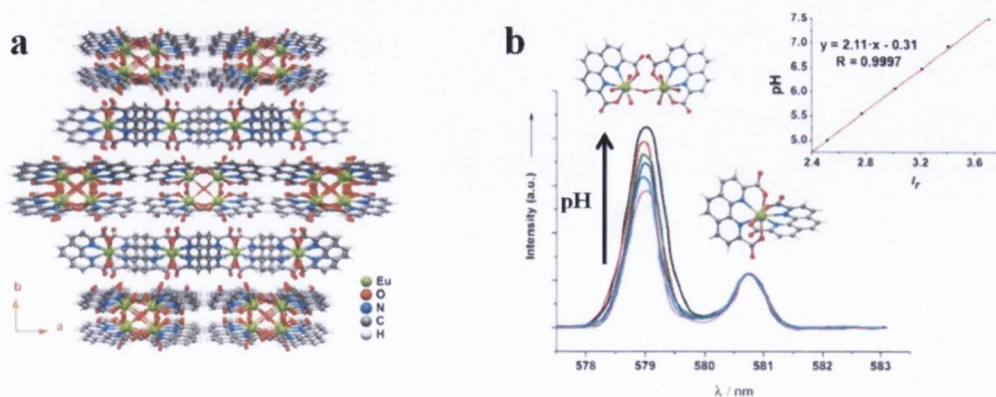


Figure 1.14: (a) Structure of the layered framework ITQMOF-3 and (b) the pH response in aqueous media by monitoring the $^5\text{D}_0 \rightarrow ^7\text{F}_0$ transition. Inset: Linear response of pH vs. ratio intensity of $\text{Eu}(2)/\text{Eu}(1)$.⁶²

Phosphate-Ln coordination polymers have proven effective in the detection of small molecules such as dipicolinic acid (DPA) (a biomarker for anthrax)⁶³ and the molecule tetracycline (TC) (a broad spectrum antibiotic) in milk.⁶⁴ In both cases, an Ln-AMP (adenosine monophosphate) coordination polymer was utilised. DPA can efficiently sensitise Tb^{III} emission due to favourable overlap of its excited triplet state. In sensing anthrax, the coordination of dipicolinic acid to form the Tb-AMP-DPA polymer results in PL enhancement and a linear response curve down to detection limits of 10 nM is achieved. Those are levels significantly lower than the maximum lethal level (~0.1 μM) of anthrax spores to human beings. For the sensing of TC, a related coordination polymer, Eu-AMP-cit (cit = citrate) was utilised. In this polymer, no PL is observed from Eu^{III} and is considered the “off” state. With the addition of TC to an aqueous solution of polymer, PL enhancement is observed due to the displacement of coordinated water molecules. A linear response allowed detection of TC to levels below the maximum limits set by the U.S Food and Drug Administration.

The development of heterogeneous methods for small molecule detection using hybrid Ln^{III}-materials is still limited and in many cases restricted to the sensing of different solvents. For example, the 2D Ln-Cd network [Eu₂Cd₃(EDTA)₃(H₂O)₄](H₂O)₁₄ (EDTA = ethylenediaminetetraacetic acid) has been shown to sense amines by the quenching of the Eu^{III} luminescence, with ethanol amine and triethyl amine showing the most significant response.⁶⁵ The analyte amines were shown to absorb strongly up to 400 nm and competitively absorb the excitation light instead of the Eu^{III} centre resulting in strongly quenched Eu^{III} intensities.

The elegant detection of biogenic amines was demonstrated using the 1D coordination polymer K{[Ru^{II}(^tBubpy)(CN)₄]₂-Ln^{III}(H₂O)₄} (where ^tBubpy = 4,4'-di-*tert*-butyl-2,2'-bipyridine).⁶⁶ The 1D coordination consists of alternating [Ru^{II}(^tBubpy)(CN)₄]₂ and K[Ln^{III}(H₂O)₄] units along the *b*-axis. The titration of alkyl amines into an ethanolic solution of the coordination polymer results in a shift of *ca.* 30 nm in the absorption spectrum. This is also reflected by a *ca.* 15-20 nm shift in the ³MLCT transfer band of the Ru^{II} unit (yellow-to-red colour change). Benesi-Hildebrand analysis suggests that two amine molecules coordinate to the Ln^{III} centre. The spectroscopic properties reflect the coordination of the amine to the Ln^{III} species and concomitant dissociation of the polymer. Using these principles, a sensor film was demonstrated, whereby the coordination polymer was blended into a polystyrene film and used as a chemical dosimeter to detect gaseous biogenic amines from fish samples (**Figure 1.15**). The blended polymer was shown to have a linear colorimetric response to increasing putrescine concentration, which can be determined with the naked eye.

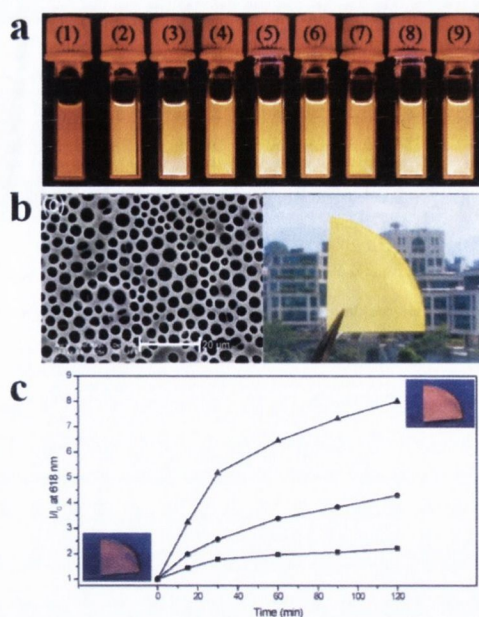


Figure 1.15: (a) Luminescence response of $K\{[Ru(II)(^tBubpy)(CN)_4]_2-Pr(III)(H_2O)_4\}$ (1×10^{-4} M) in EtOH with the analytes (1) histamine; (2) none; (3) aniline; (4-9) H_2S , CO, N_2 , CH_4 , H_2 and air, respectively. (b) SEM and photo-image of the porous polymer blended sensor films and (c) the luminescent response of the sensor films upon exposure to putrescine over 120 minutes ($\lambda_{ex} = 365$ nm).⁶⁶

The majority of studies are still largely restricted to common solvent systems and the effects on the luminescence of the material. These systems are still poorly understood; however, new insights are being gained. The flexible 3D Ln-organic framework $[Ln_2(L)_2(H_2O)_4]$ ($H_3L = tris((4\text{-carboxyl})phenylduryl)amine$) has an elegant PL response based on expansion and contraction of the framework in the presence of different solvents.⁶⁷ For DMF, an increase in the cell parameters was observed and a concomitant increase in the PL intensity. Other solvents H_2O , EtOH and CH_2Cl_2 result in a decrease of the cell parameters and a quenching of the PL.⁶⁷ A more promising approach to this style of small molecule sensing is realised in the double layered material, $[LnTCM(H_2O)_2] \cdot 3DMF \cdot H_2O$, where $H_3TCM = (4,4',4''\text{-}(((2,4,6\text{-trimethylbenzene-1,3,5-triyl})\text{-}tris(methylene))\text{-}tris(oxy))tribenzoic acid$.⁶⁸ With the packing of sequential layers through supramolecular interactions, a 3D network with $12.3 \times 12.5 \text{ \AA}^2$ channels down the a -axis form. These channels were used to sense different volatile organic molecules through host-guest interactions. By co-doping the material with Eu^{III} and Tb^{III} ions it was observed that the presence of different molecules leads to the emission colour transitioning across three different colour gamuts in the CIE diagram (**Figure 1.16**). Each organic molecule affects the efficiency of energy transfer from the antenna ligand to the Ln^{III} centres and between Tb^{III} -to- Eu^{III} centres differently resulting in a unique colour response fingerprint in the presence of each organic molecule. The common strategy for sensing in these Ln^{III} -materials is to detect changes in emission intensity of a single type of Ln^{III} ion. By co-doping, fingerprint spectral responses for a group of small molecules can be collected and greater sensitivity to different molecules are observed, resulting in this technique being a more powerful approach to small molecule sensing.

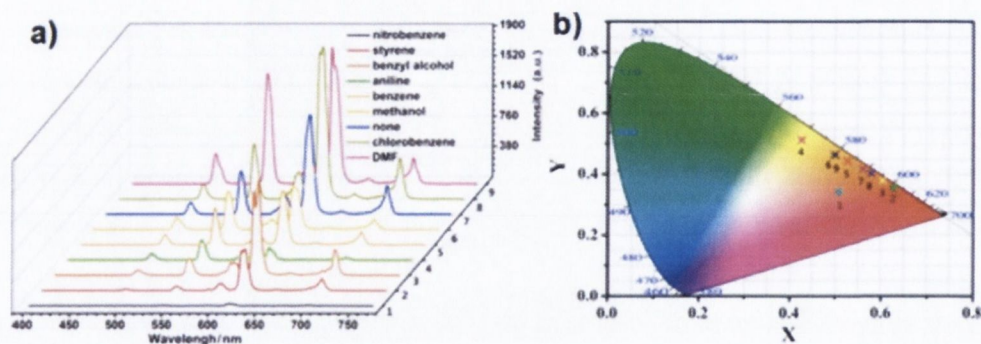


Figure 1.16: (a) Emission spectra for $[\text{Eu}_{0.35}\text{Tb}_{0.65}\text{TCM}(\text{H}_2\text{O})_2] \cdot 3\text{DMF} \cdot \text{H}_2\text{O}$ for sensing a series of organic volatile molecules and (b) the corresponding CIE chromaticity coordinates of the respective emission spectra.⁶⁸

Early examples for anion detection were made using the Tb^{III}-analogue of $[\text{Ln}(\text{BTC})] \cdot \text{MeOH}$, ($\text{H}_3\text{BTC} = 1,3,5\text{-benzenetricarboxylic acid}$).⁶⁹ When the material was exposed to solutions of halides, CO_3^{2-} or SO_4^{2-} in methanol, an increase in the emission intensity was measured. The mechanism for this intensity increase was related to hydrogen bond formation between the anion and the solvent. This interaction leads to a reduction in energy of the O-H bond and thus an increase in Ln^{III} emission was observed. Exploiting the formation of hydrogen bonds has also been demonstrated in the framework, $[\text{Ln}(\text{H}_4\text{muc})_{1.5}]$, where $\text{H}_4\text{muc} = \text{mucic acid}$.⁷⁰ In contrast to the previous example, the hydrogen bond forms directly between the O-H groups of the ligand with the anion. This results in a reduction in vibrational movements in the channels which leads to an increase in emission intensity. Many hybrid inorganic-organic materials contain ligands with many N-H and O-H functions present and the ability to form hydrogen bonds is inherent in many structures. As such, anion sensing through hydrogen bond formation in these materials is a promising area that requires further study.

An alternative approach to anion sensing takes advantage of the cationic charge on a framework material as in $[\text{Ln}_4(\mu_3\text{-OH})_4(\text{BPDC})_3(\text{BPDCA})_{0.5}(\text{H}_2\text{O})_6]\text{ClO}_4 \cdot 5\text{H}_2\text{O}$, that was discussed earlier for anion sensing.⁵⁸ When treated with aqueous solutions of the typical anions F^- , and to a lesser extent CO_3^{2-} , significant quenching was observed. The mechanism for this is likely due to the formation of hydrogen bonds inside the framework channels. Despite its cationic charge, the framework does not show an improved uptake of these small anions into the pores. In contrast, the ability to sense the toxic pollutant CrO_4^{2-} is observed with strong quenching of luminescence. This occurs through anion exchange with the comparable sized ClO_4^- counter-ion. Quenching occurs through less efficient sensitisation of Eu^{III} emission from the ligand and strong competition for the excitation light by the CrO_4^{2-} . The current examples in the literature indicate that a satisfactory understanding for anion sensing in these materials has not yet been achieved. One major problem that may need to be tackled is the accessibility (or current lack thereof) of sensing sites to the anion analyte. This will require further study into nanosized materials that have a larger active surface area, or as an alternative, a focus on the lower dimensional coordination polymers that are soluble

in aqueous media to interact in a similar manner to the successful anion sensing platforms based on supramolecular assembly.

1.4.3 Imaging and non-linear optics

The optical properties of the NIR-emitting lanthanides (Nd^{III} , Er^{III} and Yb^{III}) have potential for applications within cell imaging and non-linear optics. An early example is shown with the porous network of $[\text{Yb}_2(\text{pvdc})_3(\text{H}_2\text{O})_2] \cdot 6\text{DMF}$.⁷¹ The ligand 4,4-[2,5-dimethoxy-1,4-phenylene-di-2,1,ethenediyl]bisbenzoic acid (H_2pvdc) was shown to efficiently sensitise the luminescence of Yb^{III} at *ca.* 980 nm ($^2\text{F}_{5/2} \rightarrow ^2\text{F}_{7/2}$). By co-doping with Er^{III} , and later Nd^{III} , a method for creating NIR luminescent barcoded systems was proposed, with potential for labelling of bioanalytical assays. As the ratio of each lanthanide was varied, the respective NIR emission of each Ln^{III} centre increased linearly, enabling multiple labels to be synthesised (**Figure 1.17**).⁷¹

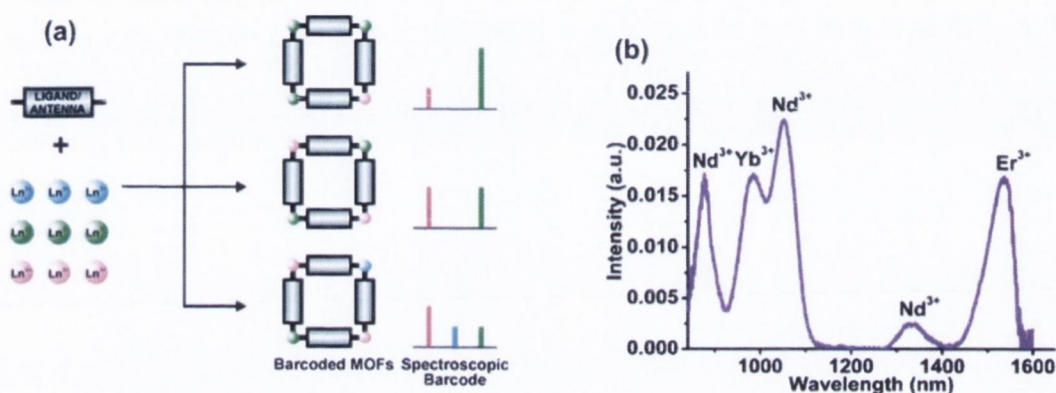


Figure 1.17: (a) Schematic for the method used to create NIR barcoded hybrid materials. (b) Barcoded emission spectrum of $[(\text{Nd}_{0.09}\text{Er}_{0.55}\text{Yb}_{0.36})(\text{pvdc})_2(\text{H}_2\text{O})_2] \cdot 6\text{DMF} \cdot 8.5\text{H}_2\text{O}$.⁷¹

Using the same ligand, an Yb^{III} -framework, $[\text{Yb}_2(\text{pvdc})_3(\text{H}_2\text{O})_3]$, was developed and nanoscale crystallites obtained using a reverse microemulsion synthesis.⁷² Despite the low emission quantum yield of the material ($5.2 \pm 0.8 \times 10^{-5}$ % in 0.1 M HEPES buffer), the nature of the framework material ensured a high number of sensitizer and Yb^{III} ions per unit volume, which reduced the impact of the low quantum yield. Using this hypothesis, the material was studied for NIR imaging of cells. The stability of the nano-framework was shown to remain intact up to four weeks, with little to no crystallinity loss and minimal leaching of Yb^{III} ions into the cellular media. After internalisation into cells, the Yb^{III} intensity was measured at regular time intervals and showed no change in emission intensity, confirming the Yb^{III} framework maintains its crystal integrity. The material was also resistant to photobleaching under constant irradiation for up to 13 hours. The combination of these factors allowed the imaging of living cells, with the material locating in the cytoplasm (**Figure 1.18**). The cytotoxicity was investigated and the compound shown to be a promising cell imaging probe.

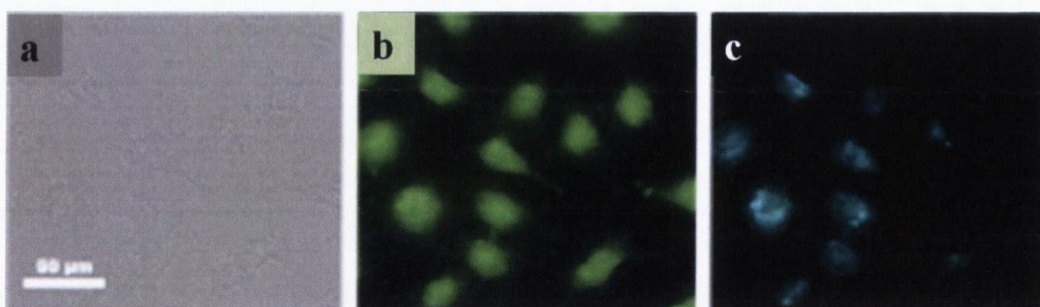


Figure 1.18: (a) Bright-field, (b) visible emission (H_2pvdc emission $\lambda_{\text{ex}} = 350 \text{ nm}$, $\lambda_{\text{em}} = 450 \text{ nm}$) and (c) NIR Yb^{III} emission images for $[\text{Yb}_2(\text{pvdc})_3(\text{H}_2\text{O})_3]$ internalised in living cells.⁷²

The NIR-emitting lanthanide ions may also be used in non-linear optics. Up-conversion (UC) falls in this area and involves a sequential photon absorption that leads to excitation of the emitting ion. Many UC processes involve the absorption of multiple NIR photons, resulting in the emission of visible light. This is a preferred approach to using organic chromophores and quantum dots in cell imaging that require UV light. By using NIR light (for UC), the effects of photobleaching, autofluorescence and photodamage to the biological sample are considerably reduced. The co-doped $[(\text{Y}: \text{Er}, \text{Yb})(\text{oba})(\text{ox})_{0.5}(\text{H}_2\text{O})_2]$ material ($\text{H}_2\text{oba} = 4,4\text{-oxybis}(\text{benzoic acid})$ and $\text{H}_2\text{ox} = \text{oxalic acid}$) has been shown to display up-converted blue, green and red emissions.⁷³ For the green (${}^2\text{H}_{11/2}$, ${}^2\text{S}_{3/2} \rightarrow {}^4\text{I}_{15/2}$, 520 and 540 nm, respectively) and red (${}^4\text{F}_{9/2} \rightarrow {}^4\text{I}_{15/2}$, 660 nm) lines a conventional two photon absorption mechanism under 980 nm laser excitation gives rise to the emission. The blue emission (${}^2\text{H}_{9/2} \rightarrow {}^4\text{I}_{15/2}$, 407 nm and ${}^4\text{F}_{5/2} \rightarrow {}^4\text{I}_{15/2}$, 455 nm), required a three photon absorption process into the ${}^2\text{H}_{9/2}$ excited state of Er^{III} followed by non-radiative relaxation into the emissive ${}^4\text{F}_{5/2}$ state (**Figure 1.19**). Two-photon mechanisms for green and red UC processes have also been observed for other lanthanide hybrids, including the co-doped $[(\text{Y}: \text{Er}, \text{Yb})(\text{pza})(\text{OH})(\text{H}_2\text{O})]$ ($\text{H}_2\text{pza} = 2,3\text{-pyrazinedicarboxylic acid}$)⁷⁴ and the co-doped $\text{Y}:\text{Er}, \text{Yb}$ polymer of $[\text{Ln}_3(\text{BDC})_{3.5}(\text{OH})_2(\text{H}_2\text{O})_2] \cdot \text{H}_2\text{O}$ ($\text{H}_2\text{BDC} = 1,4\text{-benzenedicarboxylic acid}$).⁷⁵

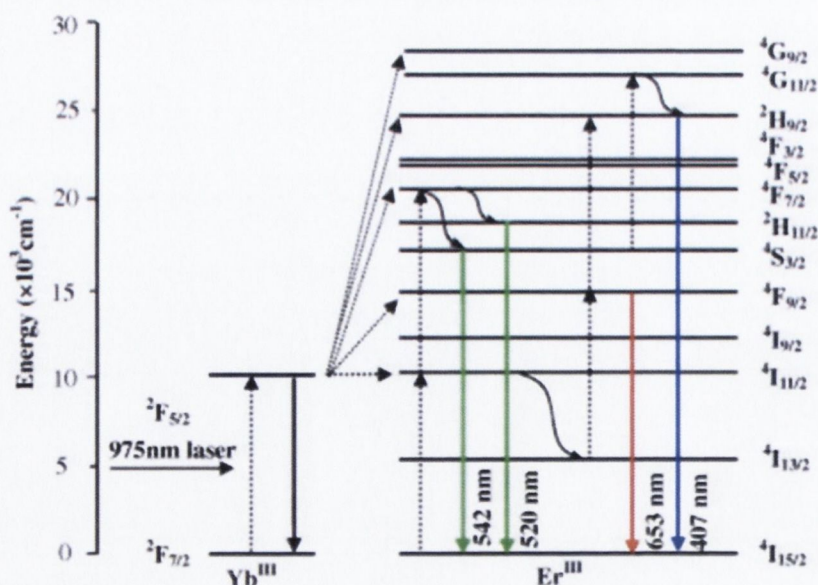


Figure 1.19: Proposed two- and three-photon mechanisms for red, green and blue UC in $\text{Yb}^{\text{III}}/\text{Er}^{\text{III}}$ doped framework materials.⁷³

Visible-to-visible UC was achieved in $[\text{Nd}_2(\text{ndc})_3(\text{DMF})_4]\cdot\text{H}_2\text{O}$ ($\text{H}_2\text{ndc} = 1,4$ -naphthalenedicarboxylic acid).⁷⁶ This framework consists of an Nd^{III} dinuclear unit that is bridged into a layered network built from 1D double chains. A 580 nm laser excitation gives rise to blue UC emission by two mechanisms, the first being a conventional two-photon absorption process to an excited state. The second mechanism involves energy transfer UC between adjacent Nd^{III} centres in close proximity (4.10 Å), where two centres absorb a photon by ground state absorption. This is followed by one centre returning to the ground state through non-radiative energy transfer to the second centre that is excited to the upper excited state (**Figure 1.20**). This gives a strong blue UC emission when excited at 580 nm (yellow) into the hypersensitive ${}^4\text{G}_{5/2} \leftarrow {}^4\text{I}_{9/2}$ transition. There are still just a few examples of UC lanthanide hybrid materials; however, the field has potential for future biological applications.

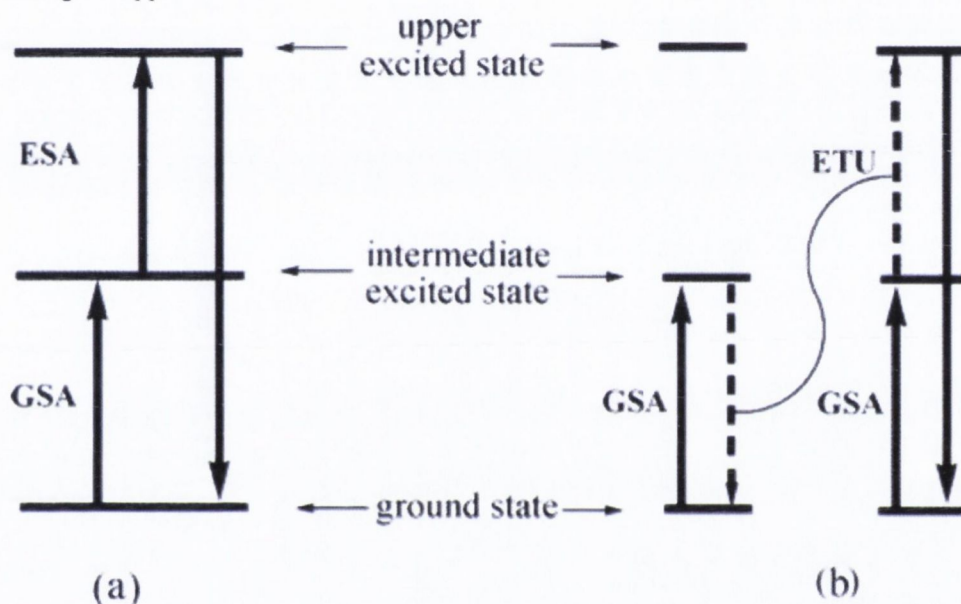


Figure 1.20: (a) Schematic representation for a traditional two-photon UC process where a ground state absorption (GSA) to an excited state occurs, followed by an excited state absorption (ESA) into a higher excited state. (b) Schematic for energy transfer UC where two centres absorb a photon by GSA followed by non-radiative relaxation of one centre to the ground state resulting in the second centre in a higher excited state by the process known as energy-transfer up-conversion (ETU).⁷⁶

Second-order harmonic generation is a non-linear optical process that has been observed in some lanthanide hybrid materials. It requires materials that crystallise in non-centrosymmetric space groups and is the result of the interaction between the electron density of the molecule/material and an alternating electric field of a laser.⁷⁷ Due to the harmonic doubling of the frequency, this field of non-linear optics primarily has applications in the laser industry and optoelectronic technologies. Due to the flexibility in controlling the dimensionality and structure of lanthanide inorganic-organic materials, there has been an interest in studying the second order generation properties of relevant complexes. In the search for new materials that display this property, second harmonic generation has been achieved in 1D,⁷⁸ 2D⁷⁹ and 3D framework materials.⁸⁰⁻⁸² In many cases, the second harmonic generation is modest, ranging from *ca.* 20× to several 100× α -quartz, which is the standard material used for comparison. These values are still

low compared to the technologically important LiNbO_3 , that has an activity $600\times$ that of α -quartz.⁸³ However, lanthanide hybrid materials do show strong potential as highlighted by the 2D non-centrosymmetric $[\text{Eu}(\text{cda})_3(\text{H}_2\text{O})_3]$ ($\text{Na}(\text{cda})$ =sodium carbamylidicyanomethanide), that far exceeds the activity of LiNbO_3 , with *ca.* $6000\times$ α -quartz.⁷⁹ In this case, the strong non-linear behaviour was characterised in terms of a strong delocalised π -system within the *ab*-plane of the crystal.

1.4.4 Magnetic properties and the magnetocaloric effect (MCE)

There have been a number of examples of discrete molecules derived from *3d*, *4f* and mixed *3d-4f* metal ions that display MCE properties but fall beyond the scope of this thesis. Instead, we shall focus on higher order Ln^{III} hybrid inorganic-organic materials. The first example is a 1D coordination polymer of Gd^{III} constructed from bridging acetates,⁸⁴ whose structure depends on the solvent. In water, a Gd^{III} -dimer is formed through a zig-zag motif, while in methanol the polymer is more linear. These polymers exhibited magnetic entropy changes, ΔS_m , with values of $47.7 \text{ J kg}^{-1} \text{ K}^{-1}$ and $45 \text{ J kg}^{-1} \text{ K}^{-1}$, respectively. The higher value in water was reasoned to be due to a lower ratio of diamagnetic components. Other 1D coordination polymers have been characterised using formate and acetate as co-ligands.⁸⁵ The polymer $[\text{Gd}(\text{HCOO})(\text{OAc})_2(\text{H}_2\text{O})_2]$ was shown to have weak antiferromagnetic coupling between centres with a large magnetic entropy change of $45.9 \text{ J kg}^{-1} \text{ K}^{-1}$.

The Gd^{III} -squarate, $[\text{Gd}(\text{C}_4\text{O}_4)(\text{OH})(\text{H}_2\text{O})_4]$ is currently the only layered magnetic cooler.⁸⁶ The layered motif arises from three of the squarate hydroxyl groups bridging to different Gd^{III} centres, while the fourth remains protonated and hydrogen bonds to the coordinated water molecules. This arrangement is favourable to a high magnetic entropy change of $47.3 \text{ J kg}^{-1} \text{ K}^{-1}$.

There have been a number of Gd^{III} - 3D framework materials that show magnetic cooling properties; however, the value of magnetic entropy change varies considerably. One consideration to make is the size of the ligand in the framework. When the ligand is reasonably large, such as fumaric acid,⁸⁷ 1,4 benzenedicarboxylic acid⁸⁵ or 4,4'-dicarboxylate-2,2'-dipyridine,⁸⁸ slightly lower magnetic entropy changes, no greater than $30 \text{ J kg}^{-1} \text{ K}^{-1}$, are obtained. To improve the values of the magnetic entropy change, smaller ligands have been used. The pillared-layered structure of $[\text{Gd}(\text{HCOO})(\text{C}_8\text{H}_4\text{O}_4)]$ contains layers of Gd^{III} ions bridged through the formate ion, which are then pillared by the terephthalate ligand.⁸⁹ The metal centres were shown to weakly interact, which leads to a large entropy change of $47 \text{ J kg}^{-1} \text{ K}^{-1}$. When the terephthalic acid is removed from the reaction system a dense 3D Gd^{III} -formate, $[\text{Gd}(\text{HCOO})_3]$, can be isolated.⁹⁰ There is a large distance (6.4 \AA) between the Gd^{III} centres that results in weak magnetic interactions and leads to a very high entropy change of $59 \text{ J kg}^{-1} \text{ K}^{-1}$. This was the first molecular based coolant that outperforms the magnetic cooling material, gadolinium gallium garnet (GGG). The use of small ligands has been proven to be a successful approach further exemplified by the Gd^{III} -hydroxy carbonate $[\text{Gd}(\text{OH})(\text{CO}_3)]$.⁹¹ This material showed an entropy change up to $66.4 \text{ J kg}^{-1} \text{ K}^{-1}$, which was high due to the increased ratio of metal/ligand and the denser packing of the Gd^{III} centres.

The above discussion has highlighted the classification of hybrid inorganic-organic materials and placed them in the context of traditional cluster coordination chemistry. Hybrid materials have developed as a field of functional materials and matured into an area where many real-world problems are being tackled. The literature reviewed above has focussed on the use of the lanthanide ions and their unique optical properties and some of the applications that can be exploited from this property. The latter end of the review also touched on the magnetic properties with a particular focus on the interesting application of lanthanide ions (namely Gd^{III}) as molecular refrigerants.

1.5 Aims and objectives

This thesis looks into combining the expertise from two research groups. The Schmitt group has expertise in synthetic approaches to inorganic-organic hybrid materials. Two types of ligand have been identified (i) the phosphonic acids and (ii) ligands that incorporate the iminodiacetic acid function.

Phosphonic acids have been identified as appropriate ligands as they contain a functional group that displays variable coordination modes which has previously resulted in the successful isolation of novel inorganic-organic capsules^{92, 93} and polyoxometalate materials.⁹⁴⁻⁹⁷ The ligands incorporating iminodiacetic acids have been shown to be flexible ligands with the ability to stabilise large clusters⁹⁸⁻¹⁰⁰ and 3D architectures.^{101, 102} It was believed these could be excellent candidates for controlling the dimensionality of the resulting inorganic-organic hybrid. The Evans group has expertise in the characterisation of lanthanide(III) ions, with notable contributions to understanding the optical properties of layered lanthanide materials¹⁰³ and the complex energy transfer dynamics involved,¹⁰⁴ as well as studies into the aggregation of trivalent lanthanides in surfactant media.¹⁰⁵ In this thesis, we wished to bring these two areas together with the aim of identifying new lanthanide-organic hybrid materials with tuneable optoelectronic and magnetic properties.

The specific goals of the thesis are outlined below:

- (a) Synthesis of novel lanthanide phosphonate hybrid materials.
- (b) Investigate morphology of the resulting materials and try to understand the controlling variables involved
- (c) Stabilise Ln(III) centres in solution to yield hybrid materials of tuneable dimensionality.
- (d) Identify structural features that can be exploited in the development of future applications.
- (e) Investigate and understand the optical properties of the hybrid materials in solution and/or the solid-state.
- (f) Determine the physicochemical properties to gauge the stability of all materials.

To achieve these goals the following strategies and techniques will be exploited.

- (i) Synthesis by traditional benchtop reactions and high pressure solvothermal conditions.
- (ii) Variation of ligand design based on steric bulk, aromaticity and position of functional groups in the ligand.
- (iii) X-ray diffraction to interrogate the structures.
- (iv) Characterise crystal morphology through scanning electron microscopy.
- (v) A combination of infrared, nuclear magnetic resonance and mass spectroscopies and thermogravimetric analysis will be used to aid structural characterisation and to determine the physicochemical properties.
- (vi) UV/Vis absorption, steady-state and time-resolved photoluminescence spectroscopies will be utilised to characterise the optical properties.

1.6 References

1. H. Li, M. Eddaoudi, M. O'Keeffe and O. M. Yaghi, *Nature*, 1999, **402**, 276-279.
2. M. Eddaoudi, J. Kim, N. Rosi, D. Vodak, J. Wachter, M. O'Keeffe and O. M. Yaghi, *Science*, 2002, **295**, 469-472.
3. H. K. Chae, D. Y. Siberio-Perez, J. Kim, Y. Go, M. Eddaoudi, A. J. Matzger, M. O'Keeffe and O. M. Yaghi, *Nature*, 2004, **427**, 523-527.
4. H. Furukawa, N. Ko, Y. B. Go, N. Aratani, S. B. Choi, E. Choi, A. O. Yazaydin, R. Q. Snurr, M. O'Keeffe, J. Kim and O. M. Yaghi, *Science*, 2010, **329**, 424-428.
5. O. K. Farha, I. Eryazici, N. C. Jeong, B. G. Hauser, C. E. Wilmer, A. A. Sarjeant, R. Q. Snurr, S. T. Nguyen, A. O. Yazaydin and J. T. Hupp, *J. Am. Chem. Soc.*, 2012, **134**, 15016-15021.
6. H. W. Langmi, J. W. Ren, B. North, M. Mathe and D. Bessarabov, *Electrochim. Acta*, 2014, **128**, 368-392.
7. M. P. Suh, H. J. Park, T. K. Prasad and D. W. Lim, *Chem. Rev.*, 2012, **112**, 782-835.
8. K. Sumida, D. L. Rogow, J. A. Mason, T. M. McDonald, E. D. Bloch, Z. R. Herm, T. H. Bae and J. R. Long, *Chem. Rev.*, 2012, **112**, 724-781.
9. J. R. Li, J. Sculley and H. C. Zhou, *Chem. Rev.*, 2012, **112**, 869-932.
10. J. Gascon, A. Corma, F. Kapteijn and F. Xamena, *ACS Catal.*, 2014, **4**, 361-378.
11. K. Biradha, A. Ramana and J. J. Vittal, *Cryst. Growth Des.*, 2009, **9**, 2969-2970.
12. A. K. Cheetham, C. N. R. Rao and R. K. Feller, *Chem. Commun.*, 2006, 4780-4795.
13. C. N. R. Rao, A. K. Cheetham and A. Thirumurugan, *J. Phys.: Condens. Matter*, 2008, **20**, 083202.
14. A. Thirumurugan, S. K. Pati, M. A. Green and S. Natarajan, *J. Mater. Chem.*, 2003, **13**, 2937-2941.
15. R. C. Wang, Y. P. Zhang, H. L. Hu, R. R. Frausto and A. Clearfield, *Chem. Mater.*, 1992, **4**, 864-871.
16. Y. G. Huang, B. L. Wu, D. Q. Yuan, Y. Q. Xu, F. L. Jiang and M. C. Hong, *Inorg. Chem.*, 2007, **46**, 1171-1176.
17. X. D. Guo, G. S. Zhu, Z. Y. Li, F. X. Sun, Z. H. Yang and S. L. Qiu, *Chem. Commun.*, 2006, 3172-3174.
18. S. Song, X. Li, Y. H. Zhang, R. Huo and D. Ma, *Dalton Trans.*, 2014, **43**, 5974-5977.
19. H. B. Zhang, Y. Peng, X. C. Shan, C. B. Tian, L. Ping and S. W. Du, *Inorg. Chem. Commun.*, 2011, **14**, 1165-1169.
20. M. J. Bialek, J. Janczak and J. Zon, *CrystEngComm*, 2013, **15**, 390-399.
21. T. Devic, C. Serre, N. Audebrand, J. Marrot and G. Ferey, *J. Am. Chem. Soc.*, 2005, **127**, 12788-12789.

22. Z. Amghouz, S. Garcia-Granda, J. R. Garcia, A. Clearfield and R. Valiente, *Cryst. Growth Des.*, 2011, **11**, 5289-5297.
23. R. D. Shannon, *Acta Crystallogr. Sect. A*, 1976, **32**, 751-767.
24. S. A. Cotton, *C. R. Chimie*, 2005, **8**, 129-145.
25. E. M. R. Kiremire, *J. Chem. Educ.*, 1987, **64**, 951-953.
26. S. V. Eliseeva and J. C. G. Bunzli, *Chem. Soc. Rev.*, 2010, **39**, 189-227.
27. A. Beeby, I. M. Clarkson, R. S. Dickins, S. Faulkner, D. Parker, L. Royle, A. S. de Sousa, J. A. G. Williams and M. Woods, *J. Chem. Soc., Perkin Trans. 2*, 1999, 493-503.
28. M. H. V. Werts, R. T. F. Jukes and J. W. Verhoeven, *Phys. Chem. Chem. Phys.*, 2002, **4**, 1542-1548.
29. S. I. Weissman, *J. Chem. Phys.*, 1942, **10**, 214-217.
30. C. Yang, L. M. Fu, Y. Wang, J. P. Zhang, W. T. Wong, X. C. Ai, Y. F. Qiao, B. S. Zou and L. L. Gui, *Angew. Chem. Int. Ed.*, 2004, **43**, 5010-5013.
31. R. Rodriguez-Cortinas, F. Avecilla, C. Platas-Iglesias, D. Imbert, J. C. G. Bunzli, A. de Blas and T. Rodriguez-Blas, *Inorg. Chem.*, 2002, **41**, 5336-5349.
32. G. F. de Sa, O. L. Malta, C. D. Donega, A. M. Simas, R. L. Longo, P. A. Santa-Cruz and E. F. da Silva, *Coord. Chem. Rev.*, 2000, **196**, 165-195.
33. M. Latva, H. Takalo, V. M. Mukkala, C. Matachescu, J. C. Rodriguez-Ubis and J. Kankare, *J. Lumin.*, 1997, **75**, 149-169.
34. E. G. Moore, A. P. S. Samuel and K. N. Raymond, *Acc. Chem. Res.*, 2009, **42**, 542-552.
35. A. P. S. Samuel, J. D. Xu and K. N. Raymond, *Inorg. Chem.*, 2009, **48**, 687-698.
36. K. Binnemans and C. GorllerWalrand, *Journal of Rare Earths*, 1996, **14**, 173-180.
37. R. M. Supkowski and W. D. Horrocks, *Inorg. Chim. Acta*, 2002, **340**, 44-48.
38. T. Kimura and Y. Kato, *J. Alloys. Compd.*, 1995, **225**, 284-287.
39. L. D. Carlos, R. A. S. Ferreira, V. D. Bermudez and S. J. L. Ribeiro, *Adv. Mater.*, 2009, **21**, 509-534.
40. P. Caravan, *Chem. Soc. Rev.*, 2006, **35**, 512-523.
41. H. U. Rashid, K. Yu and J. Zhou, *J. Struct. Chem.*, 2013, **54**, 223-249.
42. R. Sessoli, D. Gatteschi, A. Caneschi and M. A. Novak, *Nature*, 1993, **365**, 141-143.
43. H. L. C. Feltham and S. Brooker, *Coord. Chem. Rev.*, 2014, **276**, 1-33.
44. D. N. Woodruff, R. E. P. Winpenny and R. A. Layfield, *Chem. Rev.*, 2013, **113**, 5110-5148.
45. Y. Z. Zheng, G. J. Zhou, Z. P. Zheng and R. E. P. Winpenny, *Chem. Soc. Rev.*, 2014, **43**, 1462-1475.
46. X. Ma, X. Li, Y. E. Cha and L. P. Jin, *Cryst. Growth Des.*, 2012, **12**, 5227-5232.
47. A. R. Ramya, S. Varughese and M. L. P. Reddy, *Dalton Trans.*, 2014, **43**, 10940-10946.
48. Q. Tang, S. X. Liu, Y. W. Liu, D. F. He, J. Miao, X. Q. Wang, Y. J. Ji and Z. P. Zheng, *Inorg. Chem.*, 2014, **53**, 289-293.
49. S. Song, X. Li and Y. H. Zhang, *Dalton Trans.*, 2013, **42**, 10409-10412.
50. X. P. Zhang, D. G. Wang, Y. Su, H. R. Tian, J. J. Lin, Y. L. Fenga and J. W. Cheng, *Dalton Trans.*, 2013, **42**, 10384-10387.
51. J. N. Hao and B. Yan, *J. Mater. Chem. C*, 2014, **2**, 6758-6764.
52. Y. Zhou and B. Yan, *Inorg. Chem.*, 2014, **53**, 3456-3463.
53. M. L. Ma, J. H. Qin, C. Ji, H. Xu, R. Wang, B. J. Li, S. Q. Zang, H. W. Hou and S. R. Batten, *J. Mater. Chem. C*, 2014, **2**, 1085-1093.
54. L. L. da Luz, B. F. L. Viana, G. C. O. da Silva, C. C. Gatto, A. M. Fontes, M. Malta, I. T. Weber, M. O. Rodrigues and S. Alves, *CrystEngComm*, 2014, **16**, 6914-6918.
55. J. Lehr, P. D. Beer, S. Faulkner and J. J. Davis, *Chem. Commun.*, 2014, **50**, 5678-5687.
56. S. J. Butler and D. Parker, *Chem. Soc. Rev.*, 2013, **42**, 1652-1666.
57. B. Liu, W. P. Wu, L. Hou and Y. Y. Wang, *Chem. Commun.*, 2014, **50**, 8731-8734.
58. J. M. Zhou, W. Shi, H. M. Li, H. Li and P. Cheng, *J. Phys. Chem. C*, 2014, **118**, 416-426.
59. Y. M. Zhu, C. H. Zeng, T. S. Chu, H. M. Wang, Y. Y. Yang, Y. X. Tong, C. Y. Su and W. T. Wong, *J. Mater. Chem. A*, 2013, **1**, 11312-11319.
60. Q. B. Bo, H. T. Zhang, H. Y. Wang, J. L. Miao and Z. W. Zhang, *Chem. Eur. J.*, 2014, **20**, 3712-3723.
61. B. X. Liu, C. L. Sun and Y. Chen, *J. Mater. Chem. B*, 2014, **2**, 1661-1666.

62. B. V. Harbuzaru, A. Corma, F. Rey, J. L. Jorda, D. Ananias, L. D. Carlos and J. Rocha, *Angew. Chem. Int. Ed.*, 2009, **48**, 6476-6479.
63. H. L. Tan, C. J. Ma, L. L. Chen, F. G. Xu, S. H. Chen and L. Wang, *Sens. Actuators, B*, 2014, **190**, 621-626.
64. H. L. Tan, C. J. Ma, Y. H. Song, F. G. Xu, S. H. Chen and L. Wang, *Biosens. Bioelectron.*, 2013, **50**, 447-452.
65. Q. Liu, S. Z. Ge, J. C. Zhong, Y. Q. Sun and Y. P. Chen, *Dalton Trans.*, 2013, **42**, 6314-6317.
66. C. F. Chow, M. H. W. Lam and W. Y. Wong, *Anal. Chem.*, 2013, **85**, 8246-8253.
67. Y. P. He, Y. X. Tan and J. Zhang, *J. Mater. Chem. C*, 2014, **2**, 4436-4441.
68. C. Zhan, S. Ou, C. Zou, M. Zhao and C. D. Wu, *Anal. Chem.*, 2014, **86**, 6648-6653.
69. B. L. Chen, L. B. Wang, F. Zapata, G. D. Qian and E. B. Lobkovsky, *J. Am. Chem. Soc.*, 2008, **130**, 6718-6719.
70. K. L. Wong, G. L. Law, Y. Y. Yang and W. T. Wong, *Adv. Mater.*, 2006, **18**, 1051-1054.
71. K. A. White, D. A. Chengelis, K. A. Gogick, J. Stehman, N. L. Rosi and S. Petoud, *J. Am. Chem. Soc.*, 2009, **131**, 18069-18071.
72. A. Foucault-Collet, K. A. Gogick, K. A. White, S. Villette, A. Pallier, G. Collet, C. Kieda, T. Li, S. J. Geib, N. L. Rosi and S. Petoud, *Proc. Natl. Acad. Sci. U.S.A.*, 2013, **110**, 17199-17204.
73. C. Y. Sun, X. J. Zheng, X. B. Chen, L. C. Li and L. P. Jin, *Inorg. Chim. Acta*, 2009, **362**, 325-330.
74. D. F. Weng, X. J. Zheng and L. P. Jin, *Eur. J. Inorg. Chem.*, 2006, 4184-4190.
75. D. F. Weng, X. J. Zheng, X. B. Chen, L. Li and L. P. Jin, *Eur. J. Inorg. Chem.*, 2007, 3410-3415.
76. J. Yang, Q. Yuo, G. D. Li, J. J. Cao, G. H. Li and J. S. Chen, *Inorg. Chem.*, 2006, **45**, 2857-2865.
77. C. Andraud and O. Maury, *Eur. J. Inorg. Chem.*, 2009, 4357-4371.
78. J. Zhu, H. F. Song, J. W. Sun, P. F. Yan, G. F. Hou and G. M. Li, *Synth. Met.*, 2014, **192**, 29-36.
79. J. M. Shi, W. Xu, Q. Y. Liu, F. L. Liu, Z. L. Huang, H. Lei, W. T. Yu and Q. Fang, *Chem. Commun.*, 2002, 756-757.
80. Y. P. He, Y. X. Tan and J. Zhang, *Inorg. Chem.*, 2013, **52**, 12758-12762.
81. X. Q. Liang, F. Zhang, H. X. Zhao, W. Ye, L. S. Long and G. S. Zhu, *Chem. Commun.*, 2014, **50**, 6513-6516.
82. W. W. Ju, D. Zhang, D. R. Zhu and Y. Xu, *Inorg. Chem.*, 2012, **51**, 13373-13379.
83. C. Wang, T. Zhang and W. B. Lin, *Chem. Rev.*, 2012, **112**, 1084-1104.
84. F. S. Guo, J. D. Leng, J. L. Liu, Z. S. Meng and M. L. Tong, *Inorg. Chem.*, 2012, **51**, 405-413.
85. G. Lorusso, M. A. Palacios, G. S. Nichol, E. K. Brechin, O. Roubeau and M. Evangelisti, *Chem. Commun.*, 2012, **48**, 7592-7594.
86. S. Biswas, A. Adhikary, S. Goswami and S. Konar, *Dalton Trans.*, 2013, **42**, 13331-13334.
87. L. Sedlakova, J. Hanko, A. Orendacova, M. Orendac, C. L. Zhou, W. H. Zhu, B. W. Wang, Z. M. Wang and S. Gao, *J. Alloys. Compd.*, 2009, **487**, 425-429.
88. P. F. Shi, Y. Z. Zheng, X. Q. Zhao, G. Xiong, B. Zhao, F. F. Wan and P. Cheng, *Chem. Eur. J.*, 2012, **18**, 15086-15091.
89. R. Sibille, T. Mazet, B. Malaman and M. Francois, *Chem. Eur. J.*, 2012, **18**, 12970-12973.
90. G. Lorusso, J. W. Sharples, E. Palacios, O. Roubeau, E. K. Brechin, R. Sessoli, A. Rossin, F. Tuna, E. J. L. McInnes, D. Collison and M. Evangelisti, *Adv. Mater.*, 2013, **25**, 4653-4656.
91. Y. C. Chen, L. Qin, Z. S. Meng, D. F. Yang, C. Wu, Z. D. Fu, Y. Z. Zheng, J. L. Liu, R. Tarasenko, M. Orendac, J. Prokleska, V. Sechovsky and M. L. Tong, *J. Mater. Chem. A*, 2014, **2**, 9851-9858.
92. J. M. Breen and W. Schmitt, *Angew. Chem. Int. Ed.*, 2008, **47**, 6904-6908.
93. J. M. Breen, R. Clerac, L. Zhang, S. M. Cloonan, E. Kennedy, M. Feeney, T. McCabe, D. C. Williams and W. Schmitt, *Dalton Trans.*, 2012, **41**, 2918-2926.
94. L. Zhang, R. Clerac, P. Heijboer and W. Schmitt, *Angew. Chem. Int. Ed.*, 2012, **51**, 3007-3011.

95. L. Zhang, R. Clerac, C. I. Onet, C. Healy and W. Schmitt, *Eur. J. Inorg. Chem.*, 2013, 1654-1658.
96. L. Zhang, R. Clerac, C. I. Onet, M. Venkatesan, P. Heijboer and W. Schmitt, *Chem. Eur. J.*, 2012, **18**, 13984-13988.
97. L. Zhang, B. Marzec, R. Clerac, Y. H. Chen, H. Z. Zhang and W. Schmitt, *Chem. Commun.*, 2013, **49**, 66-68.
98. W. Schmitt, C. E. Anson, R. Sessoli, M. van Veen and A. K. Powell, *J. Inorg. Biochem.*, 2002, **91**, 173-189.
99. W. Schmitt, C. E. Anson, W. Wernsdorfer and A. K. Powell, *Chem. Commun.*, 2005, 2098-2100.
100. W. Schmitt, L. Zhang, C. E. Anson and A. K. Powell, *Dalton Trans.*, 2010, **39**, 10279-10285.
101. W. Schmitt, J. P. Hill, S. Malik, C. A. Volkert, I. Ichinose, C. E. Anson and A. K. Powell, *Angew. Chem. Int. Ed.*, 2005, **44**, 7048-7053.
102. G. La Spina, R. Clerac, E. S. Collins, T. McCabe, M. Venkatesan, I. Ichinose and W. Schmitt, *Dalton Trans.*, 2007, 5248-5252.
103. R. C. Evans, L. D. Carlos, P. Douglas and J. Rocha, *J. Mater. Chem.*, 2008, **18**, 1100-1107.
104. R. C. Evans, D. Ananias, A. Douglas, P. Douglas, L. D. Carlos and J. Rocha, *J. Phys. Chem. C*, 2008, **112**, 260-268.
105. R. F. P. Pereira, M. J. Tapia, A. J. M. Valente, R. C. Evans, H. D. Burrows and R. A. Carvalho, *J. Colloid Interface Sci.*, 2011, **354**, 670-676.

Chapter Two



Experimental

2.1 Materials and methods

2.1.1 Reagents

1-Bromonaphthalene ($\geq 95\%$) and *N*-(2-hydroxyethyl)iminodiacetic acid were purchased from Fluka and used without further purification. All other chemicals and solvents were of reagent grade and purchased from Sigma-Aldrich Ltd. or local solvent suppliers and were used as received, unless otherwise stated. Water was deionised before use.

2.1.2 Nuclear magnetic resonance (NMR)

Solution NMR spectroscopy was performed on a Bruker DPX 400 NMR machine. ^1H , ^{13}C and ^{31}P spectra were obtained at an operating frequency of 400, 151 and 162 MHz, respectively, and were measured by either Dr. John O'Brien or Dr. Manuel Ruether. Samples were dissolved in a suitable deuterated solvent identified in the ligand characterisation. Standard abbreviations for assignments are given: s, singlet; d, doublet; t, triplet and m, multiplet.

2.1.3 Fourier transform-infrared spectroscopy (FT-IR)

Fourier transform infrared (FT-IR) spectra were measured on a PerkinElmer Spectrum 100 FT-IR spectrometer in the range $4000\text{-}650\text{ cm}^{-1}$ using a universal attenuated total reflectance (ATR) sampling accessory. Data was collected at a scan rate of 16 scans per minute with a resolution of 4 cm^{-1} . The following abbreviations are used to describe the intensities: s, strong; m, medium; w, weak and br, broad.

2.1.4 Mass Spectrometry

Electrospray ionisation mass spectrometry was performed on a Micromass LCT Electrospray mass spectrometer by Dr. Martin Feeney or Dr. Gary Hessman. Samples were dissolved in a suitable HPLC grade solvent and are listed under the appropriate characterisation section.

2.1.5 Thermogravimetric analysis (TGA)

TGA was performed using a Perkin Elmer Pyris 1 TGA thermogravimetric analyzer in the range $30\text{-}900\text{ }^\circ\text{C}$ in an air atmosphere using *ca.* 2-5 mg sample, at a heating rate of $10\text{ }^\circ\text{C}/\text{min}$ in a ceramic crucible. The instrument was calibrated to In and Ni standards in an air atmosphere.

2.1.6 Elemental analysis

Elemental analyses (CHN) were performed on an Exeter Analytical CE 440 elemental analyser through the service provided in the Microanalysis Lab of the School of Chemistry and Chemical Biology, University College Dublin.

2.1.7 Single crystal X-ray diffraction

The data collection for crystal structures described in this report were measured by Dr. Brendan Twamley or Dr. Tom McCabe on a Bruker Apex II CCD diffractometer or a Rigaku Saturn -724 diffractometer.

Both diffractometers use a graphite monochromated Mo-K α (0.71073 Å) radiation source. The omega scan method was used to collect a full sphere or hemisphere of data for each crystal, with a detector to crystal distance of 5 or 6 cm. Data sets collected on the Bruker Apex II were processed and corrected for Lorentz and polarisation effects using the SMART¹ and SAINT-PLUS² software. The structures were solved using direct methods with the SHELXTL program package.

Data sets collected from the Rigaku Saturn-724 contained a total of 1680 diffraction images, each of 0.5° interval. Data integration, reduction and correction for absorption and polarisation effects were accounted for using the Crystalclear SM 1.4.0 software. Space group determination, structure solution and refinement were obtained using the Crystalstructure ver3.8 and the Bruker SHELXTL³ software packages.

All non-hydrogen atoms were refined anisotropically. Hydrogen atoms were assigned to calculated positions using a riding model with appropriately fixed isotropic thermal parameters.

2.1.8 Powder X-ray diffraction (PXRD)

PXRD patterns were measured on a Siemens D500 diffractometer using Cu K α_1 radiation ($\lambda = 1.54056$ Å). Samples were measured using a [100] silicon substrate to minimise for background scatter. Samples were prepared by lightly grinding the crystalline material and sprinkling onto a thin layer of petroleum jelly on the substrate. Diffraction patterns were measured in the 2θ range 2-70° using a 0.02° step size and 14.7 s counting rate. Some powder patterns exhibit additional reflections from instrumental artefacts at $2\theta = 39.4$ and 34.6° , respectively. These artefacts are highlighted in figures with a red asterisk. For space group determination, reflections in the powder pattern were deconvoluted using the software package XFIT.⁴ Space group assignment was made using the program TAUP⁵ within the CRYSFIRE Suite.⁶

2.1.9 UV/Vis absorption spectroscopy

Solution-state UV/Vis absorption spectroscopy was performed on a Shimadzu UV-2401 PC spectrometer or a Perkin Elmer, Lambda 35 UV/Vis spectrometer using matched quartz cuvettes (path length 10 mm) at room temperature. Samples made up in H₂O were of Millipore grade, while all other solvents were of HPLC grade and higher.

Solid-state UV/Vis diffuse reflectance spectroscopy was performed on a Perkin Elmer Lambda 1050 spectrometer using an integrating sphere accessory across the range 215-800 nm. The sample was held between two quartz slides and the total reflectance measured with the sample at the rear of the integrating sphere. The background for the quartz slide was accounted for by

measuring the transmission of the slide when positioned in front of the empty sphere and the reflectance of the slide positioned at the rear of the sphere. Data was treated for background correction by substituting into **Eqn. 2.1**:

$$R_S = \frac{R_S - R_B}{T_B} \quad \text{Eqn. 2.1}$$

where R_S is the sample reflectance, R_B the reflectance of a blank quartz slide and T_B is the transmission of the blank quartz slide.

2.1.10 Photoluminescence spectroscopy

Steady-state photoluminescence emission and excitation spectra were measured on a Fluorolog-3 spectrophotometer (Horiba Jobin Yvon), using the front-face configuration for solid-state samples. Low temperature phosphorescence measurements on ligands were performed at 77 K using a liquid nitrogen filled quartz dewar. Spectra measured in the UV/Vis range used a room temperature R9281x photomultiplier tube as the detector. NIR spectra were measured using a liquid nitrogen cooled R5509 photomultiplier tube as the detector. Emission and excitation spectra were corrected for the wavelength response of the system and the intensity of the lamp profile over the excitation range, respectively, using correction factors supplied by the manufacturer. Solid-state measurements in the UV/Vis region were recorded in front-face configuration with the sample held between two quartz slides. Slit widths were optimised to maximise the resolution of emission lines and to maintain intensities below 2×10^6 ; typically excitation and emission slits were ≤ 2 nm. NIR solid-state emission/excitation spectra were measured in a right-angle configuration and required larger slit widths ≤ 12 nm. Absolute photoluminescence quantum yields (Φ_{PL}) were measured using an F-3018 integrating sphere accessory (Horiba Jobin Yvon), which is calibrated between 330-850 nm. To determine Φ_{PL} , four measurements are taken; the scatter response of the empty integrating sphere, L_A , the scatter response of the sample, L_C , the emission spectrum measured in an empty sphere, E_A and the emission spectrum of the sample, E_C . With these four quantities, Φ_{PL} can be determined using the relationship:

$$\Phi_{PL} = \frac{E_C - E_A}{L_A - L_C} \quad \text{Eqn. 2.2}$$

Three measurements for each sample were taken and the average value is reported. The method has an error of 10%. Emission lifetimes in the micro-millisecond timescale were measured using a Jobin-Yvon Fluoromax-3 equipped with a Spex 1934D phosphorimeter accessory. Emission decay curves were fit in the Origin 8.0 data analysis program. Emission lifetimes in the nanosecond timescale were measured on a Horiba Jobin Yvon Fluorolog-3 equipped with a FluoroHub v2.0 single photon controller using the time-correlated single photon counting method (TCSPC), run in reverse mode. The sample solutions were excited at 294 nm or 372 nm with a pulsed nanosecond light-emitting diode (NanoLED[®]). The time distribution of the lamp pulse, < 1.0 ns ($\lambda_{ex} = 294$ nm) and 1.1 ns ($\lambda_{ex} = 372$ nm), also called the instrument response function, was recorded prior to lifetime measurements in a separate experiment using a scatter solution, in this case a solution of

Ludox (Aldrich). All the measurements were performed at 298 K. The emission decay curves were analyzed using IBH DAS6 software. Data fitted as a sum of exponentials, employing a nonlinear least-squares error minimization analysis:

$$I(t) = \sum_{i=1}^n \alpha_i \cdot \exp\left(\frac{-t}{\tau_i}\right) \quad \text{Eqn. 2.3}$$

The pre-exponential factors (α_i) are shown normalized and the errors are taken as two standard deviations. Emission decay curves were fit to either a single or double exponential decay function and the average lifetime $\langle\tau\rangle$ is given by:

$$\langle\tau\rangle = \frac{\sum \alpha_i \cdot \tau_i^2}{\sum \alpha_i \cdot \tau_i} = \sum f_i \cdot \tau_i \quad \text{Eqn. 2.4}$$

where the fractional contribution of the lifetime i, f_i , is defined as :

$$f_i = \frac{\alpha_i \cdot \tau_i}{\sum \alpha_j \cdot \tau_j} \quad \text{Eqn. 2.5}$$

The goodness of fit to all emission decay curves was assessed qualitatively by looking at the symmetric distribution of the residuals. The residuals are determined by:

$$\hat{\varepsilon} = y - \hat{y} \quad \text{Eqn. 2.6}$$

where $\hat{\varepsilon}$ is the residual, y is the observed data point and \hat{y} is the predicted data point from the model. A quantitative assessment of the fitted decay curves are made by determining the chi-squared value, χ^2 , given by:

$$\chi^2 = \frac{(O - E)^2}{\sigma^2} \quad \text{Eqn. 2.7}$$

where O is the observed data, E is the theoretical data and σ^2 is the variance of the measured point. In addition to determining χ^2 , the coefficient of determination, R^2 , is determined by the following relation:

$$R^2 = 1.0 - \frac{SS_{res}}{SS_{tot}} \quad \text{Eqn. 2.8}$$

where SS_{res} is the residual sum of the squares, given by $SS_{res} = \sum_i (\hat{y}_i - \bar{y})^2$, where \hat{y}_i is the predicted data point and \bar{y} is the mean of the observed data. SS_{tot} is the total sum of the squares, given by $SS_{tot} = \sum_i (y_i - \bar{y})^2$ where y_i is the observed data point.

2.1.11 Circular Dichroism

Circular dichroism spectra were measured on a Jasco J-815 CD spectrometer. The instrument measures the absorption of both left- and right- polarised light and the final signal is an average of these at each wavelength. A small quantity of sample was held between two quartz slides and the measurement made at 25 °C. All spectra were corrected by subtraction of the quartz slide background. For solid-state measurements the absorbance maximum should not exceed a value of 1.

2.1.12 Scanning electron microscopy (SEM)

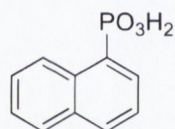
Scanning electron micrographs were recorded on a Zeiss-Ultra Scanning Electron Microscope at an accelerating voltage of 2-5 kV. Images were collected using an In-lens (Carl Zeiss) detector. Samples for SEM were prepared by dispersing 1-2 drops of the mother liquor from the sample reaction in 2 mL of H₂O and sonicated for two minutes. The dispersed material was drop-cast onto cut silicon wafers and allowed to dry. The wafer was mounted onto a carbon disc and a connection made between the wafer and stage using Ag-DAG paint to reduce charging effects on the sample.

2.1.13 Solvothermal synthesis

Solvothermal syntheses were carried out using a Parr Instrument Company Series 4760/4765 general-purpose digestion bomb with a 23 mL Teflon lined insert. Individual reactions were loaded with solvent and reagents of different quantities, as outlined in the compound synthesis list. The heating cycles are also listed here and were heated in a conventional oven.

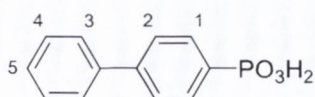
2.2 Ligand Synthesis

2.2.1 Synthesis of 1-naphthalene phosphonic acid (Naph-PO₃H₂)



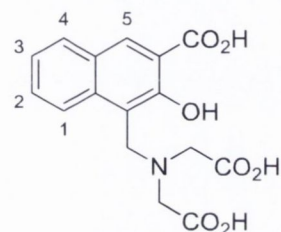
The ligand was prepared using a modified Arbusov reaction as outlined in previous syntheses of other aromatic phosphonic acids.⁷ To a 250 mL round bottom flask 1,3-diisopropyl benzene (50 mL), NiBr₂ (0.500 g) and 1-bromonaphthalene (3.380 mL, 20 mmol) were added and heated to 185 °C. Triethyl phosphite (5 mL, 29 mmol) was slowly added over six hours and the reaction mixture was left to reflux for 24 hours. Additional NiBr₂ (0.250 g) and triethyl phosphite (2.5 mL, 14.5 mmol) were subsequently added over three hours, followed by a further 24 hour reflux. The resulting black solution was distilled under vacuum to remove solvent, unreacted triethyl phosphite and side-products, leaving a viscous black oil. The black oil was dissolved in dichloromethane (DCM) and passed through a celite plug to remove nickel impurities, yielding a yellow filtrate. The DCM washings were concentrated to give a golden yellow oil, which was identified as the phosphate ester through ¹H and ³¹P NMR spectroscopy. Hydrolysis of the ester was achieved through reflux of the oil in HCl (50 mL, 37%) overnight. Upon cooling, the desired product, **Naph-PO₃H₂**, precipitated from solution, and was subsequently filtered and washed with DCM to give a white powder. Yield: 2.997 g (72%); m.p: 203-205 °C. ¹H NMR (400 MHz, *d*₆-DMSO) δ _H: 8.58 (d, 1H, H⁵), 7.54-7.63 (m, 3H), 7.98-8.09 (m, 3H). ³¹P NMR (162 MHz, *d*₆-DMSO) δ _P: 13.1 ppm. FT-IR ν _{max} (cm⁻¹): 3044 (w), 2284 (br), 1956 (w), 1726 (w), 1621 (w), 1593 (w), 1573 (w), 1508 (m), 1459 (w), 1338 (w), 1433 (w), 1224, 1189 (s), 1065 (s), 1028 (s), 996 (s), 913 (s), 861 (m), 797 (s), 770 (s), 671(s). HRMS (*m/z* -ES): Found: 207.0211 (M⁻-H. C₁₀H₈O₃P; *calc.*: 207.0211). CHN analysis for C₁₀H₉PO₃: Expected: C 57.70%; H 4.36%. Found: C 54.91%; H 4.40%.

2.2.2 Synthesis of 1-biphenyl phosphonic acid (Biphen-PO₃H₂)



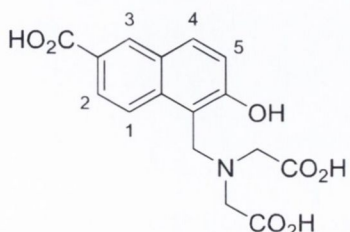
A similar procedure to **Naph-PO₃H₂** was adopted, where 1-bromonaphthalene was substituted for 4-bromobiphenyl (4.684 g, 20 mmol) and reacted with triethyl phosphite under the conditions described above. Yield: 1.306 g (56%); m.p: 237-240 °C. ¹H NMR (400 MHz, *d*₆-DMSO) δ_H: 7.42 (t, 1H, H₅), 7.50 (t, 2H, H₄), 7.71 (d, 2H, H₁), 7.77 (t, 4H, H_{4,5}). ³¹P NMR (162 MHz, *d*₆-DMSO) δ_P: 13.8 ppm. FT-IR ν_{max} (cm⁻¹): 2736 (br), 2271 (br) 1678 (w), 1602 (m), 1553 (m), 1484 (m), 1448 (w), 1391 (m), 1143 (m), 1017 (s), 1000 (s), 977 (s), 942 (s), 835 (m), 759 (s), 721 (m), 689 (m), 665 (s). HRMS (*m/z* -ES): Found: 233.0368 (M⁻-H. C₁₂H₁₀O₃P; *calc.*: 233.0368).

2.2.3 Synthesis of 2,2'-((3-carboxy-2-hydroxynaphthalen-1-yl)methylazanediy)diacetic acid (H₄C3hnida)



To 10 mL deionised water, iminodiacetic acid, (3.90 g, 29.3 mmol) was added and the pH raised to pH 6.5 using 4M NaOH. In a round-bottom flask, 3-hydroxy-2-naphthoic acid (5.00 g, 20.3 mmol) was dissolved in 100 mL acetic acid. The aqueous iminodiacetic acid solution was then added and stirred for 20 minutes, after which formaldehyde (2.85 mL, 38.3 mmol) was added dropwise and heated to 80 °C. After *ca.* 3 hours, a yellow precipitate is formed. The product was filtered and washed with cold ethanol and deionised water, before drying under vacuum. Yield: 4.53 g (67%) ¹H NMR (400 MHz, D₂O+Na₂CO₃) δ_H: 3.28 (s, 4H, 2 × N(CH₂)CO₂H), 4.26 (s, 2H, CH₂), 7.28-7.32 (t, 1H, H₃), 7.52-7.55 (t, 1H, H₂), 7.82-7.84 (d, 1H, H₄), 8.18-8.20 (d, 1H, H₁), 8.31 (s, 1H, H₅). FT-IR ν_{max} (cm⁻¹): 3117 (br), 3019 (w), 2993 (w), 2971 (w), 1738 (s), 1679 (s), 1630 (s), 1605 (m), 1583 (w), 1514 (w), 1433 (m), 1457 (s), 1288 (m), 1247 (m), 1210 (s), 1164 (s), 1098 (s), 1000 (m), 960 (m), 941 (m), 891(m), 796 (s), 754 (s), 720 (s), 674(m) HRMS (*m/z* -ES): Found: 332.0771 (M⁻-H. C₁₆H₁₄N₁O₇; *calc.*: 332.0770). CHN analysis for C₁₆H₁₄N₁O₇: Expected: C 57.66%; H 4.54%, N 4.20%. Found: C 57.08%; H 4.23%, N 3.99%.

2.2.4 Synthesis of 2,2'-((6-carboxy-2-hydroxynaphthalen-1-yl)methylazanediy)diacetic acid (H₄C6hnida)



The same synthetic procedure was used as for **H₄C3hnida**, but substituting in 6-hydroxy-2-naphthoic acid (5.00 g, 20.3 mmol) to dissolve in 100 mL acetic acid. After the reaction was left under stirring at 80 °C for *ca.* 3 hours a white precipitate is obtained. This powder was filtered and washed with cold ethanol and water, followed by drying under vacuum. Yield 3.992 g (59%) ¹H NMR (400 MHz, D₂O+Na₂CO₃) δ_H: 3.41 (s, 4H, 2 × N(CH₂)CO₂H), 4.45 (s, 2H, CH₂), 6.98-7.04 (d, 1H, H₅), 7.65-7.67 (d, 1H, H₄), 7.76-7.78 (d, 1H, H₂), 7.88-7.90 (d, 1H, H₁), 8.25-8.27 (s, 1H, H₃). FT-IR ν_{max} (cm⁻¹): 3266 (br),

3075(w), 3024(w), 2975 (w), 1688 (s), 1625 (s), 1487 (m), 1431 (m), 1338 (m), 1293 (s), 1258 (s), 1208 (s), 1156 (m), 1078 (m), 982 (m), 905 (s), 818 (m), 756 (s), 717 (s), HRMS (m/z -ES): Found: 332.0771 (M^- -H. $C_{16}H_{14}N_1O_7$; *calc.*: 332.0770). CHN analysis for $C_{16}H_{14}N_1O_7$: Expected: C 57.66%; H 4.54%, N 4.20%. Found: C 58.32%; H 4.77%, N 3.87%.

2.3 Synthesis of lanthanide-organic hybrid compounds

In a typical synthesis for the lanthanide phosphonates (**Chapter 3**), a mixture of ligand (0.4 mmol), $LnCl_3 \cdot 6H_2O$ (0.02 mmol, $Ln^{III} = Nd^{III}, Eu^{III}, Tb^{III}$ and Yb^{III}) and an appropriate solvent (5 mL) were placed in a 20 mL Teflon liner and stirred for 30 minutes to give a white cloudy suspension. The pH was adjusted to pH 2 using 1 M NaOH aqueous solution. The Teflon liner was inserted into a steel autoclave and placed in an oven at 100 °C for 48 hours. Following cooling to room temperature, the resulting material was filtered and washed with water and ethanol before drying at 80 °C.

2.3.1 Synthesis of lanthanide *tert*-butyl phosphonates (Ln-Bu').

The ligand used was *tert*-butyl phosphonic acid (0.055 g, 0.4 mmol) and the solvent was acetonitrile. For **Eu-Bu'** (1) small plate crystals suitable for single X-ray diffraction were found to form in solution. Yield: 0.078 g (67%). FT-IR ν_{max} (cm^{-1}): 2976 (m), 2952 (m), 2908 (m), 2870 (m), 1640 (m), 1475 (m), 1397 (m), 1361 (m), 1122 (s), 1051 (s), 945 (s), 888 (s), 869 (s), 832 (s), 774 (m), 658 (s). **Nd-Bu'**: Yield 65 mg (53%). FT-IR ν_{max} (cm^{-1}): 2973 (m), 2950 (m), 2904 (m), 2868 (m), 1626 (m), 1481 (m), 1393 (m), 1364 (m), 1119 (s), 1063 (s), 1028 (s), 972 (s), 898 (s), 834 (s). **Tb-Bu'**: Yield 69 mg (56%). FT-IR ν_{max} (cm^{-1}): 2952 (m), 2906 (m), 2869 (m), 1649 (m), 1479 (m), 1394 (m), 1362 (m), 1127 (s), 1061 (s), 1034 (s), 1004 (m), 966 (s), 893 (s), 836 (s), 661 (s). **Yb-Bu'**: Yield 74 mg (64%). FT-IR ν_{max} (cm^{-1}): 2973 (m), 2907 (m), 2871 (m), 1640 (m), 1480 (m), 1396 (m), 1363 (m), 1237 (m), 1115 (s), 1071 (s), 1039 (s), 981 (s), 943 (s), 914 (s), 878 (s), 834 (s), 656 (s). CHN analysis for $EuC_{12}H_{32}P_3O_{10}$: Expected: C 11.35%; H 7.62%. Found: C 11.09%; H 6.97%.

2.3.2 Synthesis of lanthanide naphthalene phosphonates (Ln-Naph)

The ligand was naphthalene phosphonic acid (0.083 g, 0.4 mmol) and deionised water was used for solvent. **Nd-Naph**: Yield 0.068 g (59%). FTIR ν_{max} (cm^{-1}): 3057 (w), 3041 (w), 1591 (w), 1574 (w), 1507 (m), 1460 (w), 1335 (m), 1211 (m), 1134 (s), 1043 (s), 1014 (s), 966 (s), 797 (s), 770 (s), 677 (s). **Eu-Naph**: Yield 0.077 g (67%). FTIR ν_{max} (cm^{-1}): 3057 (w), 1591 (w), 1506 (m), 1460 (w), 1334 (w), 1211 (m) 1140 (s), 1080 (s), 1034 (s), 1016 (s), 968 (s), 856 (m), 830 (m), 796 (s), 770 (s), 727 (m), 677 (s). **Tb-Naph**: Yield 73 mg (65%). FTIR ν_{max} (cm^{-1}): 3058 (w), 3043 (w), 1592 (w), 1507 (m), 1460 (w), 1335 (w), 1212 (m), 1142 (s), 1077 (s), 1046 (s), 1016 (s), 968 (s), 857 (m), 830 (m), 797 (s), 770 (s), 728 (m), 678 (s). **Yb-Naph**: 0.074 g (61%). FTIR ν_{max} (cm^{-1}): 3048 (w), 3009 (w), 1622 (w), 1593 (w), 1574 (w), 1507 (m), 1460 (w) 1337 (w), 1221 (m),

1135 (s), 1094 (s), 1061 (s), 991 (m), 896 (s), 797 (s), 770 (s), 675 (s). CHN analysis for $\text{EuC}_{20}\text{H}_{18}\text{P}_2\text{O}_8$: Expected: C 40.02%; H 3.02%. Found: C 39.66%; H 2.61%.

2.3.3 Synthesis of lanthanide biphenyl phosphonates (Ln-Biphen)

The ligand was biphenyl phosphonic acid (0.094 g, 0.4 mmol) and deionised water was the solvent. **Nd-Biphen**: Yield 0.108 g (85%). FTIR ν_{max} (cm^{-1}): 3054 (w), 3031 (w), 1678 (w), 1603 (m), 1554 (m), 1485 (m), 1446 (m), 1391(m), 1185 (w), 1116 (s), 1054 (s), 1025 (m), 973 (s), 933 (m), 826 (s), 755 (s), 720 (s), 687 (s), 678 (s), 661 (s). **Eu-Biphen**: Yield 0.106 g (84%). IR FTIR ν_{max} (cm^{-1}): 3054 (w), 3034 (w), 1678 (w), 1602 (m), 1555 (m), 1484 (m), 1447 (m), 1392 (m), 1185 (w), 1145 (s), 1060 (s), 1025(m), 980 (s), 933 (m), 909 (m), 833 (s), 756 (s), 719 (m), 688 (s), 673 (s). **Tb-Biphen**: Yield 0.103 g (82%). FTIR ν_{max} (cm^{-1}): 3054 (w), 3033 (w), 1678 (w), 1602 (m), 1555 (m), 1484 (m), 1447 (m), 1392 (m), 1146 (s), 1062 (s), 981 (s), 910 (s), 833 (s), 757 (s), 720 (s), 689(s), 671 (s). **Yb-Biphen**: Yield 0.102 g (82%). FTIR ν_{max} (cm^{-1}): 3056 (w), 3031 (w), 1603 (m), 1554 (m), 1484 (m), 1446 (m), 1427 (m), 1392 (m), 1241 (m), 1146 (s), 1075 (s), 1006 (m), 985 (s), 911 (s), 833 (s), 757 (s), 723 (s), 691 (s), 670 (s). CHN analysis for $\text{EuC}_{24}\text{H}_{18}\text{P}_2\text{O}_6$: Expected: C 46.77%; H 2.94%. Found: C 46.47%; H 2.54%.

2.3.4 Synthesis of $\text{Na}_2[\text{Eu}_2(\text{Hheidi})_4(\text{H}_2\text{O})(\text{MeOH})]$, (2)

The ligand *N*-(2-hydroxyethyl)iminodiacetic acid, H_3heidi , (0.089 g, 0.50 mmol) was reacted with $\text{EuCl}_3 \cdot 6\text{H}_2\text{O}$ (0.092 g, 0.25 mmol) and NaN_3 (0.244 g, 3.75 mmol) in 10 mL MeOH. Under stirring the solution was refluxed for 2 hours and then cooled to room temperature. The solution was filtered and layered with 4 mL CH_3CN . After *ca.* six days small plate crystals appeared in the solution. **2-Eu** Yield 0.055 g (9%) FT-IR ν_{max} (cm^{-1}): 3231 (br), 2971(w), 2913(w), 2863 (w), 2047 (w), 1737 (w), 1570 (s), 1404 (s), 1307 (s), 1255 (m), 1120 (m), 1062 (m), 1002 (m), 923 (m), 885 (m), 822 (m)

The same procedure was repeated using $\text{Ln}^{\text{III}} = \text{Tb}^{\text{III}}$ to yield isostructural **2-Tb**. Yield: 0.067 g (11%). FTIR ν_{max} (cm^{-1}): 3292 (br), 2972 (w), 2905 (w), 2857 (w), 2747 (w), 2039 (w), 1574 (s), 1410 (s), 1307 (s), 1259 (m), 1157 (m), 1121 (m), 1061 (m), 1004 (m), 924 (m), 888 (m), 825(m).

2.3.5 Synthesis of $\text{Na}_2[\text{Eu}(\text{Hheidi})(\text{heidi})(\text{H}_2\text{O})_2] \cdot \text{H}_2\text{O}$, (3)

A solution of $\text{EuCl}_3 \cdot 6\text{H}_2\text{O}$ (0.091 g, 0.25 mmol), H_3heidi (0.044 g, 0.25 mmol) and 1 M NaOH (0.75 mL, 0.75 mmol) was stirred for 30 minutes in 8 mL solvent [*v:v* 3:1 MeOH/ H_2O] to yield a white suspension. The Teflon liner was placed in an autoclave and heated at 100 °C for 16 hours. The autoclave was slowly cooled to room temperature and opened to yield small colourless crystals amongst some powder. The crystals were manually isolated from the mixture. **3-Eu** Yield 0.043 mg (29%) FT-IR ν_{max} (cm^{-1}): 3384(m), 3289 (br), 2971 (w), 2941 (w), 2892 (w), 2842 (w),

1599 (s), 1576 (s), 1398 (s), 1316 (m), 1257 (m), 1227 (m), 1115 (m), 1067 (m), 1019 (m), 923 (m), 886 (m), 826 (m).

The same method was applied using $\text{NdCl}_3 \cdot 6\text{H}_2\text{O}$ to isolate crystals of **3-Nd**. Yield 0.051 g (35%). FT-IR ν_{max} (cm^{-1}): 3388 (m), 3288 (br), 2971 (w), 2940, (w), 2918 (w), 2882 (w), 2854 (w), 2835 (w), 1600 (s), 1575 (s), 1397 (s), 1315 (s), 1256 (m), 1228 (m), 1150 (m), 1113 (m), 1066 (m), 1018 (m), 921 (m), 884 (m), 823 (m).

2.3.6 Synthesis of 5,5'-methylenebis(6-hydroxy-2-naphthoic acid), $\text{C}_{23}\text{H}_{16}\text{O}_6 \cdot 3\text{DMF}$, (**4**)

The ligand **H₄C6hnida** (0.033 g, 0.1 mmol) was mixed with $\text{NdCl}_3 \cdot 6\text{H}_2\text{O}$ (0.036 g, 0.1 mmol) and 1 M NaOH (0.3 mL, 0.3 mmol) in a mixed $\text{H}_2\text{O}/\text{DMF}$ solvent system (1:1 v:v) and stirred for 30 minutes to yield a white suspension. The Teflon liner was transferred to an autoclave and heated at 100 °C for 15 hours. After slow cooling to room temperature, colourless block crystals were found amongst a black powder and manually isolated. Yield 0.009 g (17%). FT-IR ν_{max} (cm^{-1}): 3398 (br), 3310 (w), 2935 (w), 2811, (w), 2695 (w), 2654 (w), 1651 (s), 1567 (s), 1497 (m), 1454 (m), 1434 (m), 1415 (s), 1389 (s), 1307 (m), 1254 (m), 1100 (s), 1064 (m), 1020 (m), 972 (m), 956 (m), 921 (m), 892 (m), 722 (m), 661 (m).

2.3.7 Synthesis of $[\text{Nd}_5(\text{HC3hnida})(\text{C3hnida})_3(\text{H}_2\text{O})_{10}] \cdot 25\text{H}_2\text{O}$, (**5**)

In 5 mL of H_2O , $\text{NdCl}_3 \cdot 6\text{H}_2\text{O}$ (0.036 g, 0.1 mmol), **H₄C3hnida** (0.033 g, 0.1 mmol) and 1 M NaOH (0.3 mL, 0.3 mmol) were stirred at room temperature for 30 minutes after which the Teflon liner was transferred to an autoclave and heated at 60 °C for 17 hours. After slow cooling to room temperature, green diamond-shaped crystals were identified in solution. **5-Nd** Yield: 0.071 g (26%) FT-IR ν_{max} (cm^{-1}): 3217 (br), 2971 (w), 2954 (w), 2921 (w), 1737 (m), 1621 (s), 1574 (s), 1540 (s), 1500 (s), 1457 (s), 1425 (s), 1393 (s), 1308 (s), 1263 (s), 1210 (s), 1177 (m), 1155 (m), 1123 (m), 1102 (m), 1042 (m), 1011 (m), 925 (m), 901 (m), 886 (m), 875 (m), 815 (m), 783 (s), 743 (m), 697 (m).

The procedure was repeated by substituting the lanthanide for $\text{EuCl}_3 \cdot 6\text{H}_2\text{O}$ (**5-Eu**), $\text{GdCl}_3 \cdot 6\text{H}_2\text{O}$ (**5-Gd**) or $\text{YbCl}_3 \cdot 6\text{H}_2\text{O}$ (**5-Yb**).

5-Eu Yield 0.016g (6%). FT-IR ν_{max} (cm^{-1}): 3215 (br), 3028 (w), 2971 (w), 2953 (w), 2920 (w), 1737 (m), 1621 (s), 1576 (s), 1499 (s), 1459 (s), 1398 (s), 1308 (s), 1264 (s), 1211 (s), 1177 (m), 1154 (m), 1125 (m), 1102 (m), 1042 (m), 1012 (m), 928 (m), 902 (m), 886 (m), 816 (m), 784 (m), 744 (m), 697 (m).

5-Gd Yield 0.083 g (31%). FT-IR ν_{max} (cm^{-1}): 3224 (br), 3073 (w), 2972 (w), 2956 (w), 2909 (w), 1737 (m), 1621 (s), 1580 (s), 1500 (s), 1460 (s), 1397 (s), 1308 (s), 1264 (s), 1211 (s), 1177 (m), 1155 (m), 1126 (m), 1103 (Mm), 1042 (m), 1012 (m), 928 (m), 903 (m), 877 (m), 816 (m), 786 (s), 744 (m), 698 (m).

5-Yb Yield 0.026 g (9%). FT-IR ν_{\max} (cm^{-1}): 3285 (br), 3076 (w), 2972 (w), 2956 (w), 2922 (w), 1737 (m), 1622 (s), 1595 (s), 1548 (s), 1503 (s), 1458 (s), 1397 (s), 1307 (s), 1264 (s), 1212 (s), 1155 (m), 1127 (m), 1103 (m), 1042 (m), 1013 (m), 890 (m), 816 (m), 790 (m), 744 (m), 699 (m).

2.3.8 Synthesis of $[\text{Nd}_{17}(\text{C3hnida})_{12}(\mu_3\text{-OH})_4(\text{H}_2\text{O})_{30}] \cdot x\text{H}_2\text{O}$, (6)

To 5 mL of H_2O , $\text{NdCl}_3 \cdot 6\text{H}_2\text{O}$ (0.036 g, 0.1 mmol), $\text{H}_4\text{C3hnida}$ (0.033 g, 0.1 mmol) and 1 M NaOH (0.3 mL, 0.3 mmol) were added and stirred for 30 minutes. The Teflon liner was placed in an autoclave and heated at 100 °C for 17 hours. Following cooling to room temperature, large green crystals were found in the solution. Yield: 0.016 g (2%). FT-IR ν_{\max} (cm^{-1}): 3269 (br), 2914 (w), 1620 (s), 1586 (s), 1533 (s), 1499 (s), 1454 (s), 1395 (s), 1308 (s), 1263 (s), 1210 (s), 1178 (m), 1155 (m), 1126 (m), 1101 (m), 1044 (m), 1013 (m), 929 (m), 902 (m), 812 (m), 780 (m), 725 (m), 698 (m).

2.3.9 Synthesis of $\text{Na}[\text{Ho}(\text{C}_6\text{H}_5\text{CO}_2)_4]$, (7)

To 10 mL of MeOH, a mixture of $\text{HoCl}_3 \cdot 6\text{H}_2\text{O}$ (0.095 g, 0.25 mmol), H_3heidi (0.044 g, 0.25 mmol), sodium benzoate (0.108 g, 0.75 mmol) and NaN_3 (0.049 g, 0.75 mmol) were added and stirred at reflux for 2 hours. The solution was cooled to room temperature, filtered into a sample tube and sealed with parafilm. Two small holes were punctured into the parafilm to allow slow diffusion. After *ca.* 12 days, small pink block crystals formed in solution. Yield: 0.054 g (32%). FT-IR ν_{\max} (cm^{-1}): 3063 (w), 3029 (w), 1600 (s), 1538 (s), 1496 (s), 1399 (s), 1308 (m), 1178 (m), 1072 (m), 1023 (m), 931 (m), 848 (m), 713 (m), 683 (m).

The same procedure was used substituting in $\text{EuCl}_3 \cdot 6\text{H}_2\text{O}$ as lanthanide to isolate the isostructural **7-Eu** Yield 0.069 g (42%) FT-IR ν_{\max} (cm^{-1}): 3062 (w), 3026 (w), 2971 (w), 1739 (w), 1600 (s), 1539 (s), 1496 (s), 1417 (s), 1308 (m), 1178 (m), 1072 (m), 1023 (m), 931 (m), 848 (m), 716 (s), 684 (s).

2.3.10 Synthesis of $[\text{Nd}_2(\text{SO}_4)_3(\text{H}_2\text{O})_8]$, (8)

A mixture of $\text{NdCl}_3 \cdot 6\text{H}_2\text{O}$ (0.072 g, 0.20 mmol), H_3heidi (0.035 g, 0.20 mmol), phenyl phosphonic acid (0.032 g, 0.20 mmol) was stirred in a 5 M H_2SO_4 solution (8 mL, 40 mmol) for 30 minutes. The resulting suspension in the Teflon liner was transferred to an autoclave and heated at 100 °C for 21 hours. After slow cooling, purple crystals were isolated from the reaction mixture. The material could be isolated by an alternative reaction in the absence of the ligands by stirring $\text{NdCl}_3 \cdot 6\text{H}_2\text{O}$ (0.072 g, 0.20 mmol) and 1 M H_2SO_4 solution (0.3 mL, 0.3 mmol) in 2 mL of H_2O for 30 minutes. The solution was layered with 1 mL CH_3CN and crystals formed in solution after one day. Yield 0.062 g (43%). FT-IR ν_{\max} (cm^{-1}): 3338 (br), 2972 (m), 2933 (m), 1637 (m), 1467 (m), 1380 (m), 1303 (m), 1116 (s), 1073 (s), 995 (s), 950 (s), 815 (s), 743 (m).

2.3.11 Synthesis of $(\text{Me}_2\text{NH}_2)_9[\text{Nd}_5(\text{SO}_4)_{12}]$, (9)

In a solution of 10 mL DMF, $\text{NdCl}_3 \cdot 6\text{H}_2\text{O}$ (0.072 g, 0.20 mmol), H_3heidi (0.018 g, 0.10 mmol), phenyl phosphonic acid (0.016 g, 0.10 mmol) and 1M H_2SO_4 (0.3 mL, 0.3 mmol) were stirred for 30 minutes. The suspensions within the Teflon liners were transferred to autoclaves and heated at 170 °C for 69 hours. After cooling, small plate-shaped crystals were observed amongst some powder. The reaction was modified and the ligands removed, where only $\text{NdCl}_3 \cdot 6\text{H}_2\text{O}$ and 1M H_2SO_4 are used in the same quantities. Yield 0.043 g (9%). FT-IR ν_{max} (cm^{-1}): 3260 (m), 2981 (w), 1595 (w), 1416 (m), 1088 (s), 1065 (s), 978 (s), 831 (m).

By substituting $\text{Ln}^{\text{III}} = \text{GdCl}_3 \cdot 6\text{H}_2\text{O}$ and $\text{DyCl}_3 \cdot 6\text{H}_2\text{O}$, the isostructural materials, **9-Gd** and **9-Dy** were isolated. **9-Gd**: Yield 0.065 g (15 %). 3520 (w), 3213 (w), 2988 (w), 1634 (w), 1465 (w), 1228 (w), 1078 (s), 1034 (s), 988 (s), 891 (m), 836 (m). **9-Dy**: Yield 0.038 g (8 %). FT-IR ν_{max} (cm^{-1}): 3469 (w), 3183 (w), 3131 (w), 2989 (w), 1644 (w), 1583 (m), 14465 (w), 1364 (w), 1206 (m), 1078 (s), 1034 (s), 991 (s), 893 (m), 818 (m), 791 (m).

2.3.12 Synthesis of $\text{NH}_4[\text{Dy}(\text{SO}_4)_2(\text{H}_2\text{O})]$, (10)

In a solution of diethylformamide (5 mL), $\text{Dy}(\text{NO}_3)_3 \cdot 6\text{H}_2\text{O}$ (0.091 g, 0.2 mmol) and 1 M H_2SO_4 (0.6 mL, 0.6 mmol) were stirred for 30 minutes. The Teflon liner was then sealed in an autoclave and heated 170 °C for 72 hours. After cooling to room temperature white plate crystals were found in solution. Yield 0.027 g (35%). FT-IR ν_{max} (cm^{-1}): 3256 (m), 3058 (m), 1628 (w), 1418 (m), 1088 (s), 1069 (s), 1001 (s), 665 (s).

2.3.13 Synthesis of $(\text{NH}_4)_3[\text{Dy}(\text{SO}_4)_3]$, (11)

A mixture of $\text{Dy}(\text{NO}_3)_3 \cdot 6\text{H}_2\text{O}$ (0.091 g, 0.2 mmol) and 5 M H_2SO_4 (0.8 mL, 4 mmol) was stirred in 5 mL diethylformamide for 30 minutes. The Teflon liner was sealed in an autoclave and heated at 170 °C for 72 hours and then allowed to slowly cool to room temperature. After cooling, small white crystals were found in the solution. Yield 0.019 g (19%). FT-IR ν_{max} (cm^{-1}): 3223 (m), 3047 (m), 2843 (m), 2508 (m), 1737(w), 1627 (w), 1410 (s), 1219 (s), 1171 (s), 1073 (s), 1014 (s), 957 (s).

2.4 References

1. B. Axs-Inc., Bruker Axs-Inc., Editon edn., 1997-2003.
2. B.-A. Inc., Bruker-Axs Inc., Editon edn., 1997-2003.
3. G. M. Sheldrick, Bruker-Axs Inc., Editon edn., 1999.
4. R. W. Cheary and A. A. Coelho, Editon edn., 1996.
5. D. Taupin, *J. Appl. Crystallogr.*, 1973, **6**, 380-385.
6. R. Shirley, The Lattice Press, 41 Guildford Park Avenue, Guildford, Surrey GU2 7NL, England., Editon edn., 2002.
7. Z. K. Wang, J. M. Heising and A. Clearfield, *J. Am. Chem. Soc.*, 2003, **125**, 10375-10383.

Chapter Three

.....

**Shedding light on two-dimensional lanthanide
phosphonates: Understanding the structure-
property relationships toward developing visible
and near-infrared emitters**

3.1 Introduction

The ability to manipulate organic and inorganic moieties as building blocks towards multidimensional materials has been exploited in the preparation of functional materials with potential applications in catalysis, ion-exchange, gas sorption and intercalation chemistry.^{1, 2} Metal phosphonates in particular display a tendency towards materials containing (2D) inorganic layers separated by hydrophobic regions due to the organic moieties protruding in to the interlamellar space.³⁻⁵ Transition metal phosphonates have been exploited extensively for use in industrial technologies such as corrosion inhibitors,⁶ waste water management⁷ and heterogeneous catalysis.⁸

With the combination of a Ln(III) centre and monofunctional organophosphonate ligands, layered materials can also be isolated.^{1, 9} However, the design and characterisation of new structures has proven difficult due to the low solubility and poor crystallinity of the lanthanide phosphonates.¹⁰ To mitigate these drawbacks, three strategies have been realised that improve the solubility and crystallinity of the lanthanide phosphonates: (i) Further functionalisation of the phosphonic acid with additional coordinating groups has been shown to work. When a carboxylic acid is introduced there is a general tendency towards novel 3D frameworks,^{11, 12} and a particularly interesting 1D triple-stranded helical chain.¹³ In the case of additional amino-functionality, 3D frameworks are favourable,¹⁴ while hydroxyl moieties encourage 1D chain structures.¹⁵⁻¹⁷ (ii) The solubility of the organic moiety may be increased by grafting phosphonic acids onto crown ethers and calixarenes where isolated clusters become favourable,¹⁸⁻²⁰ and in some cases 1D hybrid materials form,²¹ although one ligand does yield an interesting 3D porous network.²² (iii) The addition of a second coordinating ligand helps improve crystallinity by competing for the coordination sphere of the lanthanide. Oxalic acid has proven highly successful for isolating 3D networks²³⁻³¹ and 1,10-phenanthroline can yield materials from 0D to 3D frameworks.²⁵

Now that strategies have been developed to improve crystallinity in lanthanide phosphonate systems, interest is shifting towards investigating the optical properties that are still poorly understood, even in the case of simple layered lanthanide phosphonates. A step to bridging this gap was taken in the characterisation of the layered lanthanide phenyl phosphonate, whose structure was first determined in 1992.⁹ Since then, several studies probing the structure, morphology and optical properties of lanthanide phenyl phosphonates prepared from the reaction with phenyl phosphonic acid have been reported. Ma and coworkers demonstrated that addition of sodium *p*-toluene sulfonate (STS) to the reaction mixture under hydrothermal conditions promoted preferential growth of 1D nanorods.³² Comparison of Eu^{III} and La^{III}/Eu^{III} phenyl phosphonate nanorods against the corresponding bulk materials revealed that crystal size has only a negligible effect on the photoluminescence (PL) properties. Pinna *et al.* have since shown that changing from an aqueous to non-aqueous synthetic route can greatly enhance the photoluminescence quantum yields (Φ_{PL}) of the Eu^{III}-doped lanthanum phenyl phosphonate, reporting an impressive $\Phi_{\text{PL}} = 45\%$ for La(HO₃PC₆H₅)₂:0.06Eu *via* ligand sensitisation.³³ The improved PL efficiency is attributed to a combination of reduced concentration quenching *via* co-doping with La^{III} and inhibition of non-

radiative multiphonon relaxation *via* O-H oscillators through the use of an organic solvent. Pinna *et al.* further demonstrated that citric acid can act as a crystal habit-modifier for the related $\text{YH}(\text{O}_3\text{PC}_6\text{H}_5)_2\text{:Ln}0.05$ ($\text{Ln} = \text{Eu}^{\text{III}}, \text{Tb}^{\text{III}}$), promoting the formation of dandelion-like superstructures composed of multiple individual nanorods.³⁴ Notably, a ~50% increase in the Φ_{PL} of $\text{YH}(\text{O}_3\text{PC}_6\text{H}_5)_2\text{:Ln}0.05$ could be obtained in moving from plate-like to dandelion-like morphologies. It is clear from these initial studies that the chemical composition, morphology and optical properties of these materials are closely linked; an understanding of the specific nature of this relationship, however, remains elusive.

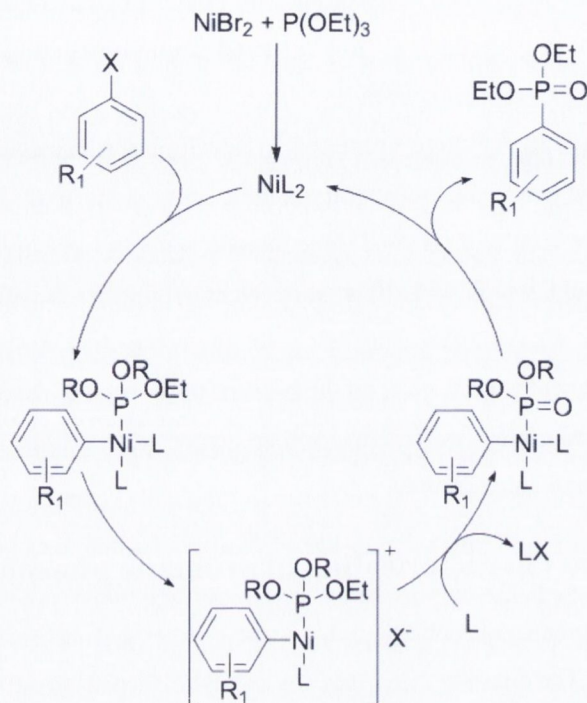
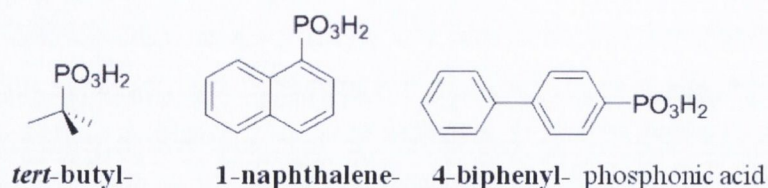
Under this premise, we were interested in developing a strategic approach to the design and synthesis of layered lanthanide phosphonates with targeted morphology and optical properties. In this chapter, we have carefully selected three ligands, namely *tert*-butyl-, 1-naphthalene- and 4-biphenyl phosphonic acid, which will allow us to selectively probe the effect of ligand size on the interlamellar spacing of the corresponding lanthanide phosphonates. Moreover, 1-naphthalene- and 1-biphenyl phosphonic acid were chosen on the basis of the energy of their excited electronic states and their high molar absorption coefficients, and are expected to efficiently sensitise the emissive Ln^{III} state of different lanthanide centres.

3.2 Synthesis and characterisation of aromatic phosphonic acids

A series of aromatic phosphonic acids were synthesised utilising a modified Michaelis-Arbusov reaction.^{35, 36} The first step involves the catalytic formation of the C-P bond of an aryl halide in the presence of NiBr_2 . The resulting aromatic phosphate ester was refluxed under acidic conditions to yield the phosphonic acid product. ^{31}P NMR spectroscopy and the chemical shift of the ^{31}P nucleus aided identification of the respective chemical environment on the phosphorus centre. The mechanism outlining the modified Michaelis-Arbusov reaction is given below in **Scheme 3.1**.

The proposed mechanism involves the reduction of Ni^{II} to a Ni^0 phosphite complex *in-situ*. The next step involves an oxidative addition of the Ni^0 phosphite intermediate into the carbon halide bond of the aryl reagent. This intermediate undergoes a reductive elimination step to produce the aryl phosphate ester (product), alkyl halides (side-product) and regenerate the Ni^0 phosphite catalyst.

The ligand *tert*-butyl phosphonic acid was purchased and used without further purification.



Scheme 3.1: (a) Structures of the ligands used in this study. (b) Proposed mechanism for the Michaelis-Arbusov reaction in the conversion of aryl halides to aryl phosphate esters. L= triethyl phosphate.

3.2.1 1-naphthalene phosphonic acid (Naph-PO₃H₂)

The ligand 1-naphthalene phosphonic acid (**Naph-PO₃H₂**) was prepared *via* the reaction of 1-bromonaphthalene with triethyl phosphite in 1,3-diisopropylbenzene (solvent) and catalytic amounts of NiBr₂. This yields the phosphate ester identified by a ³¹P shift at 19.22 ppm. Upon hydrolysis of the phosphate acid, the phosphonic acid is formed (yield 72%) and the ³¹P NMR shift at 13.10 ppm. The FT-IR spectrum indicated the presence of the phosphonic acid from stretches observed at 1506 (ν_{C-P}), 1140 (ν_{P-O}) and 1016 (ν_{P-O}) cm⁻¹, respectively. The ESI mass spectrum of **Naph-PO₃H₂** in DMSO had a molecular ion peak at 207.0211 m/z (*calc.* 207.0211).

Through a combination of solution UV/Vis absorption, steady-state photoluminescence and low temperature phosphorescence spectroscopies, the molar absorption coefficient (ϵ), excited state energies of the singlet *S*₁ and *S*₂ and excited triplet *T*₁ states have been determined and are summarised in **Table 3.1**.

3.2.2 4-biphenyl phosphonic acid (Biphen-PO₃H₂)

The synthesis of 4-biphenyl phosphonic acid was achieved under similar synthetic conditions, using 4-bromobiphenyl as the starting material. The ³¹P NMR of the phosphate reveals

a peak at 19.17 ppm, that shifts to 13.81 ppm upon formation of the phosphonic acid in good yield (56%). The phosphonic acid was identified through stretches at 1678 ($\nu_{\text{P=O}}$), 1484 ($\nu_{\text{C-P}}$), 1140 ($\nu_{\text{P-O}}$) and 1016 ($\nu_{\text{P-O}}$) cm^{-1} in the FT-IR spectrum. The molar absorption coefficient and energy of the excited S_1 state and the excited T_1 state are summarised in **Table 3.1**.

Table 3.1: The optical properties determined for **Naph-PO₃H₂** and **Biphen-PO₃H₂** including the second excited singlet state (S_2), first excited singlet state (S_1), first excited triplet state (T_1), absorption maximum (λ_{abs}) and molar absorption coefficient (ϵ).

Ligand	Energy S_2 (cm^{-1})	Energy S_1 (cm^{-1})	Energy T_1 (cm^{-1})	λ_{abs} (nm) / ϵ ($\text{dm}^3 \text{mol}^{-1} \text{cm}^{-1}$)
Naph-PO₃H₂	43,500	35,300	21,100	320/ 8500
Biphen-PO₃H₂	n/a	39,100	22,600	305/ 20,600

3.3 Synthesis and characterisation of lanthanide phosphonates

Three series of novel lanthanide phosphonates have been synthesised and characterised, as described below. The three series of materials have been identified by the names **Ln-Bu'**, **Ln-Naph** and **Ln-Biphen** where $\text{Ln}^{\text{III}} = \text{Nd}^{\text{III}}, \text{Eu}^{\text{III}}, \text{Tb}^{\text{III}}$ and Yb^{III} . Throughout the course of this thesis, where single crystal X-ray diffraction has been measured, the compound has been given a numerical label to identify all crystal structure refinement models.

3.3.1 Synthesis and crystal structure of [Eu(HO₃PC(CH₃)₃)₃]·H₂O, **Eu-Bu'**, (**1**)

[Eu(HO₃PC(CH₃)₃)₃]·H₂O, **1**, **Eu-Bu'**, was isolated using a solvothermal approach where two molar equivalents of *tert*-butyl phosphonic acid were combined with $\text{LnCl}_3 \cdot 6\text{H}_2\text{O}$ in acetonitrile and adjusted to pH 2 using 1 mol dm^{-3} NaOH. This mixture was heated at 100 °C for 15 hours. For $\text{Ln} = \text{Eu}^{\text{III}}$, following slow cooling to room temperature, small colourless plate shaped crystals suitable for single crystal diffraction were obtained. [Eu(HO₃PC(CH₃)₃)₃]·H₂O (**1**) crystallises in the monoclinic crystal system in the space group $P(1)2_1/c$. The asymmetric unit of **1** (**Figure 3.1**) consists of one crystallographically unique Eu^{III} ion, three *tert*-butyl phosphonic acid ligands and a single constituent water molecule. For each distinct ligand molecule, a single phosphonate oxygen remains protonated and the other two phosphonate oxygen atoms are free to coordinate. The proton of the phosphonate group could not be refined from the density maps and has been assigned by examining the P-O bond lengths. The P-O bond distance of O(3), O(6) and O(9) are in the range 1.559(12) – 1.593(13) Å. These values are considerably longer than the other P-O bond lengths that range 1.488(9) – 1.516(11) Å indicating the oxygen is protonated.¹³ These bond lengths are given in **Table 3.2**.

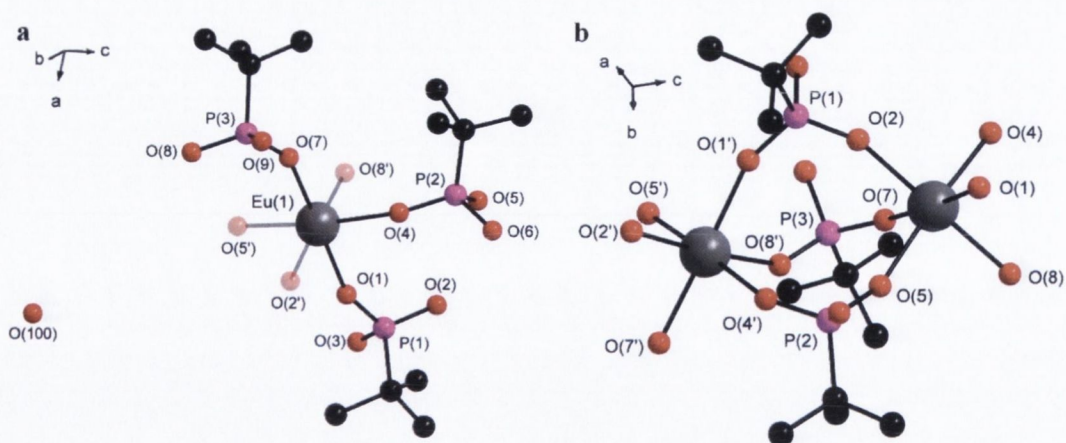


Figure 3.1: (a) Asymmetric unit of $[\text{Eu}(\text{HO}_3\text{PC}(\text{CH}_3)_3)_3] \cdot \text{H}_2\text{O}$. **1.** (b) Bridging of Eu^{III} ions along the c -axis leads to construction of 1D polymeric chain. Eu grey, P magenta, O red, C black. H atoms are omitted for clarity and faded atoms represent symmetry generated atoms.

Each Eu^{III} centre binds to six different ligands to give a distorted octahedral geometry around the europium ion. The slightly distorted octahedral geometry of the europium centre is characterised by the bond angles that are close to the ideal octahedral values. Bond angles between $\text{O}(4)\text{-Eu}(1)\text{-O}(2)$ and $\text{O}(7)\text{-Eu}(1)\text{-O}(8)$ are 89.3° and 89.2° , respectively, close to the ideal angle of 90° . However, other angles show much larger distortions. The bond angles between $\text{O}(4)\text{-Eu}(1)\text{-O}(7)$ of 176.4° and $\text{O}(2)\text{-Eu}(1)\text{-O}(1)$ of 174.0° have a greater deviation from the ideal 180° . Further distortions in the bond angles from the ideal 90° are observed with angles between $\text{O}(2)\text{-Eu}(1)\text{-O}(5)$ of 86.5° and $\text{O}(8)\text{-Eu}(1)\text{-O}(1)$ of 92.6° existing. Distortions in the octahedral geometry can be attributed to the bridging nature of the binding phosphonate groups and the steric volume occupied by the *tert*-butyl moieties. The bond angles are summarised in **Table 3.3**.

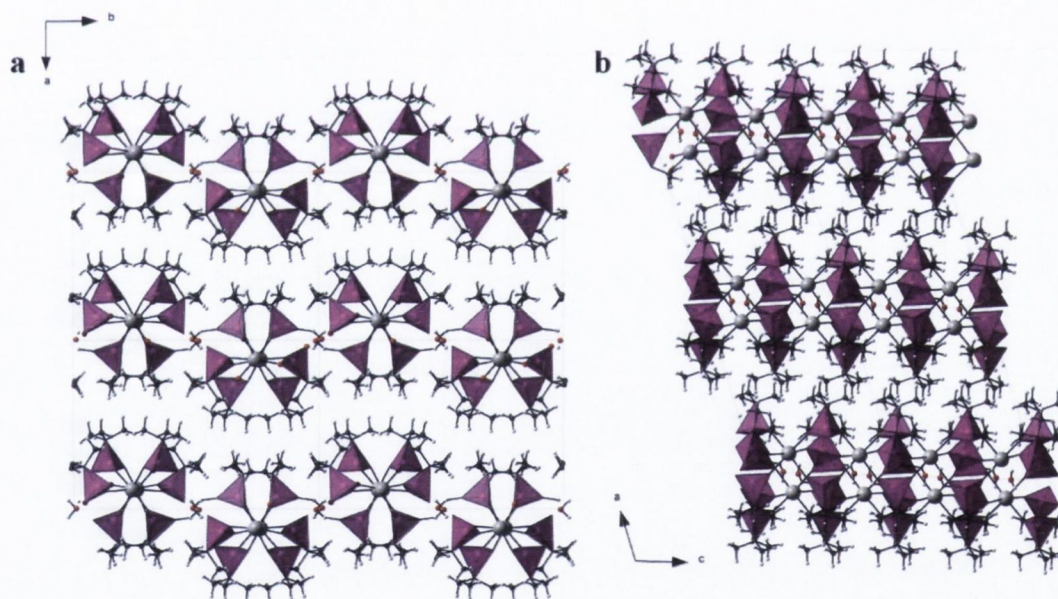
Table 3.2: Selected bond lengths for **1**.

Bond	Bond Length (Å)	Bond	Bond Length (Å)
P(1)-O(3)	1.589(13)	Eu(1)-O(1)	2.321(10)
P(2)-O(6)	1.593(13)	Eu(1)-O(2)	2.282(11)
P(3)-O(9)	1.559(12)	Eu(1)-O(4)	2.276(9)
P(1)-O(1)	1.516(11)	Eu(1)-O(5)	2.294(9)
P(1)-O(2)	1.488(12)	Eu(1)-O(7)	2.291(10)
P(2)-O(4)	1.495(9)	Eu(1)-O(8)	2.302(8)
P(2)-O(5)	1.510(11)		
P(3)-O(7)	1.495(10)		
P(3)-O(8)	1.488(9)		

Table 3.3: Selected bond angles for **1**.

	Bond Angle (°)		Bond Angle (°)
O(4)-Eu(1)-O(2)	89.3(4)	O(4)-Eu(1)-O(7)	176.4(4)
O(7)-Eu(1)-O(8)	89.2(4)	O(2)-Eu(1)-O(1)	174.0(5)
O(2)-Eu(1)-O(5)	86.5(5)		
O(8)-Eu(1)-O(1)	92.6(4)		

The three distinct ligand molecules all have the same coordination mode, bridging two Eu^{III} centres in a $\eta^1: \eta^1: \eta^0-\mu_2$ fashion. For each phosphonate, two phosphonate oxygen atoms coordinate through a monodentate interaction to Eu^{III} . The two binding phosphonate oxygen donors on each ligand bridge two europium centres to produce infinite 1D polymeric chains that extend along the c -axis (**Figure 3.2**). The infinite chains are therefore produced *via* inorganic M-O-M bonding that leads to the definition of the structure as an I^1O^0 material. Investigation of the Eu-O bond lengths match well with other known structures containing octahedral Eu^{III} ions.^{13, 37, 38} The bond lengths are observed in the range 2.276(9) to 3.321(10) Å and are in good agreement with such six-coordinate Eu^{III} complexes bound by a phosphonate ligand.

**Figure 3.2:** The packing of the 1D chains of **1** as seen down the projection of (a) the c -axis and (b) the b -axis. Eu grey, C black, O red and P purple tetrahedra. Blue dashed line represents hydrogen bonding.

The europium ion positions relate to two distinct polymeric chains in the unit cell. One chain runs parallel to the c -axis near the origin while the second chain runs parallel to the c -axis in the opposite corner of the unit cell. From the asymmetric unit, the first polymeric chain is generated *via* a c -glide plane where the reflection is in the ac -plane at $y = 0.25$. The second chain is generated through the asymmetric unit being regenerated through an inversion centre at (0.5, 0.5, 0.5) and by the operation of a 2_1 screw axes located at (0.5, y , 0.25). This produces an array of 1D chains that are located slightly above and below a plane alternately, in the bc -plane.

There is one constitutional water molecule present in the chemical formula and its presence influences the 3D packing of the compound. The polymeric chains pack within the *bc*-plane and the water molecule is positioned between adjacent chains. A hydrogen bonding interaction occurs between the water and the protonated phosphonate oxygen allowing the chains to pack tightly into a *pseudo*-layered arrangement (**Figure 3.2**). Due to the alternate packing of the chains above and below the plane, a pleated inorganic sheet is observed where the organic moieties occupy the interlamellar space. Despite the compound strictly being a 1D material, it is interesting to note that the supramolecular packing is closely related to that of other layered lanthanide phosphonates such as lanthanum phenyl phosphonate.⁹ All the data concerning the structure model refinement and crystal data are given in **Table 3.4**.

Table 3.4: Crystal data and structure refinement for **1**.

Identification code	1	
Empirical formula	C ₁₂ H ₂₉ EuO ₁₀ P ₃	
Formula weight	578.22	
Temperature	108(2) K	
Wavelength	0.71073 Å	
Crystal system	Monoclinic	
Space group	<i>P</i> (1)2 ₁ / <i>c</i>	
Unit cell dimensions	a = 13.037(3) Å	α = 90°.
	b = 17.836(4) Å	β = 108.24(3)°.
	c = 10.327(2) Å	γ = 90°.
Volume	2280.7(9) Å ³	
Z	4	
Density (calculated)	1.684 Mg m ⁻³	
Absorption coefficient	3.001 mm ⁻¹	
F(000)	1156	
Crystal size	0.2 × 0.2 × 0.2 mm ³	
Theta range for data collection	1.64 to 24.99°.	
Index ranges	-15 ≤ h ≤ 15, -21 ≤ k ≤ 21, -8 ≤ l ≤ 12	
Reflections collected	16414	
Independent reflections	3879 [R(int) = 0.0731]	
Completeness to theta = 24.99°	96.4%	
Refinement method	Full-matrix least-squares on F ²	
Data / restraints / parameters	3879 / 0 / 244	
Goodness-of-fit on F ²	1.319	
Final R indices [I > 2σ(I)]	R1 = 0.0803, wR2 = 0.2058	
R indices (all data)	R1 = 0.0849, wR2 = 0.2190	
Largest diff. peak and hole	1.736 and -1.968 e.Å ⁻³	

3.3.2 Synthesis and structural characterisation of [Ln(O₃P-Naph)₂(H₂O)₂] and [Ln(O₃P-Biphen)₂]

The synthesis of aromatic-derived Ln phosphonates was achieved using hydrothermal conditions where two molar equivalents of ligand were reacted with one molar equivalent of LnCl₃·6H₂O. Aqueous NaOH (1 mol dm⁻³) was used to adjust the reaction mixtures to pH 2, which were then transferred to Teflon lined autoclaves and heated at 100 °C for 17 hours. Upon cooling to room temperature, crystalline precipitates were isolated in good yield.

The chemical composition of the **Ln-Naph** series, [Ln(O₃P-Naph)₂(H₂O)₂] (determined using TGA data, see **Section 3.3.3**), is consistent with that of the structurally-related benzyl phosphonate, [La(O₃PCH₂C₆H₅)₂(H₂O)₂], which crystallises in the orthorhombic space group *Pbcn* with $a = 10.801(2)$ Å, $b = 10.301(2)$ Å and $c = 33.246(8)$ Å.⁹ Using the PXRD patterns of the **Ln-Naph** series, the individual reflections were indexed using the program Taup³⁹ to provide an orthorhombic unit cell with $a = 13.76$ Å, $b = 16.42$ Å and $c = 23.31$ Å. Taking into account systematic absences, the centrosymmetric space group, *Pcca*, was assigned. With the aid of photoluminescence data (**Section 3.5.1** for full detail) further insight on the structure is gained. The observation of a single component for the ⁵D₀→⁷F₀ transition confirms that there is only one unique crystallographic site of Ln in the material.^{40, 41} Secondly, for **Eu-Naph**, splitting of the ⁵D₀→⁷F₁ transition into three Stark components supports the unit cell assignment as orthorhombic.⁴² Furthermore, splitting of the ⁵D₀→⁷F₂ into only three Stark components suggests a point group symmetry close to *D*₂ indicating the coordination environment around the Eu^{III}-centre is likely a distorted dodecahedron.⁴² This information suggests that the structure of **Ln-Naph** will be related to the structure of the lanthanide benzyl phosphonate.⁹ To summarise, the Eu^{III}-centre will be eight-coordinate bound by six phosphonate oxygens, with the remaining two sites occupied by water (indicated by TGA). The phosphonate oxygens will bridge adjacent Eu^{III}-centres in the *a*- and *c*-directions to form the inorganic layer along the *ac*-plane. The organic naphthalene moieties will then extend out into the interlamellar spacings. We observe larger *a*- and *c*-unit dimensions in **Ln-Naph** (compared to lanthanide benzyl phosphonate) and this increase in unit cell parameters is to accommodate for the extra steric volume taken up by the larger naphthalene moiety in the material.

In a similar fashion, the PXRD pattern of **Ln-Biphen** has been indexed to provide a monoclinic unit cell, with dimensions $a = 23.80$ Å, $b = 6.75$ Å and $c = 5.34$ Å with $\beta = 92.95^\circ$. By considering the analysis of the **Eu-Biphen** PL spectra, the splitting of the ⁵D₀→⁷F₁ transition into three bands and the ⁵D₀→⁷F₂ into three or possibly four bands suggests an eight-coordinate environment with point group symmetry between *D*₂ and *C*_{2v}. Since no water is present (see TGA, **Section 3.3.3**) the coordination sphere will be filled by phosphonate oxygens only. Bridging of adjacent lanthanide ions occurs in the *bc*-plane forming an inorganic layer where the biphenyl moieties will protrude into the interlamellar spacings. Without single crystal data and higher resolution powder diffraction data, it is not possible to investigate and discuss further the specific

coordination sphere and the number of bridged Ln-centres along the *b*- and *c*-direction, respectively.

The PXRD patterns of these materials allow the identification of the layered nature of the lanthanide phosphonates. **Figure 3.3** shows representative PXRD patterns for **Eu-Bu'** (**1**), **Eu-Naph** and **Eu-Biphen**, which all exhibit intense periodic reflections originating from their layered lamellar structures that are characteristic for organophosphonate-stabilised lanthanide coordination compounds.³²⁻³⁴ The interlayer spacing, *d*, as determined from Bragg's law is directly proportional to the ligand size, following the order **Ln-Bu'** (12.27 Å ± 0.01) < **Ln-Naph** (16.38 Å ± 0.01) < **Ln-Biphen** (23.64 Å ± 0.01). The PXRD data shows that the *d*-spacing increases (reflected by a decrease in the 2θ value of the reflections relating to the layered plane) with the ligand size and the value reflects the presence of the ligand from two adjacent stacked layers occupying the interlamellar void.

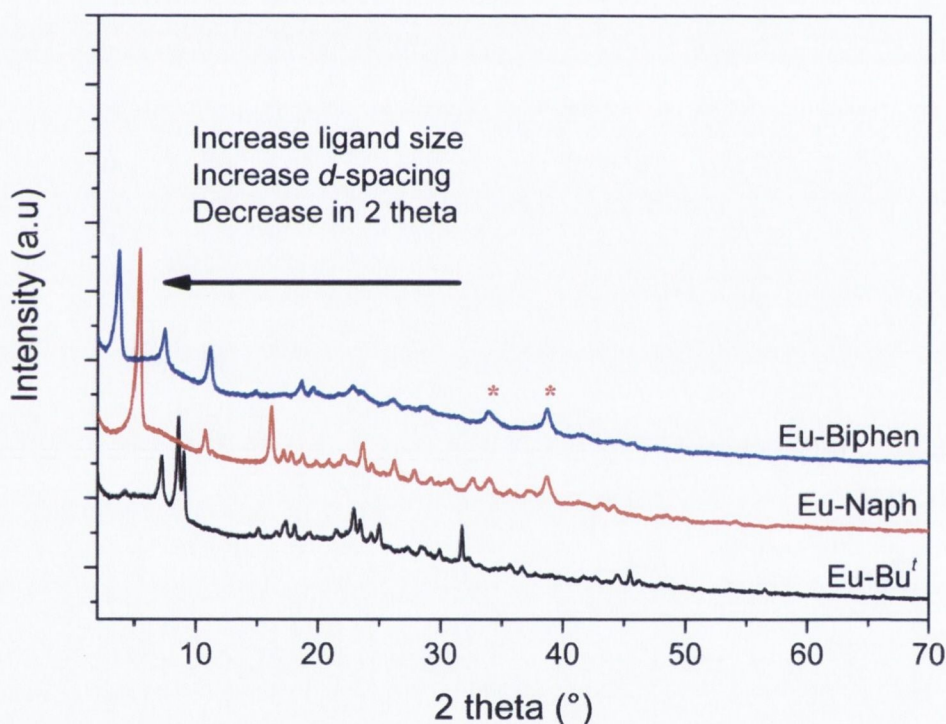


Figure 3.3: Comparison of PXRD patterns for the different Eu^{III}-phosphonates highlighting the variation in *d*-spacing with changing the ligand size. * indicate reflections from instrumental artefacts.

3.3.3 Physicochemical characterisation of Ln-phosphonates

The FT-IR spectra of all Ln-phosphonates display characteristic stretching modes associated with the deprotonated phosphonic acid group (**Figure 3.4**), namely $\nu_{\text{P-O}}$ at $\sim 1000 \text{ cm}^{-1}$ and 1100 cm^{-1} , $\nu_{\text{P=O}}$ at 1600 cm^{-1} and $\nu_{\text{P-C}}$ at 1400 cm^{-1} .³³ Typical C-H ($\sim 3000 \text{ cm}^{-1}$) and C=C stretching modes ($\sim 1600 \text{ cm}^{-1}$) associated with the organic ligand are also observed.

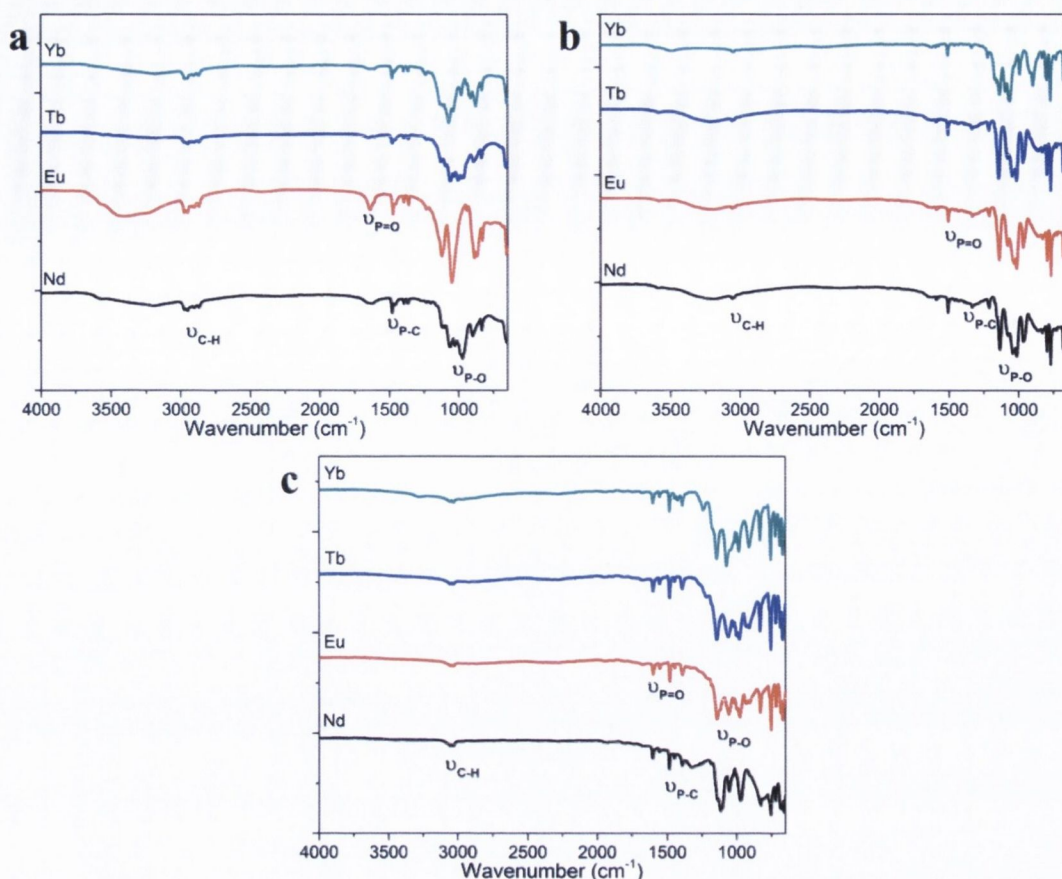


Figure 3.4: FT-IR spectra of (a) Ln-Bu', (b) Ln-Naph and (c) Ln-Biphen phosphonates in this study.

Thermogravimetric analysis (TGA) of the Ln-phosphonates was performed in air (Figure 3.5) to establish the chemical composition and thermal stability. The thermogram obtained for Ln-Bu' reveals three gravimetric events: a loss of 3.3% between 50-100 °C due to the loss of the water of crystallisation (*calc.* 3.1%) and two subsequent losses at 420-450 °C and 520-580 °C, with a combined 31% weight loss (*calc.* 29.4%), attributed to decomposition and loss of the *tert*-butyl moiety. The residual substance is assumed to be a lanthanide phosphate. Ln-Naph materials display two gravimetric events: a 6.1% weight loss at 190 °C, which is assigned to two coordinated water molecules (*calc.* 6.0%) and a loss centred at 400 °C assigned to the loss of two coordinated naphthalene ligands, yielding $[\text{Ln}(\text{O}_3\text{PC}_{10}\text{H}_7)_2(\text{H}_2\text{O})_2]$ (*calc.* 43.2-44.3%, *obs.* 40.3% [loss 2 equiv. C_{10}H_8 moieties]) as a reasonable empirical formula. A single gravimetric event centred at 500 °C due to decomposition of the organic residues for Ln-Biphen indicated two coordinated ligands with formula $[\text{Ln}(\text{O}_3\text{PC}_{12}\text{H}_9)_2]$ (*calc.* 49.1%, *obs.* 48.8 % [loss 2 equiv. C_{12}H_9 moieties]). These results demonstrate that further thermal stability can be imparted on these materials by increasing the aromatic nature of the coordinating ligands. This is an important consideration when investigating the long-term stability of these materials for use in optical applications.

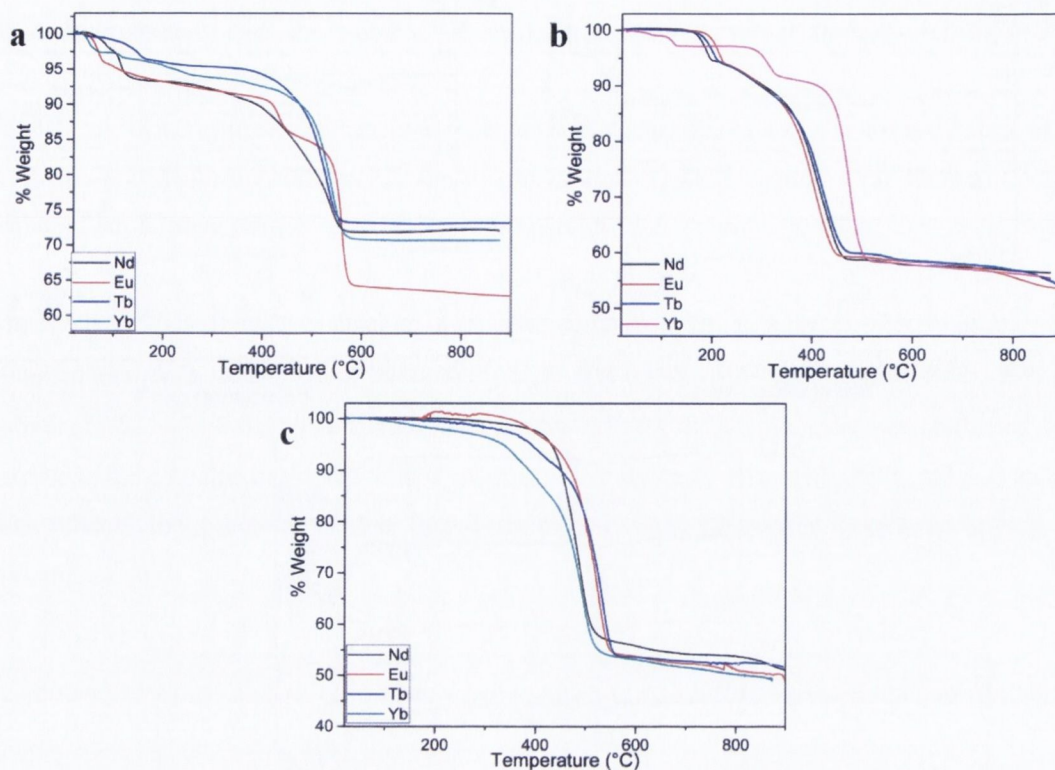


Figure 3.5: TGA thermograms of (a) Ln-Bu^I, (b) Ln-Naph and (c) Ln-Biphen phosphonates.

3.4 Controlling crystal morphology in Ln-phosphonates

An SEM study was undertaken to investigate the effect of ligand size and ionic radii on the morphologies of these materials (**Figure 3.6**). In general, the layered molecular structure is represented in the morphology and we observe platelet-type crystals of sub-micrometre dimensions for all samples. Notably, the Yb^{III}-based organophosphonates show a tendency towards anisotropic crystal growth to form rods whose aspect ratio is influenced by the nature of the organic ligand. This may in part be attributable to the smaller ionic radius of the Yb^{III} ion compared to the other Ln^{III} investigated.⁴³ Addition of the STS habit modifier improves the monodispersity of these 1D rod materials. Moreover, in agreement with our crystallographic analysis, all Ln-Bu^I exhibit rod-like crystal morphologies providing further evidence for a *pseudo*-2D structure that is assembled from 1D coordination polymers. The Ln-Biphen series gives rise to film-like assemblies (**Figure 3.6f**), whose amorphous character is consistent with the corresponding PXRD patterns (**Figure 3.3**).

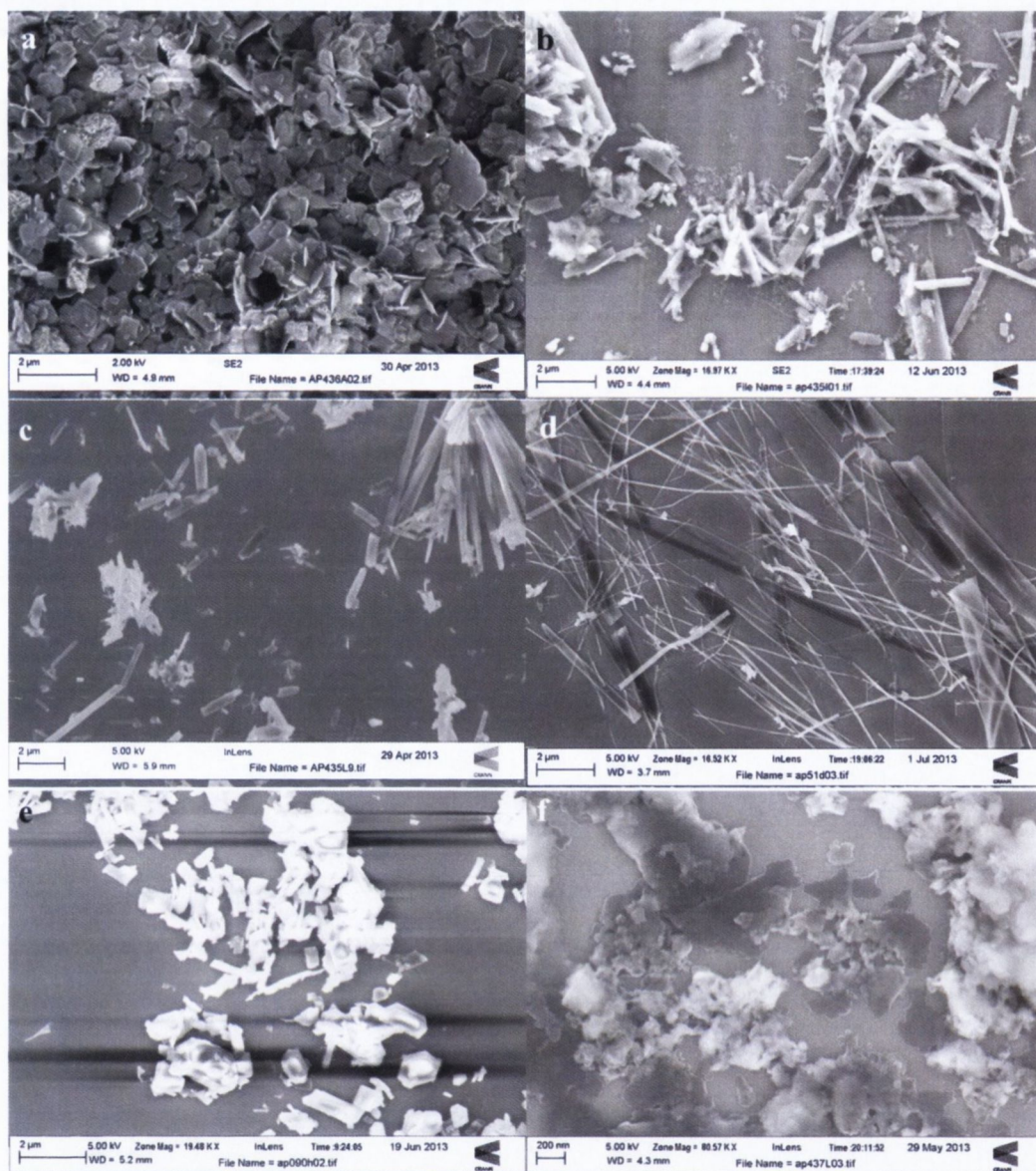


Figure 3.6: SEM images of (a) platelets of Nd-Naph (no p-STs), (b) rod structure of Yb-Naph among some nanoparticles (no p-STs), (c) phase pure rod structures of Yb-Naph (with p-STs), rod structures of (d) Yb-Bu^f and (e) Nd-Bu^f and (f) film-like assemblies of Yb-Biphen (with p-STs modifier).

Ln-phosphonates exhibit two distinct morphologies; 2D plates and 1D nanorods. We observe that a smaller ionic radius (*i.e.* Yb^{III}) favours one-dimensional growth, which is consistent with the nanomorphology reported previously for layered lanthanide phosphates (LnPO₄) and lanthanide hydroxides (Ln(OH)₃).⁴³ Moreover, Ln-Bu^f materials, in particular, exhibit rod-like crystal morphologies with a high aspect ratio, which is in excellent agreement with the formation of a 1D coordination polymer that assembles in the solid-state *via* hydrogen bonding into a *pseudo*-2D supramolecular structure, as identified by X-ray crystallography. The anisotropy of these interactions that prevail in distinct directions of space is thus reflected in the crystal habit.

The addition of STS generally leads to more uniform crystal morphologies, improving the sample monodispersity. The influence of STS was previously considered in nanorod growth in lanthanide phenyl phosphonates.³² Two growth mechanisms were proposed. In the first, the

formation of an intercalated structure where STS molecules are held between the hydrophobic lamellar phase of the lanthanide phenyl phosphonate is described; subsequent removal of the STS exfoliates the structure into the individual nanorods. The second mechanism postulates that 1D crystal growth is possible if the chemical potential of the monomers in solution are higher than the chemical potential of an atom on a crystal seed. Since we observed 1D crystal growth even in the absence of STS, we believe that for **Ln-Bu'** the connectivity of individual lanthanide phosphonate centres plays a more critical role in defining the crystal morphology.

With the exception of **Yb-Naph**, which forms rod-like structures, irregular 2D plates are more commonly observed for **Ln-Naph** materials. Considering this, it is likely that there is no or only a small anisotropic structural feature from the ligand-lanthanide bonding within the layer, so preferential favoured 1D growth is reduced or even absent. The **Ln-Biphen** series is influenced by the more extended hydrophobic ligand, which gives rise to film-like assemblies, whose amorphous character is consistent with the corresponding PXRD patterns.

3.5 Steady-state and time-resolved photoluminescence studies of Ln-phosphonates

3.5.1 Eu^{III} - and Tb^{III} -phosphonates: Emission in the visible spectral region

The PL properties of the Eu^{III} - and Tb^{III} -phosphonates were investigated to gain a quantitative understanding of the effect of ligand choice and to obtain further structural information.

The solid-state UV/Vis reflectance spectra for the Eu^{III} - and Tb^{III} -phosphonates are given in **Figure 3.7**. An intense absorption band is observed at 320 nm and 305 nm, for **Eu-Naph** and **Eu-Biphen**, respectively. This indicates that the aromatic ligands strongly absorb light in the UV region and were investigated to see if they could sensitise the Eu^{III} centre. In the reflectance spectra of **Eu-Bu'** a weak absorption band at 393 nm associated with the $^5\text{L}_6 \leftarrow ^7\text{F}_0$ transition is observed. This suggests that Eu^{III} PL may also be observed through direct excitation. **Tb-Naph** and **Tb-Biphen** are dominated by strong absorption bands in the UV at 320 and 305 nm, respectively, and direct Tb^{III} transitions could not be easily observed.

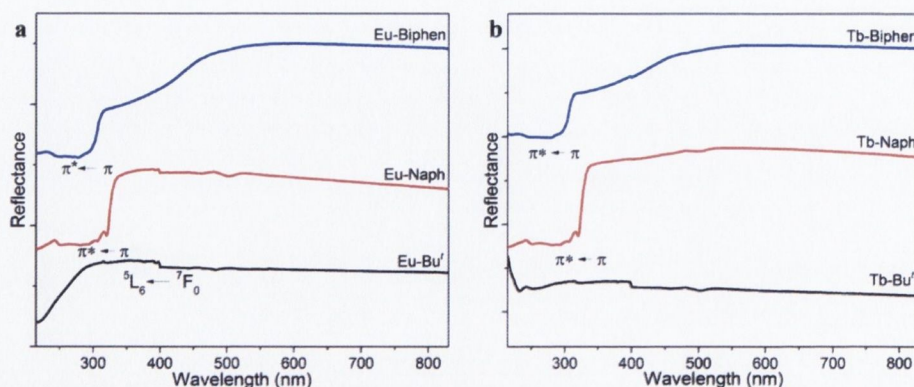


Figure 3.7: RT solid-state UV/Vis reflectance spectra for (a) Eu^{III} -phosphonates and (b) Tb^{III} -phosphonates.

Figures 3.8a and **8b** show the PL and excitation spectra of **Eu-Bu'**, **Eu-Naph** and **Eu-Biphen**. On direct excitation of the Eu^{III} centre ($\lambda_{\text{ex}} = 393 \text{ nm}$, ${}^5\text{L}_6 \leftarrow {}^7\text{F}_0$), characteristic Eu^{III} -centred red PL originating from ${}^5\text{D}_0 \rightarrow {}^7\text{F}_J$ transitions ($J = 0-4$) between 570-720 nm was observed for all samples. Emission from higher excited states (e.g. ${}^5\text{D}_1$) was not observed indicating efficient non-radiative relaxation to the ${}^5\text{D}_0$ manifold. The characteristic Eu^{III} emission spectrum was also obtained for **Eu-Naph** and **Eu-Biphen** *via* ligand sensitisation ($\lambda_{\text{ex}} = 320 \text{ nm}$ and $\lambda_{\text{ex}} = 305 \text{ nm}$ (**Figure 3.8a**), respectively). For both metal-centred and ligand excitation, the most intense transition is the hypersensitive ${}^5\text{D}_0 \rightarrow {}^7\text{F}_2$ emission line, which is common for eight-coordinate lanthanide centres.⁴⁴ The absence of ligand-centred emission in the PL spectrum suggests that energy transfer from the ligand to the metal centre is very efficient. The corresponding excitation spectra (monitored in the ${}^5\text{D}_0 \rightarrow {}^7\text{F}_2$ transition) exhibit characteristic metal-centred *ff* emission lines corresponding to transitions between the ${}^7\text{F}_0$ ground state and the ${}^5\text{D}_{4-1}$, ${}^5\text{G}_{2-6}$ and ${}^5\text{L}_6$ excited states. In addition, **Eu-Naph** and **Eu-Biphen** display broad excitation bands centred at 320 nm and 300 nm. Comparison with the UV/Vis absorption spectra of the free ligands confirms that these bands result from ligand-based excitation.

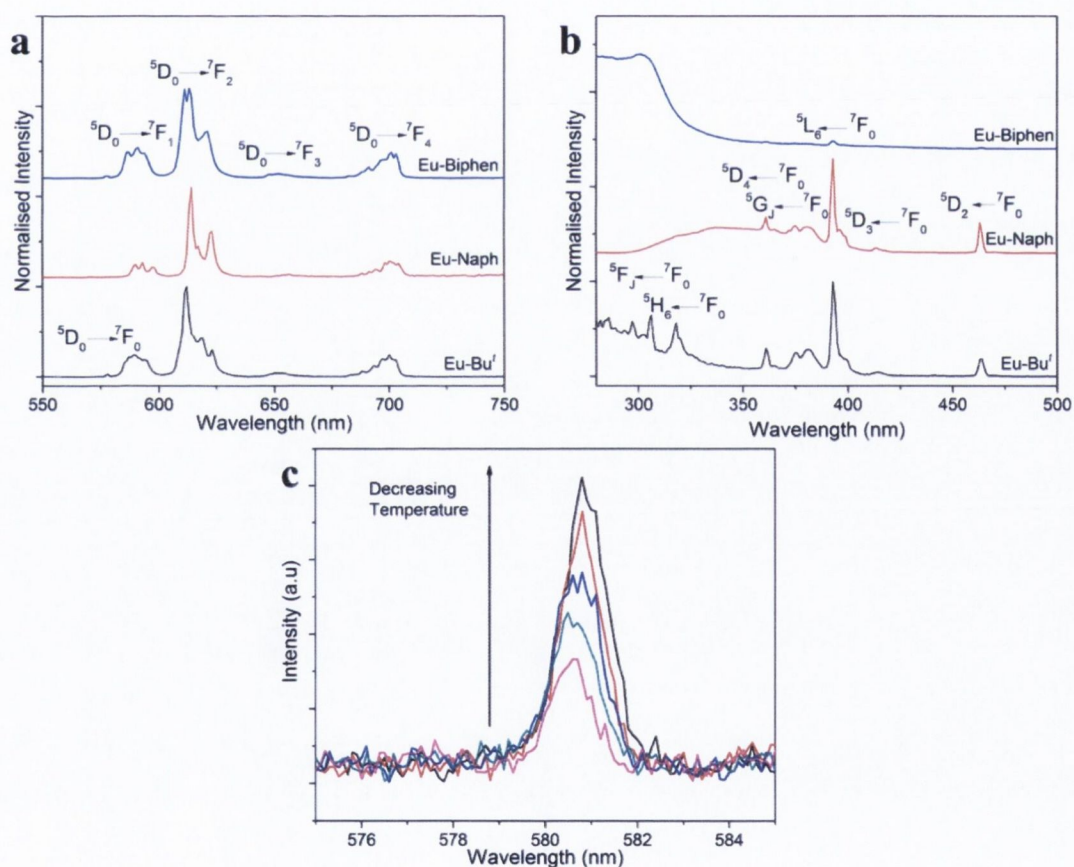


Figure 3.8: (a) RT PL spectra for **Eu-Bu'** obtained upon direct excitation at 393 nm (${}^5\text{L}_6 \leftarrow {}^7\text{F}_0$) and **Eu-Naph** and **Eu-Biphen** on ligand excitation ($\lambda_{\text{ex}} = 320 \text{ nm}$ and $\lambda_{\text{ex}} = 305 \text{ nm}$, respectively). (b) Corresponding RT excitation spectra ($\lambda_{\text{em}} = 610-614 \text{ nm}$, ${}^5\text{D}_0 \rightarrow {}^7\text{F}_2$ transition) and (c) low temperature (77-250 K) study of ${}^5\text{D}_0 \rightarrow {}^7\text{F}_0$ transition in **Eu-Naph**.

The PL characterisation of the Eu^{III}-phosphonates enabled us to investigate not only the optical properties of these materials, but also provided complementary insight into the molecular structure, which was crucial for those systems where it was not possible to obtain single crystal X-ray diffraction data. When a free ion is placed into a crystalline environment the degeneracy of the $^{2S+1}L_J$ term is removed and can be split into a number of crystal field levels. The number of crystal field levels observed is dependent on the site symmetry of the lanthanide and these have been tabulated in the literature.⁴² As such it is possible to gain structural information of the lanthanide centre. For **Eu-Naph**, splitting of the $^5D_0 \rightarrow ^7F_1$ transition into three Stark components indicates a unit cell in the orthorhombic crystal system.⁴² Furthermore, splitting of the $^5D_0 \rightarrow ^7F_2$ into only three Stark components suggests a point group symmetry close to D_2 indicating the coordination environment around the Eu^{III}-centre is likely a distorted dodecahedron.⁴² Using the same approach for **Eu-Biphen**, the $^5D_0 \rightarrow ^7F_1$ transition splitting into three bands and the $^5D_0 \rightarrow ^7F_2$ into three or possibly four bands suggests an eight-coordinate environment with point group symmetry between D_2 and C_{2v} .

The ground (7F_0) and the emissive (5D_0) states of Eu^{III} are non-degenerate and cannot be split by the crystal field.⁴⁰ As such, there is a one-to-one correspondence between the number of bands associated with the $^5D_0 \rightarrow ^7F_0$ transition in the PL spectrum and the number of distinct Eu^{III} environments.^{40, 41} Gaussian deconvolution of this band reveals a single Eu^{III} local environment for all Eu^{III}-phosphonates, which is in good agreement with the crystallographic data.

Interestingly, the $^5D_0 \rightarrow ^7F_0$ transition is absent for **Eu-Naph** at room temperature but gradually appears and increases in intensity on lowering the temperature to 77 K (**Figure 3.8c**). This observation can be explained due to the site symmetry around the europium centre and the selection rules enforced on the $^5D_0 \rightarrow ^7F_0$ transition in **Eu-Naph**.⁴² It has been determined that **Eu-Naph** crystallises in the space group *Pcca*, a centrosymmetric space group with an *mmm* point group. Analysis of the Stark splittings reveals the site symmetry of the Eu^{III} ion to be of the D_2 point group, a centrosymmetric point group with four-fold symmetry. As such, at room temperature, the $^5D_0 \rightarrow ^7F_0$ transition is absent due to the electric dipole and magnetic dipole operators both being symmetry forbidden. However, when the sample is cooled, the site symmetry of the Eu^{III} centre is lowered and shifts towards the point group C_2 , where the electric and magnetic dipole operators are symmetry allowed and the transition is weakly observed.^{45, 46}

Photoluminescence quantum yields (Φ_{PL}) for direct excitation of Eu^{III} were ~1-3% for all samples (**Table 3.5**). It is noted that emission quantum yields obtained for direct excitation of Eu^{III}-phosphonates (Φ_{PL} ~0.7, 2 and 3% for **Eu-Biphen**, **Eu-Naph** and **Eu-Bu'**, respectively) are lower than those previously reported for Eu^{III}-doped La^{III} phenyl phosphonates (e.g. Φ_{PL} = 10% for La(HO₃PC₆H₅)₂:0.06Eu).³³ This is attributed to enhanced concentration quenching in our Ln-phosphonate materials, whereby excitation energy transfer between nearest neighbour Eu^{III} lattice sites activates an additional non-radiative deactivation channel.⁴⁷

Table 3.5: Observed emission lifetime (determined from either mono- or bi-exponential decay functions) (τ_i), radiative rate constants (k_r) non-radiative rate constants (k_{nr}) absolute emission quantum yields (Φ_{PL}), calculated efficiency of metal centred emission (η_{Ln}) and number of water molecules in the first coordination sphere (n_w) for Eu^{III} - and Tb^{III} -phosphonates.

Compound	λ_{ex} (nm)	τ (ms)	k_r (s^{-1})	k_{nr} (s^{-1})	Φ_{PL} (%)	η_{Ln} (%) ^e	n_w
Eu-Bu^f	393 ^a	0.57 ± 0.05	270	1500	3	-	1.3
							2.3
Eu-Naph	393 ^a	0.37 ± 0.05	359	2457	2	-	2.3
	330 ^b	0.35 ± 0.05	390	2427	-	14	0.1
Eu-Biphen	393 ^a	0.88 ± 0.05	440	695	0.7	-	0.45
	305 ^c	1.03 ± 0.05	252	717	-	26	
Tb-Bu^f	377 ^d	1.64 ± 0.05	-	-	8	-	
Tb-Biphen	377 ^d	0.63 ± 0.05	-	-	^f	-	
	305 ^c	0.80 ± 0.05	-	-	-	-	

^a $\lambda_{ex} = 393$ nm (${}^7\text{F}_0 \leftarrow {}^5\text{L}_6$), ^b $\lambda_{ex} = 330$ nm (Naph excitation), ^c $\lambda_{ex} = 305$ nm (Biphen excitation), ^d $\lambda_{ex} = 377$ nm (${}^5\text{D}_3 \leftarrow {}^7\text{F}_6$), ^e η_{Ln} calculated using experimental lifetimes and corrected emission spectrum for Eu^{III} , ^f measured emission intensities too low to determine Φ_{PL} . N.B no emission lifetimes or quantum yields measured for **Tb-Naph** due to absence of room-temperature photoluminescence.

The observed emission lifetimes of Eu^{III} (${}^5\text{D}_0$) phosphonates are shown in **Table 3.5**. Upon direct excitation and ligand sensitisation **Eu-Naph** exhibits a monoexponential decay curve, with an observed lifetime of $\tau \sim 0.36$ ms. **Eu-Biphen** and **Eu-Bu^f** both exhibit bi-exponential decay curves, comprised of a short-lived component of similar magnitude ($\tau_1 \sim 0.30$ - 0.38 ms) and a longer lived component of $\tau_2 \sim 1.00$ - 1.32 ms, depending on the mode of excitation. Notably for **Eu-Bu^f** the long-lived component makes only a minor contribution ($\sim 7\%$), but becomes the dominant feature for **Eu-Biphen** ($\sim 73\%$). The crystallographic data and deconvolution of the ${}^5\text{D}_0 \rightarrow {}^7\text{F}_0$ transition indicate a single Ln^{III} environment. However, concentration quenching, where excitation energy migrates between Ln^{III} sites before being trapped by a quencher site is common in solid-state materials where the Ln^{III} concentration exceeds more than a few percent, as is the case here.⁴⁸ The bi-exponential decay behaviour could therefore arise due to emission from quenched (short-lived) and unquenched sites (longer lived). Concentration quenching typically results in low emission quantum yields, which is in agreement with the observed values tabulated. It has been shown in other solid-state materials that non-radiative energy transfer is dependent on both the dimensionality and the distance between the donor and acceptor sites. Therefore, the bulk material of multiple 2D sheets of **Eu-Biphen** and the packed 1D chains of **Eu-Bu^f** may observe differences in the rate of energy transfer through the material.⁴⁹

It was possible to determine the efficiency for metal centred emission (η_{Ln}) in the Eu^{III} -phosphonates from the experimental lifetimes and the corrected emission spectrum due to the presence of the purely magnetic ${}^5\text{D}_0 \rightarrow {}^7\text{F}_1$ transition (**Section 1.3.4**), using the relationship:⁵⁰

$$\eta_{Ln} = \frac{k_r}{k_r + k_{nr}} = \frac{\tau_{obs}}{\tau_r} \quad \text{Eqn. 3.1}$$

whereby the radiative lifetime, τ_r , is given by:

$$\frac{1}{\tau_r} = A_{MD} n^3 \left(\frac{I_{tot}}{I_{MD}} \right). \quad \text{Eqn. 3.2}$$

When the refractive index is taken as $n = 1.5$, η_{Ln} is determined to be 14% for **Eu-Naph** and 31% for **Eu-Biphen**. These values show that the efficiency for metal centred emission can be improved greatly by removing water from the first coordination sphere as is observed in **Eu-Biphen**. However, the absolute emission quantum yields are much lower than these calculated values for both materials and may be due to increased non-radiative pathways, which may include light absorption into the ligand that relaxes non-radiatively, preventing all the absorbed light reaching the 5D_0 manifold of the Eu^{III} centre. These low absolute emission quantum yields have been observed in this way in other lanthanide phosphonates.⁴⁴

Quenching of Ln^{III} lifetimes by coordinated water molecules occurs as a result of non-radiative deactivation of the emissive state due to coupling with O-H oscillations.⁵¹ The number of water molecules (n_w) in the Eu^{III} first coordination sphere have been determined using the empirical formula:^{52, 53}

$$n_w = 1.11 \times [\tau^{-1} - k_r - 0.31]. \quad \text{Eqn. 3.3}$$

The n_w values calculated for **Eu-Naph** and **Eu-Biphen** of ~ 2 and ~ 0 , respectively, are in excellent agreement with the constitutional and structural assignment for these materials. It is noted that for **Eu-Biphen**, a slightly elevated $n_w \approx 0.45$ is obtained upon ligand sensitisation, which suggests the contribution of additional non-radiative deactivation channels in this material. For **Eu-Bu'**, we determined $n_w \approx 1.3$, which reflects that this compound contains both a constitutional water molecule and also contains multiple partially-protonated organophosphonate ligands which supply additional O-H oscillators.

The PL and excitation spectra for **Tb-Bu'** and **Tb-Biphen** are shown in **Figure 3.9a** and **8b**. Characteristic Tb^{III} -centred green emission is observed in the range of 450-700 nm corresponding to $^5D_4 \rightarrow ^7F_J$ ($J = 6-3$) transitions upon direct excitation of the metal centre. The excitation spectrum for **Tb-Bu'** displays characteristic *ff* transitions between 300-500 nm, corresponding to transitions from the 7F_6 ground-state to the $^5D_{4-3}$, $^5L_{10}$ and 5G_J excited states. Ligand sensitisation of the Tb^{III} photoluminescence is also observed for **Tb-Biphen** (**Figure 3.9a**). The relative intensity of the observed PL is significantly greater (under the same experimental conditions) than for direct excitation of the same sample, suggesting that efficient ligand to metal energy transfer occurs. This is supported by the dominance of the broad ligand band in the excitation spectrum (monitored in the $^5D_4 \rightarrow ^7F_5$ transition), which obscures the weak *ff* transition lines.

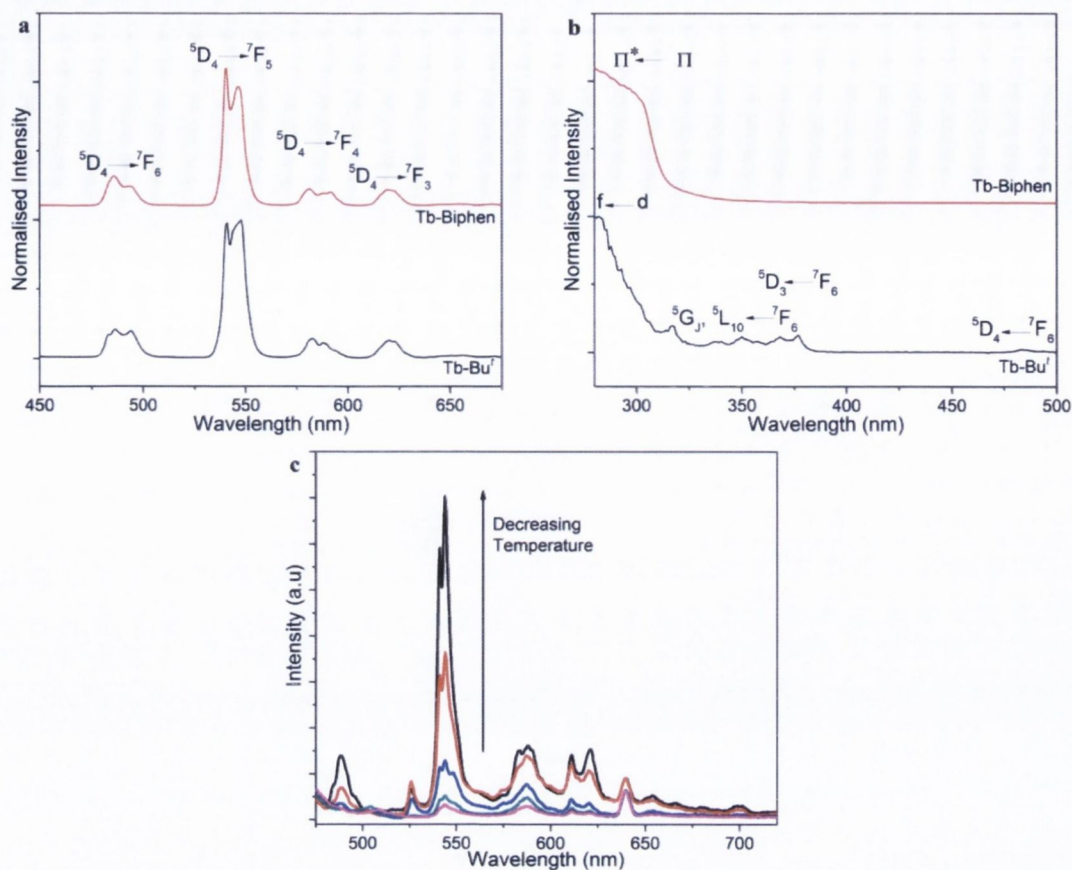


Figure 3.9: (a) RT PL spectra for **Tb-Bu'** obtained upon direct excitation at 377 nm ($^5D_3 \leftarrow ^7F_6$) and **Tb-Biphen** on ligand excitation ($\lambda_{ex} = 305$ nm). (b) Corresponding RT excitation spectra ($\lambda_{em} = 610$ - 614 nm, $^5D_4 \rightarrow ^7F_5$ transition). (c) Low temperature (77-250 K) PL spectra for **Tb-Naph** upon ligand sensitisation ($\lambda_{ex} = 320$ nm).

No PL was observed for **Tb-Naph**, for either metal-centred excitation or ligand sensitisation at room temperature. However, characteristic Tb^{III} emission was observed at 77-250 K, with the relative PL intensity increasing as the temperature decreased (**Figure 3.9c**). The excitation spectrum for **Tb-Naph** observed at 77 K is dominated by a ligand-centred band at 320 nm and a weaker emission line centred at 377 nm attributed to the $^5D_3 \leftarrow ^7F_6$ transition. Examination of the energy level diagram (**Figure 3.10**) reveals that the **Naph-PO₃H₂** T_1 state lies ~ 600 cm^{-1} above the emissive 5D_4 state ($20,490$ cm^{-1}). At room temperature, thermal population of higher vibrational levels within the 5D_4 manifold is expected, thus facilitating back energy transfer to the ligand. However, on cooling to 77 K, the characteristic Tb^{III} emission spectrum is observed for **Tb-Naph**, suggesting that the probability for back energy transfer to the ligand T_1 level is reduced due to a decreased Boltzmann population of vibrational levels. Similar observations have been made with other Tb^{III} -materials that use naphthalene-based sensitising units.⁵⁴ In contrast, for **Tb-Biphen**, the ligand T_1 state lies ~ 2100 cm^{-1} above the Tb^{III} emissive state, resulting in efficient ligand to metal energy transfer and inhibiting back energy transfer at room temperature.

The emission quantum yield could not be measured for **Tb-Naph** as it is non-emissive at room temperature. When **Tb-Biphen** was excited directly, the resulting emission was too weak to

measure and the excitation energy required to excite the ligand was outside the range of the integrating sphere. As such only the Φ_{PL} for **Tb-Bu'** was measured and found reasonable at 8%.

Tb-Biphen and **Tb-Bu'** both exhibit bi-exponential decay curves, but the lifetime and contribution of each component differs significantly. **Tb-Bu'** displays two lifetimes, $\tau_1 \sim 0.98$ ms and $\tau_2 \sim 2.69$ ms that contribute equally to the decay curve. In contrast, **Tb-Biphen** exhibits two much shorter lived components of similar magnitude that also contribute equally ($\tau_1 \sim 0.33$ and $\tau_2 \sim 0.80$ ms).

By changing the ligand, it has been shown there is a distinct effect on the photoluminescence properties. Ligand sensitisation is a desired route to photoluminescence as it can significantly improve emission quantum yields and has been quantified for these Ln-phosphonates. Ligand sensitisation proceeds *via* energy transfer from the lowest excited triplet state (T_1) of the ligand antenna. It has been previously demonstrated that energy transfer occurs most efficiently when an energy gap of $\Delta E = 2500\text{-}3000$ cm^{-1} between the triplet donor state on the ligand and the emissive state of the acceptor Ln^{III} centre is present (**Figure 3.10**).^{55, 56} By systematic variation of the ligand, it is observed that **Naph-PO₃H₂** can strongly sensitise Eu^{III} PL due to a good energy overlap of the T_1 state of the ligand and the Eu^{III} manifold (~ 17400 cm^{-1}) of ~ 3500 cm^{-1} . However, when the Tb^{III} manifold ($20,490$ cm^{-1}) is taken into consideration the energy gap is much smaller at ~ 600 cm^{-1} and through thermal population of higher vibrational levels in $^5\text{D}_4$ manifold of Tb^{III} , a route to back energy transfer to the ligand exists and no PL is observed at room temperature. In contrast, it has been shown that the ligand **Biphen-PO₃H₂** has a much more favourable T_1 state that is ~ 2100 cm^{-1} above the Tb^{III} emissive state. At room temperature, there is now a larger, more efficient ligand to metal overlap and so a route for back energy transfer is reduced. This results in a stronger Tb^{III} PL response. This indicates that with judicious matching of the ligand donor and Ln^{III} acceptor energy levels it is possible to switch the Ln^{III} photoluminescence on and off by changing the temperature and thereby tune the emissive response to a desired application.

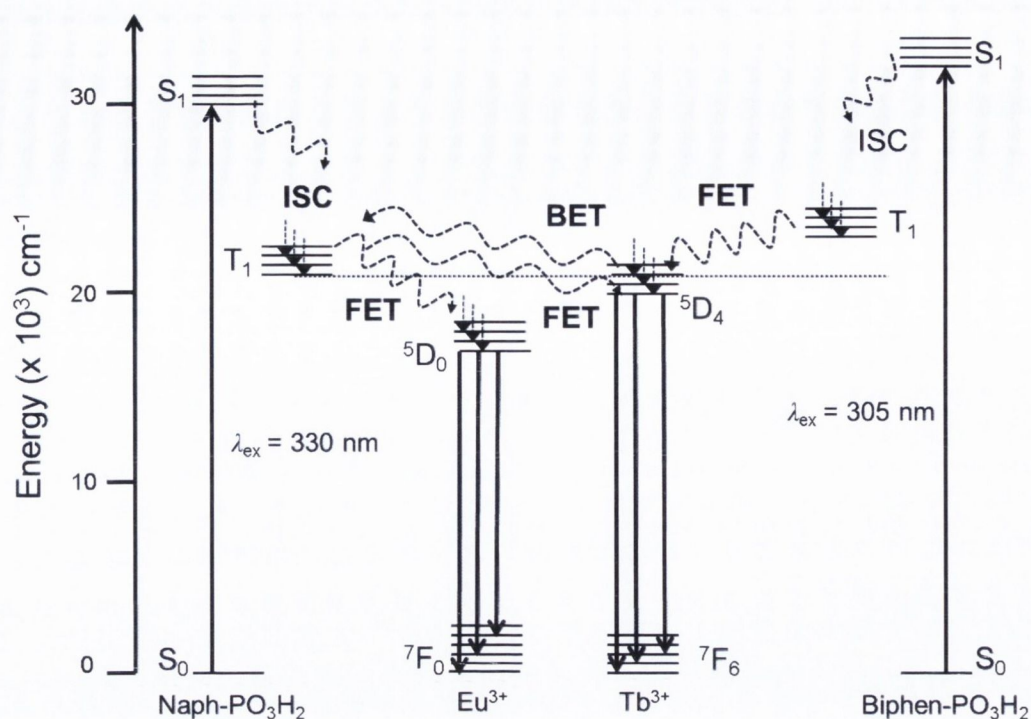


Figure 3.10: Partial energy level diagram of naphthalene- and biphenyl-phosphonic acids (**Naph-PO₃H₂** and **Biphen-PO₃H₂**, respectively) and **Eu^{III}** (intra- $4f^6$) and **Tb^{III}** (intra- $4f^8$) energy levels. Solid and dashed lines represent radiative and non-radiative transitions, respectively.

3.5.2 **Nd^{III}- and Yb^{III}-phosphonates: Emission in the Near-Infrared spectral region**

NIR-emitting lanthanides have been shown to have applications in telecommunications industry, where the host materials are required to display properties of preferential luminescence along a particular axis. As it was shown that some control over 2D to 1D nano-morphologies were attainable the NIR emissive properties of **Nd^{III}-** and **Yb^{III}-phosphonates** were investigated.

The solid-state diffuse reflectance spectra of **Nd^{III}-** and **Yb^{III}-phosphonates** were measured (**Figure 3.11**). For **Nd-Bu^f** strong absorption bands due to intra $4f$ -transitions are observed from the ground state, $^4I_{9/2}$, to the $^4S_{7/2}$, $^4F_{7/2}$, $^4G_{J/2}$ ($J = 5, 7$), $^2L_{15/2}$ $^2I_{11/2}$ and $^4D_{J/2}$, excited states, respectively. Further absorption bands in the UV were observed for **Nd-Naph** and **Nd-Biphen** at 320 and 305 nm, respectively and are due to absorption from the aromatic moiety. For **Yb-Naph** and **Yb-Biphen**, a unique intense absorption band is observed at 320 and 305 nm, respectively. The diffuse reflectance spectra show that **Nd^{III}** PL should be accessible through both direct excitation and through sensitisation when an aromatic phosphonic acid is coordinated. Due to the $4f^{13}$ electron configuration of **Yb^{III}**, PL from the **Yb^{III}** centre should be possible through a sensitisation pathway.

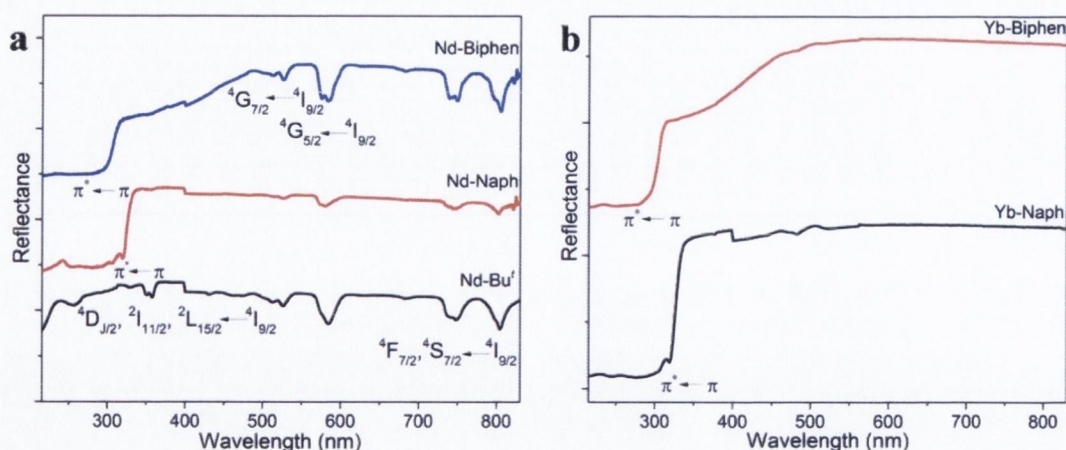


Figure 3.11: RT solid-state UV/Vis reflectance spectra for (a) Nd^{III}-phosphonates and (b) Yb^{III}-phosphonates.

Notably, NIR photoluminescence from both Nd^{III} and Yb^{III} phosphonates was observed at room temperature. For **Nd-Bu'**, **Nd-Naph** and **Nd-Biphen**, characteristic Nd^{III} emission lines assigned to the ${}^4F_{3/2} \rightarrow {}^4I_{J/2}$ ($J = 13, 11, 9$) transitions are observed for direct Nd^{III} excitation ($\lambda_{\text{ex}} = 580\text{nm}$, ${}^5G_{5/2} \leftarrow {}^4F_{9/2}$) (**Figure 3.12**), with **Nd-Biphen** exhibiting some fine splitting for these transitions. Ligand sensitisation of the emission is also observed for **Nd-Naph** and **Nd-Biphen** (**Figure 3.12**). The excitation spectra of **Nd-Bu'** monitored for the ${}^4F_{3/2} \rightarrow {}^4I_{11/2}$ transition ($\lambda_{\text{em}} \sim 1060\text{ nm}$) exhibit Nd^{III}-centred excitations in the UV to visible range of the spectrum arising from the ${}^4I_{9/2}$ ground state to the ${}^4D_{J/2}$, ${}^4I_{11/2}$, ${}^2L_{15/2}$, ${}^2D_{5/2}$, ${}^2P_{1/2}$, ${}^2K_{15/2}$, ${}^4G_{7/2-5/2}$, ${}^4S_{3/2}$ and ${}^4F_{9/2-7/2}$ excited states (**Figure 3.12**). The excitation spectra for **Nd-Naph** and **Nd-Biphen** also display broad bands at 320 and 305 nm due to absorption by the aromatic ligand antenna (**Figure 3.12**). This is in good agreement with the UV/Vis diffuse reflectance spectra.

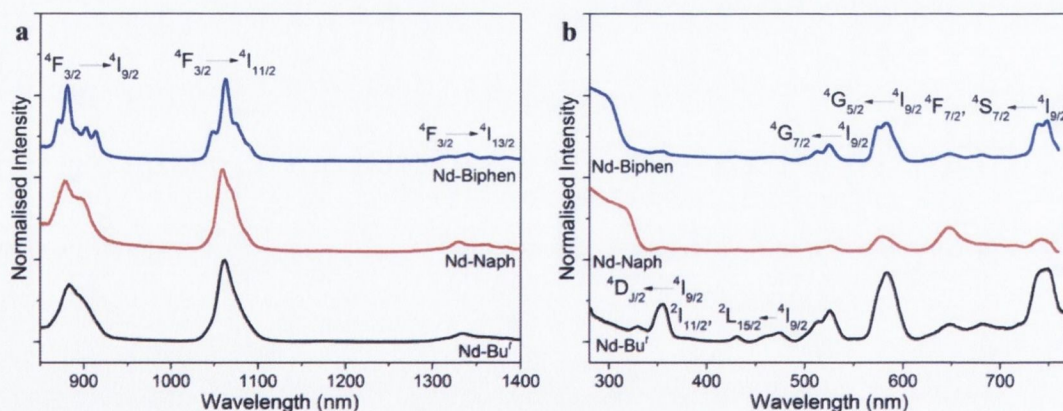


Figure 3.12: (a) RT PL spectra for **Nd-Bu'** obtained upon direct excitation at 584 nm (${}^5G_{5/2} \leftarrow {}^4F_{9/2}$) and **Nd-Naph** and **Nd-Biphen** on ligand excitation ($\lambda_{\text{ex}} = 320\text{ nm}$ and $\lambda_{\text{ex}} = 305\text{ nm}$, respectively). (b) Corresponding RT excitation spectra ($\lambda_{\text{em}} = 1057\text{-}1061\text{ nm}$, ${}^4F_{3/2} \rightarrow {}^4I_{11/2}$ transition).

Figure 3.13 shows the PL spectra for **Yb-Naph** and **Yb-Biphen** obtained upon ligand-centred excitation at 320 and 300 nm, respectively. A broad band centred at 977-978 nm corresponding to the ${}^4F_{5/2} \rightarrow {}^4F_{7/2}$ transition is observed. The excitation spectra support this

observation for **Yb-Naph** and **Yb-Biphen** where there is absorption from the ligand at 320 and 300 nm, respectively, but no *ff* transitions are observed (**Figure 3.13**).

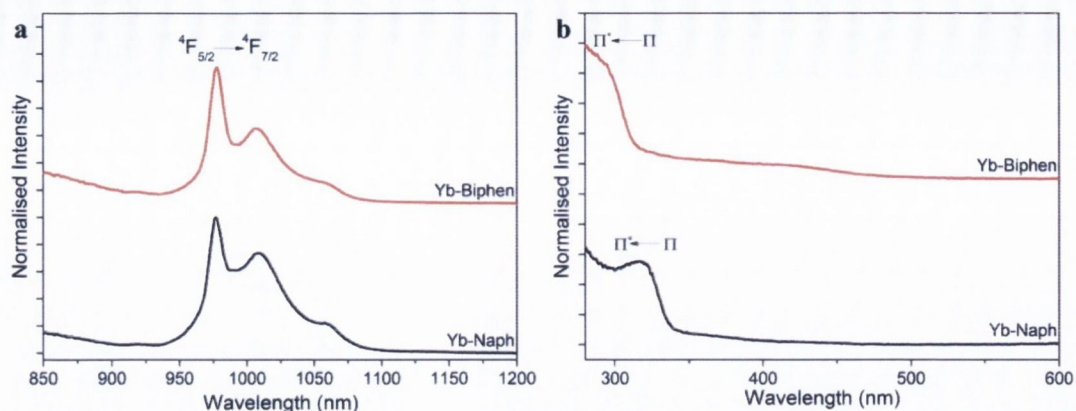


Figure 3.13: (a) RT PL spectra for **Yb-Naph** and **Yb-Biphen** upon ligand excitation ($\lambda_{\text{ex}} = 320$ nm and $\lambda_{\text{ex}} = 305$ nm, respectively) and (b) corresponding RT excitation spectra ($\lambda_{\text{em}} = 977\text{-}978$ nm, ${}^4F_{5/2} \rightarrow {}^4F_{7/2}$ transition).

Although it was not possible to determine Φ_{PL} or τ_{obs} with our experimental set-up for the Nd-phosphonate series, we note that relatively intense NIR emission was observed under moderate experimental conditions (7 and 10 nm excitation and emission slit widths, respectively), despite the propensity for non-radiative quenching through C-H, C-C and O-H oscillations on the ligands and coordinated water molecules.^{57, 58}

3.6 Conclusion and Outlook

This chapter has looked at the synthesis and characterisation of three new series of lanthanide phosphonates. The first family of lanthanide phosphonates was synthesised by reaction of the lanthanide with *tert*-butyl phosphonic acid. This reaction yields a 1D infinite chain of $[\text{Ln}(\text{HO}_3\text{PC}(\text{CH}_3)_3)_3] \cdot \text{H}_2\text{O}$ and a *pseudo*-2D material is observed through hydrogen bonding between the constitutional H_2O and adjacent Ln^{III} -phosphonate chains. Through a combination of powder X-ray diffraction, FT-IR and TGA, coupled with analysis of the Stark splitting of the emission bands in the PL of the Eu^{III} -phosphonates, a further two series of Ln^{III} -phosphonates have been characterised upon reaction with 1-naphthalene phosphonic acid and 4-biphenyl phosphonic acid.

A study of the morphology of the crystals grown in hydrothermal conditions was undertaken and we found that control from 1D nanorods to 2D plates was largely dependent on the coordination environment of the Ln^{III} -centre and whether an anisotropic growth preference was present as a result. Similarly, we found that the plates grown become more amorphous as the ligand becomes more hydrophobic as the ligand is varied from *tert*-butyl- to biphenyl-phosphonic acid.

This study shows that by introducing an aromatic ligand we can greatly improve the efficiency of lanthanide emission (η_{Ln}) by the exclusion of coordinated water molecules in the first

coordination sphere (*cf.* **Ln-Naph** vs. **Ln-Biphen**) and further introduce an additional excitation path through sensitisation for Ln^{III}-phosphonates where Ln^{III} = Eu^{III}, Tb^{III}, Nd^{III} and Yb^{III}. It was shown that the PL of the Eu^{III} ion can be exploited to collect further structural information on the materials by guiding the assignment of the crystal system and space group from the PXRD analysis. By determining the point group of **Eu-Naph** it was possible to relate the structure (in tandem with TGA) to the structure of [La(O₃PCH₂C₆H₅)₂(H₂O)₂]⁹ and allowed us to identify the cause for the absence of the ⁵D₀→⁷F₀ transition. The careful choice of the aromatic group is required to obtain efficient sensitisation of the Ln^{III} centre, especially when Ln^{III} = Tb^{III} where a temperature dependant on-off PL response was observed. The near-infrared RT PL from both Nd^{III}- and Yb^{III}-phosphonates has been shown by ligand sensitisation and, to the best of our knowledge, this is the first case where this has been observed for an Yb^{III}-phosphonate.

Previous studies have managed to exfoliate lanthanide phosphonates by dispersal within polar solvents.⁵⁹ Our approach where we have systematically varied the *d*-spacing of the material should provide an alternative route to the exfoliation of lanthanide phosphonates and formation of thin films, a requirement for the preparation of many modern optical devices.

To conclude, as outlined in the introduction and demonstrated in this chapter, the isolation of crystalline lanthanide phosphonates is still a difficult task. As such we are interested in improving solubility of lanthanide phosphonate systems by introducing a second organic ligand. Within the group, there is considerable expertise in utilising iminodiacetic acid derived ligands, and these ligands were chosen with the aim of improving lanthanide solubility, which is the focus of subsequent chapters.

3.7 References

1. A. Clearfield, *Curr. Opin. Solid State Mater. Sci.*, 1996, **1**, 268-278.
2. A. Clearfield, *Curr. Opin. Solid State Mater. Sci.*, 2002, **6**, 495-506.
3. A. Clearfield and G. D. Smith, *Inorg. Chem.*, 1969, **8**, 431-436.
4. G. Alberti, U. Costantino, S. Allulli and N. Tomassini, *J. Inorg. Nucl. Chem.*, 1978, **40**, 1113-1117.
5. M. D. Poojary, H. L. Hu, F. L. Campbell and A. Clearfield, *Acta Crystallogr., Sect. B: Struct. Sci.*, 1993, **49**, 996-1001.
6. M. Papadaki and K. D. Demadis, *Comments Inorg. Chem.*, 2009, **30**, 89-118.
7. S. Singh, P. Patel, V. K. Shahi and U. Chudasama, *Desalination*, 2011, **276**, 175-183.
8. X. Z. Lin and Z. Y. Yuan, *Eur. J. Inorg. Chem.*, 2012, 2661-2664.
9. R. C. Wang, Y. P. Zhang, H. L. Hu, R. R. Frausto and A. Clearfield, *Chem. Mater.*, 1992, **4**, 864-871.
10. J. G. Mao, *Coord. Chem. Rev.*, 2007, **251**, 1493-1520.
11. C. Serre, N. Stock, T. Bein and G. Férey, *Inorg. Chem.*, 2004, **43**, 3159-3163.
12. S. F. Tang, J. L. Song, X. L. Li and J. G. Mao, *Cryst. Growth Des.*, 2006, **6**, 2322-2326.
13. Q. Yue, J. Yang, G. H. Li, G. D. Li and J. S. Chen, *Inorg. Chem.*, 2006, **45**, 4431-4439.
14. J. A. Groves, P. A. Wright and P. Lightfoot, *Inorg. Chem.*, 2005, **44**, 1736-1739.
15. D. K. Cao, Y. Z. Li, Y. Song and L. M. Zheng, *Inorg. Chem.*, 2005, **44**, 3599-3604.
16. X. M. Gan, B. M. Rapko, J. Fox, I. Binyamin, S. Pailloux, E. N. Duesler and R. T. Paine, *Inorg. Chem.*, 2006, **45**, 3741-3745.
17. K. L. Nash, R. D. Rogers, J. Ferraro and J. Zhang, *Inorg. Chim. Acta*, 1998, **269**, 211-223.
18. A. Clearfield, C. V. K. Sharma and B. P. Zhang, *Chem. Mater.*, 2001, **13**, 3099-3112.

19. P. Vojtisek, P. Cigler, J. Kotek, J. Rudovsky, P. Hermann and I. Lukes, *Inorg. Chem.*, 2005, **44**, 5591-5599.
20. S. W. A. Bligh, N. Choi, C. Geraldes, S. Knoke, M. McPartlin, M. J. Sanganee and T. M. Woodroffe, *J. Chem. Soc., Dalton Trans.*, 1997, 4119-4125.
21. J. Rudovsky, P. Cigler, J. Kotek, P. Hermann, P. Vojtisek, I. Lukes, J. A. Peters, L. Vander Elst and R. N. Muller, *Chem. Eur. J.*, 2005, **11**, 2373-2384.
22. J. Plutnar, J. Rohovec, J. Kotek, Z. Zak and I. Lukes, *Inorg. Chim. Acta*, 2002, **335**, 27-35.
23. J. L. Song and J. G. Mao, *Chem. Eur. J.*, 2005, **11**, 1417-1424.
24. S. M. Ying and J. G. Mao, *Cryst. Growth Des.*, 2006, **6**, 964-968.
25. Z. Y. Du, H. B. Xu and J. G. Mao, *Inorg. Chem.*, 2006, **45**, 9780-9788.
26. C. M. Wang, Y. Y. Wu, Y. W. Chang and K. H. Lii, *Chem. Mater.*, 2008, **20**, 2857-2859.
27. Y. Zhao, J. Li, Z. G. Sun, J. Zhang, Y. Y. Zhu, X. Lu, L. Liu and N. Zhang, *Inorg. Chem. Commun.*, 2008, **11**, 1057-1059.
28. Y. Y. Zhu, Z. G. Sun, H. Chen, J. Zhang, Y. Zhao, N. Zhang, L. Liu, X. Lu, W. N. Wang, F. Tong and L. C. Zhang, *Cryst. Growth Des.*, 2009, **9**, 3228-3234.
29. Y. Y. Zhu, Z. G. Sun, Y. Zhao, J. Zhang, X. Lu, N. Zhang, L. Liu and F. Tong, *New J. Chem.*, 2009, **33**, 119-124.
30. L. Liu, Z. G. Sun, N. Zhang, Y. Y. Zhu, Y. Zhao, X. Lu, F. Tong, W. N. Wang and C. Y. Huang, *Cryst. Growth Des.*, 2010, **10**, 406-413.
31. L. J. Zhang, S. Xu, Y. S. Zhou, X. R. Zheng, C. Yu, Z. H. Shi, S. ul Hassan and C. Chen, *CrystEngComm*, 2011, **13**, 6511-6519.
32. S. Y. Song, J. F. Ma, J. Yang, M. H. Cao, H. J. Zhang, H. S. Wang and K. Y. Yang, *Inorg. Chem.*, 2006, **45**, 1201-1207.
33. W. H. Di, R. A. S. Ferreira, M. G. Willinger, X. G. Ren and N. Pinna, *J. Phys. Chem. C*, 2010, **114**, 6290-6297.
34. W. H. Di, X. G. Ren, N. Shirahata, C. X. Liu, L. G. Zhang, Y. Sakka and N. Pinna, *CrystEngComm*, 2011, **13**, 5226-5233.
35. A. K. Bhattacharya and G. Thyagarajan, *Chem. Rev.*, 1981, **81**, 415-430.
36. Q. Yao and S. Levchik, *Tetrahedron Lett.*, 2006, **47**, 277-281.
37. H. C. Aspinall, J. F. Bickley, J. L. M. Dwyer, N. Greeves, R. V. Kelly and A. Steiner, *Organometallics*, 2000, **19**, 5416-5423.
38. Y. Bretonniere, M. Mazzanti, J. Pecaut and M. M. Olmstead, *J. Am. Chem. Soc.*, 2002, **124**, 9012-9013.
39. D. Taupin, *J. Appl. Crystallogr.*, 1973, **6**, 380-385.
40. S. V. Eliseeva and J. C. G. Bunzli, *Chem. Soc. Rev.*, 2010, **39**, 189-227.
41. G. Muller, S. D. Kean, D. Parker and J. P. Riehl, *J. Phys. Chem. A*, 2002, **106**, 12349-12355.
42. K. Binnemans and C. GorllerWalrand, *Journal of Rare Earths*, 1996, **14**, 173-180.
43. G. F. Wang, Q. Peng and Y. D. Li, *Acc. Chem. Res.*, 2011, **44**, 322-332.
44. S. M. F. Vilela, D. Ananias, A. C. Gomes, A. A. Valente, L. D. Carlos, J. A. S. Cavaleiro, J. Rocha, J. P. C. Tome and F. A. A. Paz, *J. Mater. Chem.*, 2012, **22**, 18354-18371.
45. A. F. Kirby and F. S. Richardson, *J. Phys. Chem.*, 1983, **87**, 2544-2556.
46. S. Georgescu, A. M. Chinie, A. Stefan and O. Toma, *J. Optoelectron. Adv. Mater.*, 2005, **7**, 2985-2990.
47. N. Xue, X. P. Fan, Z. Y. Wang and M. Q. Wang, *Mater. Lett.*, 2007, **61**, 1576-1579.
48. G. Blasse and B. C. Grabmaier, in *Luminescent Materials*, Springer Berlin Heidelberg, Editon edn., 1994.
49. R. C. Evans, D. Ananias, A. Douglas, P. Douglas, L. D. Carlos and J. Rocha, *J. Phys. Chem. C*, 2008, **112**, 260-268.
50. M. H. V. Werts, R. T. F. Jukes and J. W. Verhoeven, *Phys. Chem. Chem. Phys.*, 2002, **4**, 1542-1548.
51. S. Lis, *J. Alloys. Compd.*, 2002, **341**, 45-50.
52. L. D. Carlos, R. A. S. Ferreira, V. D. Bermudez and S. J. L. Ribeiro, *Adv. Mater.*, 2009, **21**, 509-534.
53. R. M. Supkowski and W. D. Horrocks, *Inorg. Chim. Acta*, 2002, **340**, 44-48.
54. A. Beeby, D. Parker and J. A. G. Williams, *J. Chem. Soc., Perkin Trans. 2*, 1996, 1565-1579.

55. A. P. S. Samuel, J. D. Xu and K. N. Raymond, *Inorg. Chem.*, 2009, **48**, 687-698.
56. M. Latva, H. Takalo, V. M. Mikkala, C. Matachescu, J. C. Rodriguez-Ubis and J. Kankare, *J. Lumin.*, 1997, **75**, 149-169.
57. R. H. C. Tan, M. Motevalli, I. Abrahams, P. B. Wyatt and W. P. Gillin, *J. Phys. Chem. B*, 2006, **110**, 24476-24479.
58. G. Blasse and N. Sabbatini, *Mater. Chem. Phys.*, 1987, **16**, 237-252.
59. T. Araki, A. Kondo and K. Maeda, *Chem. Commun.*, 2013, **49**, 552-554.

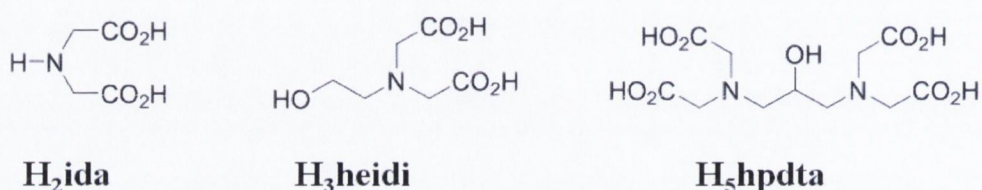
Chapter Four

.....

**Building bridges: Lanthanide complexes derived
from the ligand *N*-(2-hydroxyethyliminodiacetic
acid, H₃heidi)**

4.1 Introduction

In chapter 3, it was demonstrated that phosphonic acids bind strongly to lanthanide ions to produce stable hybrid materials. However, it is difficult to isolate crystalline material that can be characterised by single crystal X-ray diffraction. To stabilise the lanthanide ion in solution, softer coordinating groups are required. The carboxylic acid group has a lower electron charge density than phosphonic acids and can also show variable coordination modes. In particular, a set of ligands derived from iminodiacetic acid, H₂ida, are considered. **Scheme 4.1** shows the structure of H₂ida and the related ligands; *N*-(2-hydroxyethyl)iminodiacetic acid, H₃heidi, and 2-hydroxypropane-1,3-diamine-*N,N,N',N'*-tetraacetic acid, H₅hpdta, where the proton has been replaced by an additional alkyl substituent.



Scheme 4.1: Structure of iminodiacetic acid, H₂ida, and its derivatives.

These ligands bear flexible coordination functions and may bind through the O-donors of the carboxylate groups and the central N-donor. The coordination chemistry of these ligands is well developed in some transition metal compounds, particularly the Fe^{III} and Al^{III} systems. The coordination of H₂ida with Fe^{III} and Al^{III} can yield mononuclear M(ida)₂ complexes where two O-donors, one from each carboxylate, and the N-donor on each ligand coordinate to the metal centre.¹ When the ligand-to-metal ratio is varied, larger clusters may be isolated, such as [Fe₆(μ₃-O)₂(μ-OH)₆(ida)₆], where bridging oxo- and hydroxo-functions become important in stabilising the core unit.² This approach can be applied to the H₃heidi and H₅hpdta ligands. If a metal-to-ligand ratio of 1:1 is used for the H₃heidi ligand, discrete [M(Heidi)(H₂O)₂]₂ clusters are obtained, where the addition of the hydroxyethyl arm substitutes the hydroxo- and oxo-bridges for the bridging alkoxo-function of the ligand.³ Changing the Mⁿ⁺:ligand molar ratio to 1:2 results in the much larger Fe^{III} clusters [Fe₁₇(μ₃-O)₄(μ₃-OH)₆(μ-OH)₁₀(Heidi)₈(H₂O)₁₂]³⁺ and [Fe₁₉(μ₃-O)₆(μ₃-OH)₆(μ-OH)₈(Heidi)₁₀(H₂O)₁₂]⁺ and the aluminium cluster [Al₁₃(μ₃-OH)₆(μ-OH)₁₂(Heidi)₆(H₂O)₆]³⁺.^{3, 4} The H₅hpdta ligand produces equally diverse compounds in the Fe^{III} system where neutral dinuclear compounds,¹ tetranuclear clusters^{1, 5} and polynuclear structures with up to nine Fe^{III} centres^{6, 7} may be isolated.

The variable coordination ability of these ligands is promising for stabilising lanthanide ions in solution. Some insight has been gained for lanthanide stabilisation using H₂ida. Higher dimensional hybrid materials are favoured where chains of [Ln(ida)]Cl₂·3H₂O,⁸ 2D layers of [Ln(ida)(H₂O)₄]Cl₂·H₂O⁹ and [Ln₂(ida)₂(C₂O₄)₂(phen)₂]¹⁰ and 3D networks of [Ln(Hida)₂(ida)₂]Cl₂·3H₂O and [Ln(ida)₃] have all been characterised.^{11, 12} In all cases, individual

clusters have not been isolated and the carboxylate O-donors show the ability to form μ_2 -bridges to multiple Ln^{III} centres.

In contrast, the ligand 2-hydroxypropane-1,3-diamine-*N,N,N',N'*-tetraacetic acid, H₃hpdt, has been shown to form small {Ln₂}^{13, 14} and {Ln₄}¹⁵ complexes. When Na⁺ is used as a counter-ion, the binuclear compound Na₄[Nd₂(H₂O)₂(μ_2 -hdpta)₂] is isolated. As in the Fe^{III} systems, a μ_2 -alkoxo bridge forms between each Ln^{III} centre, while the acetate O-donors and coordinated water molecules complete the coordination sphere.¹³ By changing the counter-ion to K⁺ the larger cluster K₈[Nd₄(H₂O)₄(μ_2 -hpdt)₂(μ_3 -hpdt)₂] is isolated, where a familiar {Ln₂} bridged unit is observed through a μ_2 -alkoxo bridges; however, two hpdt ligands further bridge these units to form the tetranuclear cluster.¹⁵

The ligand *N*-(2-hydroxyethyl)iminodiacetic acid, H₃heidi, is relatively unstudied in its reaction with the lanthanides. To date, Na[Ln(Hheidi)(ox)] is the only lanthanide-heidi compound reported and is a layered structure stabilised by a singly protonated Hheidi ligand and oxalate ligands.¹⁶ Whilst using H₂ida results in high dimensional hybrid structures and H₃hpdt results in small clusters, the coordination behaviour of H₃heidi is still largely unknown.

The aim of this chapter is to investigate the coordination chemistry of H₃heidi upon reaction with the lanthanide series. From a structural perspective, H₃heidi can be viewed as an intermediate between H₂ida and H₃hpdt and the coordination behaviour of either ligand system could be accessible. It may be possible to synthesise small isolated clusters and larger hybrid networks that can be used in the design of higher order lanthanide hybrid materials. We also aim to investigate the optical properties of the resulting compounds to gauge the potential of these materials for incorporation of sensitising ligands for development of white-light devices or sensing platforms.

4.2 Cluster chemistry of 2-hydroxyethyliminodiacetic acid, H₃heidi

4.2.1 Crystal structure of Na₂[Eu₂(Hheidi)₄(H₂O)(MeOH)]·3MeOH, (2)

When two molar equivalents of H₃heidi were refluxed with one equivalent of EuCl₃·6H₂O and 18 equivalents of NaN₃ in MeOH, followed by slow cooling and subsequent layering of acetonitrile, small plate crystals of Na₂[Eu₂(Hheidi)₄(H₂O)(MeOH)]·3MeOH, **2**, were isolated and a suitable crystal extracted for single crystal X-ray diffraction.

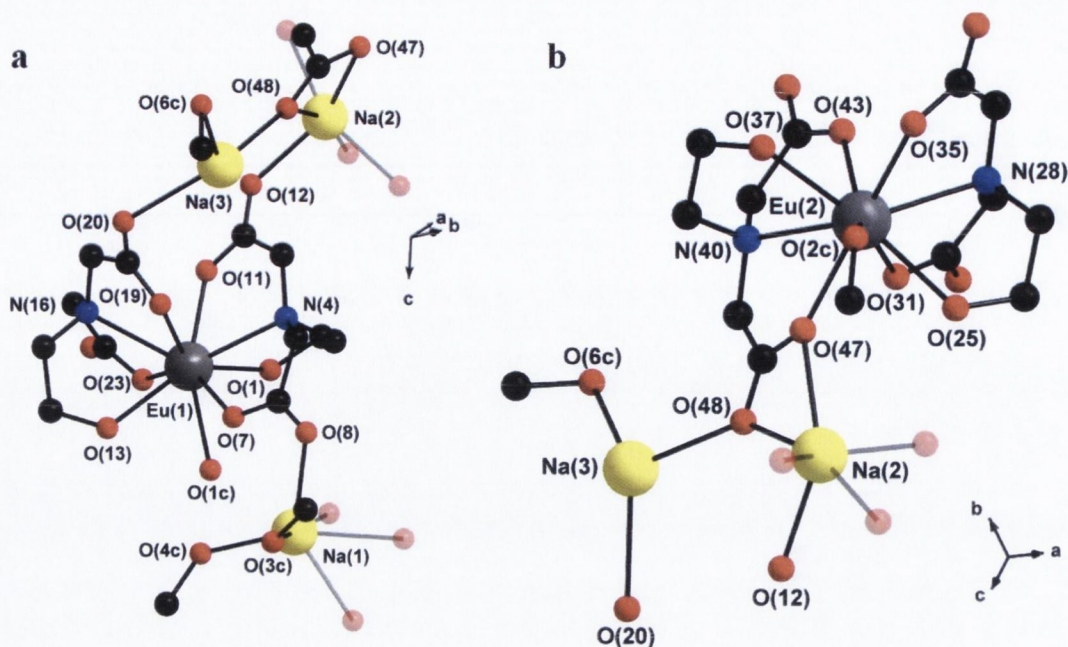


Figure 4.1: Asymmetric unit of $\text{Na}_2[\text{Eu}_2(\text{Hheidi})_4(\text{H}_2\text{O})(\text{MeOH})]$, **2**, showing the coordination around (a) Eu(1) and (b) Eu(2). Eu grey, O red, N blue, C black and Na yellow. H atoms are omitted for clarity.

The compound **2** crystallises in the triclinic crystal system in the space group $P\bar{1}$. The structure consists of mononuclear europium complexes that are connected through space by the Na^+ cations. The asymmetric unit contains two unique Eu^{III} ions, three singly protonated Hheidi ligands and one fully deprotonated heidi ligand, one coordinated H_2O and three MeOH molecules. Both Eu^{III} ions are 9-coordinate bound by two Hheidi ligands and one coordinated H_2O molecule in the case of Eu(1) and a coordinated MeOH molecule to Eu(2) (**Figure 4.1**). The coordination geometries around each Eu^{III} centre may be viewed as distorted capped square antiprisms. The Eu(1) centre is coordinated by two carboxylate, O(7), O(11), O(19), O(23) and two hydroxo O(1) and O(13) oxygen donors of two Hheidi ligands. The coordination sphere is completed by the N-donors N(4) and N(16) of the ligands and a coordinated H_2O , O(1c). The Eu(2) centre is coordinated by two different ligands in a similar fashion through O(25), O(31), O(35), N(28) and O(37), O(43), O(47), and N(40). A coordinated MeOH, O(2c) completes the coordination sphere of Eu(2). To account for charge balance there are three sodium cations. Na(1) is 6-coordinate and the coordination geometry can be best described as a distorted octahedron. The coordination is occupied by carboxylate oxygen donors O(8), O(35'), O(36') and O(44'') from three different Hheidi ligands. Two MeOH molecules, O(3c) and O(4c) complete the coordination sphere. The Na(2) is also 6-coordinate and may be better described as a highly distorted trigonal prism coordinated through six carboxylate oxygen donors O(12), O(23'), O(24'), O(47), O(32'') and O(48) of four Hheidi ligands. Na(3) has three oxygen donors coordinated to it through O(20) and O(48) of two ligands and a coordinated MeOH molecules, O(6c). The Na(3) ion is positioned adjacent to the void within the layer where heavily disordered MeOH molecules were located. To account for this disorder the SQUEEZE routine was run and the complete coordination of Na(3)

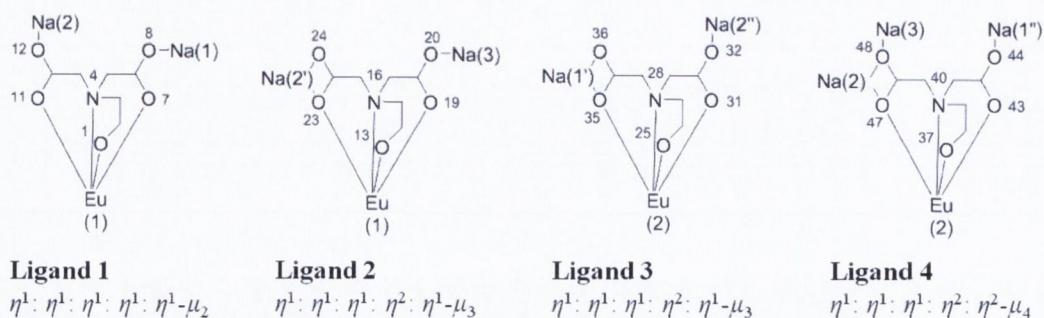
cannot be fully refined. The results from the SQUEEZE routine indicate that up to three additional MeOH molecules are located within this void space.

The Eu-O bond lengths (**Table 4.1**) cover the range 2.376-2.687 Å and the bond length depends on the interaction between oxygen donor and Eu^{III} ion. Shorter bond lengths below 2.4 Å are observed when the oxygen donor forms a μ_2 -bridge between a Eu^{III} and a Na⁺ cation. The Eu-O bonds are seen to increase slightly when they become monodentate in nature. Due to the smaller electrostatic charge of the N-donors, the Eu-N bonds are considerably longer with bond lengths above 2.6 Å.

Table 4.1: Selected bond lengths for **2**.

Bond	Bond Length (Å)	Bond	Bond Length (Å)
Eu(1)-O(1)	2.486(3)	Eu (2)-O(31)	2.409(2)
Eu (1)-O(7)	2.376(3)	Eu (2)-O(35)	2.387(3)
Eu (1)-O(11)	2.387(3)	Eu (2)-N(28)	2.630(3)
Eu (1)-N(4)	2.654(3)	Eu (2)-O(37)	2.475(3)
Eu (1)-O(13)	2.436(3)	Eu (2)-O(43)	2.407(2)
Eu(1)-O(19)	2.409(3)	Eu (2)-O(47)	2.393(3)
Eu (1)-O(23)	2.378(3)	Eu (2)-N(40)	2.639(3)
Eu (1)-N(16)	2.687(3)	Eu(1)-O(1C)	2.520(3)
Eu (2)-O(25)	2.506(3)	Eu(1)-O(2C)	2.478(3)

The four unique ligands coordinate to the Eu^{III} centre in an identical manner, but differ in their bridging modes to Na⁺ cations (**Scheme 4.2**). Around the Eu(1) centre, **Ligand 1** adopts a $\eta^1: \eta^1: \eta^1: \eta^1-\mu_3$ coordination mode to Eu(1) and two Na⁺ cations. The hydroxo-O(1) forms a monodentate bond to Eu(1) and the carboxylate O(7) and O(8) form an *anti, syn* bridge to Eu(1) and Na(1), respectively. The carboxylate O(11) and O(12) donors form an *anti, anti* bridge to Eu(1) and Na(2), respectively. **Ligand 2** bonds to a single Eu^{III} and two Na⁺ centres through a $\eta^1: \eta^1: \eta^1: \eta^2: \eta^1-\mu_3$ coordination mode where the hydroxo-O(13) forms a monodentate bond to Eu(1), while the carboxylate O(19) and O(20) donors form an *anti, syn* bridge to Eu(1) and Na(3), respectively. The additional carboxylate oxygen donors O(23) and O(24) form a chelate-bridging interaction to Eu(1) and Na(2'). The Eu(2) centre is coordinated by **ligand 3** and **ligand 4**. The **ligand 3** molecule has a $\eta^1: \eta^1: \eta^1: \eta^2: \eta^1-\mu_3$ bridging mode forming a monodentate interaction between the hydroxo-O(25) and Eu(2). The carboxylate donors O(31) and O(32) form *anti, anti* bridges to Eu(2) and Na(2''), respectively, leaving the second carboxylate O(35) and O(36) donors to form a bridging-chelate interaction to Eu(2) and Na(1'), respectively. **Ligand 4** coordinates to one Eu^{III} and three Na⁺ centres through a $\eta^1: \eta^1: \eta^1: \eta^2: \eta^2-\mu_4$ bonding description. The hydroxo-O(37) forms a monodentate interaction to Eu(2) and the carboxylate O(43) and O(44) donors form an *anti, anti* bridge to Eu(2) and Na(1''), respectively. The carboxylate O(47) and O(48) donors then adopt a bridging-chelate-bridging mode to Eu(2), Na(2) and Na(3), respectively.



Scheme 4.2: The coordination modes adopted by the four crystallographically unique heidi ligands.

Due to the bridging nature of the heidi ligands to Eu^{III} and Na^+ cations, a chain of alternating $\text{Eu}^{\text{III}}/\text{Na}^+$ polyhedra form along the b -axis (**Figure 4.2a**). The Eu(1) centre bridges to Na(2) through a common vertex, which shares a further common vertex to Eu(2). The Eu(2) is bridged to a Na(1) through a separate common vertex and Na(1) further connects to a symmetry equivalent Eu(1') through a bridging ligand. Through the presence of inversion centres, a double alternating chain of $\text{Eu}^{\text{III}}/\text{Na}^+$ polyhedra extend in the b -axis. These chains are further bridged along the c -axis from Na(2) polyhedra through O(12) to a second $\text{Eu}^{\text{III}}/\text{Na}^+$ double alternating chain forming layers in the bc -plane (**Figure 4.2b**). Within the layers are small 8-membered rings constructed from four Eu^{III} - and four Na^+ -centres (**Figure 4.2c**). The crystal data and structure refinement for **2** is provided in **Table 4.2**.

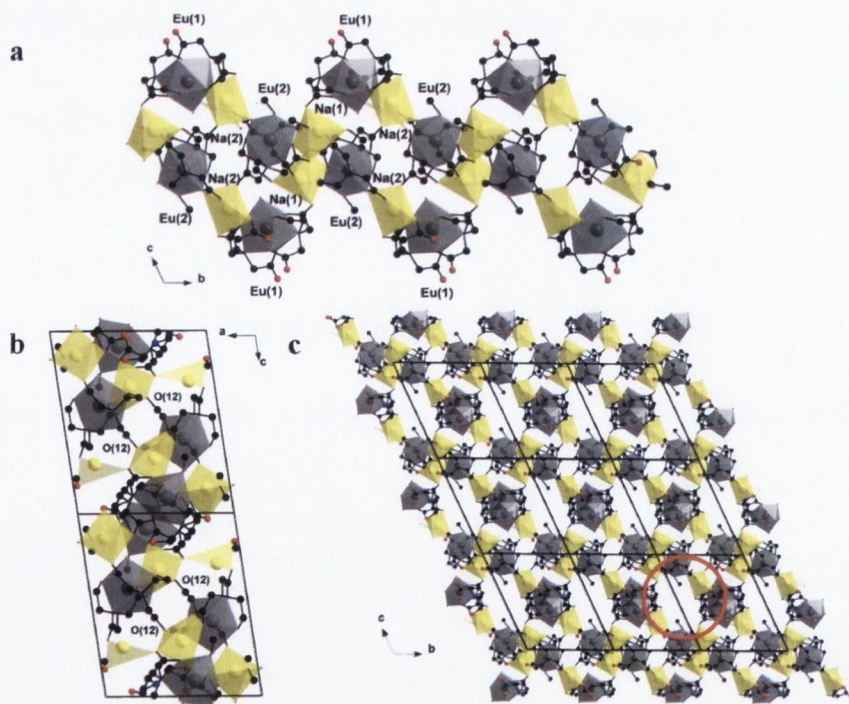


Figure 4.2: (a) Formation of an alternating chain of $\text{Eu}^{\text{III}}/\text{Na}^+$ polyhedra through sharing a common vertex and bridging ligand interactions. (b) Formation of a layer in the bc -plane through the bridging interaction of O(12) to adjacent alternating chains. (c) The layers in **2** as viewed down the a -axis. Eu grey polyhedra, Na yellow polyhedra, O red, N blue and C black. H atoms have been omitted for clarity. The red circle identifies the 8-membered ring voids in the layer.

Table 4.2: Crystal data and structure refinement for **2**.

Identification code	2	
Empirical formula	C ₂₉ H ₄₆ Eu ₂ N ₄ Na ₃ O ₂₅	
Formula weight	1223.59	
Temperature	100(2) K	
Wavelength	0.71073 Å	
Crystal system	Triclinic	
Space group	P-1	
Unit cell dimensions	a = 12.5080(6) Å	α = 114.2650(15)°.
	b = 13.2904(7) Å	β = 93.1120(17)°.
	c = 15.9129(8) Å	γ = 100.6590(19)°.
Volume	2344.8(2) Å ³	
Z	2	
Density (calculated)	1.733 Mg m ⁻³	
Absorption coefficient	2.764 mm ⁻¹	
F(000)	1214	
Crystal size	0.230 × 0.200 × 0.200 mm ³	
Theta range for data collection	1.674 to 27.506°.	
Index ranges	-16 ≤ h ≤ 16, -17 ≤ k ≤ 17, -20 ≤ l ≤ 20	
Reflections collected	120922	
Independent reflections	10759 [R(int) = 0.0375]	
Completeness to theta = 25.242°	99.9 %	
Refinement method	Full-matrix least-squares on F ²	
Data / restraints / parameters	10759 / 25 / 572	
Goodness-of-fit on F ²	1.068	
Final R indices [I > 2σ(I)]	R1 = 0.0278, wR2 = 0.0744	
R indices (all data)	R1 = 0.0351, wR2 = 0.0777	
Extinction coefficient	n/a	
Largest diff. peak and hole	3.186 and -1.546 e.Å ⁻³	

4.2.2 Physicochemical characterisation of **2**

The phase purity of **2** was confirmed through PXRD measurements with the reflections of the calculated powder pattern matching the experimental reflections obtained for the bulk material. An isostructural Tb^{III}-analogue (**2-Tb**) was synthesised and was shown to have the same structure by comparing the PXRD with the Eu^{III}-analogue.

Using FT-IR spectroscopy, common bond stretches from the Heidi ligand were identified. Weak bands from 2971-2863 cm⁻¹ were assigned to alkyl C-H stretches and the characteristic C-N stretch identified at 1255 cm⁻¹. The strong band at 1568 cm⁻¹ is assigned to the asymmetric carboxylate stretch while the symmetric stretch is identified at 1404 cm⁻¹. Using the equation $\Delta = [v_{\text{asym}}(\text{CO}_2^-) - v_{\text{sym}}(\text{CO}_2^-)]$, values ranging from 164-261 cm⁻¹ support the assignment of chelating and bridging interactions from the crystallography. The FT-IR spectra for **2-Eu** and **2-Tb** are identical.

The thermal stability of the structure was investigated by TGA in air. Two major decomposition events occur in the thermogram. An observed weight loss of 9.0% centred at 60 °C can be assigned to the loss of three constitutional MeOH and one H₂O molecule in the layer void

(*calc.* 9.4%). The thermogravimetric event centred at 371 °C is assigned to the decomposition of the four ligand molecules with an observed weight loss of 39.5% (*calc.* 36.3%).

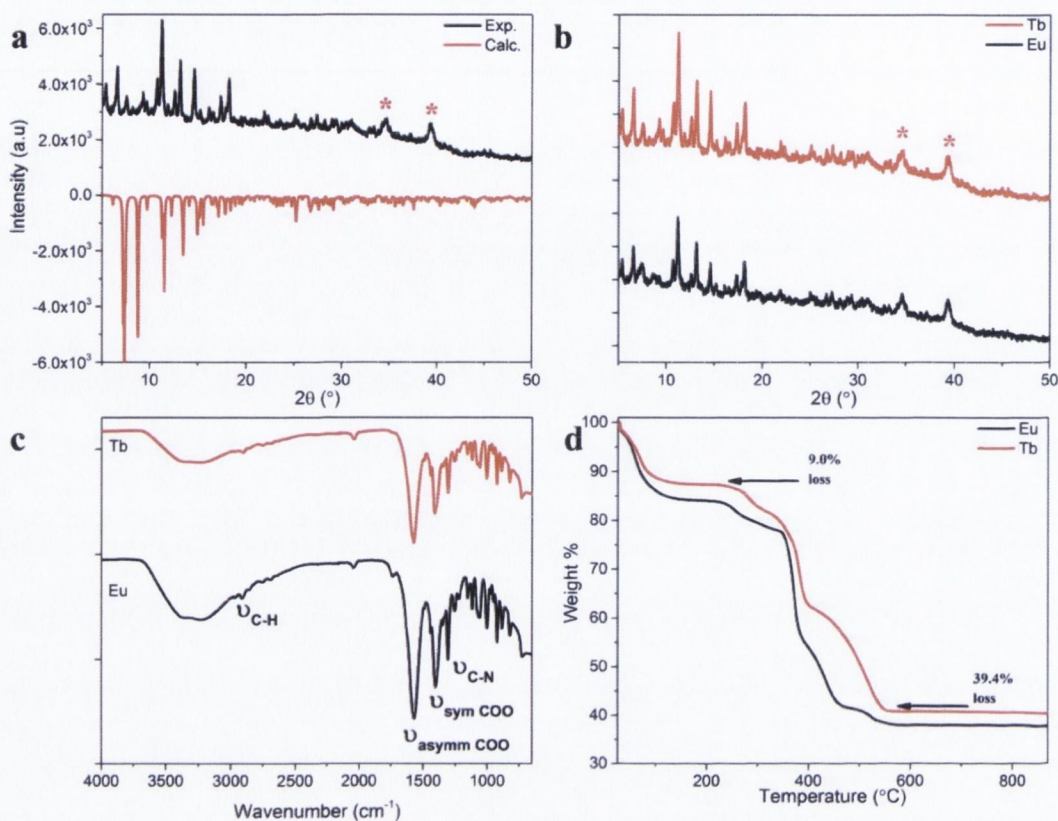


Figure 4.3: (a) Comparison of experimental *versus* calculated PXRD patterns of bulk **2-Eu** indicate phase purity. (b) Comparison of experimental PXRD patterns of **2-Eu** and **2-Tb** indicate they are isostructural materials. (c) FT-IR spectra of **2-Eu** and **2-Tb** and (d) thermograms of **2-Eu** and **2-Tb** in air. * indicate reflections from instrumental artefacts.

4.2.3 Crystal structure of $\text{Na}_2[\text{Eu}(\text{Hheidi})(\text{heidi})(\text{H}_2\text{O})_2] \cdot \text{H}_2\text{O}$, (**3**)

The compound $\text{Na}_2[\text{Eu}(\text{Hheidi})(\text{heidi})(\text{H}_2\text{O})_2] \cdot \text{H}_2\text{O}$, **3**, was synthesised from the reaction of one equivalent of H_3heidi and $\text{EuCl}_3 \cdot 6\text{H}_2\text{O}$ in the presence of NaOH in a $\text{H}_2\text{O}/\text{MeOH}$ solvent system (1:3 v:v). Following stirring the reaction mixture was heated solvothermally at 100 °C for 16 hours followed by slow cooling to room temperature. Upon cooling small plate crystals of **3** were isolated and one selected for characterisation by single crystal X-ray diffraction.

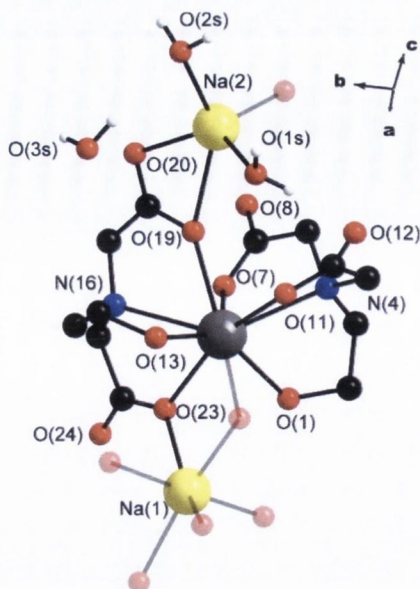
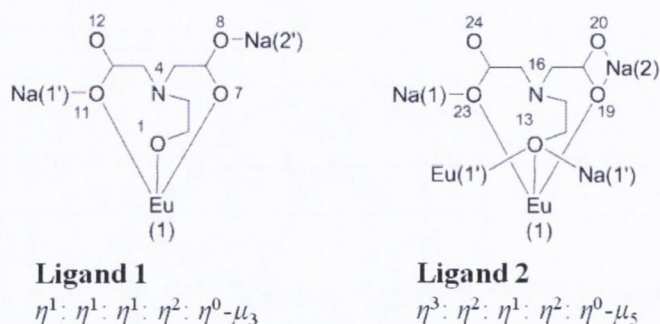


Figure 4.4: The asymmetric unit of $\text{Na}_2[\text{Eu}(\text{Hheidi})(\text{heidi})(\text{H}_2\text{O})_2] \cdot \text{H}_2\text{O}$, **3**. Eu grey, Na yellow, O red, N blue, C black. H atoms are omitted for clarity. Faded atoms represent symmetry generated atoms.

The compound **3** crystallises in the triclinic crystal system in the space group $P\bar{1}$ and consists of a dinuclear $\{\text{Eu}_2\}$ core unit stabilised by the H_3heidi ligand and packs into layers through interactions with the Na^+ cations that balance for charge. The asymmetric unit contains a single Eu(1) ion, one singly protonated Hheidi and one fully deprotonated heidi ligand, two coordinated water molecules and a constitutional water molecule (**Figure 4.4**). The Eu(1) is 9-coordinate through the coordination of the two heidi ligands. The Eu(1) is coordinated by the oxygen donors O(1), O(7) and O(11) of one ligand, O(13), O(19) and O(23) of the second ligand and a further O(13') that comes from a hydroxo-group from a symmetry related Eu(1'). The coordination is completed by N(4) and N(16) of the two ligands. There are two Na^+ cations to charge balance the system. Na(1) is 6-coordinate and may be viewed as being in a distorted octahedral geometry coordinated by O(11'), O(13'), O(19'), O(24'') and O(23) from four different ligand donors and a coordinated water molecule O(1s). The Na(2) ion is 5-coordinate and the coordination geometry can be visualised as a square based pyramid coordinated by O(19), O(20) and O(8') of two distinct ligand molecules. Two water molecules O(1s) and O(2s) complete the coordination sphere.

There are two crystallographically unique ligand molecules in the binuclear complex of **3**. **Ligand 1** has a $\eta^1: \eta^1: \eta^1: \eta^2: \eta^0-\mu_3$ bonding description where O(1) forms a monodentate interaction to Eu(1), whereas the carboxylate donors O(7) and O(8) form an *anti, syn* bridging interaction to Eu(1) and Na(2'), respectively. The donor O(11) forms a μ_2 -bridge between Eu(1) and Na(1). **Ligand 2** presents a $\eta^3: \eta^2: \eta^1: \eta^2: \eta^0-\mu_5$ bonding description, where the hydroxo-O(13) forms a μ_3 -bridge between Eu(1) and Eu(1') to form a dinuclear complex and a further bridge to Na(1). The carboxylate donors O(19) and O(20) form a bridging-chelate interaction to Eu(1) and Na(2), respectively. The carboxylate donor O(23) forms a μ_2 -bridge between Eu(1) and Na(1).



Scheme 4.3: The bonding descriptions adopted by **Ligand 1** and **Ligand 2** in the structure of **3**.

The Eu-O bond lengths are summarised in **Table 4.3**. The bond lengths range between 2.3855–2.5254 Å, depending on the type of interaction. Notably, Eu(1)-O(13) and Eu(1)-O(13') are particularly short, due to the μ_2 -bridging interaction between the ethyl hydroxo O-donor and the two Eu^{III} centres. In contrast, when the similar ethyl hydroxo-O(1) forms the monodentate interaction to Eu(1), a longer bond length of 2.5254 Å is observed, which is similar that reported for lanthanide complexes of 2-hydroxypropane-1,3-diamine-*N,N,N',N'*-tetraacetic acid.¹⁵ Due to the more electrostatic nature of the interaction, the Eu-N bonds are longer, ranging from 2.6350–2.745 Å, in agreement with similar lanthanide complexes.¹³⁻¹⁵

Table 4.3: Selected bond lengths in **3**.

Bond	Bond Length (Å)	Bond	Bond Length (Å)
Eu(1)-O(1)	2.5254(14)	Eu (1)-O(19)	2.4849(13)
Eu (1)-O(7)	2.4261(13)	Eu (1)-O(23)	2.4493(13)
Eu (1)-O(11)	2.4103(13)	Eu (1)-N(4)	2.7452(12)
Eu (1)-O(13)	2.3898(13)	Eu (1)-N(16)	2.6350(16)
Eu (1)-O(13)	2.3855(13)		

The two distinct ligand coordination modes complete the coordination around the Eu(1) centre. The coordination of O(13) is important in forming a μ_3 -bridge between Eu(1) and Eu(1') and a Na(1') centre. In the middle of the binuclear unit is an inversion centre relating the two Eu^{III} centres and ligands by symmetry. As a result, the Eu(1) and Eu(1') share a common edge through O(13) and O(13'). The charge of the binuclear unit is balanced for by the {Na₂O₉} polyhedra where the Na(1) shares a common face with Eu(1) through the oxygen donors O(11), O(13) and O(19). The Na(1) ion also shares a common edge with the symmetry-related Eu(1') through the donor atoms O(13) and O(23'). This results in a Na₄[Eu₂(Hheidi)₂(heidi)₂(H₂O)₄] repeating unit that bridges to adjacent units in the *a*-axis through the carboxylate O(23) and O(24) oxygen donors to Na(1) ions and along the *c*-axis through the donor atoms O(7) and O(8) to Na(2) centres (**Figure 4.5b**). This results in the formation of layers in the *bc*-plane (**Figure 4.6**).

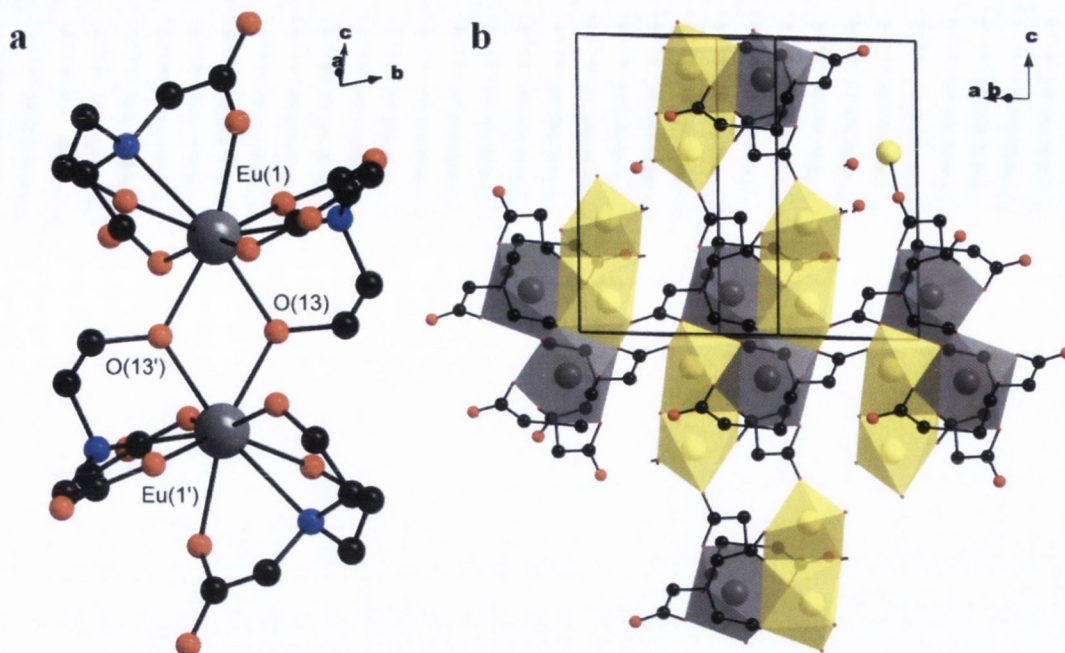


Figure 4.5: (a) Structure of the bridged {Eu₂} dimer through two μ_3 -bridging O(13) donors. (b) The {Eu₂} dimer is stabilised by {Na₂O₉} polyhedra forming a repeating unit through ligand bridges along the *a*- and *c*-axis through the O(7) and O(8) donor atoms.

These layers are further stabilised through interlayer and intralayer hydrogen bonding. Interlayer hydrogen bonds (**Figure 4.6**, blue dashed bonds) form between the constitutional water molecule O(3s) and the carboxylate donors O(12) and O(20) and the coordinated water molecule O(2s). Further hydrogen bonds between layers also form between C(9)-H(9)...O(12) of two ligands in different layers. Intralayer hydrogen bonding (**Figure 4.6**, red dashed bonds) forms between the coordinated water molecules O(1s) and O(2s) and the carboxylate donor atoms O(7), O(8) and O(12). The additional hydrogen bonds C(5)-H(5A)...O(20)#2 and C(14)-H(14B)...O(1)#1 form between ligands in proximity to each other. The hydrogen bond distances (**Table 4.4**) range between 2.739-3.530 Å and result in stabilisation of the layered motif in the structure. The structure refinement and crystal data details are summarised in **Table 4.5**.

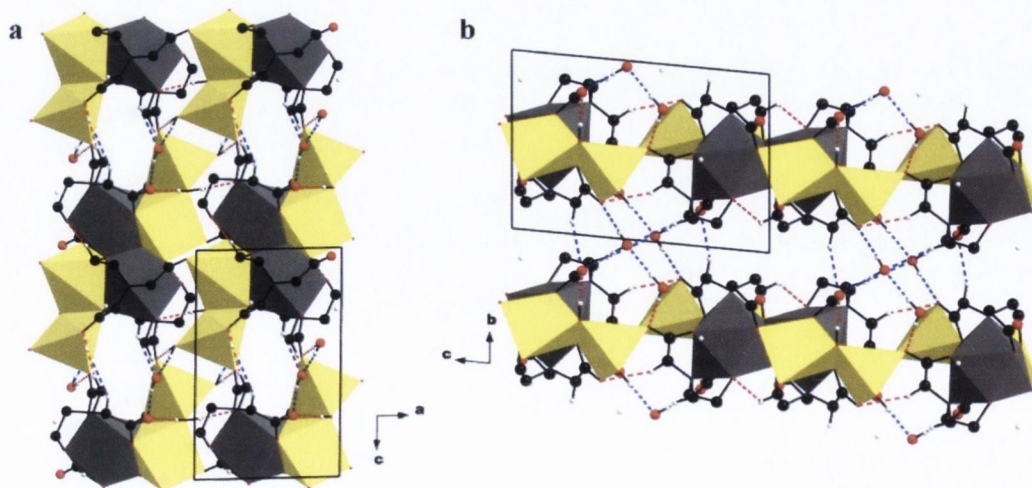


Figure 4.6: Hydrogen bonding in layers of **3** as viewed down (a) the *b*-axis and (b) the *a*-axis.

Table 4.4: Selected hydrogen bond distances in **3**.

	Donor-Acceptor Distance (Å)		Donor-Acceptor Distance (Å)
O(3S)-H(3C)...O(12)#2	2.798(2)	O(1S)-H(1C)...O(12)	2.739(2)
O(3S)-H(3D)...O(20)#6	2.828(2)	O(1S)-H(1D)...O(7A)#4	2.7914(19)
O(2S)-H(2D)...O(3S)#4	2.765(2)	O(2S)-H(2C)...O(8A)#4	2.840(2)
C(9)-H(9A)...O(3S)#5	3.530(3)	C(5)-H(5A)...O(20)#2	3.514(2)
C(17)-H(17A)...O(12)#7	3.406(2)	C(14)-H(14B)...O(1)#1	3.122(2)

Table 4.5: Crystal data and structure refinement for **3**.

Identification code	3	
Empirical formula	C ₁₂ H ₂₁ EuN ₂ Na ₂ O ₁₃	
Formula weight	599.25	
Temperature	100(2) K	
Wavelength	0.71073 Å	
Crystal system	Triclinic	
Space group	P-1	
Unit cell dimensions	a = 8.7398(6) Å	$\alpha = 84.8900(11)^\circ$.
	b = 9.6611(6) Å	$\beta = 89.7047(10)^\circ$.
	c = 12.7638(9) Å	$\gamma = 66.5894(9)^\circ$.
Volume	984.54(11) Å ³	
Z	2	
Density (calculated)	2.021 Mg m ⁻³	
Absorption coefficient	3.300 mm ⁻¹	
F(000)	592	
Crystal size	0.260 × 0.210 × 0.180 mm ³	
Theta range for data collection	1.603 to 26.043°.	
Index ranges	-10 ≤ h ≤ 10, -11 ≤ k ≤ 11, -14 ≤ l ≤ 15	
Reflections collected	6782	
Independent reflections	3732 [R(int) = 0.0072]	
Completeness to theta = 25.242°	96.9%	
Refinement method	Full-matrix least-squares on F ²	
Data / restraints / parameters	3732 / 6 / 295	
Goodness-of-fit on F ²	1.160	
Final R indices [I > 2σ(I)]	R1 = 0.0133, wR2 = 0.0350	
R indices (all data)	R1 = 0.0134, wR2 = 0.0350	
Extinction coefficient	n/a	
Largest diff. peak and hole	0.972 and -0.443 e.Å ⁻³	

4.2.4 Physicochemical characterisation of **3**

The PXRD pattern of **3-Eu** showed that the bulk material is phase pure through the agreement of the experimental reflections against those calculated from the structure model discussed above (**Figure 4.7a**). Further to this, it was possible to synthesise the Nd^{III}-analogue, **3-Nd**, which was shown to be isostructural to **3-Eu** by PXRD (**Figure 4.7b**).

Using FT-IR spectroscopy the characteristic C-N stretch of the ligand at 1255 cm⁻¹, along with C-H stretching bands at 2971-2840 cm⁻¹ from the ligand backbone were identified (**Figure**

4.7c). The carboxylate stretches give rise to two bands. Asymmetric stretching was assigned to bands at 1599 and 1576 cm^{-1} , while the symmetric stretches occur between 1413-1344 cm^{-1} . By applying the equation, $\Delta=[v_{\text{asym}}(\text{CO}_2^-)-v_{\text{sym}}(\text{CO}_2^-)]$, values in the range $\Delta=163\text{-}255 \text{ cm}^{-1}$ were calculated and complement the crystallographic identification of bridging and chelating interactions between the carboxylate to the metal centres.

The thermal stability in air was studied using TGA and revealed two main thermogravimetric events (**Figure 4.7d**). An early weight loss of 8.5% centred at 110 $^{\circ}\text{C}$ was assigned to the loss of three coordinated water molecules (*calc.* 9.0%). The material remained stable up to 300 $^{\circ}\text{C}$ where the decomposition of the ligand at 368 $^{\circ}\text{C}$ resulted in the a weight loss of 40.4% (*calc.* 36.7%).

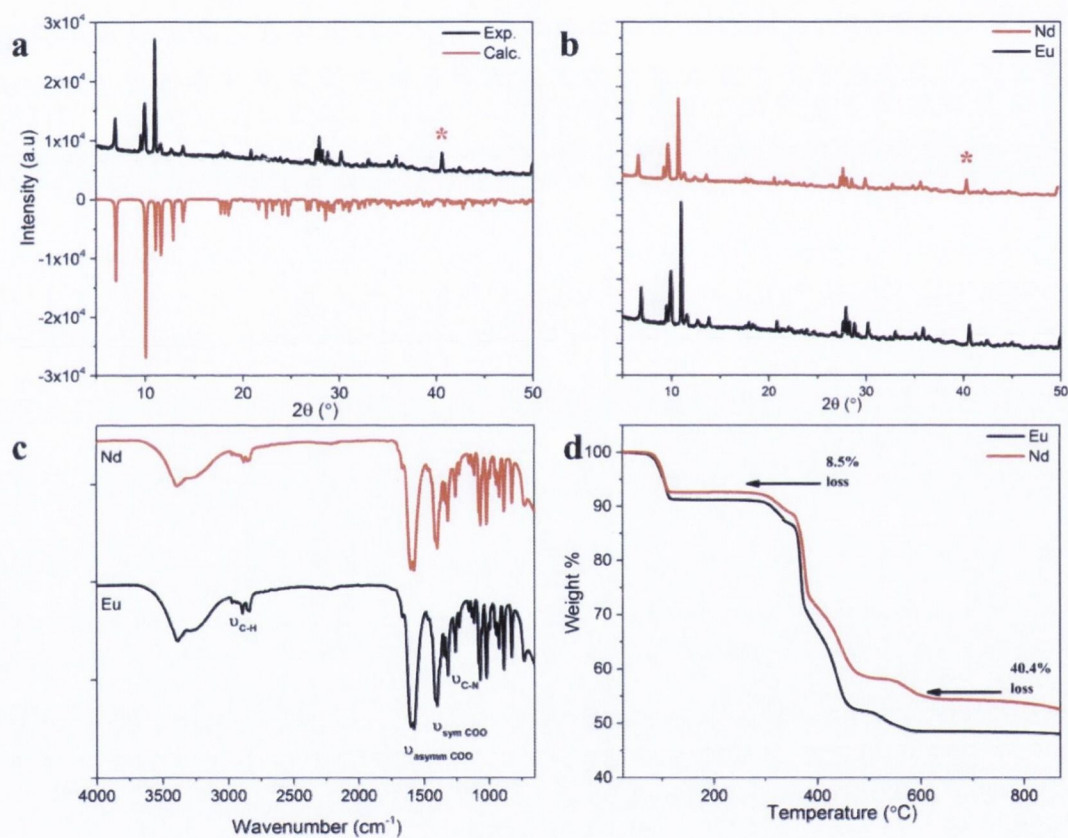


Figure 4.7: (a) Comparison of experimental *versus* calculated PXRD patterns of bulk **3-Eu** indicate phase purity. (b) Comparison of experimental PXRD patterns for the isostructural **3-Eu** and **3-Nd** materials. (c) FT-IR spectra for **3-Eu** and **2-Nd** and (d) thermograms of **3-Eu** and **3-Nd** in air. * indicate reflections from instrumental artefacts.

4.3 Solid-state and solution emission studies of lanthanide-heidi complexes: Understanding complex stability in solution

To probe the environment of the lanthanide centres, the steady-state and time-resolved emission properties of the **2-Ln** and **3-Ln** series were studied in both the solid-state and in solution.

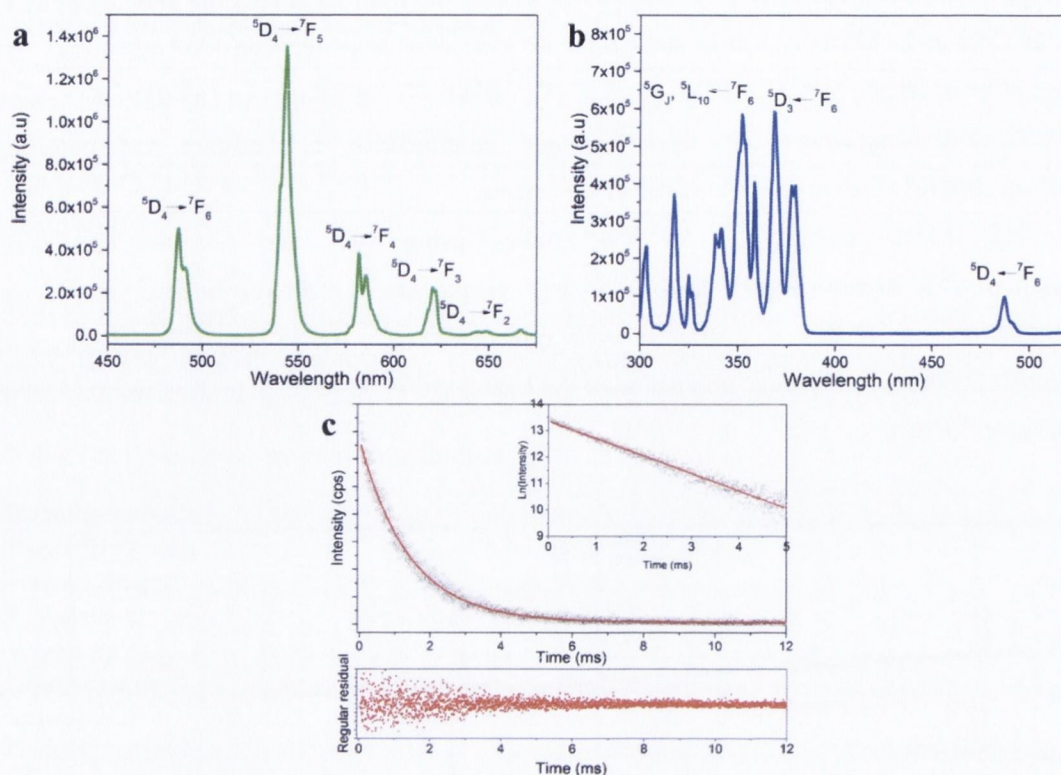


Figure 4.8: (a) Solid-state PL spectrum of mononuclear **2-Tb** under direct excitation ($\lambda_{\text{ex}} = 377 \text{ nm}$, ${}^5\text{D}_3 \leftarrow {}^7\text{F}_6$). (b) Corresponding excitation spectrum ($\lambda_{\text{em}} = 544 \text{ nm}$, ${}^5\text{D}_4 \rightarrow {}^7\text{F}_5$). (c) Emission decay curve (open symbols) and monoexponential fit (red line) for **2-Tb** in the solid-state ($\lambda_{\text{ex}} = 377 \text{ nm}$, $\lambda_{\text{em}} = 544 \text{ nm}$). **Inset:** Ln (intensity) vs. time linear fit supporting a single exponential fit to the decay data.

In the solid-state, upon excitation into the Tb^{III} centre, emission in the range 450–670 nm is observed for the mononuclear **2-Tb**, which arises from ${}^5\text{D}_4 \rightarrow {}^7\text{F}_J$ transitions ($J = 6-2$) (**Figure 4.8a**). The same emission bands are also observed in aqueous solution, with some loss in the resolution of the line splitting due to interaction with the solvent. The excitation spectrum was measured monitoring the ${}^5\text{D}_4 \rightarrow {}^7\text{F}_5$ transition and shows metal-centred excitation bands from the ground state, ${}^5\text{D}_4$, to the ${}^5\text{D}_3$, ${}^5\text{L}_{10}$ and ${}^5\text{G}_J$ excited states (**Figure 4.8b**). The characteristic emission can be observed when excited into these levels. The solid-state emission quantum yield of **2-Tb** is reasonable at $\Phi_{\text{PL}} = 7.7\%$ and the observed emission lifetime (determined from a monoexponential fit to the emission decay) was found to be $\tau_{\text{obs}} = 1.40 \pm 0.07 \text{ ms}$ (**Figure 4.8c**).

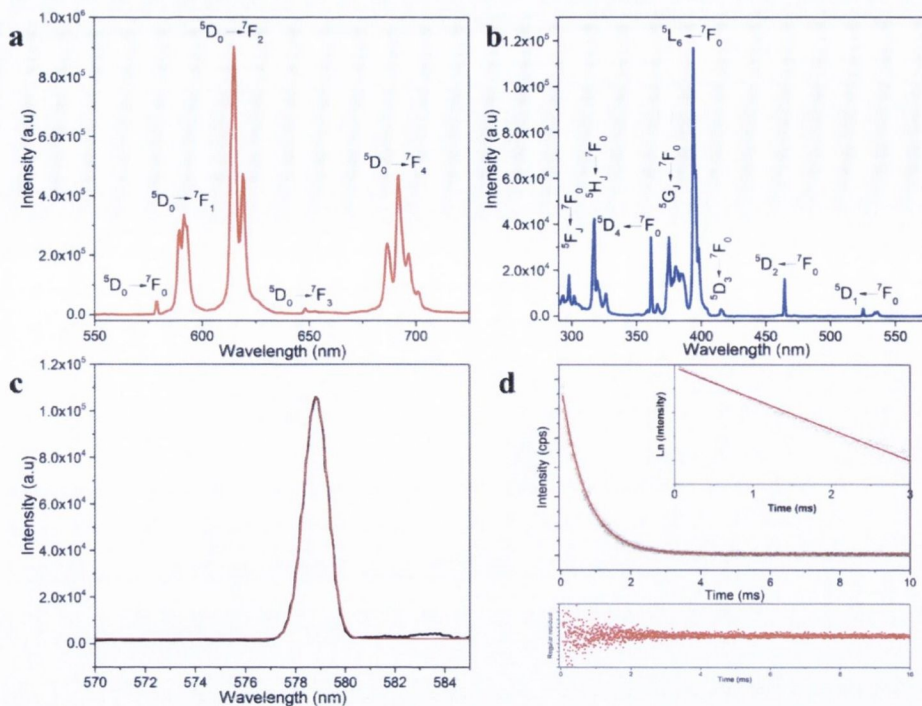


Figure 4.9: (a) Solid-state PL spectrum of **2-Eu** under direct excitation ($\lambda_{\text{ex}} = 394 \text{ nm}$, ${}^5\text{L}_6 \leftarrow {}^7\text{F}_0$). (b) Corresponding excitation spectrum ($\lambda_{\text{em}} = 615 \text{ nm}$, ${}^5\text{D}_0 \rightarrow {}^7\text{F}_2$). (c) Experimental trace of the ${}^5\text{D}_0 \rightarrow {}^7\text{F}_0$ transition (black line) and the Gaussian deconvolution fit to a single peak (red line) indicating one Eu^{III} site. (d) Emission decay curve (open symbols) and monoexponential fit (red line) for **2-Eu** in the solid-state ($\lambda_{\text{ex}} = 394 \text{ nm}$, $\lambda_{\text{em}} = 615 \text{ nm}$). **Inset:** Ln (intensity) vs. time linear line fit supporting a single exponential fit to the decay data.

The photophysical analysis of the Eu^{III} -analogues of the mononuclear (**2-Eu**) and binuclear (**3-Eu**) complexes provide further insight into the stability. When **2-Eu** is excited directly into the Eu^{III} centre in the solid-state, a red PL is observed from the ${}^5\text{D}_0 \rightarrow {}^7\text{F}_J$ transitions ($J = 0-4$) in the range 550-725 nm. No additional emission bands are observed from the ${}^5\text{D}_1$ manifold indicating that relaxation from the higher excited states is efficient (**Figure 4.9a**). A distinct splitting pattern for the ${}^5\text{D}_0 \rightarrow {}^7\text{F}_J$ transitions ($J = 1, 2$ and 4) into three, two and four bands at the resolution of the measurement is observed. Gaussian deconvolution of the ${}^5\text{D}_0 \rightarrow {}^7\text{F}_0$ revealed a single component at 578.8 nm (**Figure 4.9c**). The crystal structure indicates that there are two unique Eu^{III} centres which differ in the nature of the coordinating solvent (water or MeOH molecule). Because the coordination environment of the Eu(1) and Eu(2) centres are very similar and both are coordinated by a solvent molecule with a O-H group present, the value of the separate ${}^5\text{D}_0 \rightarrow {}^7\text{F}_0$ band of each Eu^{III} centre are too close to be differentiated. The corresponding excitation spectrum for **2-Eu** monitored in the ${}^5\text{D}_0 \rightarrow {}^7\text{F}_2$ manifold identifies excitation bands in the Eu^{III} centre from the ground state ${}^7\text{F}_0$ to the ${}^5\text{D}_{4-1}$, ${}^5\text{G}_{2-6}$, ${}^5\text{L}_6$, ${}^5\text{H}_J$ and ${}^5\text{F}_J$ excited states (**Figure 4.9b**). The emission quantum yields in the solid-state were determined to be $\Phi_{\text{PL}} = 8.7\%$ under excitation at $\lambda_{\text{ex}} = 393 \text{ nm}$. The observed emission lifetime was determined from a monoexponential fit to the emission decay to give a value of $\tau_{\text{obs}} = 0.69 \pm 0.04 \text{ ms}$. The emission lifetime was used to determine the number of coordinated water molecules, n_{w} , using the equation:

$$n_w = 1.11 \left[\frac{1}{\tau_{obs}} - k_{rad} - 0.31 \right] \quad \text{Eqn. 4.1}$$

where τ_{obs} is the observed lifetime and k_r is the radiative rate constant. For **2-Eu** k_r was determined as 1.456 ms^{-1} (from **Eqn. 1.3**) and when substituted into **Eqn. 4.1**, the number of coordinated water molecules, $n_w = 0.97$ is calculated, which clearly supports the crystallographic data. In aqueous solution, the PL spectrum was found to match the solid-state material with some slight broadening of the emission bands, however, the same band splitting is still observed. This suggests that the ligand coordination in the mononuclear $[\text{Eu}(\text{Hheidi})(\text{heidi})(\text{H}_2\text{O})]^{2-}$ moiety remains the same. The emission lifetimes were measured in H_2O and D_2O after initial dissolution and repeated 12 hours later. The lifetime in H_2O at $\tau_{obs} = 0.41 \pm 0.02 \text{ ms}$ is shorter than the solid-state due to quenching by O-H oscillators from the solvent. As expected, the observed lifetime is longer in D_2O ($\tau_{obs} = 2.49 \pm 0.09 \text{ ms}$). Using these values, the number of water molecules is determined to be, $n_w = 1.89$, which suggests that although the Eu^{III} centre maintains the ligand coordination, in solution, the coordination sphere expands to accommodate a second coordinated water molecule, forming a slightly different stable species in solution with the formula, $[\text{Eu}(\text{Hheidi})(\text{heidi})(\text{H}_2\text{O})_2]^{2-}$. After 12 hours, the observed lifetimes were $\tau_{obs} = 0.41 \pm 0.02 \text{ ms}$ (H_2O) and $\tau_{obs} = 2.52 \pm 0.09 \text{ ms}$ (D_2O) showing no significant change in the n_w . This suggests that the modified $[\text{Eu}(\text{Hheidi})(\text{heidi})(\text{H}_2\text{O})_2]^{2-}$ species remains stable in solution. This provides insight into the potential of this H_3heidi for stabilisation of lanthanide ions in solution and will be considered in **Chapter 6** where H_3heidi is used to aid coordination of additional organic ligands to lanthanides.

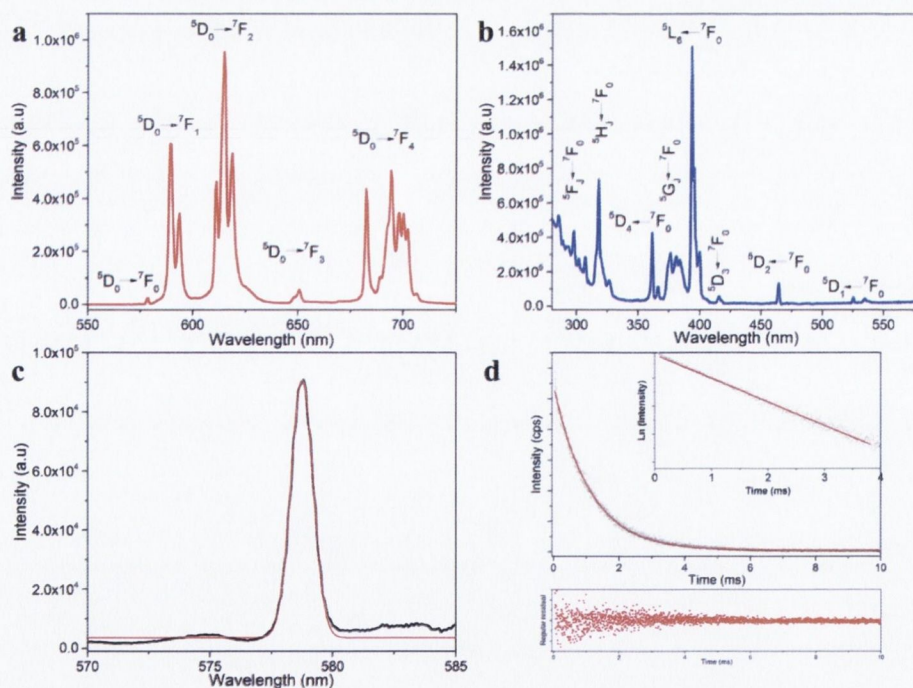


Figure 4.10: (a) Solid-state PL spectrum of binuclear **3-Eu** under direct excitation ($\lambda_{ex} = 393.5 \text{ nm}$, $^5\text{L}_6 \leftarrow ^7\text{F}_0$). (b) Corresponding excitation spectrum ($\lambda_{em} = 615 \text{ nm}$, $^5\text{D}_0 \rightarrow ^7\text{F}_2$). (c) Experimental trace of the $^5\text{D}_0 \rightarrow ^7\text{F}_0$ transition (black line) and the Gaussian deconvolution fit to a single peak (red line) indicating one Eu^{III} site. (d) Emission decay curve (open symbols) and monoexponential fit (red line) for **3-Eu** in the solid-state ($\lambda_{ex} = 393.5 \text{ nm}$, $\lambda_{em} = 615 \text{ nm}$). **Inset:** $\text{Ln}(\text{intensity})$ vs. time linear fit supporting a single exponential fit to the decay data.

The binuclear complex, **3-Eu**, also displays emission bands in the range 550-720 nm arising from $^5D_0 \rightarrow ^7F_J$ transitions ($J = 0-4$) upon direction excitation of the metal centre. Due to the different coordination environment of **3-Eu**, the splitting of the $^5D_0 \rightarrow ^7F_J$ transitions ($J = 1, 2$ and 4) into two, three and seven bands can be observed. No emission from the higher 5D_1 excited state suggesting efficient relaxation into the 5D_0 manifold (**Figure 4.10a**). The $^5D_0 \rightarrow ^7F_0$ transition was deconvoluted using a single Gaussian band centred at 578.5 nm, supporting a single Eu^{III} environment in the crystal structure (**Figure 4.10c**). The excitation spectrum while monitoring the $^5D_0 \rightarrow ^7F_2$ transition ($\lambda_{\text{em}} = 615$ nm) indicates transitions from the ground state into the 7F_0 to the 5D_J ($J = 1-4$), 5G_J ($J = 2-6$), 5L_6 , 5H_J and 5F_J excited states. Direct excitation into these transitions also yielded the characteristic Eu^{III} PL spectrum. The emission quantum yield for **3-Eu** was determined to be $\Phi_{\text{PL}} = 11.9\%$ and the observed emission lifetime in the solid-state was $\tau = 1.10 \pm 0.06$ ms (monoexponential decay fit). The increased lifetime and improvement in the emission quantum yield reflect the absence of a coordinated water molecule. Using **Eqn. 4.1** the n_w value was determined as $n_w = 0.37$ and the slightly elevated value above zero suggests that the two μ_2 -OH bridges between the Eu^{III} centres provide an additional non-radiative pathway. Following sonication, the binuclear **3-Eu** dissolved in aqueous solution and the PL properties were investigated. When excited into the $^5L_6 \rightarrow ^7F_0$ excited state, the emission spectrum resembles that of the mononuclear, **2-Eu**, discussed above, and was observed by the change in the Stark splitting of the $^5D_0 \rightarrow ^7F_J$ transitions ($J = 1, 2$ and 4) to match that of **2-Eu**. The emission lifetime in H_2O determined to be $\tau_{\text{obs}} = 0.42 \pm 0.02$ ms, which matches that measured for **2-Eu** under comparable conditions. This indicates that in dissolving the binuclear **3-Eu**, the μ_2 -OH bridges are broken and the excess of solvent water in the system favours the formation of the mononuclear complex. This indicates that in solution there is a stable species and in synthesising new clusters, the synthetic conditions need to be varied in terms of solvent and pressure as shown by the isolation of the binuclear **3-Eu**. The summary of the emission quantum yield and lifetime measurements for **2-Ln** and **3-Ln** are provided in **Table 4.6**.

Table 4.6: Optical properties determined for **2-Ln** and **3-Ln** including the emission quantum yield, Φ_{PL} , observed lifetime emission lifetime (in solid-state), τ_{ss} , observed emission lifetime in H_2O and D_2O , $\tau_{\text{H}_2\text{O}}$ and $\tau_{\text{D}_2\text{O}}$, respectively, and the number of water molecules in the first coordination sphere, n_w .

Name	Φ_{PL} (%)	τ_{ss} (ms)	$\tau_{\text{H}_2\text{O}}$ (ms)	$\tau_{\text{D}_2\text{O}}$ (ms)	n_w
2-Eu	8.7 (solid-state)	0.69 ± 0.04	0.42 ± 0.02	2.49 ± 0.09	0.97 solid-state
+12 hours			0.41 ± 0.02	2.52 ± 0.09	1.89 aq
3-Eu	11.9 (solid-state)	1.10 ± 0.06	0.43 ± 0.02		
2-Tb	7.7 (solid-state)	1.40 ± 0.07			

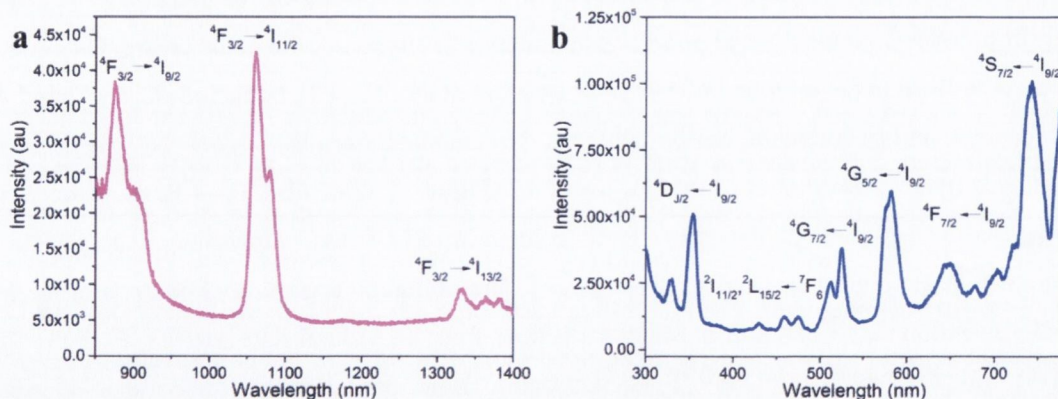


Figure 4.11: (a) Solid-state PL spectrum of binuclear **3-Nd** under direct excitation ($\lambda_{\text{ex}} = 582 \text{ nm}$, ${}^4G_{5/2} \leftarrow {}^4I_{9/2}$). (b) Corresponding excitation spectrum ($\lambda_{\text{em}} = 1061 \text{ nm}$, ${}^4F_{3/2} \rightarrow {}^4I_{11/2}$).

Direct excitation of the binuclear complex **3-Nd** results in characteristic Nd^{III} emission in the NIR region (**Figure 4.11a**) arising from the ${}^4F_{3/2} \rightarrow {}^4I_{J/2}$ ($J = 9, 11, 13$). Under the same slit widths and excitation wavelength, it is noted that the absolute emission intensity is weaker than that observed for the Nd-phosphonates reported in **Chapter 3** and may be due to the lack of a ligand sensitisation pathway. When the emission maximum of the ${}^4F_{3/2} \rightarrow {}^4I_{11/2}$ transition is monitored, the excitation spectrum in the visible range displays excitation bands from the ground state ${}^4I_{9/2}$ to the ${}^4S_{7/2}$, ${}^4F_{7/2}$, ${}^4G_{J/2}$ ($J = 5, 7$), ${}^2L_{15/2}$, ${}^2I_{11/2}$ and ${}^4D_{J/2}$ excited states (**Figure 4.11b**).

Lanthanide ions that emit in the NIR are promising agents for imaging of cells.¹⁷⁻²⁰ The addition of a sensitising organic moiety ensures that the lanthanide remains emissive and the NIR emission ensures that autofluorescence does not interfere with the measurement. In the case of a NIR metal organic framework, it was shown that the high density of Yb^{III} ions in the structure was favourable to a strong NIR response in cell tissues.²⁰ The synthesis of these binuclear complexes shows that lanthanide centres can be brought in closer proximity to one another through μ_2 -bridging interactions. If the iminodiacetic acid group is attached onto aromatic backbones and synthetic conditions found to promote μ_2 -bridging interactions, with the potential to sensitise NIR emission from the lanthanides, a new group of hybrid materials may be accessible that could be investigated as imaging agents in cells and other media. This concept will be considered further in **Chapter 5**.

4.4 Conclusions and Outlook

The ligand H_3heidi has been used to synthesise two novel lanthanide complexes. The ligand coordination in both complexes is similar where the three arms of the ligand coordinate to the lanthanide centre providing a coordination sphere that minimises multiple water molecules coordinating to the lanthanide centre. We show that by controlling the solvent system, base strength and by increasing the synthetic pressure conditions we can favour complexes where multiple Ln^{III} centres are bridged by the formation of μ_2 -hydroxo-bridges. The PL properties of the resulting complexes have been studied. With a particular focus on the Eu^{III} -analogues of these materials, the mononuclear species has been identified to favourably form in solution, as

demonstrated when binuclear **3-Eu** is dissolved in water. This shows that in solution two ligands favourably coordinate around the lanthanide centre. This is a particularly useful situation when a second ligand is intended to coordinate to the lanthanide centre as it must gradually displace the heidi ligand and so favour slow crystallising conditions. This approach to crystallisation will be exploited in **Chapter 6**.

Through direct excitation of the Ln^{III} centre, the emission quantum yields of the Eu^{III}- and Tb^{III}-complexes are reasonable at *ca.* 10%, and these properties could be improved by the inclusion of the iminodiacetic acid moiety onto an aromatic backbone, where sensitisation could be used to improve the PL efficiency. By combining an aromatic sensitiser and the bridging nature of the ligand to lanthanide centres, it may be possible to synthesise hybrid materials that are 2D or 3D in nature with a high density of lanthanide centres. If a material has a high density of NIR-emitting lanthanide centres coupled with sensitisation to improve the PL properties, they may be envisioned for applications in cell imaging. This idea is considered further in **Chapter 5**.

4.5 References

1. W. Schmitt, P. A. Jordan, R. K. Henderson, G. R. Moore, C. E. Anson and A. K. Powell, *Coord. Chem. Rev.*, 2002, **228**, 115-126.
2. C. J. Harding, R. K. Henderson and A. K. Powell, *Angew. Chem. Int. Ed.*, 1993, **32**, 570-572.
3. S. L. Heath, P. A. Jordan, I. D. Johnson, G. R. Moore, A. K. Powell and M. Helliwell, *J. Inorg. Biochem.*, 1995, **59**, 785-794.
4. S. L. Heath and A. K. Powell, *Angew. Chem. Int. Ed.*, 1992, **31**, 191-193.
5. W. Schmitt, C. E. Anson, R. Sessoli, M. van Veen and A. K. Powell, *J. Inorg. Biochem.*, 2002, **91**, 173-189.
6. W. Schmitt, C. E. Anson, W. Wernsdorfer and A. K. Powell, *Chem. Commun.*, 2005, 2098-2100.
7. W. Schmitt, L. Zhang, C. E. Anson and A. K. Powell, *Dalton Trans.*, 2010, **39**, 10279-10285.
8. A. Oskarsson, *Acta Chem. Scand.*, 1971, **25**, 1206-1216.
9. J. R. Li, Z. M. Wang, C. H. Yan, L. P. Zhou and T. Z. Jin, *Acta Crystallogr., Sect. C: Cryst. Struct. Commun.*, 1999, **55**, 2073-2075.
10. H. L. Dong and L. Xu, *Inorg. Chem. Commun.*, 2006, **9**, 379-382.
11. J. Albertss and A. Oskarsson, *Acta Chem. Scand. A*, 1974, **A 28**, 347-355.
12. C. Kremer, P. Morales, J. Torres, J. Castiglioni, J. Gonzalez-Platas, M. Hummert, H. Schumann and S. Dominguez, *Inorg. Chem. Commun.*, 2008, **11**, 862-864.
13. Y. Miyashita, M. Sanada, Y. Yamada, K. Fujisawa and K. Okamoto, *Chem. Lett.*, 2002, **31**, 840-841.
14. G. Tircso, A. Benyei, E. Brucher, A. Kis and R. Kiraly, *Inorg. Chem.*, 2006, **45**, 4951-4962.
15. Y. Miyashita, M. Sanada, M. M. Islam, N. Amir, T. Koyano, H. Ikeda, K. Fujisawa and K. Okamoto, *Inorg. Chem. Commun.*, 2005, **8**, 785-788.
16. L. Zhao, S. Y. Lin, S. Shen and J. K. Tang, *Inorg. Chem. Commun.*, 2011, **14**, 1928-1931.
17. S. V. Eliseeva and J. C. G. Bunzli, *Chem. Soc. Rev.*, 2010, **39**, 189-227.
18. J. C. G. Bunzli and S. V. Eliseeva, *Chem. Sci.*, 2013, **4**, 1939-1949.
19. F. Caille, C. S. Bonnet, F. Buron, S. Villette, L. Helm, S. Petoud, F. Suzenet and E. Toth, *Inorg. Chem.*, 2012, **51**, 2522-2532.
20. A. Foucault-Collet, K. A. Gogick, K. A. White, S. Villette, A. Pallier, G. Collet, C. Kieda, T. Li, S. J. Geib, N. L. Rosi and S. Petoud, *Proc. Natl. Acad. Sci. U.S.A.*, 2013, **110**, 17199-17204.

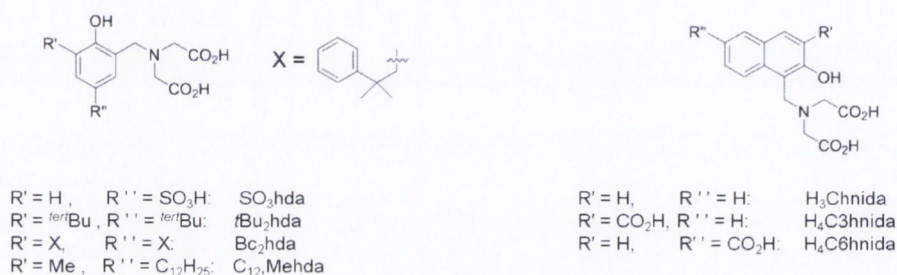
Chapter Five

.....
**Synthesis and characterisation of novel lanthanide-
organic hybrid materials using iminodiacetic acid
substituted aromatic ligands**

5.1 Introduction

In chapter 4 we successfully characterised new lanthanide clusters derived from the ligand *N*-(2-hydroxyethyl)iminodiacetic acid, H₃heidi. We have shown, through careful choice of the base, solvent and pressure conditions of the reaction, that we can tune the nature of the bridging bonds from monodentate or chelating interactions, to bridging interactions between multiple lanthanide centres.

Having established the coordination and PL properties of these clusters, we wanted to combine the flexible coordination of the iminodiacetate group with the potential to sensitise lanthanide PL through an aromatic platform and take the first steps towards identifying new lanthanide-organic hybrid materials that will have optical properties suitable for advanced optical applications such as sensing and white-lighting.



Scheme 5.1: The library of iminodiacetic acid substituted naphthol- and phenol-type ligands discussed below.

A library of iminodiacetic acid substituted naphthol- and phenol-type ligands have been studied with different metal ions (**Scheme 5.1**). Fe^{III} complexes have previously been isolated using these ligands with resulting 2D and 3D architectures in which the hydrophobic aromatic backbone influences the final structure.¹⁻⁵ Using the substituted naphthol, H₄C3hnida, results in the dense honeycomb structure of Na₆[Fe₂(μ-O)(μ-CO₃)(C3hnida)₂] where the iron dinuclear unit crystallises into a honeycomb motif through bridging Na⁺ cations.¹ The Fe^{III} and Na⁺ ions sit in the walls of the structure and the hydrophobic naphthyl moieties occupy the channel space forming a dense network.¹ Changing the ligand to the substituted phenol, SO₃hda, the addition of the sulfonic group results in an open framework K₆[Fe₂(μ-O)(μ-CO₃)(SO₃hda)₂] that retains the honeycomb motif.² The presence of the sulfonic group forces the ligand to align within the walls of the network to produce the open framework. This approach can also be expanded to other metal ions. For example, by reaction of Cu^{II} with the naphthol, H₃hnida, dense honeycomb networks of K₂[Cu^{II}(hnida)₂]·2H₂O are isolated.³ Modifying the ligand to have an extra carboxylic acid group in the 6-position allowed the structure to be tuned from the 3D honeycomb framework to a layered-pillared 3D structure, where the additional carboxylic acid group orientates the ligand so that layers of K₄[(Cu^{II}(C6hnida))₂]·4H₂O·4MeOH are pillared by the ligand.³

Utilising phenol-type ligands with bulky side groups produces the layered hybrid materials [(Fe(*t*Buhda)(H₂O)₂)₂]·3H₂O,⁴ [(Fe(Bchda)(H₂O)(MeOH))]·4H₂O and

$[(\text{Fe}(\text{C}_{12}\text{Mehda})(\text{H}_2\text{O})_2)] \cdot n\text{H}_2\text{O}$.⁵ These layered complexes are favoured in neutral solvent conditions (*e.g.* $\text{H}_2\text{O}/\text{EtOH}$ 1:1 *v/v*). In addition, there are ordered hydrogen bonded H_2O chains between the inorganic-organic layers, which are structurally related to the ice polymorph, I_h , that allowed the self-assembly of spherical aggregates on the nanometre scale and its potential to model properties in biological systems was observed.⁵

The reaction of these types of ligands with lanthanide ions is still unknown. The aim of this chapter is to address this issue and synthesise new lanthanide-organic hybrid materials using iminodiacetic acid substituted naphthol ligands. We will study the synthetic conditions that lead to different hierarchical structures and look for structural features that will favour potential sensing applications based on the optical properties of the resulting materials.

5.2 Synthesis and characterisation of the ligands

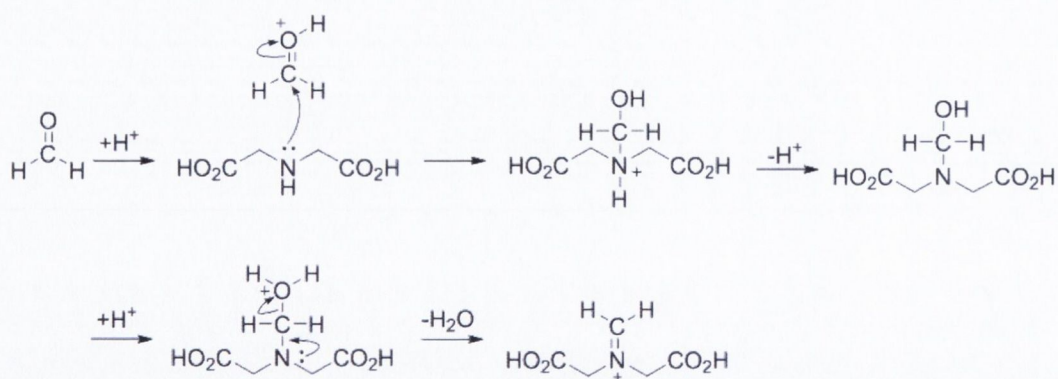
The two ligands investigated are 2,2'-((3-carboxy-2-hydroxynaphthalen-1-yl)methylazanediy)ldiacetic acid ($\text{H}_4\text{C3hnida}$) and 2,2'-((6-carboxy-2-hydroxynaphthalen-1-yl)methylazanediy)ldiacetic acid ($\text{H}_4\text{C6hnida}$). Both ligands contain an iminodiacetic acid functionality in the 1-position with an adjacent hydroxyl group. The ligands vary in the position of a third carboxylate group grafted directly to the aromatic ring in the 3- and 6-position, respectively. The ligands are shown in **Scheme 5.2**.



Scheme 5.2: Structure of the two ligands, $\text{H}_4\text{C3hnida}$ and $\text{H}_4\text{C6hnida}$, used in this study.

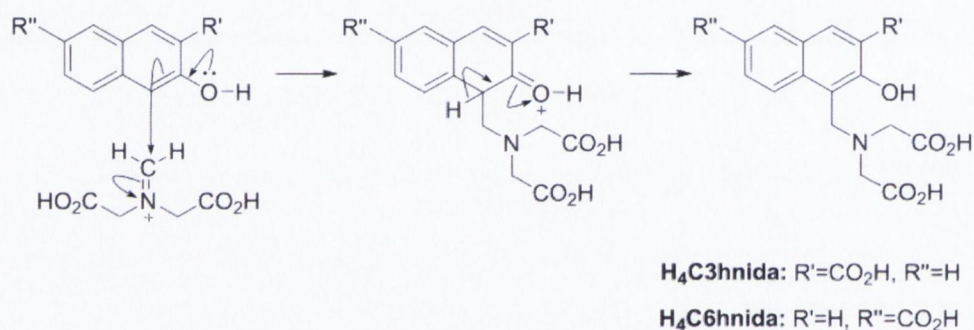
5.2.1 Synthetic mechanism for naphthol substituted iminodiacetic acids

The synthesis of these ligands has been reported previously^{2,3} and they were prepared by reacting the corresponding naphthols, iminodiacetic acid and formaldehyde using the Mannich reaction under acidic conditions. The first step requires the formation of the iminium ion by the nucleophilic addition from the lone pair of electrons on the N-atom in iminodiacetic acid to the C-atom on formaldehyde. This is followed by the internal rearrangement of a proton from the nitrogen to the aldol oxygen centre. A subsequent dehydration step results in the iminium ion (**Scheme 5.3**).



Scheme 5.3: Formation of the iminium ion under acidic conditions.

In the second step, an electrophilic substitution of the iminium ion onto the naphthol reagent results in the formation of C-C bond between the aromatic ring and the iminium ion to yield the product. The mechanism for the electrophilic substitution is summarised in **Scheme 5.4**.



Scheme 5.4: Mechanism for the electrophilic aromatic substitution of the iminium ion to the naphthol.

Identification and purity of the ligand products was confirmed through a combination of ¹H NMR, FT-IR and mass spectrometry (**Experimental, Chapter 2**) to identify aliphatic and aromatic protons and the characteristic C-N bond stretches. All ligands were made in good yield (*ca.* 60-65%).

5.2.2 Optical properties of H₄C3hnida and H₄C6hnida

The optical properties of the ligands were investigated using UV/Vis absorption, steady-state and time-resolved PL spectroscopies. Three different solvents, H₂O, CH₃CN and THF, were investigated, which vary from polar to non-polar, and protic to aprotic solvent systems. The polarity of these solvents is reflected by their dielectric constants (**Table 5.1**)

Table 5.1: The dielectric constants of the solvents used to study the optical properties of H₄C3hnida and H₄C6hnida.

	Dielectric Constant
H₂O	78.54
CH₃CN	36.64
THF	7.52

The ligand H₄C3hnida is yellow and the UV/Vis absorption spectrum contains three bands in the range 200-500 nm. Two bands below 300 nm can be assigned to the naphthalene backbone, an *S*₂ band at 237 nm (42,194 cm⁻¹) and *S*₁ band at 286 nm. (34,965 cm⁻¹) (**Figure 5.1a, Table 5.2**). The *S*₁ band has vibrational fine structure as observed for naphthalene.^{6, 7} However, the molar absorption coefficient ($\epsilon = 5375 \text{ dm}^3 \text{ mol}^{-1} \text{ cm}^{-1}$ in H₂O) of H₄C3hnida is considerably higher than naphthalene (250 dm³ mol⁻¹ cm⁻¹).⁸ The highly symmetrical nature of the structure of naphthalene results in the *S*₁←*S*₀ transition being forbidden due to symmetry arguments of the molecular orbitals involved.⁹ The addition of extra functionality in the 1-, 2- and 3- positions lowers the symmetry in H₄C3hnida and so the *S*₁←*S*₀ becomes more allowed. There is a further absorption band in H₄C3hnida centred at 357 nm ($\epsilon = 2887 \text{ dm}^3 \text{ mol}^{-1} \text{ cm}^{-1}$ in H₂O). This band is not observed in naphthalene and could be explained through resonance effects where the lone pairs of electrons on the alcohol and carboxylic acid group extend the conjugation of the naphthalene chromophore. This effect is well documented in phenols and the relationship of substituent effects is well documented; however, predicting this effect in naphthols is less straightforward.¹⁰⁻¹⁴

When the carboxylic acid group is moved further away from the alcohol group to the 6-position, the appearance of the resulting ligand, H₄C6hnida, is white. The UV/Vis absorption spectrum in H₂O contains two bands; the *S*₂ band at 238 nm (42,017 cm⁻¹) is still observed and a weaker band at 303 nm (33,003 cm⁻¹) that red-shifts to 311 nm (32,154 cm⁻¹) in the less polar solvents, CH₃CN and THF, respectively, is assigned to the *S*₁ excited state (**Figure 5.1c, Table 5.2**). The moderate red-shift of the *S*₁←*S*₀ band to lower energy may be due to the extended conjugation of the chromophore through resonance induction through the -CO₂H and -OH functional groups.

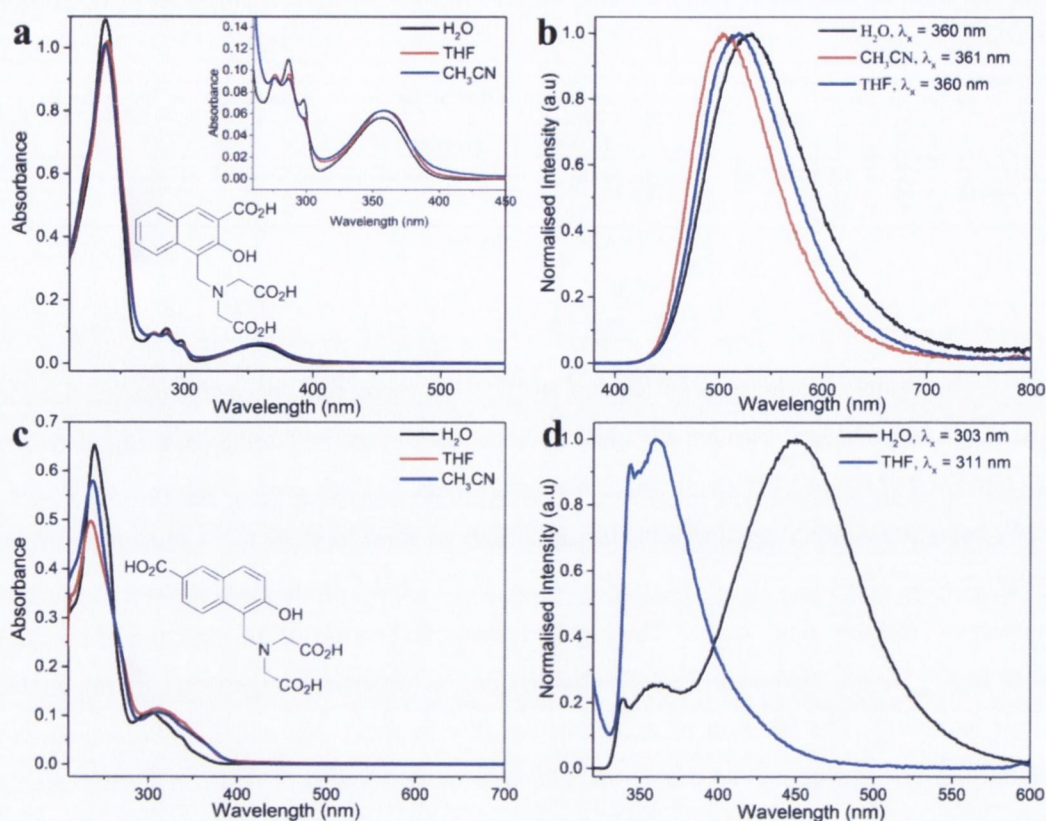


Figure 5.1: Solution UV/Vis absorption and normalised solution PL spectra (absorbance 0.1) for H₄C₃hnida (a, b) and H₄C₆hnida (c, d).

Table 5.2: Table of optical properties for H₄C₃hnida and H₄C₆hnida in H₂O, THF and CH₃CN. λ_{abs} is the absorption maximum, ϵ is the molar absorption coefficient, τ_{obs} is the observed emission lifetime and τ_{r} is the radiative lifetime determined from $\tau_{\text{r}} = \frac{10^{-4}}{\epsilon}$ where ϵ is the molar absorption coefficient.

Ligand	Solvent	λ_{abs} (nm)/ ϵ (dm ³ mol ⁻¹ cm ⁻¹)	λ_{abs} (nm)	τ_{obs} (ns)	τ_{r} (ns)
H ₄ C ₃ hnida	H ₂ O	285/ 5375, 357/ 2887	529	3.1	19, 34
	THF	357	516		
	CH ₃ CN	358	504		
H ₄ C ₆ hnida	H ₂ O	303/ 7120	367(w), 450	3.7	14
	THF	311	360		
	CH ₃ CN	311	-		

The PL spectrum of H₄C₃hnida upon excitation in the 360 nm band reveals a single broad band across the visible region centred around 500 nm. Changing the solvent results in a shift in the emission maximum (λ_{em}) from 529 nm in H₂O, to 504 nm in CH₃CN (Figure 5.1b, Table 5.2). The emission maximum does not vary in accordance with solvent polarity as the $\lambda_{\text{em}} = 516$ nm in THF (least polar). The observed shifts in λ_{em} may be explained through the ability of the solvent to hydrogen bond with the excited state. The lone pair electrons on oxygen in H₂O and THF facilitate

the ability of the solvent to form hydrogen bonds and will stabilise the excited state resulting in the red-shift in λ_{em} compared to CH_3CN , which does not facilitate hydrogen bonding.

The PL spectra for $\text{H}_4\text{C6hnida}$ (**Figure 5.1d**) differ considerably. When excited into the S_1 band, a broad emission band in the range 340–600 nm is observed in H_2O . Closer inspection indicates the presence of two emission bands; a weaker band centred at 367 nm and a more intense band at 450 nm. In THF, the emission spectrum changes further, with a unique broad emission band in the range 340–500 nm and the observed band at 450 nm in H_2O , appears to be quenched or significantly blue-shifted. Notably, in CH_3CN , the ligand is non-emissive.

To understand the emission dynamics for both ligands, the emission lifetimes in H_2O were measured. The observed lifetime, τ_{obs} , for $\text{H}_4\text{C3hnida}$ was found to be 3.1 ns and for $\text{H}_4\text{C6hnida}$ to be 3.7 ns (**Table 5.2**). The radiative lifetimes for the ligands were estimated using the molar absorption coefficients and were found to range between 14 and 34 ns (**Table 5.2**). The short observed and radiative emission lifetime suggest that the origin of the absorption bands is $\pi^* \leftarrow \pi$, in nature.

To summarise, the two ligands display significant differences in the UV/Vis absorption and PL properties in different solvents. The change in the absorption maximum of $\text{H}_4\text{C3hnida}$ is small whereas $\text{H}_4\text{C6hnida}$ displays a 9 nm shift in absorption maximum. The changes in absorption maximum do not agree with the change in polarity of solvent and so other factors such as solvent-solute hydrogen-bonding is inferred. The origin of the large Stokes shift in absorption maximum is thought to arise from resonance effects where the additional alcohol in the 2-position and the carboxylic acid in the 3- or 6-position extend the conjugation in the naphthalene chromophore. The larger Stokes shift in $\text{H}_4\text{C3hnida}$ may also be due to greater stabilisation of the chromophore by their position adjacent to each other. For $\text{H}_4\text{C6hnida}$, the effect of resonance conjugation results in a greater charge separation across the ligand that raises the energy of the excited state. This effect may explain the significant changes in the PL spectra in H_2O and THF where hydrogen bonding will be more abundant in H_2O and so can stabilise the excited state further and results in the longer emission maximum. In comparison, the ability to form hydrogen bonds in THF is reduced and so the excited state will remain at a higher energy, resulting in a blue-shift in the emission band. The magnitude of the observed and radiative emission lifetime and the molar absorption coefficients suggest that the transitions involved are of a $\pi^* \leftarrow \pi$ origin.

5.3 The ligand chemistry of $\text{H}_4\text{C6hnida}$

The synthesis of new lanthanide–organic hybrid materials using these ligands was investigated by a number of different approaches. When the ligand and lanthanide were refluxed with an appropriate base, a precipitate would be observed and crystallisation of quality crystals for characterisation was not possible. Methods to use the layering of solvents were attempted, but do not yield reliable crystallisation conditions for these materials. Of the methods surveyed, the use of

hydro/solvo-thermal reaction conditions was found to be the most consistent approach to grow quality single crystals for further structural characterisation by X-ray crystallography. Using hydro-/solvo-thermal conditions is a delicate balance on a number of parameters that result in the isolation of new lanthanide-organic hybrid materials, but, may also result in decomposition of the ligands through C-C bond breaking and formation.

5.3.1 Crystal structure of 5,5'-methylenebis(6-hydroxy-2-naphthoic acid), $C_{23}H_{16}O_6 \cdot 3DMF$, (**4**)

Crystals of 5,5'-methylenebis(6-hydroxy-2-naphthoic acid), **4**, were isolated from a reaction mixture containing equimolar equivalents of H_4C_6hnida and $NdCl_3 \cdot 6H_2O$ in the presence of sodium hydroxide under solvothermal conditions at 100 °C in a H_2O/DMF (1:1 v/v) solvent system. Under these conditions, **4** forms from the decomposition of the initial ligand, H_4C_6hnida through loss of the iminodiacetate moiety to regenerate 6-hydroxy-2-naphthoic acid. The new molecule is known in the literature, however, no crystal structure has been reported and can be viewed as two 6-hydroxy-2-naphthoic acid units that contain a methylene bridge.

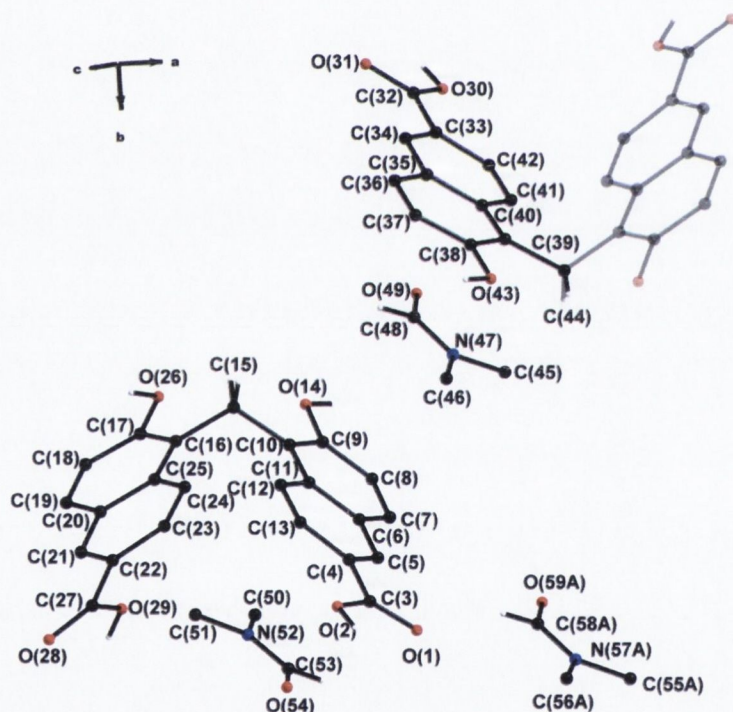


Figure 5.2: Asymmetric unit of 5,5'-methylenebis(6-hydroxy-2-naphthoic acid), **4**. C black, N blue, O red and H white. Faded atoms represent symmetry generated atoms. H atoms (except acid protons) have been removed for clarity.

The molecule crystallises in the monoclinic crystal system in the space group $I2/a$ and the asymmetric unit consists of one and a half ligand molecules and three solvent DMF molecules (**Figure 5.2**). The ligand may be described as a planar naphthalene backbone with a carboxylic acid functionality in the 2-position and a hydroxyl moiety in the 6-position. In the former 1-position, the iminodiacetate moiety has been replaced by a $-CH_2$ methylene (C(15) and C(44))

group which bridges to a second naphthyl ring. The second naphthyl ring has the same structural feature as the first; however, the aromatic carboxylic acid is oriented in the opposite direction. This is reflected by the torsion angles of 115.9 and 121.1° for C(9)-C(10)-C(15)-C(16) and C(10)-C(15)-C(16)-C(17), respectively (**Table 5.3**). The carboxylic acids C(3) and C(27) align in the plane of the naphthalene ring through the presence of weak intramolecular C-H \cdots O interactions with hydrogen bonding distances of 2.47 Å and 2.48 Å for the C(21)-H(21A) \cdots O(28) and C(5)-H(5A) \cdots O(1) interactions, respectively. The small torsion angles between the -C=O oxygen donor and the aromatic C centre also reflect this as given in **Table 5.3**. The second ligand molecule is positioned so that the methylene group, C(44), is positioned on a two-fold rotation axis and through rotational symmetry the molecule is completed. The same features are observed as in the first molecule, where the carboxylic acid is held in-plane with the aromatic ring through weak C(34)-H(34A) \cdots O(31) interaction of length 2.47 Å. The rings are oriented away from each other to minimise steric interactions from the two rings with a torsion angle between C(38)-C(39)-C(44)-C(39') of 119.1°.

Table 5.3: Selected torsion angles in **4**.

	Torsion Angle (°)	
O(1)-C(3)-C(4)-C(5)	7.8(2)	C(9)-C(10)-C(15)-C(16) 115.9(16)
C(21)-C(22)-C(27)-O(28)	-5.1(2)	C(10)-C(15)-C(16)-C(17) 121.1(16)
O(31)-C(32)-C(33)-C(34)	0.1(2)	C(38)-C(39)-C(44)-C(39') 119.1(14)

Table 5.4: Selected hydrogen bonds in **4**.

	Donor-Acceptor Distance (Å)
O2-H2A \cdots O28	2.62(16)
O29-H29A \cdots O1	2.61(17)
O30-H30A \cdots O31	2.65(16)
O14-H14A \cdots O49	2.68(16)
O26-H26A \cdots O59A	2.70(3)
O43-H43A \cdots O54	2.67(16)

The packing of the ligand is stabilised by hydrogen bonding interactions between adjacent molecules, through the carboxylic acid groups. These hydrogen bonds have distances on the order of 2.62 and 2.65 Å for the O(2)-H(2A) \cdots O(28) and O(30)-H(30A) \cdots O(31) interactions, respectively (**Table 5.4**). The three distinct DMF molecules are located near the hydroxyl function of the ligands and the DMF molecule with N(57) is disordered over two positions. These molecules are also involved in hydrogen bonding to the acid functionalities, showing distances of 2.68 Å, 2.70 Å and 2.67 Å for O(14)-H(14A) \cdots O(49), O(26)-H(26A) \cdots O(59A) and O(43)-

H(43A)···O(54), respectively, and further stabilising the structure. The hydrogen bonding enforces the herring-bone packing motif that the molecules adopt, as viewed down the [111] direction (**Figure 5.3**). The structure refinement and crystal data for **4** are provided in **Table 5.5**.

The molecule **4** described is an isomer of the compound 4,4'-methylenebis(3-hydroxy-2-naphthoic acid), also known as pamoic acid, that is used in the pharmaceutical industry to produce salts with products to lower solubilities and help allow separation of products.¹⁵ To understand the role of pamoic acid in this process, interest has been given to understanding the solid-state packing of such systems. However, it is noted that due to its insolubility in many common solvents; pamoic acid is difficult to crystallise and so the structure and packing effects of pamoic acid with isomers of lutidine, a dimethyl-substituted derivative of pyridine has been investigated.¹⁵⁻¹⁷ With the crystal structure of 5,5'-methylenebis(6-hydroxy-2-naphthoic acid), **4**, we have identified a potential strategy to isolate single crystals of pamoic acid that may be adapted by forcing the decomposition of our second ligand H₄C3hnida, an area that will be investigated in the future. In addition, the structure of **4** identifies the ability of these ligands to pack through herring-bone motifs where hydrogen bonding is important for stabilising the solid-state packing. These particular packing interactions have not been identified in the current lutidinium pamoate salts and further add to the knowledge in this area.

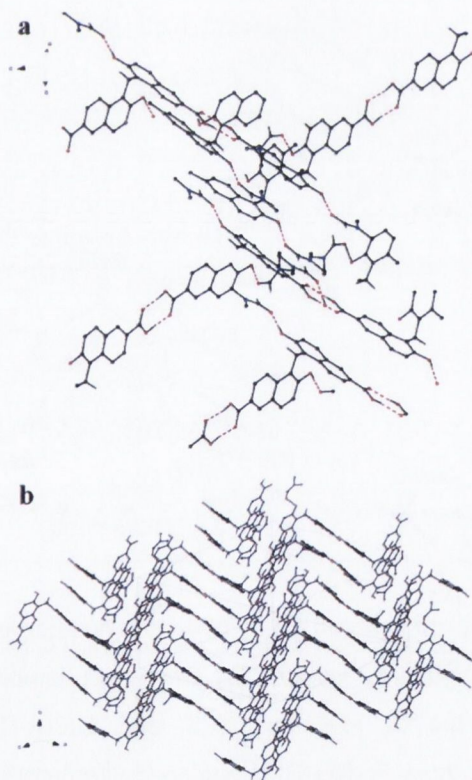


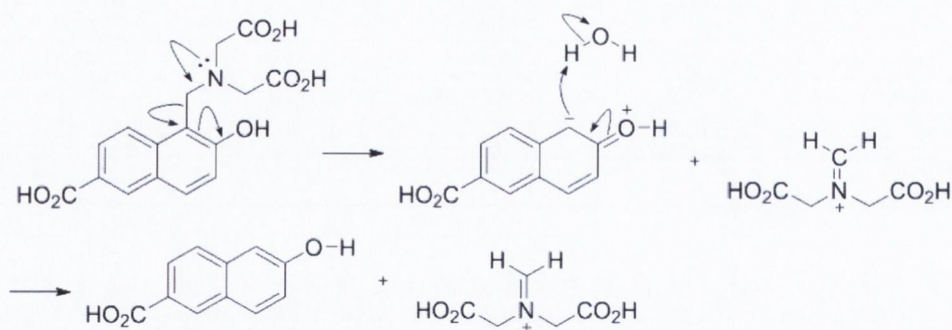
Figure 5.3: (a) Hydrogen bonding interactions (red dashed bonds) between adjacent acid protons and acid protons with DMF solvent molecules. (b) Herring-bone packing motif of the ligand molecules. Molecules generated through symmetry operations related by (0,0,0) Bravais translations have been removed for clarity.

Table 5.5: Crystal data and structure refinement for **4**.

Identification code	4	
Empirical formula	C ₂₉ H ₃₃ N ₂ O ₈	
Formula weight	534.55	
Temperature	100(2) K	
Wavelength	0.71073 Å	
Crystal system	Monoclinic	
Space group	<i>I</i> 1 2/a 1	
Unit cell dimensions	a = 22.177(4) Å	α = 90°.
	b = 13.8936(16) Å	β = 104.196(10)°.
	c = 25.602(2) Å	γ = 90°.
Volume	7647.6(17) Å ³	
Z	12	
Density (calculated)	1.393 Mg m ⁻³	
Absorption coefficient	0.102 mm ⁻¹	
F(000)	3384	
Crystal size	0.260 × 0.170 × 0.100 mm ³	
Theta range for data collection	1.641 to 27.487°.	
Index ranges	-28 ≤ h ≤ 28, -17 ≤ k ≤ 17, -32 ≤ l ≤ 33	
Reflections collected	35361	
Independent reflections	8743 [R(int) = 0.0466]	
Completeness to theta = 25.242°	100.0 %	
Absorption correction	Semi-empirical from equivalents	
Max. and min. transmission	0.7456 and 0.6636	
Refinement method	Full-matrix least-squares on F ²	
Data / restraints / parameters	8743 / 24 / 581	
Goodness-of-fit on F ²	1.007	
Final R indices [I > 2σ(I)]	R1 = 0.0442, wR2 = 0.1052	
R indices (all data)	R1 = 0.0770, wR2 = 0.1191	
Extinction coefficient	n/a	
Largest diff. peak and hole	0.325 and -0.353 eÅ ⁻³	

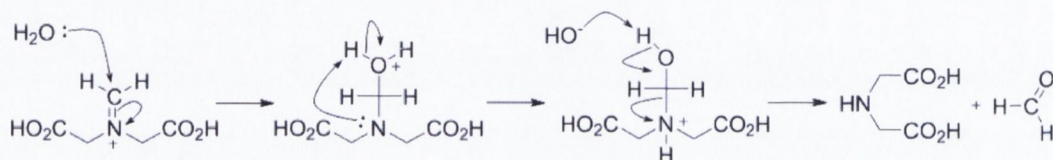
5.3.2 Mechanism for the decomposition of H₄C₆hnida

The crystal structure data clearly show the decomposition of the ligand, H₄C₆hnida, followed by the formation of a new C-C bond to yield the new organic molecule **4**. This can be interpreted as the formation of **4** through a reverse Mannich reaction that regenerates formaldehyde, which subsequently reacts with two equivalents of 6-hydroxy-2-naphthoic acid. The strong basic conditions from the presence of NaOH and DMF activate the reverse Mannich reaction, generating the starting material, 6-hydroxy-2-naphthoic acid and the iminium ion through the mechanism provided in **Scheme 5.5**.



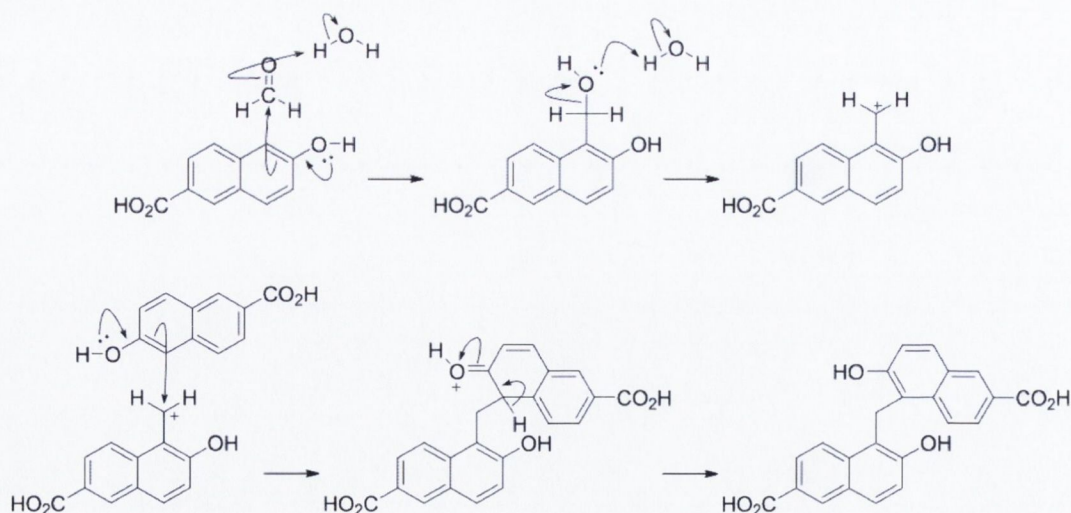
Scheme 5.5: Reverse Mannich reaction generates a 6-hydroxy-2-naphthoic acid and an iminium ion.

Scheme 5.6 shows the mechanism for the nucleophilic addition of water to the iminium ion, which undergoes an internal rearrangement with a subsequent dehydration step to regenerate iminodiacetic acid and formaldehyde.



Scheme 5.6: Nucleophilic addition of water to the iminium ion, followed by an internal rearrangement and dehydration step generate iminodiacetic acid and formaldehyde.

In the third step, an electrophilic substitution of formaldehyde onto 6-hydroxy-2-naphthoic acid and a subsequent dehydration generates a (6-carboxy-2-hydroxynaphthalen-1-yl)methyl cation which undergoes a further electrophilic substitution reaction with a second molecule of 6-hydroxy-2-naphthoic acid (**Scheme 5.7**). The basic conditions and equal solvent ratio of H₂O/DMF is the probable stimulus to drive the equilibrium backwards strongly towards the starting reagents of the Mannich reaction and forces the formaldehyde and substituted naphthoic acid to react directly.



Scheme 5.7: Mechanism for electrophilic substitution of formaldehyde on to 6-hydroxy-2-naphthoic acid generates (6-carboxy-2-hydroxynaphthalen-1-yl)methyl cation that undergoes a further electrophilic substitution with a second molecule of 6-hydroxy-2-naphthoic acid.

5.4 Lanthanide hybrid networks using the ligand H₄C3hnida

The decomposition of H₄C6hnida to form the new fused binaphthyl organic molecule showed that the ligand was sensitive to the reverse Mannich reaction under the basic and hydrothermal conditions adopted. As the hydrothermal approach is required to avoid precipitation in the isolation of many lanthanide hybrid networks, we chose to change our ligand to H₄C3hnida, where the iminodiacetic acid, naphthol and the aromatic carboxylic acid groups are in adjacent positions. By moving the aromatic carboxylic acid we intended to stabilise the imino-functionality by forming a stable delocalised ligand system.

5.4.1 [Nd₅(HC3hnida)(C3hnida)₃(H₂O)₁₀]·25H₂O, (**5**)

5.4.1.1 Synthesis and structural characterisation of **5**

The hydrothermal reaction of one molar equivalent of LnCl₃·6H₂O with one equivalent of H₄C3hnida, in the presence of sodium hydroxide in water results in the isolation of **5**. After heating at 60 °C for 14 hours, followed by slow cooling, the medium yielded diamond shaped crystals (**Figure 5.4**) of [Nd₅(HC3hnida)(C3hnida)₃(H₂O)₁₀]·25H₂O, **5**, that were characterised by single crystal X-ray diffraction.

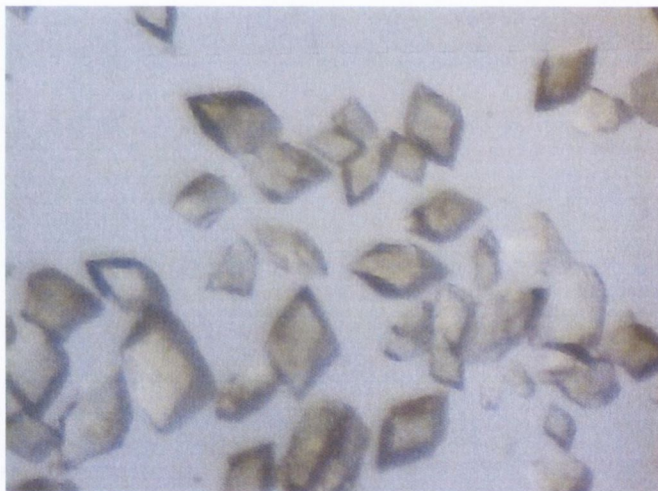


Figure 5.4: Colour photograph of representative crystals of **5**.

Compound **5** crystallises in the trigonal crystal system in the space group *P*3₂21 and consists of a pentanuclear core sub-unit of formula [Nd₅(HC3hnida)(C3hnida)₃(H₂O)₁₀]·25H₂O. The structure of the pentanuclear unit resembles a distorted tetrahedron whereby the Nd^{III} centres constitute the vertices of the tetrahedron that are bridged through donor atoms of four distinct organic ligand molecules. The asymmetric unit contains half of the pentanuclear unit, consisting of three independent neodymium ions; Nd(2) is positioned on a special site through which a two-fold rotation axis runs. There are two crystallographically unique ligand molecules whereby one ligand is fully deprotonated (C3hnida) and the second ligand is singly protonated through O(44) located on the imino-moiety (HC3hnida). This proton is disordered over the two ligand positions in the pentanuclear unit.

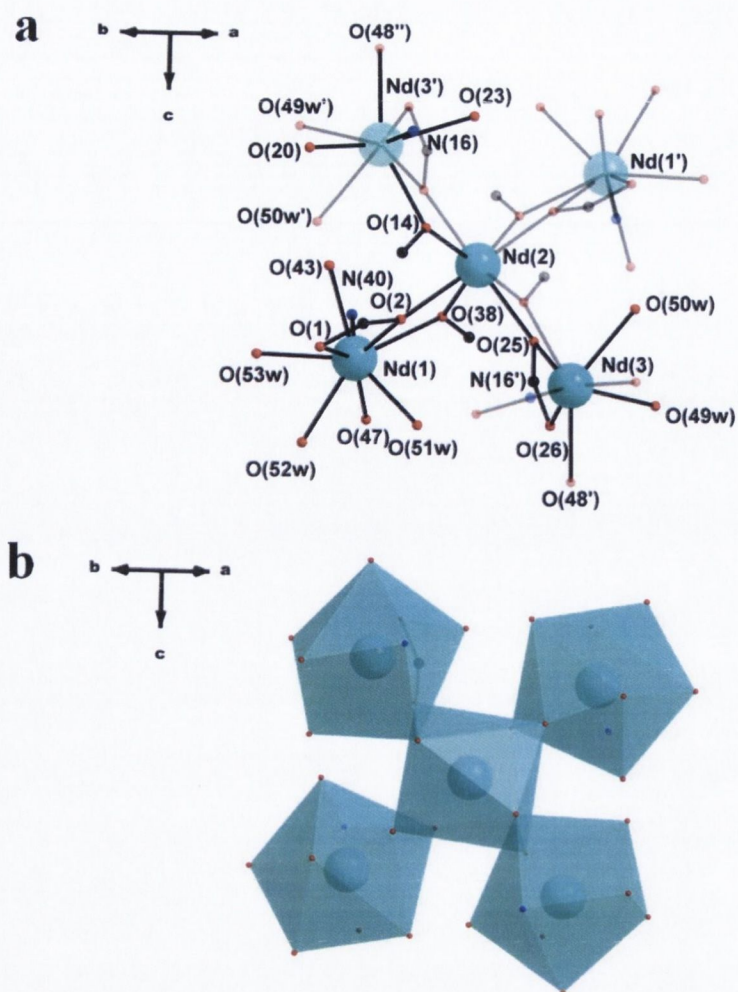
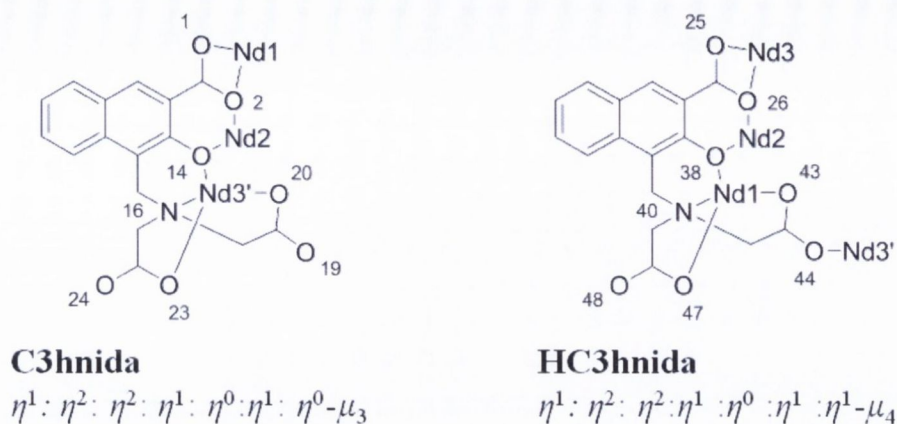


Figure 5.5: (a) Pentanuclear unit of $[\text{Nd}_5(\text{HC3hnida})(\text{C3hnida})_3(\text{H}_2\text{O})_{10}] \cdot 25\text{H}_2\text{O}$, **5**, as viewed down the $[110]$ axis. Non-coordinating atoms have been removed for clarity. The asymmetric unit contains atoms represented in bold, faded atoms represent symmetry generated atoms to produce the pentanuclear unit. (b) Polyhedral view of the pentanuclear building unit in **5**. Nd cyan, C black, N blue. H atoms omitted for clarity.

Figure 5.5 shows the coordination environments around the Nd^{III} centres where Nd(1) is best described as a 9-coordinate distorted capped square antiprism. The coordination sites are occupied by two naphthyl- O_{COO} donor atoms O(1) and O(2) of C3hnida, two O_{COO} donor atoms, O(43) and O(47) of each imino-moiety from HC3hnida, one hydroxo-donor O(38) of HC3hnida, one N(40) donor of HC3hnida and three coordinated water molecules O(51w), O(52w) and O(53w). The coordination environment of Nd(2) may be viewed as an 8-coordinate distorted dodecahedron. The coordination sites are provided by four naphthyl- O_{COO} donor atoms, the hydroxo-O(2) of two HC3hnida³⁻ and O(25) of two C3hnida⁴⁻ ligands and four hydroxo-O donors of the same two HC3hnida³⁻ (O(14)) and two C3hnida⁴⁻(O(38)) molecules. The inner coordination sphere of the 9-coordinate Nd(3) centre is completed by the O-donor atoms of the two coordinated water molecules O(49w) and O(50w), two naphthyl- O_{COO} atoms, O(25) and O(26) of one HC3hnida³⁻ ligand, two O_{COO} centres, O(20) and O(23), one from each acetate moiety of C3hnida,

one hydroxo-O(14) atom from C3hnida⁴⁻ and one N-donor atom, N(16) of C3hnida⁴⁻ to form a distorted capped square antiprism.



Scheme 5.8: Atom labelling for coordinating centres in (a) C3hnida and (b) HC3hnida in $[\text{Nd}_5(\text{HC3hnida})(\text{C3hnida})_3(\text{H}_2\text{O})_{10}] \cdot 25\text{H}_2\text{O}$, **5**.

In **5**, the deprotonated ligand **C3hnida** adopts a $\eta^1: \eta^2: \eta^2: \eta^1: \eta^0: \eta^1: \eta^0-\mu_3$ coordination mode that bridges three Nd^{III} centres in the pentanuclear unit (**Scheme 5.8a**). In this fashion, the carboxylate atoms O(1) and O(2) chelate the Nd(1) centre and O(2) further bridges to Nd(2) in an μ_2 -mode. The hydroxo donor O(14) adopts a μ_2 -bridge between Nd(2) and Nd(3'). The O-donor atoms O(20) and O(23) from each acetate moiety coordinate in a monodentate fashion to Nd(3'), and O(19) and O(24) of the acetates do not coordinate. The coordination mode of the singly protonated **HC3hnida** differs slightly, bridging four Nd^{III} centres and adopting a $\eta^1: \eta^2: \eta^2: \eta^1: \eta^0: \eta^1: \eta^1-\mu_4$ binding mode (**Scheme 5.8b**). The carboxylate O-donor atoms O(25) and O(26) display a chelate-bridging mode to Nd(3) and Nd(2). The hydroxo O(38) adopts a μ_2 -coordination mode to bridge Nd(2) and Nd(1). This leaves O(43) and O(47) on each acetate group to coordinate to Nd(1). A further bridge to Nd(3') is provided by the acetate O-donor O(48) and completes the coordination sphere. The atom O(44) of the protonated carboxylic acid group is not involved in any coordinative bonding. Three and two water molecules complete the coordination sphere of Nd(1) and Nd(3), respectively.

The bond lengths for the Nd-O_{carboxylate} are in the range 2.370–2.465 Å, with the exception of Nd(1)–O(1) (2.642 Å) and Nd(3)–O(26) (2.681 Å) and are summarised in **Table 5.6**. The former distances are consistent with previously reported lanthanide carboxylates,¹⁸ while the latter, longer bond distances may be explained due to the weaker interaction of the O-donor with the lanthanide centre as a consequence of the chelate-bridging mode and the rigidity of the aromatic carboxylate imparted by the naphthalene backbone. The bridging hydroxo-interactions are generally longer than the carboxylate bond lengths and have Nd–O bond lengths in the range 2.456–2.472 Å. These bond lengths are slightly longer than bridging hydroxo-interactions reported for lanthanide complexes of 2-hydroxy-1,3-diaminopropane-*N,N,N',N'*-tetraacetic acid and may be a result of the steric demand of the naphthalene backbone in tandem with the effect of the adjacent aromatic and

imino-carboxylates coordinating to the lanthanide centre.¹⁹⁻²¹ The bond angles given in **Table 5.7** show that the bridging hydroxo-interactions are sensible, since the Nd-O-Nd bond angles are slightly distorted from 120° in the range 112.57-115.67° in agreement with literature values.²⁰⁻²² Nd-O bond lengths from coordinated water are slightly longer (2.451-2.579 Å) than the ligand oxygen donors, as anticipated due to the less electronegative nature of the coordinating water molecules.

Table 5.6: Selected bond lengths for **5**.

Bond	Bond Length (Å)	Bond	Bond Length (Å)
Nd(1)-O(1)	2.642(5)	Nd(1)-O(38)	2.465(4)
Nd(1)-O(2)	2.475(4)	Nd(2)-O(38)	2.472(4)
Nd(2)-O(2)	2.399(4)	Nd(2)-O(14)	2.458(4)
Nd(3)-O(26)	2.681(5)	Nd(3)-O(14)#1	2.456(4)
Nd(3)-O(25)	2.465(4)	Nd(1)-O(51w)	2.451(4)
Nd(2)-O(25)	2.422(4)	Nd(1)-O(52w)	2.530(4)
O(20)-Nd(3)#1	2.401(5)	Nd(1)-O(53w)	2.505(5)
O(23)-Nd(3)#1	2.460(4)	Nd(3)-O(49w)	2.579(4)
Nd(1)-O(43)	2.423(4)	Nd(3)-O(50w)	2.534(4)
Nd(1)-O(47)	2.370(4)		
O(48)-Nd(3)#3	2.435(4)		

Table 5.7: Selected bond angles for **5**.

Bonds	Bond Angle (°)
Nd(3)#1-O(14)-Nd(2)	112.57(15)
Nd(1)-O(38)-Nd(2)	113.41(16)
Nd(2)-O(2)-Nd(1)	115.67(18)
Nd(2)-O(25)-Nd(3)	113.56(16)

The C3hnida⁴⁻ ligand coordinates directly to three Nd^{III} centres, while the protonated HC3hnida³⁻ bridges four Nd^{III} centres, three from within a pentanuclear unit and the fourth from a separate symmetry-generated unit. The Nd(2) ion locates on a two-fold rotation axis, **Figure 5.6a** and **Figure 5.8b**, and by applying this symmetry element, the symmetry partners of Nd(1) and Nd(3) as well as symmetry related C3hnida⁴⁻ and HC3hnida³⁻ are generated. This yields the core pentanuclear unit that can be viewed as a highly distorted tetrahedron with four Nd^{III} centres [Nd(1), Nd(1'), Nd(3) and Nd(3')] forming the vertices and Nd(2) residing in the centre (**Figure 5.6**). Adjacent polyhedra within this unit share a common edge (**Figure 5.5b**). From here on, this unit will be referred to as the 'tetrahedral' SBU of the structure.

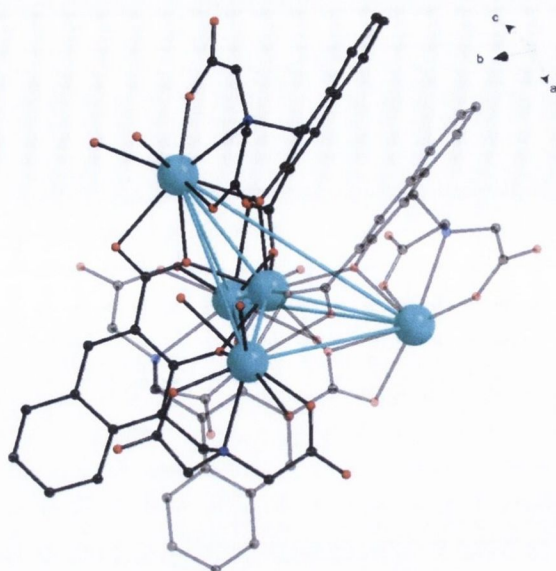


Figure 5.6: The complete tetrahedral building unit in **5**. Cyan vertices highlight the highly distorted tetrahedron. Nd cyan, C black, N blue, O red. H atoms omitted for clarity. Symmetry generated atoms are faded.

The tetrahedral SBU can be viewed as having four points of extension (**Figure 5.7**) provided by an acetate moiety of $\text{HC}_3\text{hnida}^{3-}$ at each vertex atom. This connecting moiety involves C(46), O(48) and O(47). The latter O-donor atoms bridge to symmetry equivalents of Nd(3) and Nd(1) centres, respectively, each from separate SBUs.

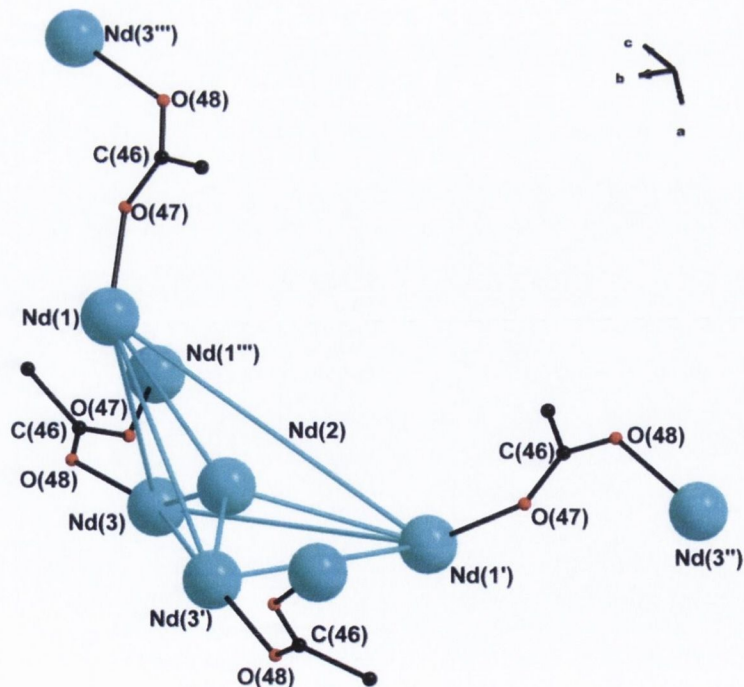


Figure 5.7: Tetrahedral secondary building unit in **5** with four points of extension provided through the coordinating C(46) acetate of $\text{HC}_3\text{hnida}^{3-}$. Nd cyan, C black, O red.

The asymmetric unit is characterised by a two-fold rotational axis running through [110] at $(x, x, 0.5)$ which generates the tetrahedral SBU through symmetry. The rest of the unit cell is filled

through a combination of complementary three-fold screw and two-fold rotation axes (**Figure 5.8**). The upper third of the unit cell is generated through one equivalent three-fold screw axes at $[1/3, 1/3, z]$ and $[2/3, 2/3, z]$, shifting the SBU position in space. To complete each tetrahedral SBU, a two-fold axis along $[100]$ and located at $(x, 0, 5/6)$. The lower third of the unit cell is similarly reproduced through two consecutive screw axis operations. The tetrahedral SBU is completed by two fold-rotation axes along $[010]$ located at $(0, y, 1/6)$ to generate equivalent atom positions. This produces a unit cell with $Z = 3$.

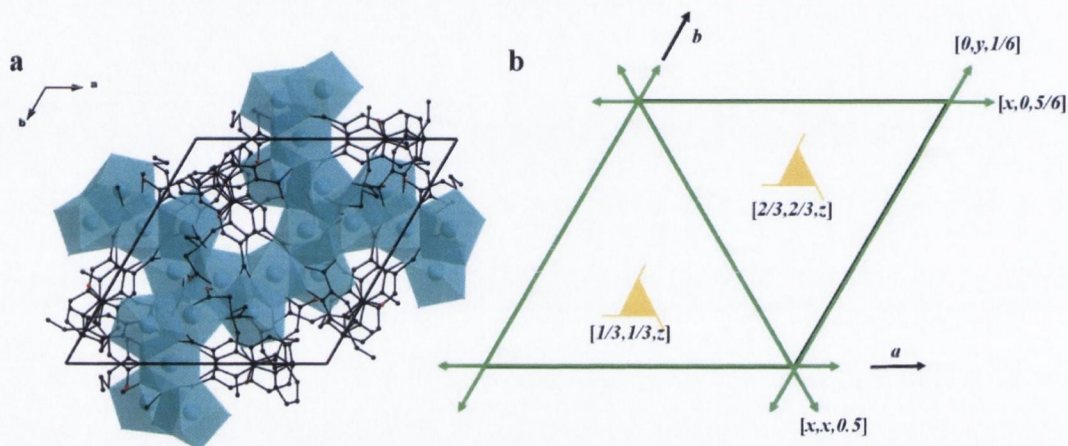


Figure 5.8: (a) The unit cell of **5** looking down the c -axis with the central secondary building unit and the four symmetry related building units. (b) Diagram of symmetry operations in the unit cell looking down the c -axis that produce equivalent building units. Green double headed arrows are two-fold rotation axes, yellow bladed-triangle are three-fold screw axes, italic coordinates relate to position of the symmetry elements in the unit cell.

The packing of **5** can be visualised as being generated through the stacking of three layers, A , B and C in $[001]$ (**Figure 5.9a**). Each layer contains different symmetry generated tetrahedral SBUs and each layer is contained throughout the unit cell. As consecutive unit cells are packed in space, an infinite double helical chain grows along the c -axis (**Figure 5.9b**) with the repeating stacking motif, ABC , where the B -layer connects both helical moieties. The 3-fold screw axes organise the connected double helical chains into chiral blade-like channels that extend along the c -axis.

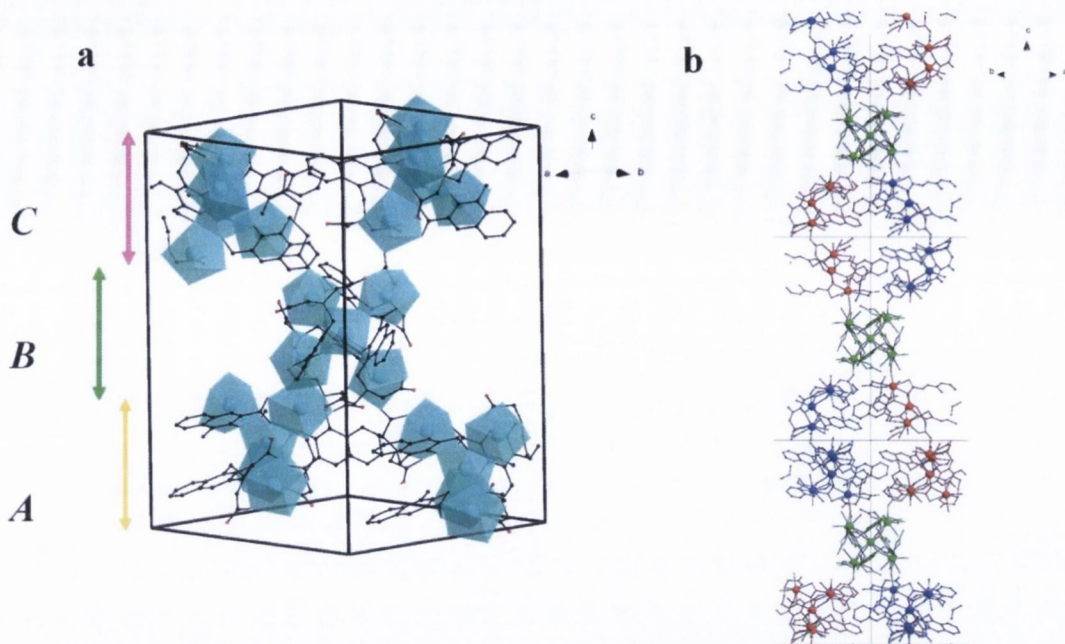


Figure 5.9: (a) The unit cell of **5** looking down the $[111]$ direction with a central building unit and its four connected neighbours coordinated through its points of extension and (b) three stacked unit cells viewed down the $[110]$ axis showing an infinite double helical chain running along the c -axis through the presence of three-fold screw axes. Colour code: red, one chiral helix; blue, second chiral helix and green, SBU connecting both helices. Black outlines denote unit cell edges.

When viewed in a polyhedral representation, the double chiral chain has the effect of creating a chiral blade-like channel running along the c -axis. The channel is built from the sequential ABC layer motif and thus creates a truly chiral channel that repeats with each repeat unit cell (**Figure 5.10**).

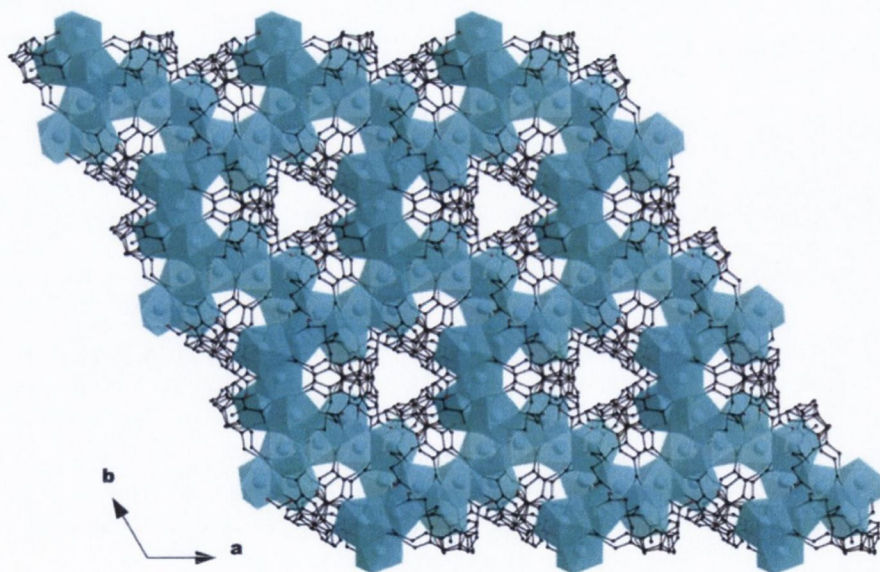


Figure 5.10: The view of blade-like chiral channels running down the c -axis in **5** arising as a consequence of the infinite helical chains.

Two additional types of channel are viewed along the a - and b -axes in **Figure 5.11**; hydrophobic channels built from a 6-membered ring of SBUs and a hydrophilic channel built from 4-membered ring of four tetrahedral SBUs. In the hydrophobic channels, the cross-sectional

dimension is *ca.* 16.5 Å in the *b*-direction, as represented by the Nd(3)-Nd(3') centroid distances and 24.5 Å in the *c*-direction, represented by the Nd(3) to Nd(3') centroid distance. In the channels, the ligands orientate so that the hydrophobic naphthalene moiety occupies the channel space. The smaller hydrophilic channel is *ca.* 14.1 Å along the *b*-direction (given by the Nd(1)-Nd(3) centroid distance) and 17.5 Å along the *c*-direction (Nd(1)-Nd(1') centroid distance). The channels are lined with the hydrophilic {Nd-O} polyhedra and are likely to accommodate the solvent water of crystallisation molecules. The constitutional solvent molecules (*ca.* 25 H₂O molecules per formula unit) in **5** are partly disordered and to improve the refinement of the crystal structure, the Platon routine SQUEEZE was used to account for this disorder in the structure. The final structure refinement and further crystal data details are provided in **Table 5.8**.

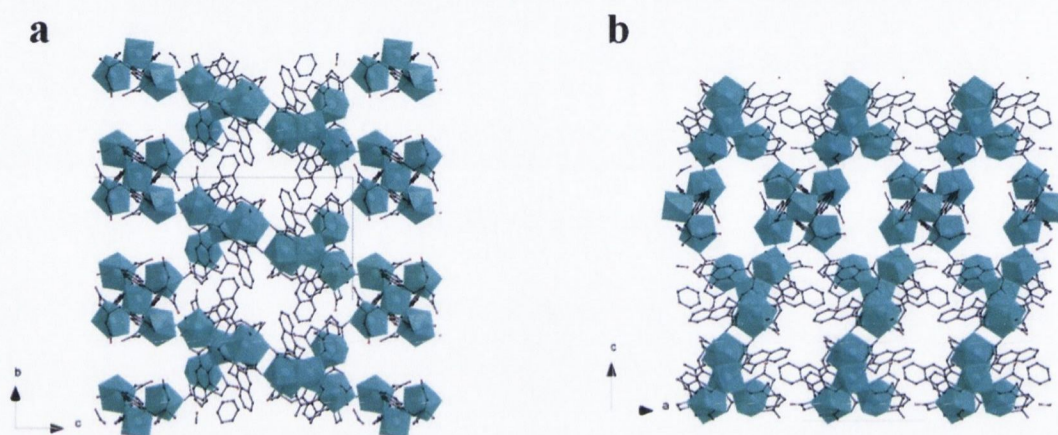


Figure 5.11: View of hydrophobic and hydrophilic channels in **5** as viewed down the (a) *a*-axis and (b) *b*-axis.

Table 5.8: Crystal data and structure refinement for **5**.

Identification code	5	
Empirical formula	C ₆₄ H ₄₅ N ₄ Nd ₅ O ₃₈	
Formula weight	2199.24	
Temperature	100(2) K	
Wavelength	0.71073 Å	
Crystal system	Trigonal	
Space group	<i>P</i> 3 ₂ 1	
Unit cell dimensions	a = 16.5265(5) Å b = 16.5265(5) Å c = 29.9268(10) Å	α = 90°. β = 90°. γ = 120°.
Volume	7078.7(5) Å ³	
Z	3	
Density (calculated)	1.548 Mg m ⁻³	
Absorption coefficient	2.779 mm ⁻¹	
F(000)	3183	
Crystal size	0.090 × 0.080 × 0.080 mm ³	
Theta range for data collection	1.577 to 29.595°.	
Index ranges	-22 ≤ h ≤ 22, -22 ≤ k ≤ 22, -41 ≤ l ≤ 41	
Reflections collected	272396	
Independent reflections	13249 [R(int) = 0.0654]	
Completeness to theta = 25.242°	100.0 %	
Absorption correction	Semi-empirical from equivalents	
Max. and min. transmission	0.7459 and 0.7093	
Refinement method	Full-matrix least-squares on F ²	
Data / restraints / parameters	13249 / 0 / 502	
Goodness-of-fit on F ²	1.042	
Final R indices [I > 2σ(I)]	R1 = 0.0307, wR2 = 0.0685	
R indices (all data)	R1 = 0.0403, wR2 = 0.0729	
Absolute structure parameter	-0.011(3)	
Extinction coefficient	n/a	
Largest diff. peak and hole	1.415 and -1.064 e.Å ⁻³	

5.4.1.2 Physicochemical characterisation of **5**

Compound **5** was further characterised by FT-IR spectroscopy (**Figure 5.12a**). The presence of $\nu(\text{CO}_2^-)$ stretches provides complementary evidence to the crystal structure of the coordination modes adopted. A weak ν_{asym} stretch at 1737 cm⁻¹ identifies that there is a singly protonated acetic acid of one ligand in the formula of **5**. Further asymmetric (1574 and 1457 cm⁻¹) and symmetric stretches (1393 and 1308 cm⁻¹) are significantly shifted from the signals observed for the free ligand, indicating coordination to the Nd^{III} centre. Furthermore, the $\Delta = [\nu_{\text{asym}}(\text{CO}_2^-) - \nu_{\text{sym}}(\text{CO}_2^-)]$ values ranging between 64-266 cm⁻¹ indicate the different binding modes adopted include chelating and bridging. Weak stretching vibrations at 2974, 2954 and 2921 cm⁻¹ attributed to CH₂ groups on the imino-functionality are superimposed on the strong, broad OH stretch between 3000-3500 cm⁻¹. The retention of the C-N stretch at 1211 cm⁻¹ indicates the imino-functionality remains intact. Powder X-ray diffraction was used to investigate the phase purity of the bulk material. The bulk material is a single phase as identified by the matching reflections in

Figure 5.12b from the raw diffraction data to the calculated powder pattern derived from the structure refinement model. The thermal stability of **5** was probed by thermogravimetric analysis (TGA) using a freshly prepared crystalline sample (**Figure 5.12c**) heated in an air atmosphere up to 900 °C at a rate of 10 °C/min. There are two main decomposition steps. The first weight loss of 15.3% occurs up to 120 °C, and is related to the loss of the 25 solvent water molecules (*calc.* 16.9%). The composition remains unchanged up to 400 °C, after which the organic ligand decomposes through a 39.4% weight loss (*calc.* 41.3%). The remaining material is assumed to be composed of neodymium oxides. An isostructural series was created by varying the lanthanide centre, Ln^{III} = Eu^{III}, Gd^{III} and Yb^{III}. The FT-IR spectra and powder diffraction patterns confirmed that the new lanthanide materials are isostructural. Of the above materials the photoluminescence properties of the Nd^{III}, Yb^{III} and Eu^{III} analogues have been studied and given the names, **5-Nd**, **5-Yb** and **5-Eu**, respectively.

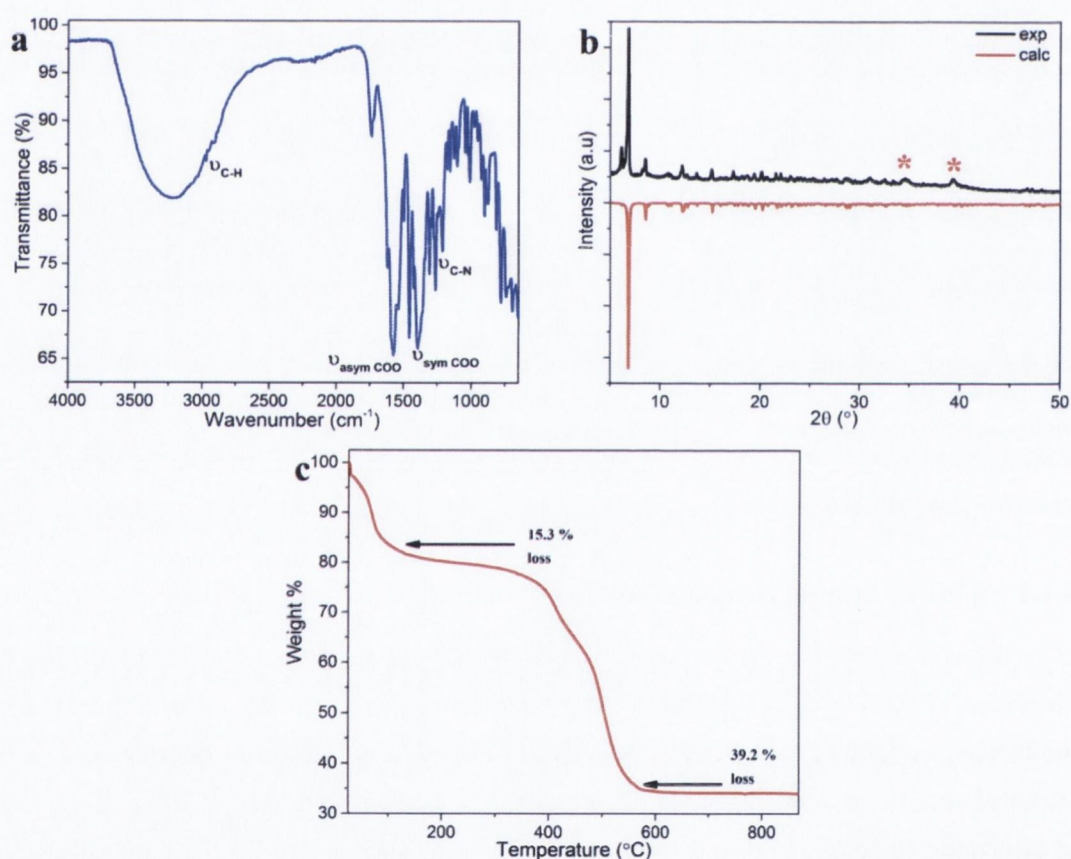


Figure 5.12: (a) The FT-IR spectrum for **5**, (b) the powder X-ray diffraction pattern for a bulk crystalline sample of **5** and (c) the thermogram of **5** (fresh crystalline sample). * indicate reflections from instrumental artefacts.

5.4.1.3 Photoluminescence properties of **5-Nd**, **5-Yb** and **5-Eu**.

The compound **5-Nd** displays NIR emission bands when excited directly into the Nd^{III} centre or *via* sensitisation through the coordinated ligand. Emission lines originating from $^4F_{3/2} \rightarrow ^4I_{J/2}$ ($J = 13, 11, 9$) transitions are assigned to the bands at 1328, 1056 and 870 nm,

respectively (**Figure 5.13a**). The room temperature excitation spectrum in **Figure 5.13b** shows that the compound exhibits typical Nd^{III}-centred excitation bands in the visible originating from the ground state, $^4I_{9/2}$, to the $^2L_{15/2}$, $^4G_{7/2-5/2}$, $^4S_{7/2}$ and $^4F_{7/2}$ excited states. The compound also strongly absorbs in the UV from 300-420 nm. This is assigned to the ligand absorption that was shown to absorb at 370 nm in **Figure 5.1a**, corroborating ligand sensitisation of the Nd(III) emission.

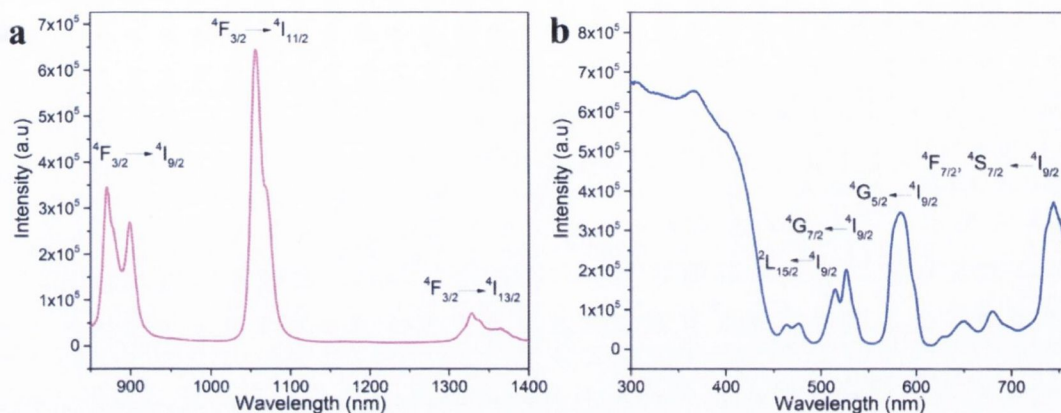


Figure 5.13: (a) Room temperature (RT) PL spectrum for **5-Nd** following ligand sensitisation ($\lambda_{\text{ex}} = 400$ nm) and (b) corresponding RT excitation spectrum ($\lambda_{\text{em}} = 1056$ nm, $^4F_{3/2} \rightarrow ^4I_{11/2}$ transition).

When **5-Yb** is excited into the ligand at 400 nm, a NIR band at 978 nm from the $^4F_{5/2} \rightarrow ^4F_{7/2}$ transition is observed (**Figure 5.14a**). The excitation spectrum in **Figure 5.14b** has a strong absorption band between 300-430 nm that is assigned to ligand absorption. Despite the high number of coordinated water molecules in the structure, that introduce non-radiative decay channels, the NIR emission from Ln^{III} = Nd^{III} and Yb^{III} appears to be strong, suggesting the ligand is a good sensitiser for emission from NIR-active Ln^{III} centres.

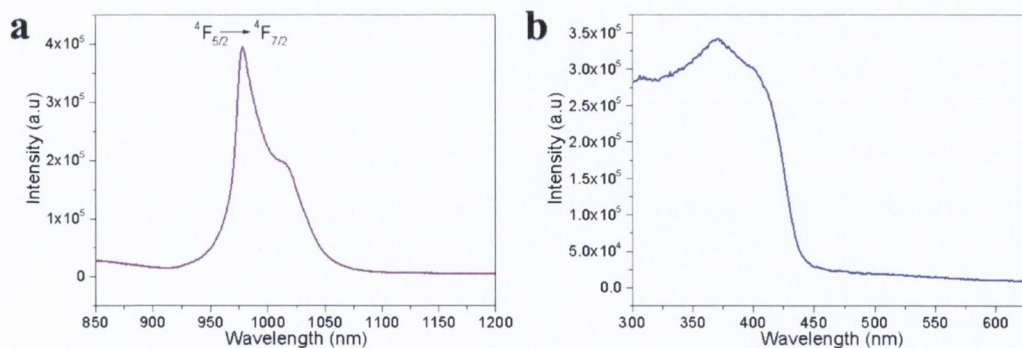


Figure 5.14: (a) RT PL spectrum for **5-Yb** under ligand excitation ($\lambda_{\text{ex}}=400$ nm) and (b) corresponding RT excitation spectrum ($\lambda_{\text{ex}}=978$ nm, $^4F_{5/2} \rightarrow ^4I_{7/2}$ transition).

When **5-Eu** is excited directly into the Eu^{III} centre ($\lambda_{\text{ex}} = 393 \text{ nm}$ ($^5\text{L}_6 \leftarrow ^7\text{F}_0$)) or through ligand sensitisation ($\lambda_{\text{ex}} = 350\text{-}420 \text{ nm}$) a very weak emission is observed (**Figure 5.15a.**) in the range 580-700 nm and assigned to the $^5\text{D}_0 \rightarrow ^7\text{F}_J$ transitions ($J = 1, 2$ and 4). The weak photoluminescence of **5-Eu** may be due to a number of mechanisms. Mechanism I considers the significant quenching from both the coordinated water molecules and the high number of crystallisation of water molecules present within the structure. The combined effect of both sources of water molecule may result in significant reduction of the PL intensities measured. Mechanism II considers the triplet energy of the ligand itself. Unfortunately, the energy of the triplet level of C3hnida was not obtained, however, if it has an energy resonant or just below the energy of the $^5\text{D}_0$ manifold, then non-radiative energy transfer from the $^5\text{D}_0$ manifold into the triplet level of the ligand could lead to non-radiative loss of the light supplied to the system (**Figure 5.15b**). A third possibility may involve quenching of the S_1 state of the ligand directly by the Eu^{III} whereby an electron transfer mechanism is involved with the transient formation of Eu^{II} . Such a mechanism has been identified in other systems with naphthalene-based ligands that are coordinated to Eu^{III} -centres.^{23, 24}

Of the possible mechanisms involved it seems reasonable that the poor PL of the Eu^{III} centres could be a combined effect of mechanism I and mechanism II working in tandem. To gain further insight into the actual mechanism, future experiments plan to determine the triplet energy of the ligand using the Gd^{III} -analogue of the reported structure to determine whether mechanism II is a valid possibility. Based on the outcome of this experiment, subsequent determination of the validity of mechanism III will need to be undertaken.

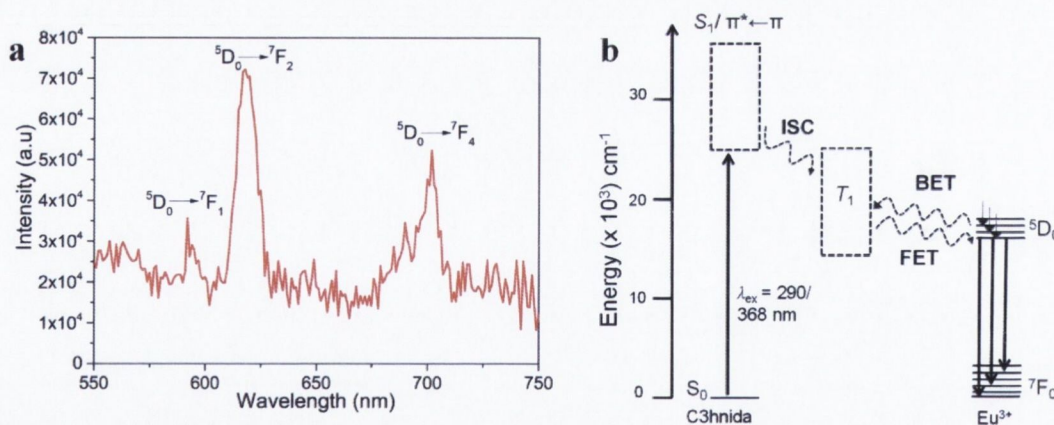


Figure 5.15: (a) RT PL spectrum for **5-Eu** under ligand excitation ($\lambda_{\text{ex}} = 420 \text{ nm}$) using large slit widths 5/5 nm. (b) Schematic energy level diagram highlighting how the triplet energy state of the ligand, C3hnida, may result in the poor PL intensities from the Eu^{III} centre by increasing the number of non-radiative pathways for relaxation of the energy. ISC: Intersystem crossing, FET: Forward energy transfer, BET: Backwards energy transfer. Solid and dashed lines represent radiative and non-radiative transitions, respectively. The dashed boxes represent the energy levels occupied by the S_1 and $\pi^* \leftarrow \pi$ transition and the plausible energy region occupied by the T_1 energy level of the ligand, C3hnida.

5.4.2 $[\text{Nd}_{17}(\text{C3hnida})_{12}(\mu_3\text{-OH})_4(\text{H}_2\text{O})_{30}] \cdot x\text{H}_2\text{O}$, (6)

5.4.2.1 Synthesis and structural characterisation of 6

The reaction of one equivalent of $\text{H}_4\text{C3hnida}$ with $\text{NdCl}_3 \cdot 6\text{H}_2\text{O}$ in the presence of sodium hydroxide yields green crystals of $[\text{Nd}_{17}(\text{C3hnida})_{12}(\mu_3\text{-OH})_4(\text{H}_2\text{O})_{30}] \cdot \text{H}_2\text{O}$, **6**. The reaction takes place under hydrothermal conditions in H_2O at a temperature of $100\text{ }^\circ\text{C}$. After 15 hours, the reaction vessel was slowly cooled to room temperature where the crystalline product was isolated for characterisation by single crystal X-ray diffraction measurements.

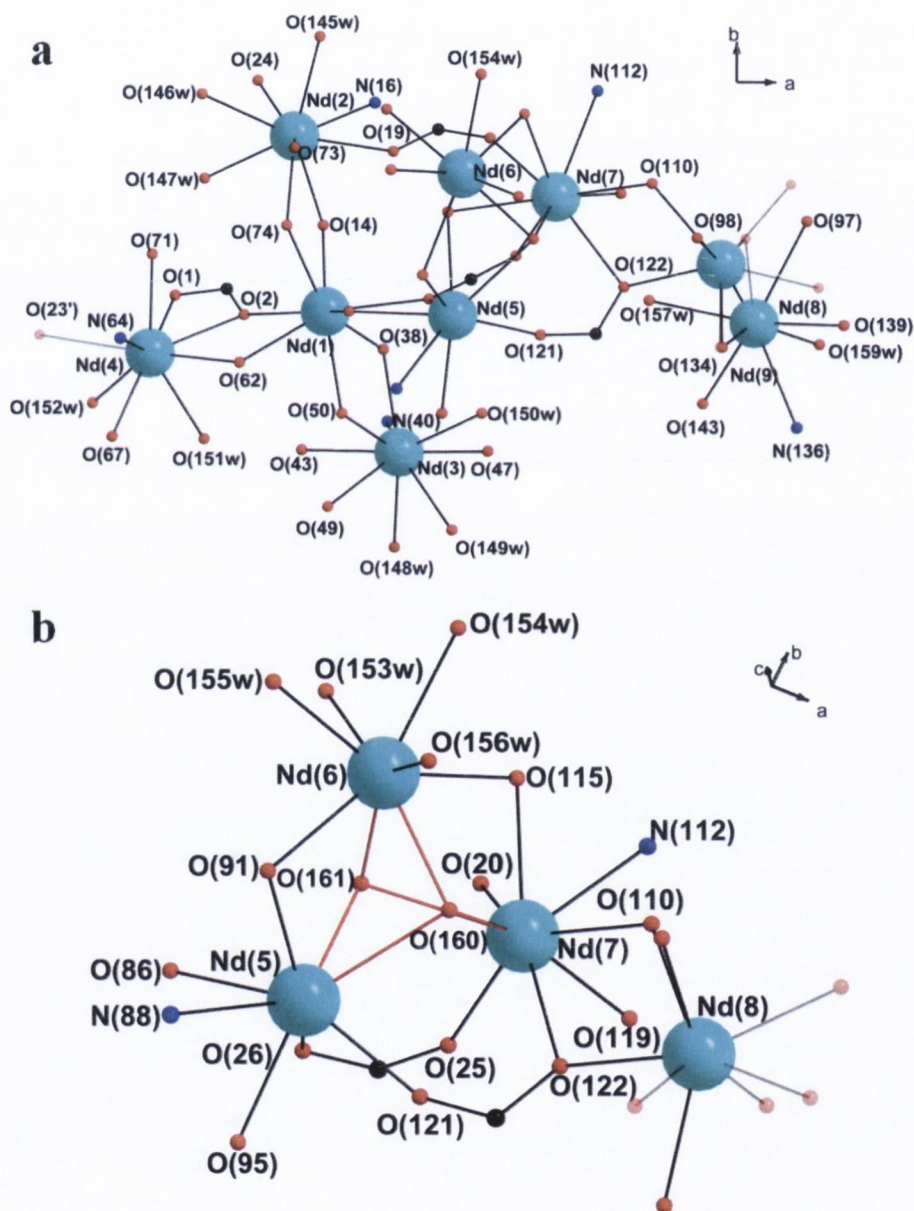


Figure 5.16: (a) Asymmetric unit of $[\text{Nd}_{17}(\text{C3hnida})_{12}(\mu_3\text{-OH})_4(\text{H}_2\text{O})_{30}] \cdot \text{H}_2\text{O}$, **6**, displaying donor atoms coordinated directly to the Nd^{III} centres. (b) Selected view around Nd(5), Nd(6), Nd(7) and Nd(8) to identify atom labels coordinated around the Nd^{III} centres. The μ_3 -hydroxo-bridges to the Nd^{III} centres have been highlighted using red bonds. Faded atoms identify symmetry generated atoms. Nd cyan, C black, N blue, O red.

The compound $[\text{Nd}_{17}(\text{C3hnida})_{12}(\mu_3\text{-OH})_4(\text{H}_2\text{O})_{30}] \cdot x\text{H}_2\text{O}$, **6** crystallises in the monoclinic crystal system in the space group $C2/c$ and the asymmetric unit contains nine Nd^{III} centres, six fully deprotonated ligands and 15 coordinated H_2O molecules (**Figure 5.16a, b**). $\text{Nd}(1)$, $\text{Nd}(6)$ and $\text{Nd}(8)$ are eight-coordinate. The coordination environment of $\text{Nd}(1)$ can be visualised as a distorted dodecahedron, coordinated through eight $\mu_2\text{-O}$ bridges from four hydroxo O-donors and four carboxylate oxygen donors of four distinct ligands. The $\text{Nd}(8)$ coordination geometry can also be described as a distorted dodecahedron in which the $\text{Nd}(8)$ ion is positioned on a two-fold rotation axis that runs along the b -axis. The coordination environment of $\text{Nd}(8)$ is completed by four hydroxo- and four carboxylate oxygen donors of four different ligand molecules. $\text{Nd}(6)$ is an eight-coordinate distorted square antiprism and the inner coordination sphere is filled by two carboxylate-O centres of two ligands, four water molecules $\text{O}(153\text{w})$, $\text{O}(154\text{w})$, $\text{O}(155\text{w})$ and $\text{O}(156\text{w})$ and completed by two bridging $\mu_3\text{-OH}$ centres. The remaining Nd^{III} ions, $\text{Nd}(2)$, $\text{Nd}(3)$, $\text{Nd}(4)$, $\text{Nd}(5)$, $\text{Nd}(7)$ and $\text{Nd}(9)$ are all 9-coordinate. The coordination geometry of $\text{Nd}(2)$, $\text{Nd}(3)$ and $\text{Nd}(9)$ can be viewed as a distorted capped square antiprism comprised of four carboxylate oxygen donors of two ligands, one hydroxo-donor and one N-donor of one organic ligand and three water molecules; $\text{O}(145\text{w})$, $\text{O}(146\text{w})$ and $\text{O}(147\text{w})$ for $\text{Nd}(2)$, $\text{O}(148\text{w})$, $\text{O}(149\text{w})$ and $\text{O}(150\text{w})$ for $\text{Nd}(3)$ and $\text{O}(157\text{w})$, $\text{O}(158\text{w})$ and $\text{O}(159\text{w})$ for $\text{Nd}(9)$. $\text{Nd}(4)$ is also 9-coordinate but may be viewed as a distorted tricapped-trigonal prism consisting of five carboxylate O-donors on four distinct ligand molecules, one hydroxo oxygen-donor $\text{O}(62)$ and a nitrogen atom $\text{N}(64)$ of one of these ligands. The remaining coordination sites are occupied by two water molecules $\text{O}(151\text{w})$ and $\text{O}(152\text{w})$. The $\text{Nd}(5)$ centre may be visualised as a distorted capped square antiprism stabilised by five carboxylate O-donors originating from four ligands, one hydroxo-donor $\text{O}(86)$ and the nitrogen atom $\text{N}(88)$ of one of these ligands. Two $\mu_3\text{-OH}$ bridging groups, $\text{O}(160)$ and $\text{O}(161)$, complete the coordination sphere. The $\text{Nd}(7)$ centre is a 9-coordinate distorted capped square antiprism coordinated through five carboxylate O-donors originating from four ligands including the hydroxo $\text{O}(110)$ and $\text{N}(112)$ of one of these ligands. The remaining sites are occupied by the μ_3 -hydroxo, $\text{O}(160)$ and $\text{O}(161)$, centres.

The Nd-O bond lengths vary considerably depending on the nature of the interaction as summarised **Table 5.6**. Longer Nd-O bond lengths are observed for the chelating O-donor atoms when the aromatic carboxylate adopts a chelate-bridging mode. The bond lengths of the chelating O-donors range between 2.608–2.807 Å. These longer bond distances are due to the O-centre bearing less of the negative charge of the carboxylate function and as a result of the steric restraints placed by the aromatic ligand and its adjacent coordinating moieties.²⁵ The remaining Nd-O bond lengths are shorter, ranging between 2.371–2.570 Å, and reflect standard Ln-O distances as reported in the literature.¹⁸ The N-atom of each ligand coordinates a Nd^{III} centre with long bond distances of the order 2.658–2.749 Å. The bonding interaction is electrostatic through the lone pair of electrons, resulting in the long distances. The bond lengths for coordinated water molecules

range between 2.457-2.660 Å. Such long bond lengths are due to the more electrostatic nature of the coordination.

Table 5.9: Selected bond lengths for **6**.

Bond	Bond Length (Å)	Bond	Bond Length (Å)
Nd(4)-O(1)	2.807(8)	Nd(1)-O(14)	2.453(7)
Nd(4)-O(2)	2.546(7)	Nd(1)-O(38)	2.440(7)
Nd(1)-O(2)	2.430(7)	Nd(4)-O(62)	2.475(7)
Nd(1)-O(50)	2.421(7)	Nd(5)-O(86)	2.470(7)
Nd(2)-O(73)	2.608(7)	Nd(8)-O(110)	2.456(6)
Nd(2)-O(74)	2.470(7)	Nd(8)-O(134)	2.469(7)
Nd(1)-O(74)	2.442(7)	Nd(9)-O(134)	2.448(7)
Nd(8)-O(98)	2.443(7)	Nd(2)-O(145w)	2.505(8)
Nd(7)-O(25)	2.392(7)	Nd(2)-O(146w)	2.598(7)
Nd(5)-O(26)	2.658(6)	Nd(3)-O(149w)	2.660(8)
Nd(5)-O(121)	2.371(7)	Nd(3)-O(150w)	2.505(8)
O(23)-Nd(4)#1	2.570(9)	Nd(6)-O(154w)	2.542(8)
Nd(7)-O(20)	2.540(7)	Nd(6)-O(156w)	2.457(8)
O(140)-Nd(5)#1	2.516(7)	Nd(9)-O(158w)	2.616(9)
Nd(3)-O(43)	2.418(7)	O(160)-Nd(6)	2.380(8)
Nd(4)-O(67)	2.408(7)	O(160)-Nd(7)	2.427(7)
Nd(5)-O(95)	2.435(7)	O(161)-Nd(5)	2.421(7)
Nd(7)-O(119)	2.419(7)	O(161)-Nd(6)	2.415(7)
Nd(9)-O(143)	2.446(8)	Nd(4)-N(64)	2.718(9)
Nd(2)-N(16)	2.658(9)	Nd(7)-N(112)	2.749(9)

As in the structure of **5**, the arrangement of the Nd^{III} centres in **6** leads to the formation of two different distorted tetrahedrons, *TH1* and *TH2* (**Figure 5.17**). At the centre of *TH1* is Nd(1) with Nd(2), Nd(3), Nd(4) and Nd(5) at the four vertices. Each Nd^{III} centre in this tetrahedral unit is connected to the adjacent centres through edge-sharing interactions, being bridged by four ligand molecules. The second tetrahedral unit, *TH2*, is also stabilised by four ligand molecules. It consists of a Nd(8) in the centre, while the vertices are represented by Nd(7), Nd(9) and their symmetry equivalents Nd(7') and Nd(9'). The units, *TH1* and *TH2*, are bridged by a {NdO₈} polyhedra, Nd(6), which shares a common face with Nd(5) through O(160), O(161) and O(91) and a separate common face with Nd(7) of *TH2* through O(160), O(161) and O(115). By bridging the tetrahedral units through the Nd(6) polyhedra, an infinite 1D chain [Nd₁₇(C₃hnda)₁₂(μ₃-OH)₄(H₂O)₃₀]_n is generated through an *TH1*:Nd(6):*TH2*:Nd(6):*TH1* arrangement (**Figure 5.18a**).

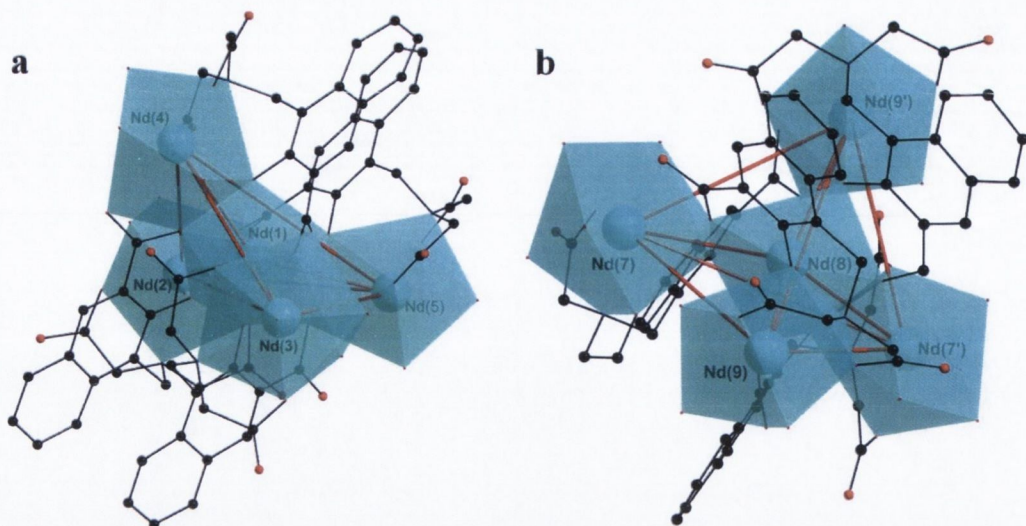


Figure 5.17: Polyhedral representations of the individual units used to construct $[\text{Nd}_{17}(\text{C3hnida})_{12}(\mu_3\text{-OH})_4(\text{H}_2\text{O})_{30}]_n$ in **6** (a) Tetrahedral unit 1, *TH1* and (b) tetrahedral unit 2, *TH2*. Nd cyan polyhedra, C black, N blue, O red. Red bonds denote the imaginary Nd-Nd bonds that identify the unit description.

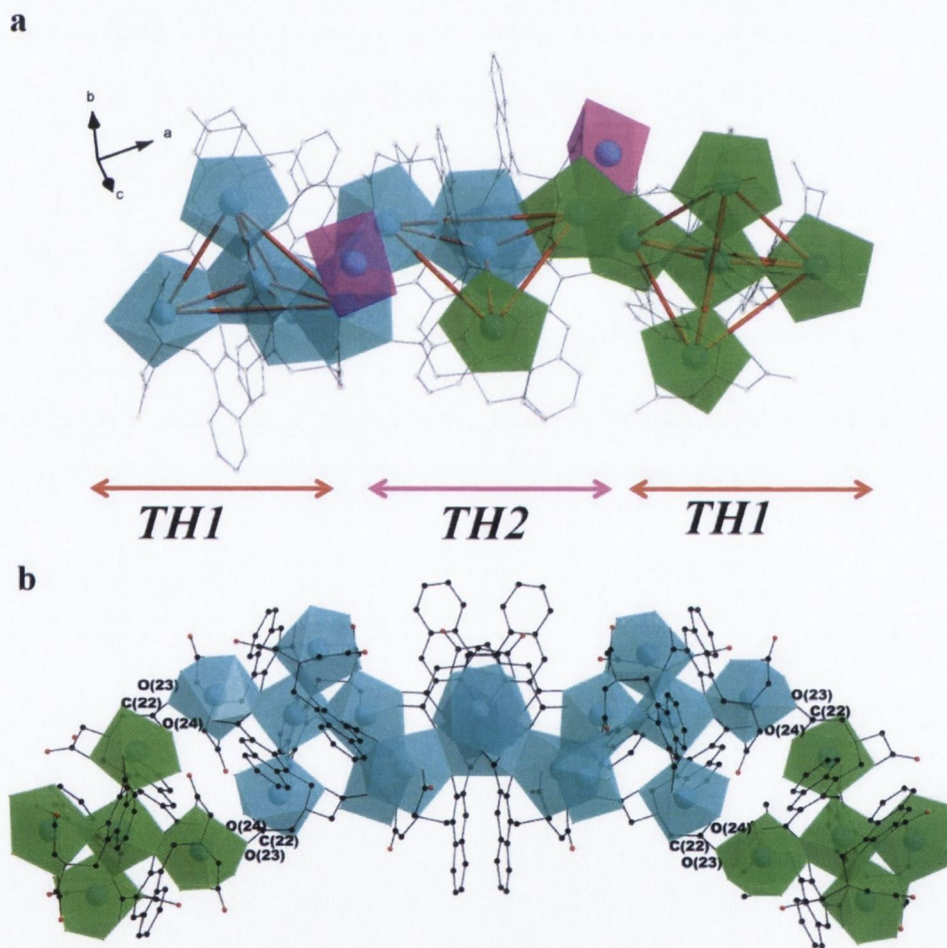
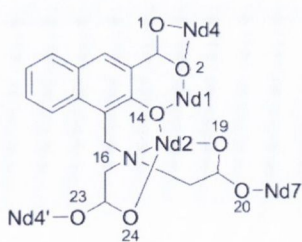
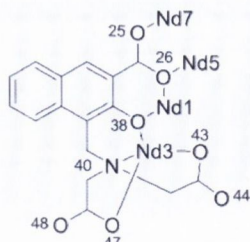


Figure 5.18: Polyhedral representation of **6** to show (a) the $[\text{Nd}_{17}(\text{C3hnida})_{12}(\mu_3\text{-OH})_4(\text{H}_2\text{O})_{30}]_n$ unit built from two asymmetric units. The individual asymmetric units have been identified for clarity as blue and green polyhedral representations. Nd(6) that bridges *TH1* and *TH2* are highlighted as purple polyhedra. Ligand molecules are faded for clarity. (b) A central $[\text{Nd}_{17}(\text{C3hnida})_{12}(\mu_3\text{-OH})_4(\text{H}_2\text{O})_{30}]$ unit (blue polyhedra) and the coordination bonds to adjacent $[\text{Nd}_{17}(\text{C3hnida})_{12}(\mu_3\text{-OH})_4(\text{H}_2\text{O})_{30}]$ units (green polyhedra) in the formation of 1D infinite chains.



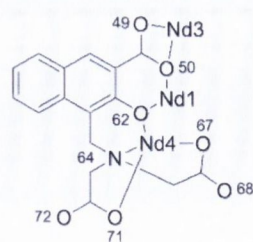
Ligand 1

$\eta^1: \eta^2: \eta^2: \eta^1: \eta^1: \eta^1: \eta^1-\mu_5$



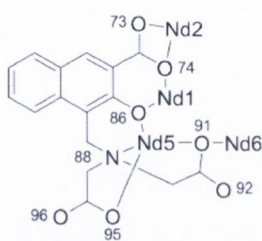
Ligand 2

$\eta^1: \eta^2: \eta^2: \eta^1: \eta^1: \eta^1: \eta^0-\mu_4$



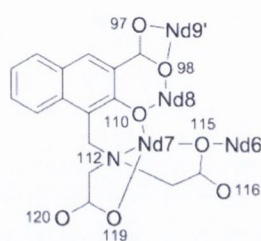
Ligand 3

$\eta^1: \eta^2: \eta^2: \eta^1: \eta^0: \eta^1: \eta^0-\mu_3$



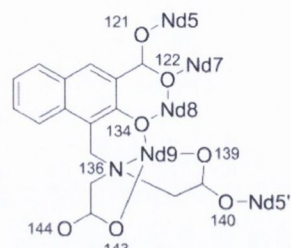
Ligand 4

$\eta^1: \eta^2: \eta^2: \eta^2: \eta^0: \eta^1: \eta^0-\mu_4$



Ligand 5

$\eta^1: \eta^2: \eta^2: \eta^2: \eta^0: \eta^1: \eta^0-\mu_4$



Ligand 6

$\eta^1: \eta^2: \eta^2: \eta^1: \eta^1: \eta^1: \eta^0-\mu_5$

Scheme 5.9: Atom numbering for **Ligand 1-6** and the coordination modes adopted to the Nd^{III} centres in **6**.

There are six crystallographically-unique ligand molecules required to describe the coordination in **6**. **Ligand 1** adopts a $\eta^1: \eta^2: \eta^2: \eta^1: \eta^1: \eta^1: \eta^1-\mu_5$ bonding description (**Scheme 5.9**) where the carboxylate O(1) and O(2) donors display a chelate-bridging mode to Nd(4) and O(2) further bridges to Nd(1). The hydroxo-O(14) forms a further μ_2 -bridge between Nd(1) and Nd(2). On the acetate arms, the donor atoms O(19) and O(20) form an *anti, syn*-bridge to Nd(2) and Nd(7), respectively. The oxygen donor atoms O(23) and O(24) further bridge Nd(2) and symmetry related Nd(4'), respectively, through an *syn, anti*-interaction. The N(16) donor atom coordinates to Nd(2). The bonding description of **Ligand 2** is $\eta^1: \eta^2: \eta^2: \eta^1: \eta^1: \eta^1: \eta^0-\mu_4$ and bonds to four Nd centres. The aromatic carboxylate forms a *syn*-monodentate interaction to Nd(7) through the donor atom O(25), while the donor O(26) bridges Nd(5) and Nd(1) in a μ_2 -manner. The hydroxo-O(38) bridges the Nd(1) and Nd(3) in a μ_2 -bridging mode. The oxygen donors, O(43) and O(47), of each acetate coordinate the Nd(3) centre through a monodentate *anti*-interaction along with a bond formed from the N(40) donor atom. The O(44) and O(48) do not bond with any Nd^{III} ions. **Ligand 3** coordinates only three Nd^{III} centres in a $\eta^1: \eta^2: \eta^2: \eta^1: \eta^0: \eta^1: \eta^0-\mu_3$ bridging mode. The naphthyl carboxylate donors, O(49) and O(50) form a chelate-bridging interaction to Nd(3) and Nd(1). The adjacent hydroxo-O(62) forms μ_2 -bridge between Nd(1) and Nd(4). This leaves the oxygen centres, O(67) and O(71), of each acetate to bond through a monodentate-*anti* fashion to Nd(4). The N(64) atom completes the ligand coordination to Nd(4). **Ligand 4** adopts a $\eta^1: \eta^2: \eta^2: \eta^2: \eta^0: \eta^1: \eta^0-\mu_4$ bridging mode to four Nd^{III} ions. A chelate-bridging mode is adopted by the aromatic carboxylate through the donors, O(73) and (74), to Nd(2) and Nd(1), respectively. The O(86) of the hydroxo-moiety bridges Nd(1) and Nd(5). Nd(5) is further bonded by the N(88) donor atom from the imino-

moiety. A monodentate-*anti* bond forms between Nd(5) and the donor O(95) whereas the O(91) forms a μ_2 -bridge between Nd(5) and Nd(6). The donor atoms O(92) and O(96) of each acetate remain uncoordinated. **Ligand 5** adopts a $\eta^1: \eta^2: \eta^2: \eta^2: \eta^0: \eta^1: \eta^0-\mu_4$ bridging mode to four Nd^{III} centres, similar to the previous ligand. The familiar chelate-bridging interaction from the donor atoms O(97) and O(98) to a symmetry equivalent Nd(9') and Nd(8) centres is observed. The hydroxo-O(110) coordinates two centres, Nd(8) and Nd(7). The imino-moiety is involved in bonding to Nd(7) through N(112) while O(115) forms a μ_2 -bridge between Nd(7) and Nd(6). On the remaining acetate arm, only the donor atom, O(119) coordinates Nd(7) through a monodentate-*anti* interaction. **Ligand 6** displays a $\eta^1: \eta^2: \eta^2: \eta^1: \eta^1: \eta^1: \eta^0-\mu_5$ binding scheme to five Nd^{III} centres. On the aromatic carboxylate, the donor O(121) binds through a monodentate-*syn* interaction to Nd(5), while O(122) binds through a μ_2 -bridge to Nd(7) and Nd(8). The hydroxo-O(134) has a similar μ_2 -connection but to Nd(8) and Nd(9). On the imino-functionality, N(136) coordinates Nd(9), as do O(139) and O(143) through monodentate-*anti* coordination modes. The donor, O(140) forms a monodentate-*syn* interaction with a symmetry related Nd(5') while O(144) remains uncoordinated.

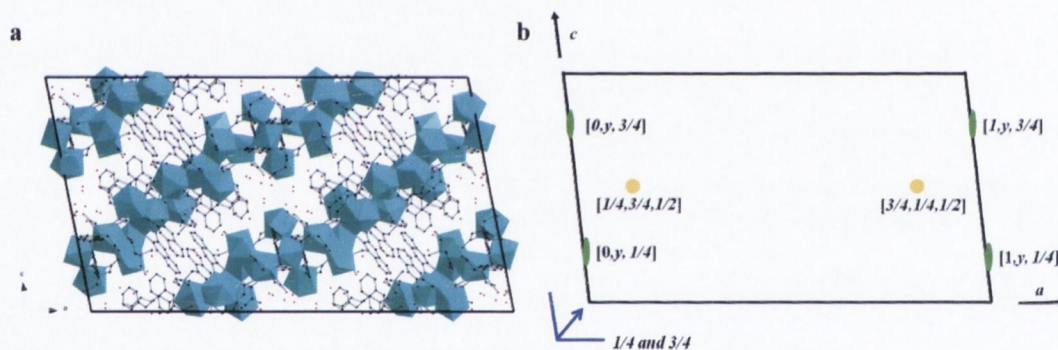


Figure 5.19: (a) View in the *ac*-plane of *Y* where chains of $[\text{Nd}_{17}(\text{C3hnida})_{12}]_n$ run in the $[1,0,1]$ direction and (b) symmetry elements and their coordinates used to generate infinite 1D chains as viewed in the *ac*-plane.

The $[\text{Nd}_{17}(\text{C3hnida})_{12}(\text{H}_2\text{O})_{30}]_n$ unit can be expanded in space through the presence of inversion centres at $(1/4,1/4,1/2)$ and its related positions and a glide plane that runs perpendicular to the *b*-axis with translation component $[1/2,0,1/2]$, resulting in infinite 1D chains that run along the $[1,0,1]$ direction (**Figure 5.19**).

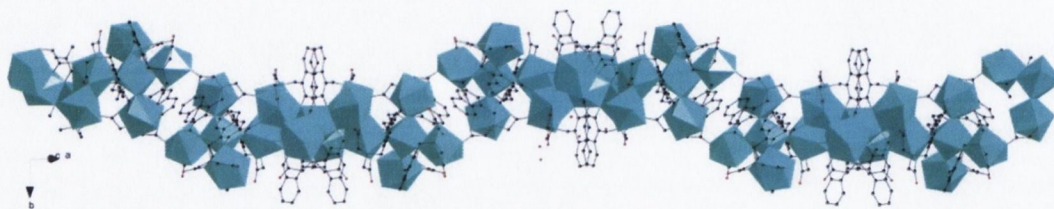


Figure 5.20: Wave-like motif adopted by infinite 1D chains of **6**.

Each $[\text{Nd}_{17}(\text{C3hnida})_{12}(\mu_3\text{-OH})_4(\text{H}_2\text{O})_{30}]_n$ unit is bridged through two **Ligand 1** molecules. This bridge is made between one acetate arm of each ligand where O(23) bonds to Nd(4) and O(24) bonds to Nd(2), both through a monodentate-*anti* interaction (**Figure 5.18b**). These bonding interactions create a small cavity and it is at the centre of this cavity that an inversion centre resides that generates the symmetry equivalent along [1,0,1]. The consequence of the glide plane is to displace two adjacent $[\text{Nd}_{17}(\text{C3hnida})_{12}(\mu_3\text{-OH})_4(\text{H}_2\text{O})_{30}]_n$ units above and below the plane of the glide-component. This leads to the wave-like motif of the 1D chains that run along [1,0,1] (**Figure 5.20**).

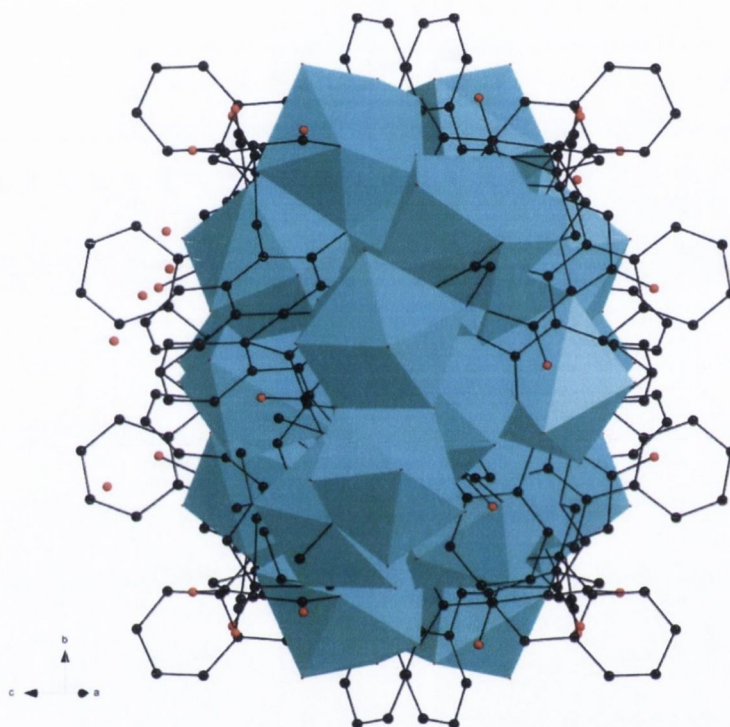


Figure 5.21: View down an infinite 1D chain of **6** looking down the [101] axis. The stabilisation of the chain by the ligand molecules leads to a hydrophobic exterior.

The nature of the chain itself can be described as an inorganic core of repeating $\{\text{Nd}_{17}\}$ units surrounded on the outside by the hydrophobic organic moieties (**Figure 5.21**). Due to the imposed symmetry, the chains pack in the [1,0,1] plane and result in hydrophobic areas occupied by naphthyl moieties and hydrophilic pockets where the solvent water molecules are located in a disordered state (**Figure 5.19a**). The structure data and refinement details for the structure model are summarised in **Table 5.10**.

Table 5.10: Crystal data and structure refinement for **6**.

Identification code	6	
Empirical formula	C ₁₉₂ H ₁₉₂ N ₁₂ Nd ₁₇ O ₁₁₈	
Formula weight	6947.17	
Temperature	293(2) K	
Wavelength	0.71073 Å	
Crystal system	Monoclinic	
Space group	C 2/c	
Unit cell dimensions	a = 53.298(11) Å	α = 90°.
	b = 17.206(3) Å	β = 101.03(3)°.
	c = 30.488(6) Å	γ = 90°.
Volume	27442(10) Å ³	
Z	4	
Density (calculated)	1.681 Mg m ⁻³	
Absorption coefficient	3.240 mm ⁻¹	
F(000)	13328	
Crystal size	0.250 × 0.200 × 0.200 mm ³	
Theta range for data collection	1.692 to 27.500°.	
Index ranges	-51 ≤ h ≤ 68, -22 ≤ k ≤ 13, -39 ≤ l ≤ 39	
Reflections collected	130353	
Independent reflections	30959 [R(int) = 0.0814]	
Completeness to theta = 25.242°	99.3 %	
Refinement method	Full-matrix least-squares on F ²	
Data / restraints / parameters	30959 / 38 / 1537	
Goodness-of-fit on F ²	1.227	
Final R indices [I > 2σ(I)]	R1 = 0.0824, wR2 = 0.1623	
R indices (all data)	R1 = 0.0938, wR2 = 0.1671	
Extinction coefficient	n/a	
Largest diff. peak and hole	2.775 and -4.151 e.Å ⁻³	

5.4.2.2 Physicochemical characterisation of **6**

The FT-IR spectrum of **6** in **Figure 5.22a** confirms the coordination of the ligand to the Nd^{III} centres. In **6**, the asymmetric (1584 and 1533 cm⁻¹) and symmetric (1393 and 1308 cm⁻¹) CO₂⁻ stretches are significantly shifted from the free ligand, indicating coordination to Nd^{III} centres. The values for Δ=[ν_{asym}(CO₂⁻)-ν_{sym}(CO₂⁻)] are found to range between 140-276 cm⁻¹ and support the observation that monodentate and bridging interactions are adopted as the coordination modes of the ligand. The structural rigidity of the ligand is maintained as the C-N stretch of the imino-moiety is identified at 1210 cm⁻¹. There are additional weak C-H stretches at 2975, 2955 and 2914 cm⁻¹ which are superimposed on the broad band between 3000-3500 cm⁻¹ arising from stretches of coordinated and solvent water molecules. The PXRD pattern indicates the bulk phase is crystalline and by matching the reflections with the calculated pattern (**Figure 5.22b**) shows the material is phase pure. The thermal stability of **6** was investigated by TGA in an air atmosphere and heated between 30-900 °C at a rate of 10 °C/min (**Figure 5.22c.**) The first gravimetric event below 100 °C is assigned to the loss of 25 solvent water molecules resulting in a loss of 6.0% (*calc.* 6.0%). The second weight loss occurs above 400 °C, resulting from the oxidative decomposition of the organic

ligands (obs. 45.2%, calc. 34.9%). It is noted that the void space contained a high number of disordered solvent molecules and the Platon routine SQUEEZE was used to refine the structure to account for this. The SQUEEZE results indicate a considerably higher solvent water count in the structure. This disagreement with the thermal analysis may be understood through the loss of solvent water molecules to the atmosphere from the bulk sample as a consequence of the loose packing of the individual chains in the structure.

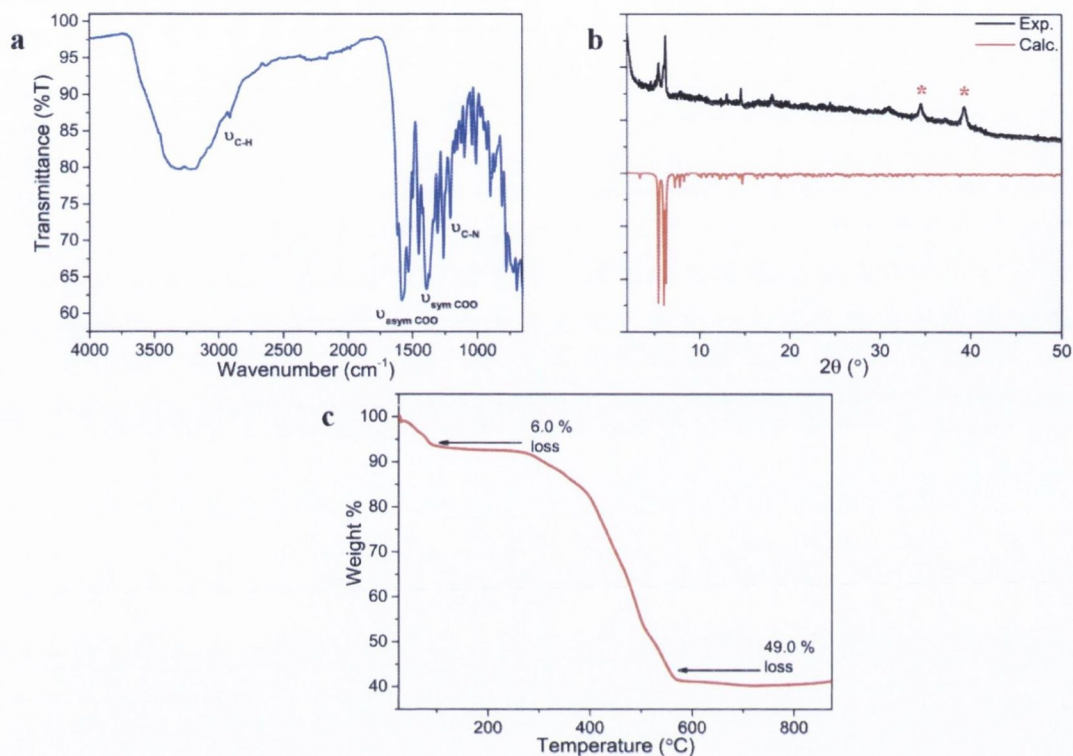


Figure 5.22: (a) The FT-IR spectrum for **6**, (b) the powder X-ray diffraction pattern for a bulk crystalline sample of **6** and (c) the thermogram of **6** in air (fresh crystalline sample). * indicate reflections from instrumental artefacts.

5.4.2.3 Photoluminescence properties of **6**

As observed for **5-Nd**, the NIR emission bands from the $^4F_{3/2} \rightarrow ^4I_{J/2}$ ($J = 13, 11, 9$) transitions of Nd^{III} are observed at 872, 1056 and 1328 nm, respectively (**Figure 5.23a**) by direct excitation into the Nd^{III} centre or *via* ligand excitation. Direct excitation of the Nd^{III} centres is achieved by exciting in the visible region into the $^2L_{15/2}$, $^4G_{7/2-5/2}$, $^4S_{7/2}$ and $^4F_{7/2}$ excited states. This is reflected in the RT excitation spectrum (**Figure 5.23b**), which also has an intense absorption in the UV region (367 nm) and originates from ligand absorption, as identified in **Figure 5.1a**. When excited in this range, the Nd^{III} emission spectrum is observed, indicating sensitisation from the ligand.

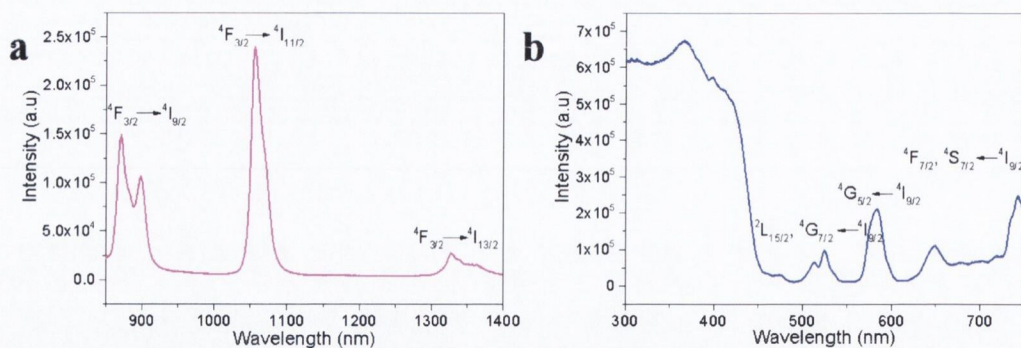


Figure 5.23: (a) RT PL spectrum of **6** following ligand sensitisation ($\lambda_{\text{ex}} = 415$ nm) and (b) corresponding RT excitation spectrum ($\lambda_{\text{em}} = 1056$ nm, ${}^4F_{3/2} \rightarrow {}^4I_{11/2}$ transition) in the solid-state.

5.5 Conclusions

The chemistry of two naphthol-substituted ligands has been investigated. When the ligand $H_4C6hnida$ is reacted solvothermally, the ligand undergoes decomposition and a subsequent reaction between formaldehyde and two equivalents of 6-hydroxy-2-naphthoic acid yields an isomer of pamoic acid, an important ingredient in pharmaceutical work-ups. Our synthesis provides a route to which crystallisation of similar compounds can be achieved and provides important structural information on the packing of these compounds in the pharmaceutical industry.

By tuning towards milder reactions conditions (lower temperatures and basicity), we have demonstrated these ligands can be used to isolate new lanthanide hybrid materials, **5** and **6**. These are the first lanthanide compounds reported to date with these ligands. The structure of **5** forms a 3D network with chiral channels along the c -axis and contains both hydrophobic and hydrophilic channels along the a - and b -axes. These channels offer opportunities for future work to investigate chiral separations and through careful selection of the lanthanide centre may allow opportunities for sensing of small molecules and ions that can be screened by exploiting the hydrophobic and hydrophilic nature of the channels. We have already investigated the PL properties of the isostructural analogues of **5**, where $\text{Ln}^{\text{III}} = \text{Nd}^{\text{III}}, \text{Yb}^{\text{III}}$ and Eu^{III} , which show that the ligand $H_4C3hnida$ is particularly good at sensitising NIR emission. We also note the space group, $P3_221$, is one of the polar space groups and these materials may show interesting ferroelectric properties. These avenues will be investigated in future work.

Increasing the temperature results in the 1D wave-like chains of **6**, which was shown to display a strong Nd^{III} PL response upon ligand sensitisation. This shows that iminodiacetic acid substituted naphthols display a coordination tendency towards high dimensional hybrid networks that can be controlled through variation of reaction temperature. In contrast, if cluster-based materials are desired, then the ligands such as H_3heidi of Chapter 4 are favoured. This chapter further expands on previous work of these ligands with Fe^{III} and Cu^{II} ions that resulted in large 3D networks and provides an alternative synthetic approach with the use of solvothermal conditions.

These early structures suggest that a wealth of new materials may be accessed by adapting these synthetic approaches to related substituted naphthol and phenol derived ligands.

5.6 References

1. W. Schmitt, J. P. Hill, S. Malik, C. A. Volkert, I. Ichinose, C. E. Anson and A. K. Powell, *Angew. Chem. Int. Ed.*, 2005, **44**, 7048-7053.
2. W. Schmitt, J. P. Hill, M. P. Juanico, A. Caneschi, T. Costantino, C. E. Anson and A. K. Powell, *Angew. Chem. Int. Ed.*, 2005, **44**, 4187-4192.
3. G. La Spina, R. Clerac, E. S. Collins, T. McCabe, M. Venkatesan, I. Ichinose and W. Schmitt, *Dalton Trans.*, 2007, 5248-5252.
4. W. Schmitt, M. Murugesu, J. C. Goodwin, J. P. Hill, A. Mandel, R. Bhalla, C. E. Anson, S. L. Heath and A. K. Powell, *Polyhedron*, 2001, **20**, 1687-1697.
5. I. McKeogh, J. P. Hill, E. S. Collins, T. McCabe, A. K. Powell and W. Schmitt, *New J. Chem.*, 2007, **31**, 1882-1886.
6. F. Bayrakceken, *Spectrochim. Acta, Part A*, 2008, **71**, 603-608.
7. T. Suthan, N. P. Rajesh, P. V. Dhanaraj and C. K. Mahadevan, *Spectrochim. Acta, Part A*, 2010, **75**, 69-73.
8. H. Peters, *Anal. Chem.*, 1959, **31**, 1326-1331.
9. H. Sponer and G. P. Nordheim, *Discuss. Faraday Soc.*, 1950, 19-26.
10. V. J. Hammond, W. C. Price, J. P. Teegan and A. D. Walsh, *Discuss. Faraday Soc.*, 1950, 53-60.
11. K. Kimura, H. Tsubomura and S. Nagakura, *Bull. Chem. Soc. Jpn.*, 1964, **37**, 1336-1346.
12. M. Godfrey and J. N. Murrell, *Proc. R. Soc. London, Ser. A*, 1964, **278**, 57-63.
13. M. Godfrey and J. N. Murrell, *Proc. R. Soc. London, Ser. A*, 1964, **278**, 64-70.
14. M. Godfrey and J. N. Murrell, *Proc. R. Soc. London, Ser. A*, 1964, **278**, 71-90.
15. D. A. Haynes, W. Jones and W. D. S. Motherwell, *CrystEngComm*, 2005, **7**, 538-543.
16. D. A. Haynes, Z. F. Weng, W. Jones and W. D. S. Motherwell, *CrystEngComm*, 2009, **11**, 254-260.
17. H. Wahl, D. A. Haynes and T. le Roex, *Chem. Commun.*, 2012, **48**, 1775-1777.
18. P. Silva, L. Cunha-Silva, N. J. O. Silva, J. Rocha and F. A. A. Paz, *Cryst. Growth Des.*, 2013, **13**, 2607-2617.
19. Y. Miyashita, M. Sanada, Y. Yamada, K. Fujisawa and K. Okamoto, *Chem. Lett.*, 2002, **31**, 840-841.
20. G. Tircso, A. Benyei, E. Brucher, A. Kis and R. Kiraly, *Inorg. Chem.*, 2006, **45**, 4951-4962.
21. Y. Miyashita, M. Sanada, M. M. Islam, N. Amir, T. Koyano, H. Ikeda, K. Fujisawa and K. Okamoto, *Inorg. Chem. Commun.*, 2005, **8**, 785-788.
22. E. E. Martsinko, S. S. Smola, L. K. Minacheva, Seifullina, II and V. S. Sergienko, *Russ. J. Inorg. Chem.*, 2009, **54**, 1041-1048.
23. A. Beeby, D. Parker and J. A. G. Williams, *J. Chem. Soc., Perkin Trans. 2*, 1996, 1565-1579.
24. N. Sabbatini, M. T. Indelli, M. T. Gandolfi and V. Balzani, *J. Phys. Chem.*, 1982, **86**, 3585-3591.
25. S. M. F. Vilela, D. Ananias, P. Silva, M. Nolasco, L. D. Carlos, V. de Zea Bermudez, J. Rocha, J. P. C. Tome and F. A. Almeida Paz, *CrystEngComm*, 2014, **16**, 8119-8137.

Chapter Six

.....

Probing the optical activity of chiral networks derived from achiral ligands

6.1 Introduction

Chirality in lanthanide complexes can be achieved through two main strategies: (i) The chiral arrangement of the ligands around the lanthanide centre, where examples of the formation of double and triple helices are known.¹⁻⁴ This may also be achieved through the twist of a macrocycle ligand.^{5, 6} Alternatively, achiral ligands can be used where the arrangement of the ligand around the centre imparts the chirality. (ii) Introduction of at least one asymmetric carbon centre *via* a chiral ligand results in the chiral lanthanide complex. To interrogate the chiral nature of these complexes, two techniques are often used; circular dichroism (CD) and circularly polarised luminescence (CPL).⁷ CD is the measurement of the difference in absorption between left- and right-polarised light and can be viewed as probing the environment of the complex while in the ground state. In contrast, CPL measures the difference of the emission intensity of left- and right-circularly polarised light and probes the environment of the complex in its excited state.

Chiral lanthanide complexes are typically studied in solution and, as such, have been developed towards sensing of amino acids and metal ions of biological importance.⁸⁻¹² The method of sensing depends on the type of complex investigated. Lanthanide complexes of 2,6-pyridinedicarboxylic acid, DPA, $[\text{Ln}(\text{DPA})_3]^{3-}$ form as a racemic equilibrium of the chiral isomers, Δ - and Λ -, in solution. In sensing of chiral organic molecules, such as tartrate and amino acids, addition of the analyte results in a perturbation of the racemic equilibrium between Δ - and Λ -isomers and a non-racemic ground state is obtained.⁹⁻¹²

In lanthanide complexes derived from chiral ligands, the sensing of ions has been probed through coordination to the lanthanide centre, where the anion-lanthanide complex results in a structural change which generates a “fingerprint” chiral response. This approach often requires the substitution of a labile coordinated water molecule by the analyte. From this approach, two different ligand families have been developed. In non-aqueous media, tripodal ligands derived from an amine backbone have proven successful at sensing inorganic anions, in particular, the ligand tri(2-pyridylmethyl)amine displayed anion selectivity just by changing the lanthanide ion (Eu^{III} or Tb^{III}).¹³ In aqueous media, derivatives of the 1,4,7,10-tetraazacyclododecane-1,4,7,10-tetraacetic acid (DOTA) have also proven very successful in sensing organic anions including bicarbonate,¹⁴ α -hydroxy acids,^{15, 16} amino acids^{17, 18} and dipeptides.¹⁷ These systems are well-understood and may now be used in selective sensing of particular proteins such as binding sites in serum albumin.¹⁹ These DOTA-derived ligands have also proven useful at sensing through coordination to the antenna ligand/ receptor. With this approach, sensing of nucleotides and nucleic acids has been shown through intercalation between the antenna receptor and the base pairs of the analyte.²⁰⁻²⁵

Despite the extensive research into the aqueous characterisation of chiral lanthanide complexes, understanding of these properties in the solid-state is still limited. Recently a few reports have started to look at aspects of optical activity of chiral materials in the solid-state. In this respect, CD spectroscopy has successfully been used to demonstrate chiral resolution and

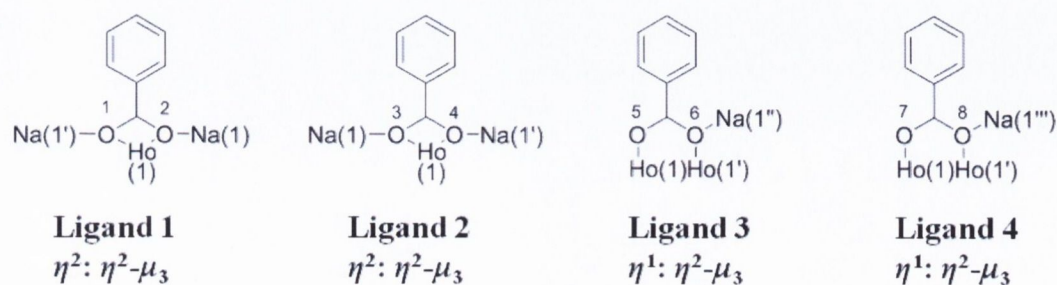
separation of opposite enantiomers of solid-state complexes.^{26, 27} In one case of a chiral lanthanide silico-germanate, steady-state PL measurements using unpolarised light could also probe the chirality. When a high-energy charge-transfer band was excited, the number of Stark components of the $^5D_0 \rightarrow ^7F_{1,2}$ transitions was found to double compared to the number of bands observed following direct $f-f$ excitation. This was found to be due to the detection of enantiomeric domains in the structure. To the best of our knowledge, however, no CPL measurements have been performed in the solid-state on chiral lanthanide complexes.^{28, 29}

The aim of this chapter is to investigate the optical activity of chiral 3D networks derived from the achiral ligand, benzoic acid, by a combination of X-ray crystallography and CD spectroscopy. By identifying chiral properties in the structure, the potential for development of the materials for further study in the solid-state will be discussed.

6.2 Crystal structure of $\text{Na}[\text{Ho}(\text{C}_6\text{H}_5\text{CO}_2)_4]$, (7)

The reaction of $\text{HoCl}_3 \cdot 6\text{H}_2\text{O}$ with one molar equivalent of H_3heidi and three molar equivalents of sodium benzoate in the presence of NaN_3 results in the crystallisation of pink cube crystals of $\text{Na}[\text{Ho}(\text{C}_6\text{H}_5\text{CO}_2)_4]$ after refluxing in 10 mL of MeOH followed by slow evaporation of the solvent. A suitable crystal was isolated from solution and characterised by single crystal X-ray diffraction.

The structure of $\text{Na}[\text{Ho}(\text{C}_6\text{H}_5\text{CO}_2)_4]$, **7**, is a 3D network built from chiral chains of alternating Ho/Na polyhedra and chiral channels occupied by benzoate ligands that run along the c -axis. **7** crystallises in the tetragonal crystal system in the space group $I4_1$. The asymmetric unit consists of one crystallographically unique Ho^{III} centre, four benzoate ligands and a sodium ion to balance for the charge of the complex. The coordination environment of each Ho^{III} centre is 8-coordinate and stabilised by six benzoate molecules (**Figure 6.1**). The organic molecules bind through O(1) and O(2) of **Ligand 1**, O(3) and O(4) of **Ligand 2**, O(5) and O(6') of two **Ligand 3** molecules and the O(7) and O(8') from two **Ligand 4** molecules, respectively, resulting in the formation of a binuclear building unit $\{\text{Ho}_2(\text{CO}_2\text{C}_6\text{H}_5)_8\}^{2-}$ (**Figure 6.1b**). The coordination geometry around the Ho^{III} centre may be visualised as distorted dodecahedron. The Na(1) ion is 6-coordinate and is stabilised through O(2), O(1'), O(3) and O(4') from four terminal benzoates and O(6') and O(8'') from two bridging benzoates.



Scheme 6.1: The coordination modes adopted by **Ligands 1-4** towards Ho^{III} - and Na^+ -centres.

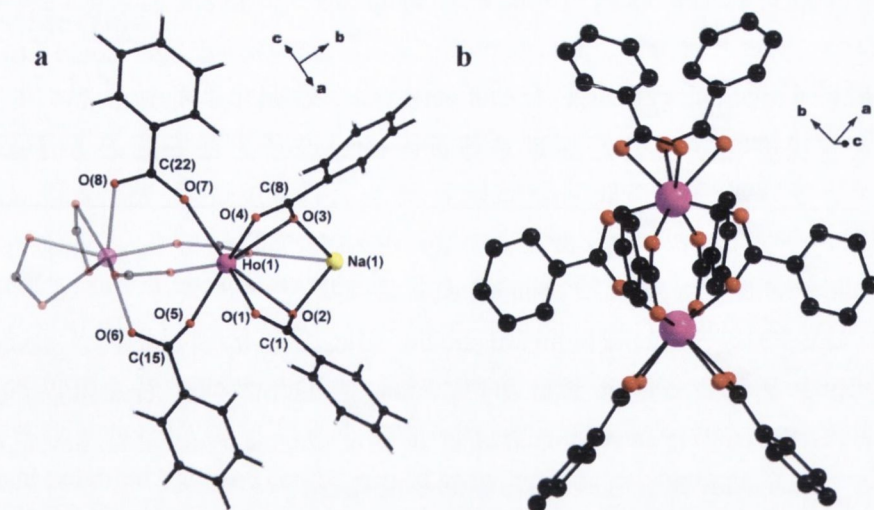


Figure 6.1: (a) Asymmetric unit of $\text{Na}[\text{Ho}(\text{C}_6\text{H}_5\text{CO}_2)_4]$, **7**. Faded atoms highlight symmetry generated atoms to identify the coordination sphere of $\text{Ho}(1)$. (b) The binuclear building unit $\{\text{Ho}_2(\text{CO}_2\text{C}_6\text{H}_5)_8\}^{2-}$ in **7**. Ho magenta, Na yellow, O red, C black and H white.

The four distinct ligand molecules adopt two different coordination modes as visualised in **Scheme 6.1**. **Ligand 1** displays a $\eta^2:\eta^2-\mu_3$ coordination mode and forms chelate-bridging interactions to $\text{Ho}(1)$, $\text{Na}(1')$ and $\text{Na}(1)$ through the $\text{O}(1)$ and $\text{O}(2)$ donors, respectively. **Ligand 2** has the same binding description, where the $\text{O}(3)$ and $\text{O}(4)$ donors form a chelate-bridging interactions to $\text{Ho}(1)$, $\text{Na}(1)$ and $\text{Na}(1')$. **Ligand 3** and **Ligand 4** are described by a $\eta^1:\eta^2-\mu_3$, bridging mode. In **Ligand 3**, $\text{O}(5)$ and $\text{O}(6)$ bridge $\text{Ho}(1)$ and $\text{Ho}(1')$ through a *syn, syn*-interaction and $\text{O}(6)$ forms a μ_2 -bridge between $\text{Ho}(1')$ and $\text{Na}(1'')$. **Ligand 4**, likewise coordinates to $\text{Ho}(1)$ and $\text{Ho}(1')$ through $\text{O}(7)$ and $\text{O}(8)$ by *syn, syn* bridges and $\text{O}(8)$ forms the μ_2 -bridge between $\text{Ho}(1')$ and $\text{Na}(1''')$. The Ho-O bonds range between 2.265–2.478 Å and selected bond lengths are given in **Table 6.1**. The chelating terminal ligands are characterised by one long and one shorter Ho-O bond length, while the ligands that bridge two Ho^{III} centres have the shortest bond lengths between 2.265–2.365 Å.

Table 6.1: Selected bond lengths for **7**.

Bond	Bond Length (Å)	Bond	Bond Length (Å)
Ho(1)-O(1)	2.382(5)	Ho(1)-O(5)	2.271(5)
Ho(1)-O(2)	2.474(5)	Ho(1)-O(6)#1	2.358(5)
Ho(1)-O(3)	2.371(4)	Ho(1)-O(7)	2.265(5)
Ho(1)-O(4)	2.478(5)	Ho(1)-O(8)#1	2.365(5)

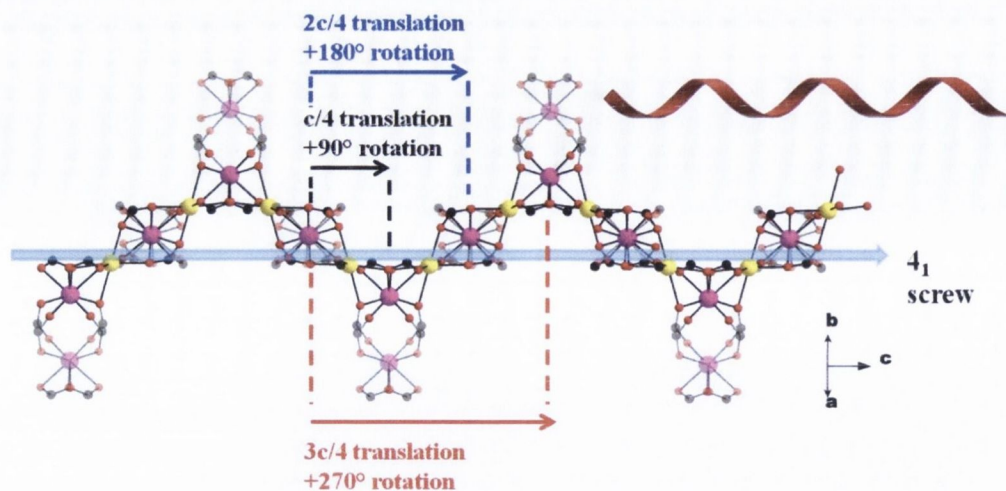


Figure 6.2: Growth of chiral $\text{Ho}^{\text{III}}/\text{Na}^+$ chain along the c -axis through a 4_1 screw axis generating a right-handed helical twist. The upper right inset is a right-hand helix to aid visualisation. Ho magenta, Na yellow, O red, C black. The aromatic ring of the ligand has been removed for clarity.

The building unit $\{\text{Ho}_2(\text{C}_6\text{H}_5\text{CO}_2)_8\}^{2-}$ (**Figure 6.1b**) is bridged in space through the Na^+ counter-ions. There are four unique four-fold screw axes that run along the c -axis and this symmetry generates a chiral chain of alternating $\text{Ho}^{\text{III}}/\text{Na}^+$ polyhedra along this projection with a right-handed helical twist (**Figure 6.2**). Along the chiral chain, the $\{\text{Ho}_2(\text{CO}_2\text{C}_6\text{H}_5)_8\}^{2-}$ building unit orientates perpendicular to the direction of the screw translation in the ab -plane (**Figure 6.3a**). This results in the building units acting as points of extension in the equivalent $[110]$ and $[1\bar{1}0]$ directions. This leads to each chiral chain being bridged to adjacent chains through the $\{\text{Ho}_2(\text{CO}_2\text{C}_6\text{H}_5)_8\}^{2-}$ building unit. In the packing of the unit cell, there are areas of the $\text{Ho}^{\text{III}}/\text{Na}^+$ chains and larger channel voids occupied by the bridging ligand molecules. At the centre of these channel voids runs a four-fold screw axis and results in the chiral packing of the bridging benzoate ligands in space. This creates a 3D network of $\text{Na}[\text{Ho}(\text{C}_6\text{H}_5\text{CO}_2)_4]$ where the structure is mediated by the sodium ions, as shown in **Figure 6.3b**. The 3D structure has two types of channel as a result of the inorganic $\text{Ho}^{\text{III}}\text{-Na}^+$ infinite chain along the c -axis and an adjacent larger channel occupied by the benzoate ligands. The crystal data and structure refinement details are given in **Table 6.2**.

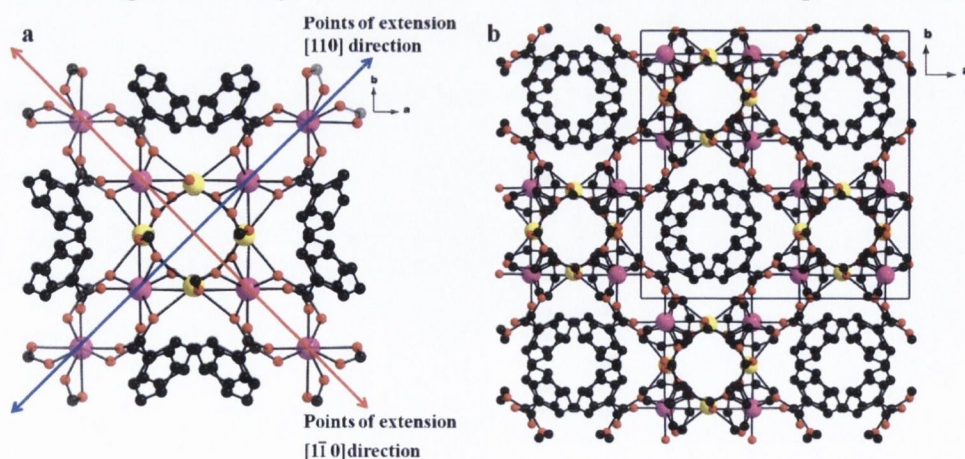


Figure 6.3: (a) View of the chiral $\text{Ho}^{\text{III}}/\text{Na}^+$ chain down the c -axis with the $\{\text{Ho}_2(\text{C}_6\text{H}_5\text{CO}_2)_8\}^{2-}$ orientated in the ab -plane resulting in points of extension in the $[110]$ and $[1\bar{1}0]$ directions to form (b) the 3D network of chiral chains and channels occupied by the bridging benzoate ligands.

Table 6.2: Crystal data and structure refinement for **7**.

Identification code	7	
Empirical formula	NaHoC ₂₈ H ₂₀ O ₈	
Formula weight	672.36	
Temperature	293(2) K	
Wavelength	0.71073 Å	
Crystal system	Tetragonal	
Space group	<i>I</i> ₄	
Unit cell dimensions	a = 16.128(2) Å	α = 90°.
	b = 16.128(2) Å	β = 90°.
	c = 19.534(4) Å	γ = 90°.
Volume	5081.3(18) Å ³	
Z	8	
Density (calculated)	1.758 Mg m ⁻³	
Absorption coefficient	3.182 mm ⁻¹	
F(000)	2640	
Crystal size	0.2 × 0.2 × 0.2 mm ³	
Theta range for data collection	1.637 to 25.022°.	
Index ranges	-18 ≤ h ≤ 19, -18 ≤ k ≤ 17, -19 ≤ l ≤ 22	
Reflections collected	12963	
Independent reflections	4126 [R(int) = 0.0331]	
Completeness to theta = 25.242°	96.1 %	
Refinement method	Full-matrix least-squares on F ²	
Data / restraints / parameters	4126 / 147 / 409	
Goodness-of-fit on F ²	1.178	
Final R indices [I > 2σ(I)]	R1 = 0.0324, wR2 = 0.0848	
R indices (all data)	R1 = 0.0332, wR2 = 0.0854	
Absolute structure parameter	-0.092(7)	
Extinction coefficient	n/a	
Largest diff. peak and hole	0.549 and -0.415 e.Å ⁻³	

It was later found that **7** had already been isolated previously from a reaction of the holmium salt with glycerol, benzoic acid and sodium azide.³⁰ This synthesis uses a co-solvent with methanol and does not appear in the final structure. A similar observation is seen in the isolation of **7** by our synthesis using H₃heidi in our reaction. To understand the influence of H₃heidi in our system, the reaction was repeated in the absence of H₃heidi and it was found that the reaction does not proceed due to early precipitation of the reactants. In **Chapter 4**, it was shown that [Ln(Hheidi)(heidi)]²⁻ is stable in solution. In the synthesis of **7**, it would appear that the H₃heidi ligand initially coordinates the lanthanide centre, as was observed for compound **2** in solution, and over time the H₃heidi is progressively displaced by the benzoate ligands that are present in a larger excess than H₃heidi.

In the previous publication, only the structures of Ho^{III} and Dy^{III} had been isolated. Due to the two sources of chirality in the structure, the compound of **7** seemed an excellent candidate for displaying optical activity that could be exploited in generating circularly polarised luminescence. From this observation, we proceeded to synthesise the Eu^{III}-analogue of **7**, which shall be called **7-Eu** from here on.

6.3 Physicochemical characterisation of 7

The PXRD pattern of **7-Ho** was measured to confirm the purity of the bulk phase. The calculated powder diffraction pattern from the structure model was found to be in excellent agreement with the experimental reflections (**Figure 6.4a**). Efforts were made to isolate single crystals of the Eu^{III}-analogue, **7-Eu**, and quality crystalline material was successfully isolated, however, single crystal XRD showed the crystals to be twinned and a data set suitable for solving could not be measured. To check that **7-Eu** was isostructural, the PXRD pattern of **7-Eu** and **7-Ho** were compared (**Figure 6.4b**) and were found to be in good agreement, indicating that the **7-Eu** displays the same chiral structure.

The FT-IR spectra were measured (**Figure 6.4c**) and both materials show stretching bands originating from the aromatic C=C-H bond around 3000 cm⁻¹ and a weak band at 1738 cm⁻¹ due to C=C stretch. The asymmetric and symmetric stretches of the carboxylate group are located in the range 1614-1496 cm⁻¹ and 1447-1330 cm⁻¹, respectively. By using $\Delta = [v_{\text{asym}}(\text{CO}_2^-) - v_{\text{sym}}(\text{CO}_2^-)]$, Δ values of 92-211 cm⁻¹ were obtained and support assignments of the bridging and chelating coordination modes from the benzoate ligand to the lanthanide centre.

The thermal stability was investigated by TGA (**Figure 6.4d**) in air between 30-900 °C. The compound is stable up to 400 °C where a gravimetric event occurs. This is assigned to the decomposition of four benzoate ligands and results in a 59.4% weight loss (*calc.* 60.1 %). The remaining residue is presumed to be lanthanide oxide.

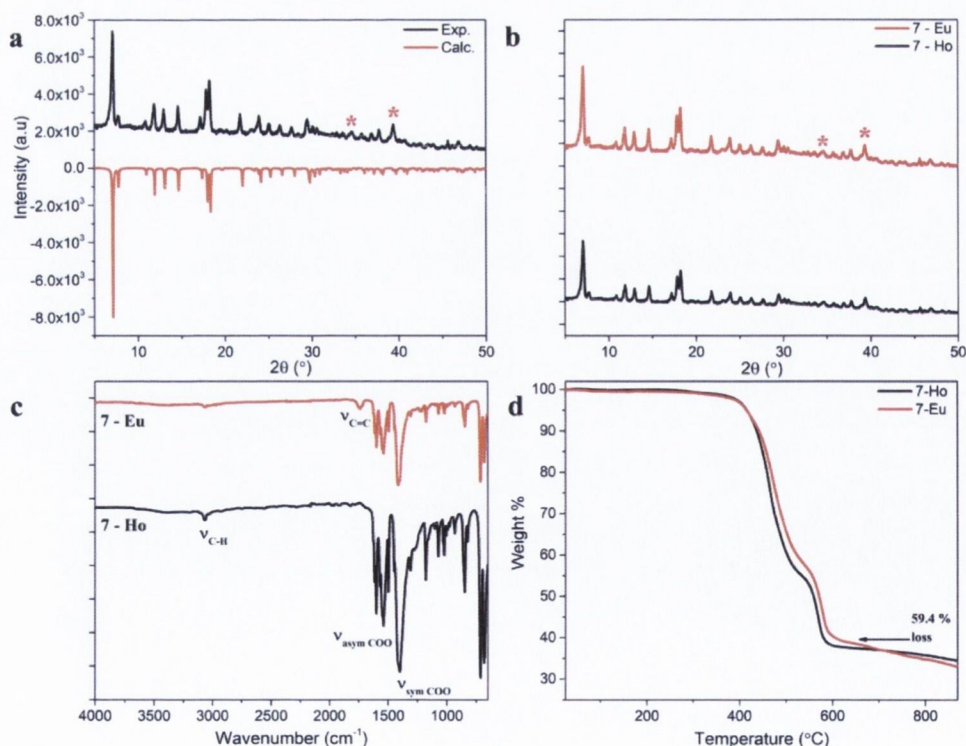


Figure 6.4: (a) Comparison of the experimental vs. calculated PXRD patterns for **7-Ho**. (b) Comparison of the experimental PXRD patterns of **7-Ho** and **7-Eu**. (c) The FT-IR spectra for **7-Ho** and **7-Eu**. (d) Thermogram of **7-Ho** and **7-Eu** in air between 30-900°C. * indicate reflections from instrumental artefacts.

6.4 Investigating the optical activity and emission properties of 7-Eu

6.4.1 UV/Vis Diffuse Reflectance and Circular Dichroism of 7-Eu

The structures of **7-Ho** and **7-Eu** are 3D networks constructed from chiral chains of $\text{Ln}^{\text{III}}/\text{Na}^+$ polyhedra down the *c*-axis with adjacent channel voids occupied by bridging benzoate ligands in a chiral arrangement around a four-fold screw axis. The structure therefore provides two sources of chirality, the $\text{Ln}^{\text{III}}/\text{Na}^+$ chains and the ligand occupied channels, that may interact with polarised light and could result in polarised emission from the lanthanide centres.

The solid-state UV/Vis diffuse reflectance spectrum of **7-Eu** was measured between 215–420 nm (**Figure 6.5a**) and a broad band centred between 240–285 nm has been assigned to the absorption of the benzoate ligand. The $^5\text{L}_6 \leftarrow ^7\text{F}_0$ and $^5\text{G}_7 \leftarrow ^7\text{F}_0$ transitions within the Eu^{III} centre are also observed at 395 and 382 nm, respectively. Having identified the ligand absorption band and direct $\text{Eu}^{\text{III}} f\text{-}f$ transitions, the CD spectrum was measured in the solid-state. **Figure 6.5b** shows the sample response to circularly polarised light and a clear band above the signal/noise ratio is observed with a maximum at 239 nm. The CD spectrum provides strong evidence that a chiral response is observed by the absorption of light through the ligands, presumably those in the chiral void channel. The CD response of the ligands provides an intriguing possibility that if the ligand was functionalised to sense small ions, then the chiral channel voids can potentially be developed towards a sensing response. As the CD measurement was performed without an integrating sphere, it is still unclear whether the chiral lanthanide chain interacts with the polarised light directly. The current data indicates that during crystallisation there does not appear to be a 1:1 racemic equilibrium of the two enantiomer structures (one enantiomer crystallised in $I4_1$ and the second enantiomer in $I4_3$) forming. It cannot be stated that the phase is enantio-pure, but the positive band does show a clear excess of one enantiomer. With the current evidence for chiral absorption, it will be particularly interesting to investigate the sample for a CPL response in the solid-state; an approach that still appears scarce in the literature for lanthanide compounds.

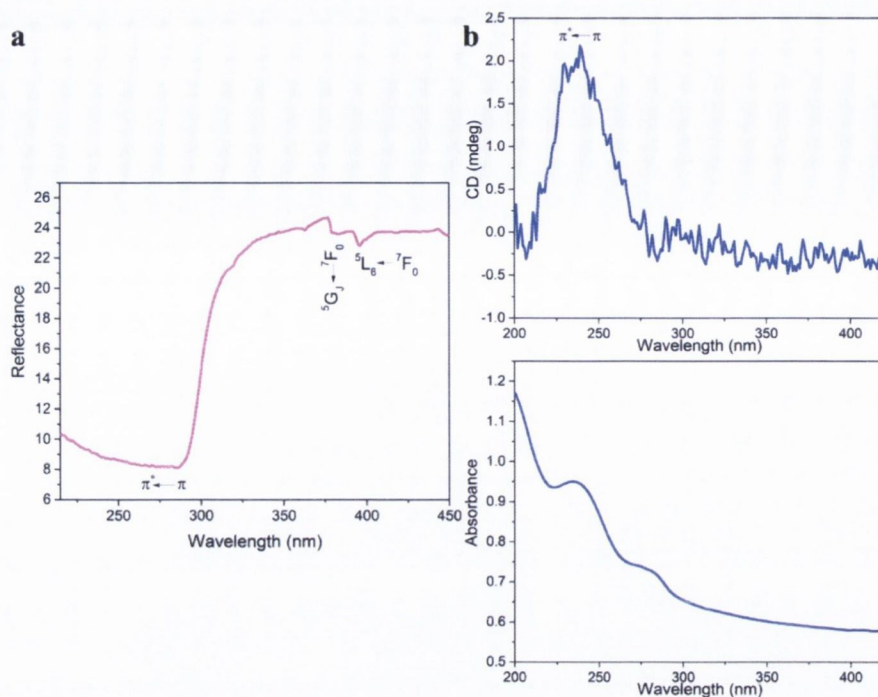
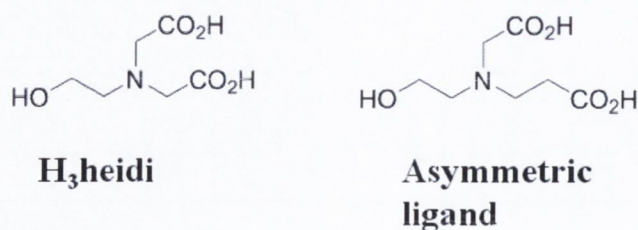


Figure 6.5: (a) The solid-state diffuse reflectance spectrum of **7-Eu** and (b) the CD spectrum of **7-Eu** and the associated absorption spectrum.

It is of particular interest to further understand the crystallisation conditions to investigate whether enantiomerically pure phases can be isolated. In this respect, there are a number of methods that may be pursued. In the 1D coordination polymer of $[\text{DyCl}_3(\text{dicnq})_2]$ (dicnq = 6,7-dicyanodipyridoquinoline) a conglomerate crystallisation was adopted that allowed different batches of homochiral material to be isolated.²⁷ Investigation by CD spectroscopy revealed that both enantiomers could be isolated in enantiomeric excess. Another factor that could be investigated in the reaction system of **7** is the choice of solvent. In the current synthesis of **7**, MeOH is used; however, if the solvent is replaced by a longer chain alcohol that is more asymmetric, it may become possible to favour the growth of a single enantiomer through additional solvent effects. An alternative strategy is to reduce the symmetry of the H_3heidi ligand, to become chiral, by replacing one acetic acid moiety by a propanoic acid, for example (**Scheme 6.2**). It is believed that the lanthanide centre is initially stabilised by the H_3heidi ligand in solution. If the new ligand bears three different coordinating groups, the binding of the ligand around the lanthanide centre will be less symmetrical. By altering the chain length of one carboxylic acid group, the binding strength of the carboxylate to the lanthanide may alter and so displacement of the asymmetric “heidi” may occur through a specific order and the resulting benzoate would bind through a preferential arrangement around the lanthanide centre that favours the crystallisation of a single enantiomer.



Scheme 6.2: Strategy to alter the symmetry of the H₃heidi ligand.

6.4.2 The emission properties of 7-Eu in the visible spectral range

To consider these chiral networks for potential applications in sensing or as chiral security tags,³¹ it is important to understand the emission properties of the material. For **7-Eu**, direct excitation of the Eu^{III} centre into the $^5L_6 \leftarrow ^7F_0$ transition ($\lambda_{\text{ex}} = 393$ nm) yielded the characteristic Eu^{III} PL spectrum in the range 550-725 nm arising from the $^5D_0 \rightarrow ^7F_J$ ($J = 0-4$) transitions (**Figure 6.6a**). There is no observation of emission from the higher 5D_1 manifold indicating efficient non-radiative relaxation to the 5D_0 level from higher excited states. At room temperature, there is some Stark splitting of the $^5D_0 \rightarrow ^7F_J$ lines ($J = 2$ and 4) into two and three bands, respectively. At room temperature, any resolution in the splitting of the $^5D_0 \rightarrow ^7F_1$ is not observed. However, knowing the compound crystallises in the tetragonal system from the XRD and the splitting that can be determined of the other transition bands, a D_{2d} point group symmetry can be reasonably assigned and matches the distorted dodecahedron description of the lanthanide centre. The excitation spectrum of **7-Eu** was measured by monitoring the $^5D_0 \rightarrow ^7F_2$ transition ($\lambda_{\text{em}} = 615$ nm) and sharp intra-*ff* transitions between 300-560 nm were assigned to excitation from the ground state, 7F_0 , to the 5H_J , 5G_J , 5L_6 and 5D_J ($J = 1-4$) excited states (**Figure 6.6b**). A further broad band was observed with a maximum at 280 nm and assigned to absorption from the benzoate ligand. To investigate the sensitisation pathway, the ligand was excited at $\lambda_{\text{ex}} = 290$ nm and the strong Eu^{III}-emission bands are still observed, indicating reasonable sensitisation through the ligand. The absolute emission quantum yield was measured at $\lambda_{\text{ex}} = 393$ nm, and a high value of $\Phi_{\text{PL}} = 23.8\%$ was obtained. In addition to the absence of water molecules in the Eu^{III} coordination sphere, two additional factors may account for the impressive emission quantum yield of **7-Eu**. Due to favourable packing of the ligands with respect to the Eu^{III} centre the weaker C-H quenching pathways may be minimised. The nature of the alternating Eu^{III}/Na⁺ arrangement increases the Eu^{III}-Eu^{III} distances between the binuclear building units and may reduce concentration self-quenching from energy transfer to nearest neighbour Eu^{III} centres. The absolute emission quantum yield for ligand excitation could not be measured under our experimental configuration. The emission lifetimes were measured under both direct excitation ($\lambda_{\text{ex}} = 393$ nm) and ligand excitation ($\lambda_{\text{ex}} = 290$ nm) to yield lifetime values of 1.07 ± 0.05 and 1.12 ± 0.06 ms, respectively (**Figure 6.6c, d**). To determine the number of coordinated water molecules, n_w , to the Eu^{III} centre, the following equation was used:

$$n_w = 1.11 \left[\frac{1}{\tau_{\text{obs}}} - k_r - 0.31 \right] \quad \text{Eqn. 6.1}$$

By substituting the observed emission lifetime, τ_{obs} , and calculating k_r using **Eqn. 1.3** (0.925 ms^{-1}), the number of coordinated water molecules, n_w , is 0.005 and is in excellent agreement with the crystallographic data.

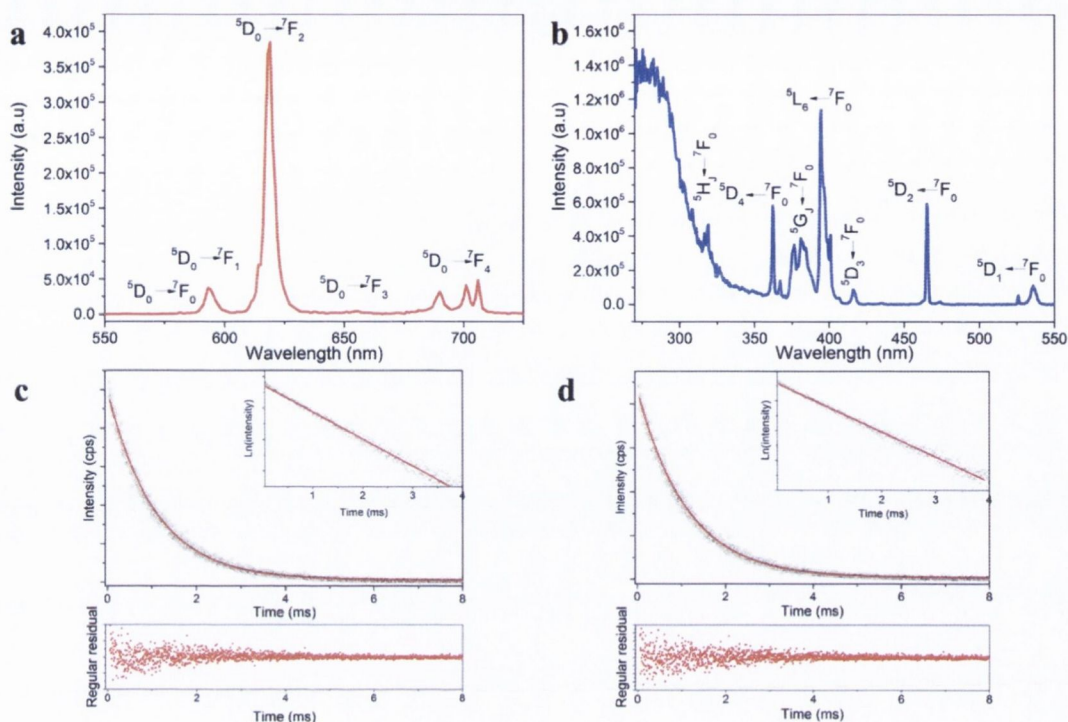


Figure 6.6: (a) PL spectrum for **7-Eu** upon ligand excitation ($\lambda_{\text{ex}} = 290 \text{ nm}$). (b) Excitation spectrum for **7-Eu** monitoring the ${}^5\text{D}_0 \rightarrow {}^7\text{F}_2$ transition ($\lambda_{\text{em}} = 615 \text{ nm}$). (c) Emission decay curve (open symbols) and monoexponential fit (red line) for **7-Eu** in the solid-state. ($\lambda_{\text{ex}} = 393 \text{ nm}$, $\lambda_{\text{em}} = 615 \text{ nm}$). **Inset:** $\text{Ln}(\text{intensity})$ vs. time, linear fit supporting a single exponential fit. (d) Emission decay curve (open symbols) and monoexponential fit (red line) for **7-Eu** in the solid-state. ($\lambda_{\text{ex}} = 290 \text{ nm}$, $\lambda_{\text{em}} = 615 \text{ nm}$). **Inset:** $\text{Ln}(\text{intensity})$ vs. time, linear fit supporting a single exponential fit.

6.5 Conclusions and Outlook

This chapter has shown the synthesis of **7-Ho** and **7-Eu**. It was realised that **7-Ho** had already been isolated previously, however, using different reaction conditions where glycerol, sodium benzoate and sodium azide were reacted with the lanthanide salt. We have been able to isolate **7-Ho** by different means, where H₃heidi has been substituted for glycerol in the reaction system. The crystal structure shows that the ligand H₃heidi is not involved in the final product; however, we have shown that the addition of the H₃heidi is a requirement for the chiral network to condense. We have been able to synthesise the novel Eu^{III}-analogue, **7-Eu**, of this material and due to the multiple sources of chirality we are interested in the solid-state optical activity of the material. CD spectroscopy indicates an absorption band to polarised light that has been assigned to absorption from the ligand molecules that in the least indicate the preferable crystallisation of one enantiomer. The first goal for future work is to study the CPL spectra of **7-Eu** in the solid-state. The emission properties of **7-Eu** were investigated and shown to be promising materials that display high emission quantum yields when the Eu^{III} centre is excited directly and we were able to

show that ligand sensitisation is possible. The strong emissive properties of **7-Eu** illustrates the potential of these materials for use in solid-state sensing devices. The mode of action that needs to be investigated is the interaction between ligand and analyte inside the channel voids. Furthermore, it has been recently suggested that CPL spectroscopy can be used for a new generation of chiral security tags.³¹ For this to be viable, a solid-state material is preferable to the aqueous complexes already developed. In a solid-state matrix, the ability to tune the spectral emission range by co-doping of multiple lanthanide centres is possible and similar strategies have been shown in MOF materials with the synthesis of NIR bar-coded systems (**Section 1.4.3**).³² Based on these considerations, should circularly polarised emission from **7-Eu** be observed, these materials will be excellent candidates for this application.

To understand the properties of this system further, future work will consider a number of points. (i) Identify if a solid-state CPL response from **7-Eu** is observed. (ii) Develop strategies to isolate homochiral material for full characterisation of the optical activity of both enantiomers. (iii) Introduce ligand substitution into the reaction system, initially by phenyl acetic acid, and 1- and 2-naphthoic acid to understand the structural chemistry and how ligand size affects the final structure. (iv) Introduce functionality to the ligands to allow selective coordination to transition metal ions.

6.6 References

1. J. P. Leonard, P. Jensen, T. McCabe, J. E. O'Brien, R. D. Peacock, P. E. Kruger and T. Gunnlaugsson, *J. Am. Chem. Soc.*, 2007, **129**, 10986-10987.
2. F. Stomeo, C. Lincheneau, J. P. Leonard, J. E. O'Brien, R. D. Peacock, C. P. McCoy and T. Gunnlaugsson, *J. Am. Chem. Soc.*, 2009, **131**, 9636-9637.
3. C. Lincheneau, C. Destribats, D. E. Barry, J. A. Kitchen, R. D. Peacock and T. Gunnlaugsson, *Dalton Trans.*, 2011, **40**, 12056-12059.
4. J. C. G. Bunzli and C. Piguet, *Chem. Rev.*, 2002, **102**, 1897-1928.
5. K. K. Nanda, S. Mohanta, U. Florke, S. K. Dutta and K. Nag, *J. Chem. Soc., Dalton Trans.*, 1995, 3831-3836.
6. P. Comba, A. Kuhner and A. Peters, *J. Chem. Soc., Dalton Trans.*, 1999, 509-516.
7. G. Muller, *Dalton Trans.*, 2009, 9692-9707.
8. T. Gunnlaugsson and J. P. Leonard, *Chem. Commun.*, 2005, 3114-3131.
9. D. Parker, R. S. Dickins, H. Puschmann, C. Crossland and J. A. K. Howard, *Chem. Rev.*, 2002, **102**, 1977-2010.
10. H. Tsukube and S. Shinoda, *Chem. Rev.*, 2002, **102**, 2389-2403.
11. E. Huskowska and J. P. Riehl, *Inorg. Chem.*, 1995, **34**, 5615-5621.
12. G. Muller and J. P. Riehl, *J. Fluorescence*, 2005, **15**, 553-558.
13. G. Muller, S. D. Kean, D. Parker and J. P. Riehl, *J. Phys. Chem. A*, 2002, **106**, 12349-12355.
14. R. S. Dickins, T. Gunnlaugsson, D. Parker and R. D. Peacock, *Chem. Commun.*, 1998, 1643-1644.
15. R. S. Dickins, C. S. Love and H. Puschmann, *Chem. Commun.*, 2001, 2308-2309.
16. R. S. Dickins, S. Aime, A. S. Batsanov, A. Beeby, M. Botta, J. Bruce, J. A. K. Howard, C. S. Love, D. Parker, R. D. Peacock and H. Puschmann, *J. Am. Chem. Soc.*, 2002, **124**, 12697-12705.
17. R. S. Dickins, A. S. Batsanov, J. A. K. Howard, D. Parker, H. Puschmann and S. Salamano, *Dalton Trans.*, 2004, 70-80.

18. R. S. Dickins and A. Badari, *Dalton Trans.*, 2006, 3088-3096.
19. C. P. Montgomery, E. J. New, D. Parker and R. D. Peacock, *Chem. Commun.*, 2008, 4261-4263.
20. D. Parker, *Coord. Chem. Rev.*, 2000, **205**, 109-130.
21. L. J. Govenlock, C. E. Mathieu, C. L. Maupin, D. Parker, J. P. Riehl, G. Siligardi and J. A. G. Williams, *Chem. Commun.*, 1999, 1699-1700.
22. A. Beeby, R. S. Dickins, S. FitzGerald, L. J. Govenlock, C. L. Maupin, D. Parker, J. P. Riehl, G. Siligardi and J. A. G. Williams, *Chem. Commun.*, 2000, 1183-1184.
23. G. Bobba, R. S. Dickins, S. D. Kean, C. E. Mathieu, D. Parker, R. D. Peacock, G. Siligardi, M. J. Smith, J. A. G. Williams and C. Geraldes, *J. Chem. Soc., Perkin Trans. 2*, 2001, 1729-1737.
24. G. Bobba, S. D. Kean, D. Parker, A. Beeby and G. Baker, *J. Chem. Soc., Perkin Trans. 2*, 2001, 1738-1741.
25. G. Bobba, J. C. Frias and D. Parker, *Chem. Commun.*, 2002, 890-891.
26. S. Chorazy, K. Nakabayashi, M. Arczynski, R. Pelka, S. Ohkoshi and B. Sieklucka, *Chem. Eur. J.*, 2014, **20**, 7144-7159.
27. H. F. Chen, G. C. Guo, M. S. Wang, G. Xu, W. Q. Zou, S. P. Guo, M. F. Wu and J. S. Huang, *Dalton Trans.*, 2009, 10166-10168.
28. D. Ananias, F. A. A. Paz, L. D. Carlos and J. Rocha, *Microporous Mesoporous Mat.*, 2013, **166**, 50-58.
29. D. Ananias, F. A. A. Paz, L. D. Carlos, C. Geraldes and J. Rocha, *Angew. Chem. Int. Ed.*, 2006, **45**, 7938-7942.
30. Z. Majeed, K. C. Mondal, G. E. Kostakis, Y. H. Lan, C. E. Anson and A. K. Powell, *Chem. Commun.*, 2010, **46**, 2551-2553.
31. R. Carr, N. H. Evans and D. Parker, *Chem. Soc. Rev.*, 2012, **41**, 7673-7686.
32. K. A. White, D. A. Chengelis, K. A. Gogick, J. Stehman, N. L. Rosi and S. Petoud, *J. Am. Chem. Soc.*, 2009, **131**, 18069-18071.

Chapter Seven



Exploiting organic templates to develop novel lanthanide sulphate frameworks

7.1 Introduction

The sulphate group is a tetrahedral negative ion that has been shown to stabilise lanthanide ions through the formation of inorganic network structures. These structures can be tuned between 1D, 2D and 3D through the careful choice of an organic templating agent. This method has already been widely used in the synthesis of inorganic zeolite materials that have been developed for use in petroleum refinement,¹ catalysis² and ion-exchange.³ In particular, the development of porosity in zeolites was shown to be strongly dependent on the choice of organic template and has led to structures with pore sizes up to 16 Å in diameter.⁴ Successful organic templates included linear diamines, where the size of the ring's channels was dependent on the linear chain length of $\text{NH}_2\text{-(CH}_2\text{)}_n\text{-NH}_2$.⁵⁻⁷ Tuning n produces 10-membered ring ($3 \leq n \leq 5$) channels,⁵ 16-membered ring ($6 \leq n \leq 8$)⁶ channels and 18-membered ring ($9 \leq n \leq 10$) channels.⁷

To date, the organic templates used in lanthanide sulphate synthesis include cyclic amines,⁸⁻¹⁵ diamines^{8, 10, 11, 16-18} and tri-^{9, 19-21} and tetra-amines.²² The cyclic amines are particularly good at templating 2D and 3D structures. The cyclic amine, piperazine, produces multiple 3D structures depending on the reaction conditions. These materials include $(\text{C}_4\text{H}_{12}\text{N}_2)[\text{Ln}_2(\text{SO}_4)_4(\text{H}_2\text{O})_2]$ ⁸ which takes on a 3D architecture with two different types of channels constructed from 8-membered rings of alternating lanthanide/sulphate polyhedra with the piperazinium cations sitting in these channels. Furthermore, the shape of these channels was shown to resemble that seen in the zeolitic material ZK-5.⁸ Using a smaller quantity of solvent (H_2O) and H_2SO_4 result in the different 3D framework of $(\text{C}_4\text{H}_{12}\text{N}_2)[\text{Ln}_2(\text{SO}_4)_4(\text{H}_2\text{O})_2]$ ¹⁰, where the bridging sulphates form a central channel of an 8-membered ring construction that is surrounded by four 12-membered ring channels that run along the a -axis. The piperazine is located in the channels and stabilises the structure through hydrogen bonding to the sulphate oxygen centres.¹⁰ The vital addition of glycol as a co-solvent to water results in the isolation of the honeycomb open framework structure of $(\text{C}_4\text{H}_{12}\text{N}_2)_3[\text{Ln}_3(\text{OH})(\text{SO}_4)_7]$ ¹⁵ that contains large channels down the c -axis from a 24-membered ring construction. These tubular channels are further built from 12-membered ring side pockets that maintain the structural integrity of the channel.¹⁵ The amine 1,4-diazabicyclo[2.2.2]octane (DABCO) is good at forming layered lanthanide sulphates with an 8-membered ring being a common feature in the structure of these layers.^{10, 12, 14} The addition of Na^+ as an additional structure-directing agent leads to the 3D open framework $\text{Na}(\text{C}_6\text{H}_{14}\text{N}_2)[\text{Ln}_3(\text{SO}_4)_6(\text{H}_2\text{O})_3]$.¹³ 1D zig-zag chains are connected to each other to form infinite tubes and are stabilised through the Na^+ ions. Protonated DABCO molecules further template six 8-membered rings to form cubic cages that link the 1D infinite tubes into a 3D open framework.

The use of diamines has largely focussed on the diethylene amine molecule, which is a good template for both 3D structures^{10, 11, 18} and layered lanthanide sulphates.^{8, 10, 17} To date only one lanthanide sulphate templated by 1,3-diaminopropane is known, and the templating effect led to a layered material.¹⁰ Unlike in zeolite chemistry, the effect of chain length has not been studied beyond $n=3$ and the effect of the template needs to be explored further. Expanding the template to

From the literature, some patterns in the templating of lanthanide sulphates are starting to appear. However, no strong conclusions can be drawn. In addition, the properties of these materials are still largely unexplored. In **Section 1.4.4** the properties of lanthanide hybrid materials and their potential for magnetic cooling was discussed. The conclusion from the literature was that lanthanide hybrid structures constructed from small ligands result in improved magnetic cooling properties. The small size of the sulphate as a ligand could lead to promising magnetic properties that are yet unknown. The aim of this chapter is to synthesise and characterise new lanthanide sulphate materials and investigate the effect of the template on the resulting structure. In characterising these materials, we aim to investigate the surface area of any porous materials and look into the magnetic properties of lanthanide sulphates.

7.2 Crystal structure of $[\text{Nd}_2(\text{SO}_4)_3(\text{H}_2\text{O})_8]$, **(8)**

The reaction of $\text{NdCl}_3 \cdot 6\text{H}_2\text{O}$ with phenyl phosphonic acid in 5 mL water and a large excess of sulphuric acid at 150°C under hydrothermal conditions for 15 hours results in the crystallisation of pink block crystals of $[\text{Nd}_2(\text{SO}_4)_3(\text{H}_2\text{O})_8]$, **8**. A suitable crystal was isolated from the reaction medium and characterised by means of single X-ray crystal diffraction.

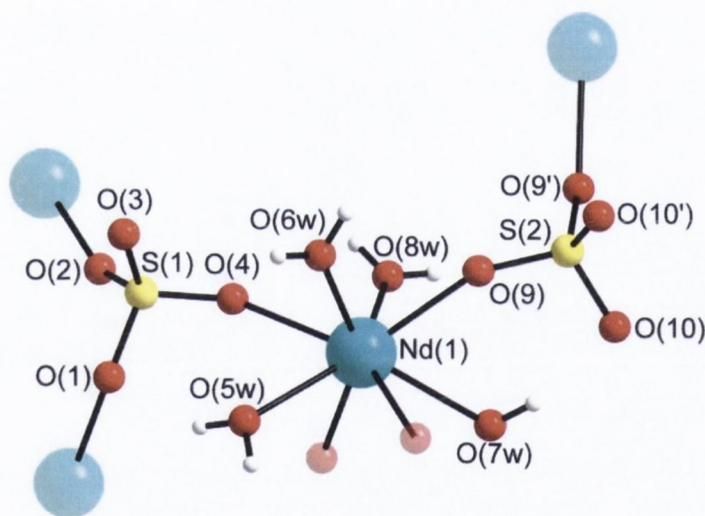
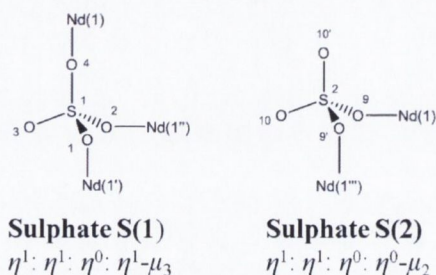


Figure 7.1: The asymmetric unit of $[\text{Nd}_2(\text{SO}_4)_3(\text{H}_2\text{O})_8]$ identified by the filled atoms. Faded atoms represent symmetry generated atoms that complete the coordination geometry around Nd(1) and the sulphate groups. Nd cyan, S yellow, O red and H white.

The compound $[\text{Nd}_2(\text{SO}_4)_3(\text{H}_2\text{O})_8]$, **8**, crystallises in the monoclinic crystal system in the space group, $C(1)2/c(1)$. The asymmetric unit contains a single Nd^{III} centre, two sulphate groups (the sulphate S(2) is located on a special position (through which a 2-fold rotation axis runs along the b -axis)) and four coordinated water molecules. The Nd^{III} centre is eight coordinate and may be visualised as a distorted square antiprism. Beyond the asymmetric unit, the Nd^{III} centre is stabilised by four sulphate groups and four coordinated water molecules (**Figure 7.1**). The sulphate S(1)

bridges three different Nd^{III} centres with the bonding description $\eta^1: \eta^1: \eta^0: \eta^1-\mu_3$ (**Scheme 7.1**). The oxygen donor atom O(4) forms a monodentate bond to Nd(1), and O(1) and O(2) form monodentate bonds to Nd(1') and (Nd(1'')), respectively. The oxygen atom O(3) is not involved in any coordination bonds. The bonding description for S(2) is $\eta^1: \eta^1: \eta^0: \eta^0-\mu_2$ and forms monodentate bonds to Nd(1) and Nd(1''') through the donor atoms O(9) and O(9'), respectively (**Scheme 7.1**). The oxygen centres O(10) and O(10') are not involved in bonding to the Nd^{III} centres.



Scheme 7.1: The coordination modes of the sulphate groups in **8**.

The Nd-O bond lengths are in the range 2.376-2.548 Å (**Table 7.1**). The shorter Nd-O bond lengths are from the coordinated sulphate O-donors due to the stronger electrostatic attraction from the negative sulphate group. The Nd-O_w bond lengths from coordinated water molecules are longer above 2.40 Å due to the weaker electrostatic attraction between the neutral water molecule and the Nd^{III} centre.

Table 7.1: Selected bond lengths for **8**.

Bond	Bond Length (Å)	Bond	Bond Length (Å)
Nd(1)-O(1)#2	2.5120(8)	Nd(1)-O(5w)	2.4907(9)
Nd(1)-O(2)#1	2.3844(9)	Nd(1)-O(6w)#1	2.4009(9)
Nd(1)-O(4)	2.4293(8)	Nd(1)-O(7w)#2	2.5484(8)
Nd(1)-O(9)	2.3769(9)	Nd(1)-O(8w)	2.4411(9)

A double chain of $\{\text{Nd}_2(\text{SO}_4)_3(\text{H}_2\text{O})_8\}_n$ polyhedra extends along the *b*-axis through bridging S(1) sulphates (**Figure 7.2a**). Along the chain, S(2) sulphate moieties bridge a double chain to two other chains along the [101] direction. This results in layers in the [101]-plane that contain 8-membered rings constructed from four $\{\text{NdO}_8\}$ polyhedra, two S(1) and two S(2) tetrahedra (**Figure 7.2b**).

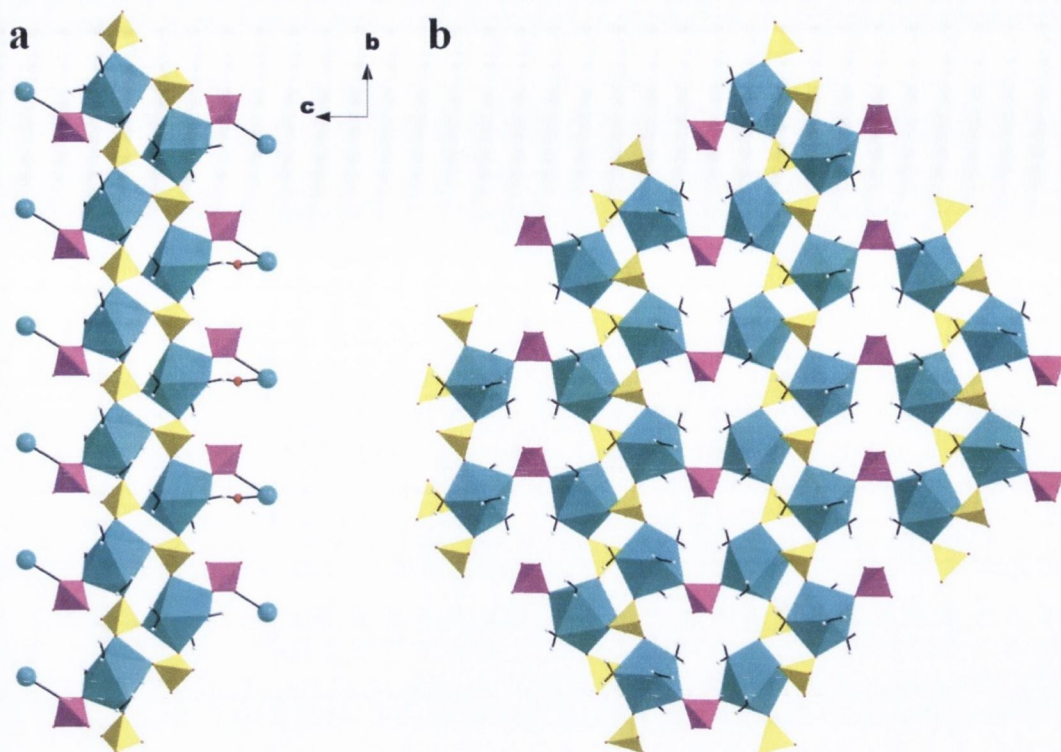


Figure 7.2: (a) A double chain of $[\text{Nd}_2(\text{SO}_4)_3(\text{H}_2\text{O})_8]$ built from a repeating unit along the b -axis. (b) A layer of $[\text{Nd}_2(\text{SO}_4)_3(\text{H}_2\text{O})_8]$ in the $[101]$ plane. The bridging S(2) group is highlighted in magenta to highlight how they bridge adjacent chains. 8-membered rings are seen to form consisting of four $\{\text{NdO}_8\}$, two S(1) and two S(2) polyhedra. Nd cyan, S(1) yellow, S(2) magenta and O red.

Two discrete layers fill the unit cell running in the $[101]$ projection. Each layer is generated through different symmetry elements. One such layer may be considered as taking the asymmetric unit, along with atoms generated through a two-fold rotation axis at $(0.5, b, 0.25)$, an n -glide plane perpendicular to the b -axis at $b=0.25$ and an inversion centre at $(0.75, 0.25, 0.5)$. The second layer that runs through the unit cell is generated by applying the centring vector $[0.5, 0.5, 0]$ to the asymmetric unit, a two-fold screw axis at $(0.75, b, 0.25)$, a c -glide plane perpendicular to the b -axis at $b=0.5$ and an inversion centre at $(0.5, 0.5, 0.5)$. The relation of the symmetry to the unit cell is given in **Figure 7.3**.

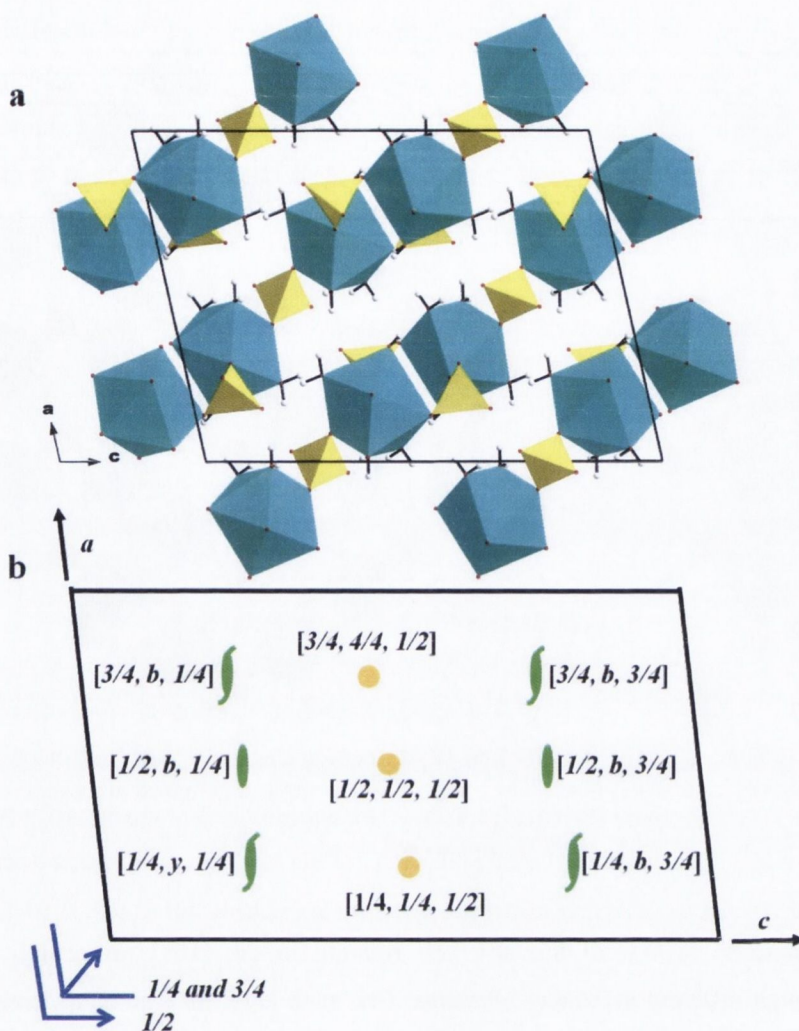


Figure 7.3: (a) The unit cell of $[\text{Nd}_2(\text{SO}_4)_3(\text{H}_2\text{O})_8]$ as viewed down the b -axis. (b) The symmetry elements required to generate the structure of **8** as viewed down the b -axis.

To stabilise the overall structure, two types of hydrogen bond are observed; intra- and inter-layer hydrogen bonding. Within each individual layer there are intra-layer hydrogen bonds formed between the S(2) sulphate oxygen atom O(10) and the coordinated water molecules through O(7w)-H(5)...O(10) and O(8w)-H(8)...O(10) interactions (red dash bond in **Figure 7.4**). Further intramolecular hydrogen bonding exists between the S(1) sulphate and coordinated water molecules and between individual water molecules. Adjacent layers are additionally stabilised through hydrogen bonding from oxygen atoms on both the S(1) and S(2) sulphates to coordinated water molecules (blue dashed bonds in **Figure 7.4**). The hydrogen bonds are weak, as characterised by the long donor acceptor distances between 2.766-2.961 Å, as summarised in **Table 7.2**.

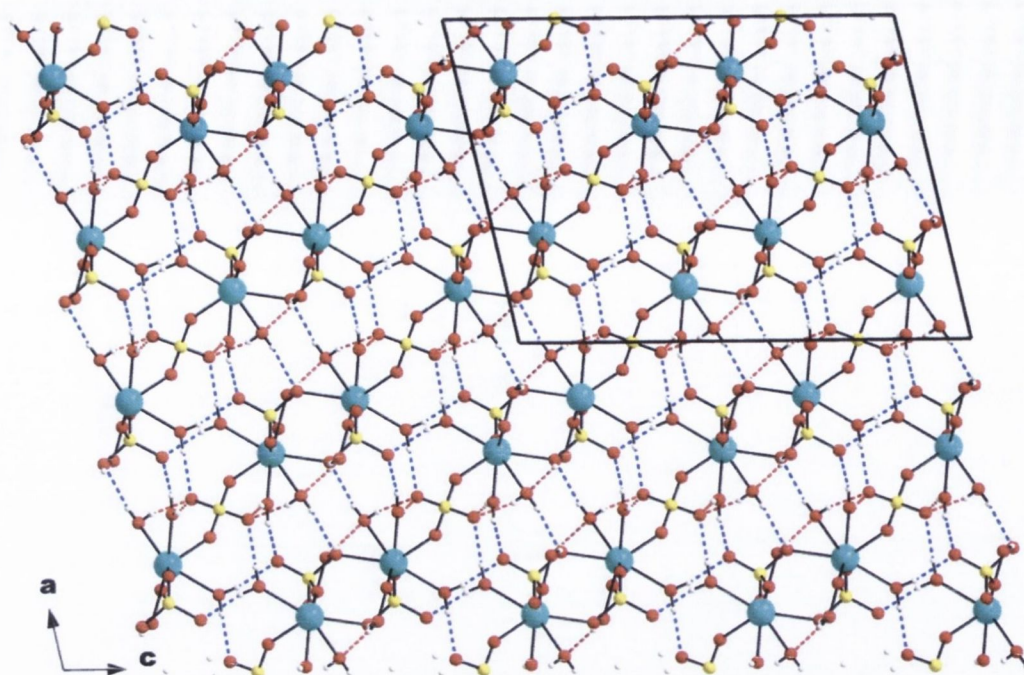


Figure 7.4: The hydrogen bonding network of **8** as viewed down the *b*-axis. Interlayer hydrogen bonds between different layers are blue dashed bonds, while intralayer hydrogen bonds within the same layer are identified by red dashed bonds.

Table 7.2: Selected hydrogen bond distances in **8**.

	Donor-Acceptor Distance (Å)		Donor-Acceptor Distance (Å)
O(5w)-H(2)...O(7)#5	2.8849(12)	O(6w)-H(3)...O(10)#6	2.7822(12)
O(5w)-H(1)...O(1)	2.7665(12)	O(6w)-H(4)...O(3)#7	2.7463(13)
O(7w)-H(5)...O(10)	2.7703(12)	O(7w)-H(6)...O(1)#8	2.9618(12)
O(8w)-H(8)...O(10)#3	2.8119(12)	O(8w)-H(7)...O(3)#8	2.7119(13)

Table 7.3 Crystal data and structure refinement for **8**.

Identification code	8	
Empirical formula	$H_{16}Nd_2O_{20}S_3$	
Formula weight	720.79	
Temperature	100(2) K	
Wavelength	0.71073 Å	
Crystal system	Monoclinic	
Space group	$C(1) 2/c(1)$	
Unit cell dimensions	$a = 13.5997(4)$ Å	$\alpha = 90^\circ$.
	$b = 6.8357(2)$ Å	$\beta = 102.6220(10)^\circ$.
	$c = 18.3596(5)$ Å	$\gamma = 90^\circ$.
Volume	1665.52(8) Å ³	
Z	4	
Density (calculated)	2.875 Mg m ⁻³	
Absorption coefficient	6.642 mm ⁻¹	
F(000)	1376	
Crystal size	0.190 × 0.190 × 0.100 mm ³	
Theta range for data collection	2.274 to 40.341°.	
Index ranges	-24 ≤ h ≤ 24, -12 ≤ k ≤ 12, -33 ≤ l ≤ 33	
Reflections collected	80657	
Independent reflections	5269 [R(int) = 0.0152]	
Completeness to theta = 25.242°	99.1%	
Absorption correction	Semi-empirical from equivalents	
Max. and min. transmission	0.7479 and 0.5403	
Refinement method	Full-matrix least-squares on F ²	
Data / restraints / parameters	5269 / 12 / 146	
Goodness-of-fit on F ²	1.472	
Final R indices [I > 2σ(I)]	R1 = 0.0139, wR2 = 0.0337	
R indices (all data)	R1 = 0.0139, wR2 = 0.0337	
Extinction coefficient	n/a	
Largest diff. peak and hole	0.636 and -2.108 e.Å ⁻³	

7.3 The crystal structure of $(Me_2NH_2)_9[Nd_5(SO_4)_{12}]$, (**9**)

The reaction of $NdCl_3 \cdot 6H_2O$, phenyl phosphonic acid and sulphuric acid as a 1:2:4 molar ratio in 10 mL DMF yielded crystalline plates of $(Me_2NH_2)_9[Nd_5(SO_4)_{12}]$, **9**, after heating at 170 °C for 72 hours and subsequent slow cooling to room temperature. A suitable small plate was isolated from the crystal mixture and analysed using single crystal X-ray diffraction. The reaction was repeated using only $LnCl_3$, DMF and H_2SO_4 and the product could be isolated indicating that the uncoordinated ligands are not important in the synthesis. Isostructural materials were synthesised for $Ln^{III} = Gd^{III}$ and Dy^{III} and the materials shall be named **9-Gd** and **9-Dy**.

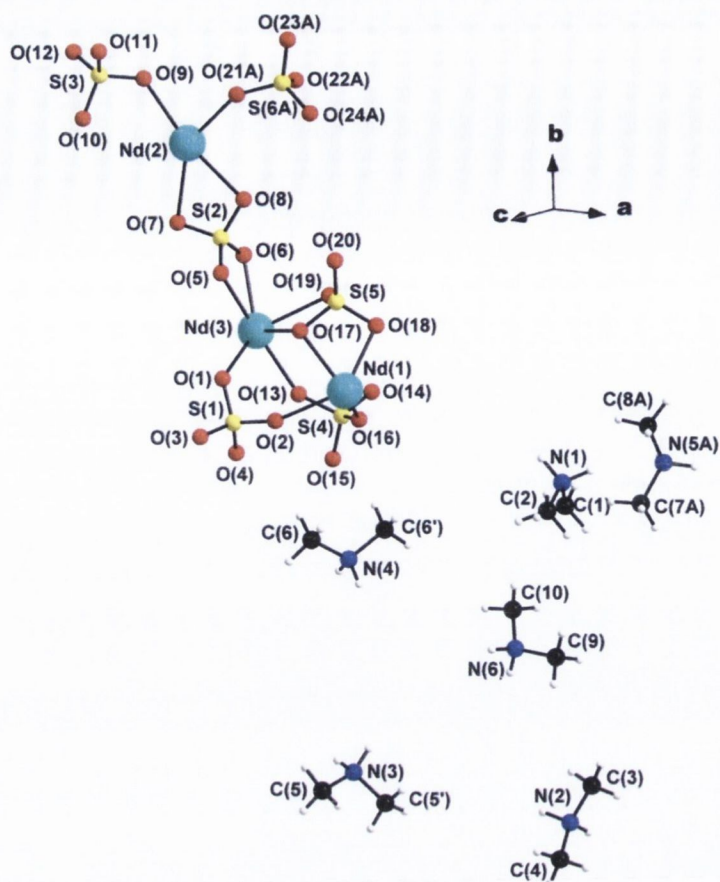
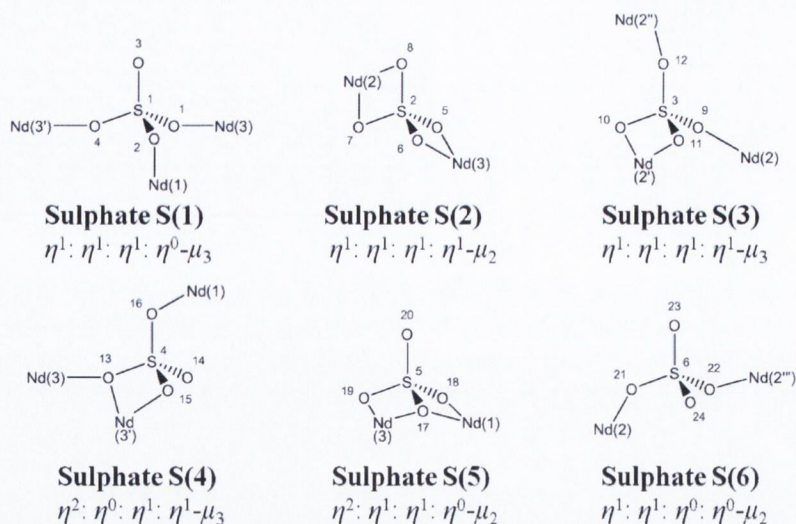


Figure 7.5: Asymmetric unit of $(\text{Me}_2\text{NH}_2)_9[\text{Nd}_5(\text{SO}_4)_{12}]$, **9**. Nd cyan, O red, S yellow, N blue, C black and H white.

The compound, **9**, is a 3D open framework that is constructed from two different chain motifs that connect to form a structure with three different channels, 10- and 20-membered ring channels that run along the c -axis and another 20-membered ring channel that projects along the $[101]$ direction. The open framework bears an overall negative charge and is balanced by the presence of dimethyl ammonium $([\text{Me}_2\text{NH}_2]^+)$ cations residing within the channels. The cations are presumed to form *in-situ* through the decomposition of the solvent, DMF, by hydrolysis under increased temperature and pressure while under acidic conditions as seen in the literature.^{23, 24}

The compound $(\text{Me}_2\text{NH}_2)_9[\text{Nd}_5(\text{SO}_4)_{12}]$, **9**, crystallises in the monoclinic crystal system in the space group $C(1)2/c(1)$ where $\text{Me}_2\text{NH}_2 =$ dimethyl ammonium cation. The asymmetric unit is half of the unit formula consisting of three Nd^{III} centres, Nd(1), Nd(2) and Nd(3) (**Figure 7.5**). The Nd(1) centre is located on a special position where a 2-fold rotation axis runs along the direction of the b -axis. The Nd^{III} centres are stabilised by six sulphate groups in the asymmetric unit, where the sulphate, S(6) is disordered over two positions (70:30%). The Nd^{III} -sulphate coordination network is charge balanced by six dimethyl ammonium cations, the cations of N(3), N(4) and N(5) are half occupied by their location on special positions.



Scheme 7.2: Coordination modes adopted by the different sulphate moieties in the asymmetric unit of **9**.

The different sulphate moieties display a number of different bridging modes (**Scheme 7.2**). The S(1) sulphate has a $\eta^1: \eta^1: \eta^1: \eta^0-\mu_3$ bonding scheme where the O(1) donor coordinates a Nd(3) centre, O(2) bridges to Nd(1) and the donor O(4) coordinates a different Nd(3') centre. All three oxygen donors coordinate through a monodentate interaction. The S(2) sulphate displays a $\eta^1: \eta^1: \eta^1: \eta^1-\mu_2$ bridging mode where the oxygen donors, O(5) and O(6) chelate the Nd(3) centre, while the donors O(7) and O(8) chelate Nd(2). The S(3) sulphate moiety bridges three Nd^{III} centres through a $\eta^1: \eta^1: \eta^1: \eta^1-\mu_3$ mode. The oxygen donor atom O(9) forms a monodentate bond to Nd(2), while O(10) and O(11) forms a chelating interaction with a symmetry Nd(2') and the donor O(12) forms an monodentate bond to another symmetry related Nd(2'') centre. A $\eta^2: \eta^0: \eta^1: \eta^1-\mu_3$ bonding description to three Nd^{III} centres is adopted by the S(4) sulphate. A bridging-chelate interaction is adopted from the donor atoms O(13) and O(15) to Nd(3) and Nd(3'), leaving the donor atom O(16) to form an monodentate interaction to Nd(1). Two Nd^{III} centres are bridged from the S(5) sulphate by a $\eta^2: \eta^1: \eta^1: \eta^0-\mu_2$ description, where two chelate-bridging modes are adopted in coordinating Nd(1) and Nd(3) through the donor atoms O(17), O(18) and O(19). O(17) is the bridging donor atom, forming a μ_2 -bridge between the Nd(1) and Nd(3) centres. The oxygen atom O(18) and O(19) complete the chelate interaction to Nd(1) and Nd(3), respectively. The S(6) sulphate bridges two Nd^{III} centres through a $\eta^1: \eta^1: \eta^0: \eta^0-\mu_2$ bonding description. The oxygen atom O(21) forms a monodentate bond to Nd(2), while the donor O(22) forms a separate monodentate bond to a symmetry related Nd(2''').

The Nd(1) centre is 8-coordinate and bound by six different sulphates through O(2), O(2'), O(16), O(16'), O(17), O(17'), O(18) and O(18') of S(1), S(4), S(5) sulphates. The Nd(2) centre may be viewed as an 8-coordinate distorted dodecahedron. The coordination sphere is completed through O(7) and O(8) of S(1) and O(21) of S(6) sulphates. Three different S(3) sulphates coordinate to Nd(2) through O(9), O(10') and O(12''). The coordination environment of Nd(3) is 9-coordinate and stabilised through six different sulphate moieties. The Nd(3) centre is bound by O(1) and O(4') of two S(1) sulphates, O(5) and O(6) of an S(2) sulphate, O(17) and O(19) of the

S(5) sulphate. Two S(4) sulphates bond through O(13), O(15) and O(13') to complete the coordination.

The Nd-O bond lengths (**Table 7.4**) range between 2.322-2.560 Å, are in good agreement with literature values reported for Nd^{III} sulphates and vary according to the bonding interaction between the oxygen donor and the Nd^{III} centre. The shorter bond lengths are generally due to the monodentate interactions with the Nd^{III} centre, while the longer bond lengths, up to *ca.* 2.5 Å, are a consequence of the chelating and bridging interactions observed in the structure.

Table 7.4: Selected bond lengths for **9**.

Bond	Bond Length (Å)	Bond	Bond Length (Å)
Nd(1)-O(2)	2.404(3)	Nd(3)-O(13)	2.382(3)
Nd(3)-O(1)	2.442(3)	Nd(3)-O(15)#5	2.468(3)
O(4)-Nd(3)#5	2.423(3)	Nd(1)-O(16)	2.369(3)
Nd(3)-O(5)	2.545(3)	Nd(1)-O(17)	2.549(3)
Nd(3)-O(6)	2.487(3)	Nd(1)-O(18)	2.535(3)
Nd(2)-O(7)	2.533(3)	Nd(3)-O(19)	2.531(3)
Nd(2)-O(8)	2.537(3)	Nd(2)-O(21A)	2.360(6)
Nd(2)-O(9)	2.474(3)	Nd(2)-O(22A)#2	2.322(5)
Nd(2)-O(10)#4	2.560(3)		
Nd(2)-O(11)#4	2.549(3)		
O(12)-Nd(2)#3	2.440(3)		

Two different chain motifs are constructed through symmetry. The first motif, **chain 1**, is an infinite wave-like chain built from Nd(1) and Nd(3) centres and their symmetry-related centres (**Figure 7.6a**). With respect to the unit cell, these wave-like chains orientate and pack along the [101] axis (**Figure 7.6b**).

The second motif present in the structure, **chain 2**, is a double infinite chain of symmetry-related Nd(2) centres that runs along the *c*-axis (**Figure 7.7a**). This motif is constructed entirely from Nd(2) centres that are linked through S(2) and S(6) sulphates along the *c*-axis in a single chain. The S(3) sulphates act to bridge two like-chains along the *a*-axis and so create the double chain motif. With respect to the unit cell, the chains orientate and pack along the *c*-axis (**Figure 7.7b**).

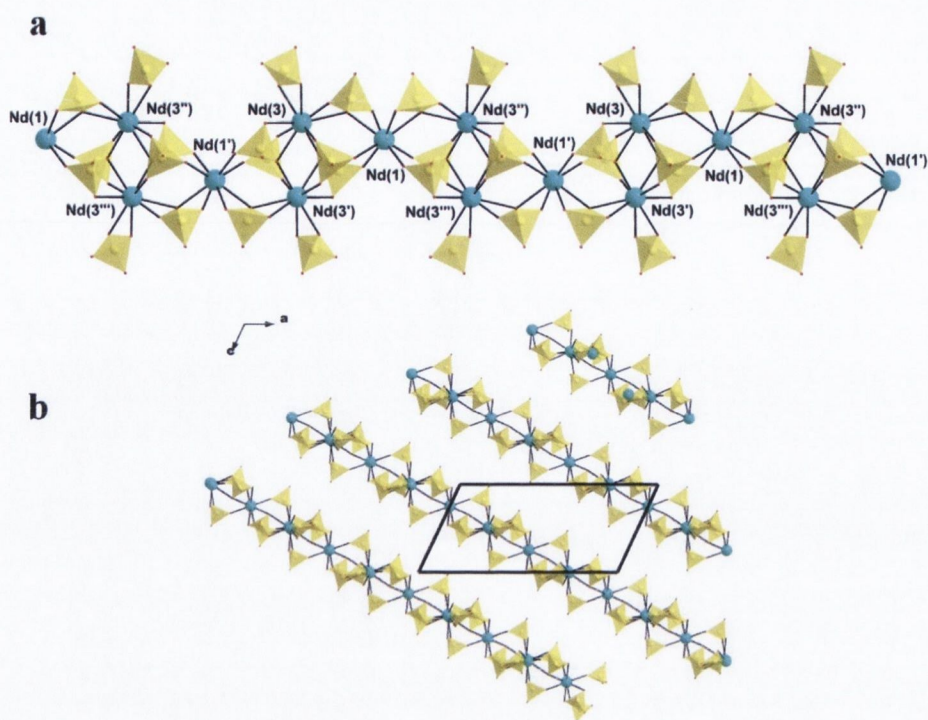


Figure 7.6: (a) The wave-like motif of **chain 1** that grows in the [101] direction. (b) The packing of multiple **chain 1** motifs in the [101] plane as viewed down the *b*-axis. **Chain 2** and dimethyl ammonium cations have been omitted for clarity. Nd cyan, S yellow polyhedra, O red.

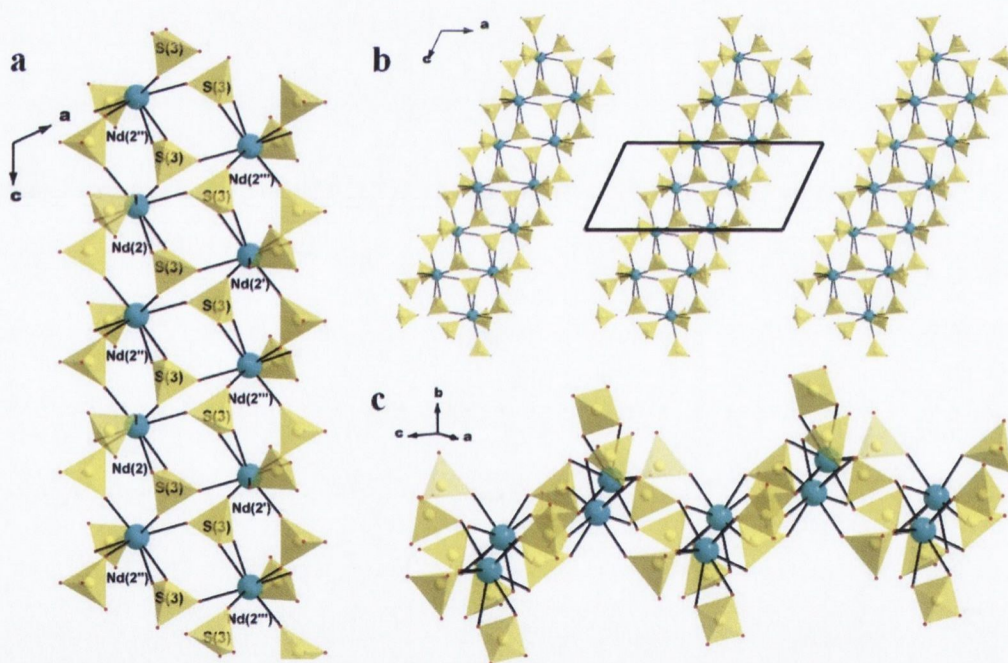


Figure 7.7: (a) The growth of the double infinite **chain 2** along the *c*-axis. Note the multiple S(3) sulphates that bridge the two chains. (b) The packing of the double chains as viewed down the *b*-axis and (c) the wave-like nature of the infinite double chain motif. Nd cyan, S yellow polyhedra, O red, **chain 1** and dimethyl ammonium cations have been removed for clarity.

The wave-like motif of **chain 1** is a consequence of an inversion centre at (0.25,0.25,0) and its related positions, an *n*-glide plane perpendicular to the *b*-axis with glide component [0.5,0,0.5] and the two fold rotation axis running down the *b*-axis through Nd(1). The wave-like

nature of the double infinite chain (**chain 2**) is a consequence of a c -glide plane perpendicular to the b -axis and two-fold rotation axis at $(0.5, b, 0.25)$ and inversion centres at $(0.5, 0.5, 0)$. The position of the symmetry elements and their equivalent positions in the unit cell with respect to the structure are shown in **Figure 7.8**.

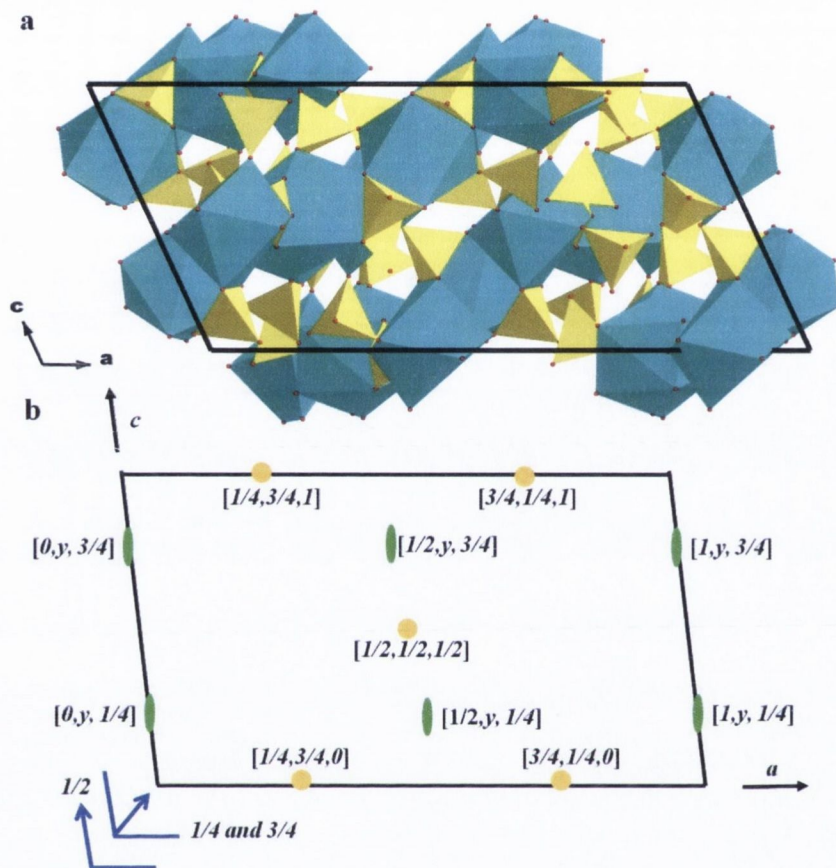


Figure 7.8: (a) Polyhedral representation of the unit cell as viewed down the b -axis. Nd cyan, S yellow O red. (b) Scheme of the unit cell viewed down the b -axis showing all symmetry elements that relate to molecule generation in the unit cell.

These two independent motifs are connected in space through S(2) sulphate moieties along the b -axis. This leads to the construction of a 3D open framework structure with three different channels. The S(2) sulphates bridge the Nd(2) and Nd(3) centres and this leads to the double infinite **chain 2** running perpendicular to the wave-like **chain 1** positioned between two different Nd(3) centres and forming a small 10-membered ring channel. This channel consists of three $\{\text{NdO}_8\}$, two $\{\text{NdO}_9\}$ and five $\{\text{SO}_4\}$ polyhedra (**Figure 7.9a**) and is stabilised by dimethyl ammonium cations that reside in the centre. A larger 20-membered ring channel also forms from the arrangement of six $\{\text{NdO}_8\}$, four $\{\text{NdO}_9\}$ and ten $\{\text{SO}_4\}$ polyhedra. These rings form adjacent to the 10-membered ring and are also stabilised by dimethyl ammonium cations residing towards the perimeter of the ring channels and located towards the corners of these channels showing the directional templating effect of the cation. These two different types of channel run in the direction of the crystallographic c -axis. A further 20-membered ring channel also forms in the $[101]$ projection and is built from six $\{\text{NdO}_8\}$, four $\{\text{NdO}_9\}$ and ten $\{\text{SO}_4\}$ polyhedra. In this channel,

some of the sulphate moieties are oriented towards the centre of the ring. A high density of dimethyl ammonium cations are located (**Figure 7.9b**) in these channels and form hydrogen bonds to the sulphate oxygen atoms to stabilise the negative charge on the framework. The formation of the 10- and 20-member rings result in channels that run down the *c*-axis and the [101] projection. These channels result in porosity in the framework structure in two directions of space. The dimethyl ammonium cations are located within these channels and stabilise the framework as structure directing agents as is observed by their position within the channels.

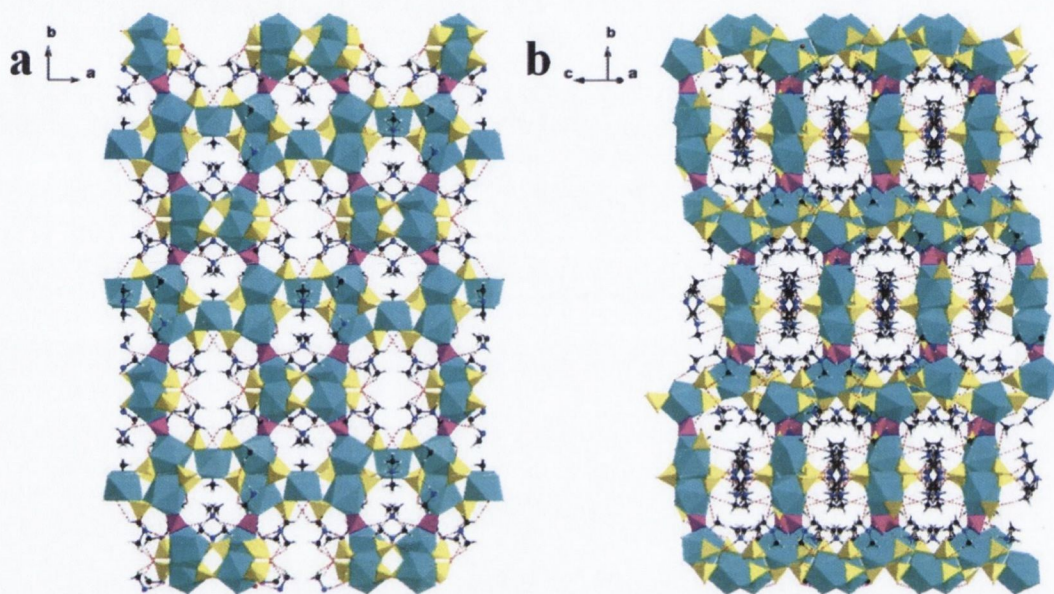


Figure 7.9: 3D framework built from intersecting **chain 1** and **chain 2** motifs result in 10- and 20 membered ring channels that are viewed down **(a)** *c*-axis and **(b)** the [101] direction. Bridges between the two different chain moieties are made by S(2) sulphates, identified as magenta polyhedra. Nd cyan polyhedra, S yellow polyhedra (S(2) magenta polyhedra), C black, N blue, H-bonds red-dashed lines.

The dimethyl ammonium cations act to stabilise the framework structure through an extensive hydrogen bonding network with the sulphate oxygen donor atoms. There are a large number of weak hydrogen bonds between both the ammonium nitrogen-hydrogens and some C-H protons on the methyl arms of the cation. The hydrogen bond distances are summarised in **Table 7.5** and are in the range 2.796-3.487 Å. The variation in the hydrogen bond distance may be seen as a consequence of the nature of the hydrogen bond, where the more electropositive hydrogens on the ammonium nitrogen will have a stronger attraction to the sulphate oxygen donors and are reflected by the shorter hydrogen bonds on the whole. Many of the hydrogen bonds above 3 Å originate from the less electropositive C-H protons to the sulphate oxygen donors.

The dimethyl ammonium cations are generated *in-situ* through the decomposition of the solvent dimethylformamide under elevated pressure and temperature. The templating effect of the cations on the overall structure is clear through isolation of larger ring channels in **9** and their position relative to the sulphates to stabilise this configuration. It was hypothesised that the gradual evolution of the templating cation over time plays an important role in the resulting structure through the stabilising interactions and the presumable change in pH over time with template

formation. To investigate the role of the solvent towards template generation, the solvent was changed to the larger diethylformamide with the aim of generating a larger diethylammonium cation that can template the structure of the resulting lanthanide sulphate.

Table 7.5: Selected hydrogen bond distances for **9**.

	Donor-Acceptor Distance (Å)		Donor-Acceptor Distance (Å)
N(1)-H(1E)...O(1)#6	2.901(4)	N(4)-H(4D)...O(11)#9	3.064(6)
C(1)-H(1A)...O(3)#6	3.197(6)	N(6)-H(6E)...O(8)#7	2.900(7)
N(2)-H(2D)...O(23A)#7	2.818(8)	C(9)-H(9A)...O(24A)#7	3.065(11)
N(2)-H(2E)...O(20)#9	2.872(7)	C(10)-H(10A)...O(11)#9	3.349(7)
N(3)-H(3D)...O(10)#11	2.796(5)	C(10)-H(10C)...O(19)#7	3.487(7)

Table 7.6: Crystal data and structure refinement for **9**.

Identification code	9	
Empirical formula	C ₁₈ H ₇₂ N ₉ Nd ₅ O ₄₈ S ₁₂	
Formula weight	2288.76	
Temperature	100(2) K	
Wavelength	0.71073 Å	
Crystal system	Monoclinic	
Space group	C (1) 2/c	
Unit cell dimensions	a = 20.5928(18) Å	α = 90°.
	b = 35.696(3) Å	β = 114.7194(11)°.
	c = 10.0723(9) Å	γ = 90°.
Volume	6725.5(10) Å ³	
Z	4	
Density (calculated)	2.260 Mg m ⁻³	
Absorption coefficient	4.275 mm ⁻¹	
F(000)	4476	
Crystal size	0.200 × 0.160 × 0.100 mm ³	
Theta range for data collection	2.028 to 27.493°.	
Index ranges	-26 ≤ h ≤ 24, -45 ≤ k ≤ 46, -11 ≤ l ≤ 13	
Reflections collected	24151	
Independent reflections	7729 [R(int) = 0.0138]	
Completeness to theta = 25.242°	100.0 %	
Absorption correction	Semi-empirical from equivalents	
Max. and min. transmission	0.7460 and 0.6566	
Refinement method	Full-matrix least-squares on F ²	
Data / restraints / parameters	7729 / 40 / 440	
Goodness-of-fit on F ²	1.040	
Final R indices [I > 2σ(I)]	R1 = 0.0310, wR2 = 0.0710	
R indices (all data)	R1 = 0.0337, wR2 = 0.0726	
Extinction coefficient	n/a	
Largest diff. peak and hole	2.912 and -1.873 e.Å ⁻³	

7.4 The crystal structure of $(\text{NH}_4)[\text{Dy}(\text{SO}_4)_2(\text{H}_2\text{O})]$, **10**

Using the solvent diethylformamide, the reaction of $\text{Dy}(\text{NO}_3)_3 \cdot x\text{H}_2\text{O}$ with sulphuric acid in the mole ratio 1:6 under solvothermal conditions at 170°C for 72 hours results in colourless plate shaped crystals of $(\text{NH}_4)[\text{Dy}(\text{SO}_4)_2(\text{H}_2\text{O})]$, **10**. From the collection of crystals synthesised a suitable crystal was isolated for characterisation by X-ray crystallography.

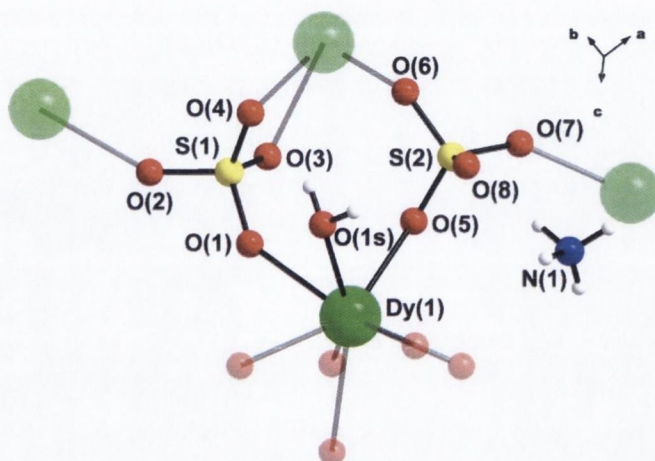
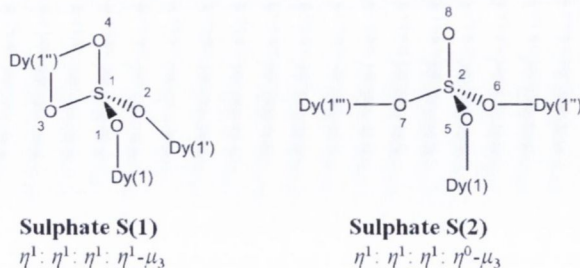


Figure 7.10: Asymmetric unit of $(\text{NH}_4)[\text{Dy}(\text{SO}_4)_2(\text{H}_2\text{O})]$, **10**, identified as bold filled atoms. Faded atoms represent symmetry generated atoms that complete the coordination around Dy(1) and the two sulphate moieties. Dy green, S yellow, O red, N blue and H white.

The structure of **10** can be described as a dense 3D network of $[\text{Dy}(\text{SO}_4)_2(\text{H}_2\text{O})]_n^{1-}$ chains that are cross-linked in the $[110]$ direction through sulphate bridges. The structure is further stabilised through a dense hydrogen bonding network between the negative sulphate network and ammonium (NH_4^+) counter-ion. The origin of the ammonium ion is from *in-situ* decomposition of the solvent diethylformamide.

The compound, **10**, crystallises in the monoclinic crystal system in the space group $P(1)2_1/c$. The asymmetric unit of **10** consists of one Dy^{III} centre, two sulphates and an ammonium counter-ion that forms *in-situ* through the decomposition of diethylformamide (**Figure 7.10**). The Dy^{III} centre is eight-coordinate and stabilised by six sulphate moieties and one coordinated water molecule. The sulphate S(1) bridges three different Dy^{III} centres through a $\eta^1: \eta^1: \eta^1: \eta^1-\mu_3$ bonding description. The oxygen donor atoms O(1) and O(2) form monodentate bonds to Dy(1) and Dy(1'), respectively, while O(3) and O(4) form chelating bonds to Dy(1''). The sulphate S(2) also bridges three Dy^{III} centres by a $\eta^1: \eta^1: \eta^1: \eta^0-\mu_3$ bonding scheme, where the donor atoms O(5), O(6) and O(7) form monodentate bonds to Dy(1), Dy(1'') and Dy(1''') centres, respectively, while O(8) remains uncoordinated.



Scheme 7.3: Coordination modes adopted by sulphate S(1) and S(2) in **10**.

The Dy-O bond lengths summarised in **Table 7.7** are in the range 2.300–2.555 Å. The monodentate bonds are shorter with values below 2.350 Å and the chelate bonds formed from O(3) and O(4) result in longer bonds up to 2.555 Å. The coordinated water (O1s) also forms a longer Dy-O bond distance of 2.417 Å due to the weaker electrostatic nature of the bond.

Table 7.7: Selected bond lengths in **10**.

Bond	Bond Length (Å)	Bond	Bond Length (Å)
Dy(1)-O(1)	2.3971(11)	Dy(1)-O(5)	2.3124(12)
Dy(1)-O(2)#3	2.3393(12)	Dy(1)-O(6)#1	2.3005(12)
Dy(1)-O(3)#1	2.3723(12)	Dy(1)-O(7)#2	2.3120(12)
Dy(1)-O(4)#1	2.5559(12)	Dy(1)-O(1s)	2.4175(12)

The structure can be viewed as infinite chains of $[\text{Dy}(\text{SO}_4)_2(\text{H}_2\text{O})]_n^{1-}$ that run along the *c*-axis (**Figure 7.11a**). The chain has a zig-zag motif (**Figure 7.11b**) constructed from discrete $\{\text{DyO}_8\}$ polyhedra that are connected through two sulphates (S(1) and S(2)) along the *c*-axis. Of the six sulphates that stabilise each Dy^{III} centre, four sulphates are involved in the directional connectivity along the *c*-axis. This leaves one S(1) moiety to bridge adjacent chains through the oxygen donor atom O(2) and a S(2) moiety bridges to a different chain through the O(7) donor atom. These bridging interactions link adjacent chains along the [110] direction.

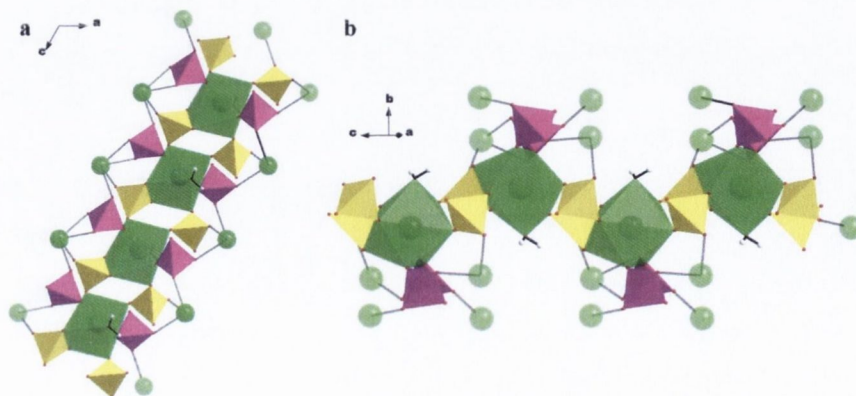


Figure 7.11: (a) Individual chain of discrete $\{\text{DyO}_8\}$ polyhedra bridged by four sulphates along the *c*-axis in **10** as viewed down the *b*-axis. (b) Wave-like motif of the chain in **10** when viewed down the [101] projection. Dy green and O red. Yellow polyhedra denote sulphates that bridge the Dy^{III} centres to form the chain, while magenta polyhedra denote sulphates that are only involved in bridging adjacent chains.

A single unit cell contains two chains, one chain can be visualised from the generation of a c -glide plane perpendicular to the b -axis creating one zig-zag chain from the asymmetric unit. The second chain can be viewed as a result of an inversion centre at $(0.5, 0.5, 0.5)$ and a 2_1 screw axis along the b -axis at $(0.5, b, 0.25)$ and $(0.5, b, 0.75)$. The symmetry elements are shown in relation to the unit cell contents in **Figure 7.12**.

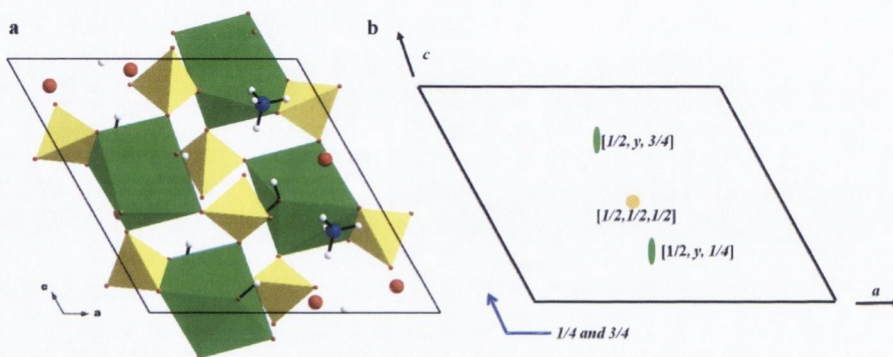


Figure 7.12: (a) Unit cell of **10** as viewed down the b -axis. (b) Diagram of symmetry elements required to generate all atoms within the unit cell of **10** as viewed down the b -axis.

The cross-linking between adjacent chains creates a dense 3D framework structure that contains channels that run along the a -axis and the c -axis (**Figure 7.13**). The channels along the a -axis are constructed from small 8-membered rings of four $\{\text{DyO}_8\}$ polyhedra and four sulphate tetrahedra from two adjacent chains. The channels down the c -axis consist of different 8-membered rings of four $\{\text{DyO}_8\}$ polyhedra and four sulphate tetrahedra from four different chains.

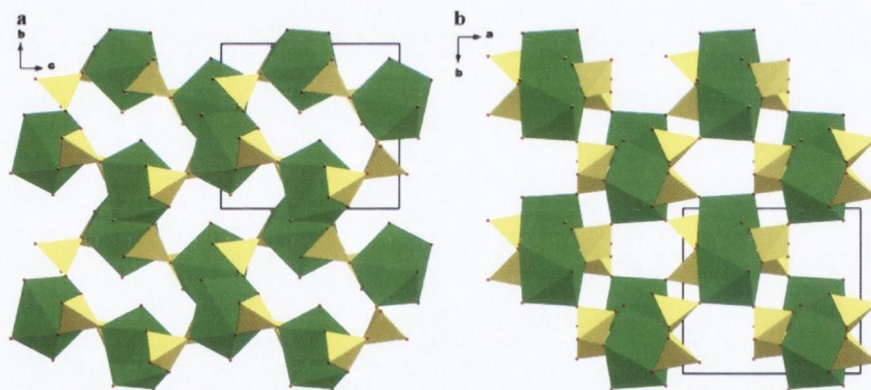


Figure 7.13: Packing of **10** into a dense 3D framework through bridging sulphates of adjacent chains produces (a) 8-membered ring channels from two adjacent chains along the a -axis and (b) 8-membered ring channels along the c -axis from four adjacent chains. The ammonium cations have been removed for clarity. Dy green, S yellow and O red.

The coordinated water molecules extend out into the middle of these channels and stabilise the structure through hydrogen bonding between the water hydrogen donor atom H(1A) with O(4) and O(8) and through H(1B) to the O(6) and O(7) centres with hydrogen bond lengths in the ranges 2.892–3.139 Å. The ammonium counter-ion resides inside the channels and forms hydrogen bonds to further stabilise the framework structure. The ammonium hydrogen atoms H(1), H(3) and H(4) form hydrogen to sulphate oxygen acceptors O(1), O(2), O(3), O(7) and O(8) with bond lengths in

the range 2.788–3.381 Å. The H(2) atom of the ammonium ion also hydrogen bonds to the coordinated water O(1s) with a long hydrogen bond of 3.022 Å (Table 7.8). The hydrogen bonding network is shown in Figure 7.14.

Table 7.8: Selected hydrogen bond distances in **10**.

	Donor-Acceptor Distance (Å)	Donor-Acceptor Distance (Å)	Donor-Acceptor Distance (Å)
O(1S)-H(1A)...O(4)#4	3.1397(17)	N(1)-H(1)...O(7)#1	3.074(2)
O(1S)-H(1C)...O(8)#6	2.8921(17)	N(1)-H(3)...O(8)	2.7886(19)
O(1S)-H(1C)...O(6)#6	2.9840(17)	N(1)-H(4)...O(1)#9	2.975(2)
O(1S)-H(1B)...O(7)#1	3.0592(17)	N(1)-H(4)...O(3)#7	2.8816(19)
N(1)-H(1)...O(2)#7	3.381(2)	N(1)-H(2)...O(1S)#8	3.0222(19)

Table 7.9: Crystal data and structure refinement for **10**.

Identification code	10	
Empirical formula	DyH ₆ NO ₉ S ₂	
Formula weight	390.68	
Temperature	100(2) K	
Wavelength	0.71073 Å	
Crystal system	Monoclinic	
Space group	<i>P</i> (1) 2 ₁ /c	
Unit cell dimensions	a = 10.2397(6) Å	α = 90°.
	b = 8.3040(5) Å	β = 119.4569(6)°.
	c = 10.3055(6) Å	γ = 90°.
Volume	763.00(8) Å ³	
Z	4	
Density (calculated)	3.401 Mg m ⁻³	
Absorption coefficient	10.370 mm ⁻¹	
F(000)	732	
Crystal size	0.110 × 0.070 × 0.060 mm ³	
Theta range for data collection	2.284 to 30.567°.	
Index ranges	-14 ≤ h ≤ 14, -11 ≤ k ≤ 11, -14 ≤ l ≤ 14	
Reflections collected	27866	
Independent reflections	2327 [R(int) = 0.0158]	
Completeness to theta = 25.242°	100.0%	
Absorption correction	Numerical	
Max. and min. transmission	0.6867 and 0.4622	
Refinement method	Full-matrix least-squares on F ²	
Data / restraints / parameters	2327 / 0 / 136	
Goodness-of-fit on F ²	0.937	
Final R indices [I > 2σ(I)]	R1 = 0.0092, wR2 = 0.0270	
R indices (all data)	R1 = 0.0097, wR2 = 0.0273	
Largest diff. peak and hole	0.384 and -0.614 e.Å ⁻³	

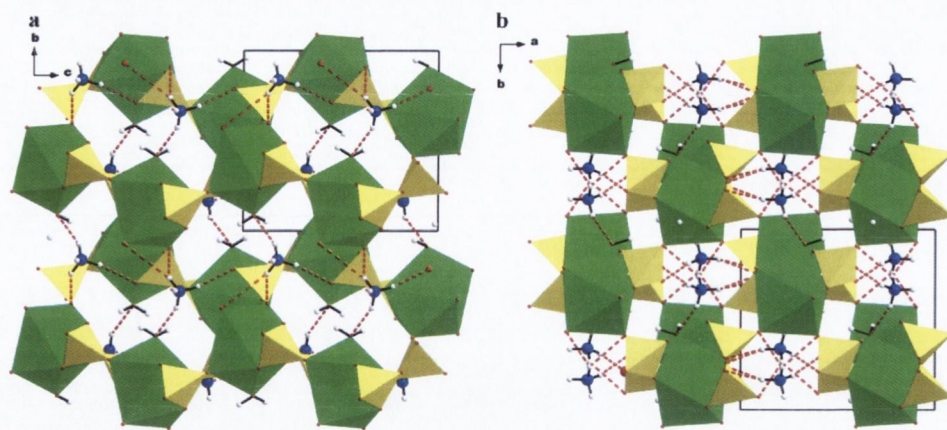


Figure 7.14: The hydrogen bonding network in **10** as viewed down the (a) *a*-axis and (b) *c*-axis.

7.5 Crystal structure of $(\text{NH}_4)_3[\text{Dy}(\text{SO}_4)_3]$, (**11**)

The solvothermal reaction of $\text{Dy}(\text{NO}_3)_3 \cdot x\text{H}_2\text{O}$ with sulphuric acid in the molar ratio of 1:15 in 5 mL of diethylformamide when heated at 170 °C for 72 hours yields colourless plates of $(\text{NH}_4)_3[\text{Dy}(\text{SO}_4)_3]$, **11**, following the decomposition of the solvent. A suitable crystal from the reaction mixture was selected and characterised by means of single crystal X-ray diffraction.

Compound **11** has a layered structure consisting of corrugated layers of $(\text{NH}_4)_3[\text{Dy}(\text{SO}_4)_3]$ that form in the *bc*-plane, which are stabilised by a hydrogen bonding network arising from the position of the ammonium cations in between adjacent layers.

The compound, **11**, crystallised in the monoclinic crystal system in the space group $C(1)2/c(1)$ with unit formula $(\text{NH}_4)_3[\text{Dy}(\text{SO}_4)_3]$. The asymmetric unit of **11** consists of one Dy^{III} centre, three sulphate moieties and four ammonium cations that form *in-situ* from the decomposition of diethylformamide at elevated temperature and pressure (**Figure 7.15**). The dysprosium centre is stabilised by six sulphate moieties. Of the three unique sulphate moieties, the S(3) also displays some positional disorder of the O(10), O(11) and O(12) atoms over two positions. The Dy^{III} -sulphate network is charge balanced through four NH_4^+ cations, where the N(3) and N(4) cations are half occupied from disorder over special positions.

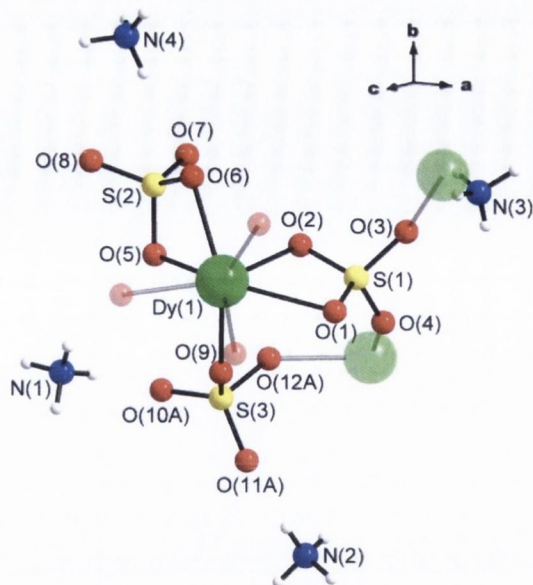
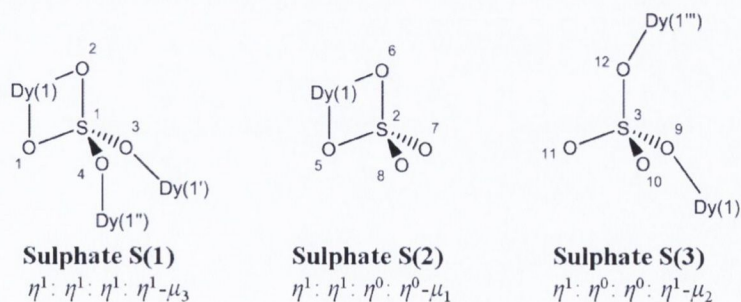


Figure 7.15: The asymmetric unit of **11**. Faded atoms represent symmetry generated atoms to complete Dy^{III} and sulphate coordination spheres. Dy green, S yellow, O red, N blue and H white.

The Dy(1) is 8-coordinate and can be visualised as distorted dodecahedron where the inner coordination sphere is completed from the donors atoms O(1) and O(2) of a S(1) sulphate, O(3') from a symmetry S(1') sulphate and O(4'') from a second S(1'') symmetry equivalent. The oxygen atoms O(5) and O(6) of the S(2) sulphate and O(9) and O(12A') from two S(3) sulphates fill the remaining coordination sites.

The bonding description of the S(1) sulphate is $\eta^1: \eta^1: \eta^1: \eta^1-\mu_3$ (**Scheme 7.4**) bridging three Dy^{III} centres where the oxygen donors O(1) and O(2) chelate Dy(1) and O(3) and O(4) each form monodentate bonds to two symmetry related Dy^{III} centres, Dy(1') and Dy(1''). The S(2) sulphate binds to a single Dy^{III} centre by a $\eta^1: \eta^1: \eta^0: \eta^0-\mu_1$ description where the donor atoms O(5) and O(6) chelate Dy(1). Two Dy^{III} centres are bridged by the S(3) sulphate through a $\eta^1: \eta^0: \eta^0: \eta^1-\mu_2$ bonding description where the oxygen atoms O(9) and O(12) form monodentate bonds to Dy(1) to Dy(1''), respectively.



Scheme 7.4: Coordination modes adopted from the three unique sulphate moieties in **11**.

The bond distances in **Table 7.10** vary between 2.296–2.487 Å as a result of the bonding interaction. The monodentate interactions to a Dy^{III}-centre are often shorter, whilst the chelating interactions result in the longer bond distances observed. The bond distances are generally shorter than those for Nd–O in **9** and are a consequence of lanthanide contraction.

Table 7.10: Selected bond distances for **11**.

Bond	Bond Length (Å)	Bond	Bond Length (Å)
Dy(1)-O(1)	2.4865(8)	Dy(1)-O(5)	2.4221(9)
Dy(1)-O(2)	2.4136(7)	Dy(1)-O(6)	2.3452(8)
Dy(1)-O(3)#2	2.3470(8)	Dy(1)-O(9)	2.2768(8)
Dy(1)-O(4)#1	2.3392(8)	Dy(1)-O(12A)#1	2.2961(18)

The Dy^{III} centres are stabilised as discrete polyhedra that are bridged by the S(1) and S(3) sulphates into a “chain” along the *c*-axis. (**Figure 7.16a**). The S(2) sulphate chelates a single Dy^{III} centre and acts to complete the coordination sphere; it does not bridge any centres. The S(1) sulphate further bridges adjacent chains through the oxygen donor atom O(3) and creates a corrugated 2D layer in the *bc*-plane as shown in **Figure 7.16b**.

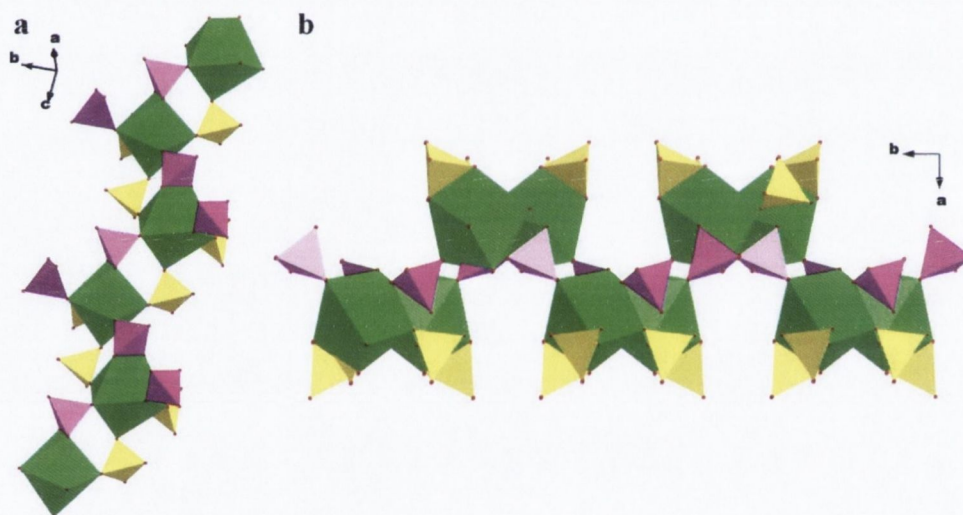


Figure 7.16: (a) The formation of chains of $[\text{Dy}(\text{SO}_4)_3]_n^{3-}$ along the *c*-axis through bridging from S(1) and S(3) sulphate. (b) Corrugated layer forming in the *bc*-plane through the bridging of adjacent chains through O(3) of the S(1) sulphate. Dy green polyhedra and O red. Yellow polyhedra denote S(2) and S(3) sulphates that form the $[\text{Dy}(\text{SO}_4)_3]_n^{3-}$ chain, while magenta polyhedra denote S(1) sulphates which also bridge adjacent chains to form the corrugated layer.

Within the unit cell, two corrugated layers are contained. One layer may be viewed as taking the asymmetric unit and applying a *c*-glide plane perpendicular to the *b*-axis at $b=0.5$, an inversion centre at coordinates (0.25, 0.25, 0.5) and a 2_1 screw axis along the *b*-axis at (0.25, *b*, 0.75). The second corrugated layer is shifted half a unit cell and may be considered by applying the centring vector to the asymmetric unit. The result of an *n*-glide plane perpendicular to the *b*-axis with projection [101], a two-fold rotation axis at (0.5, *b*, 0.75) and an inversion centre at (0.5, 0.5, 0.5) complete the second layer within the unit cell. The position of the symmetry elements down the *c*-projection are identified in **Figure 7.17**.

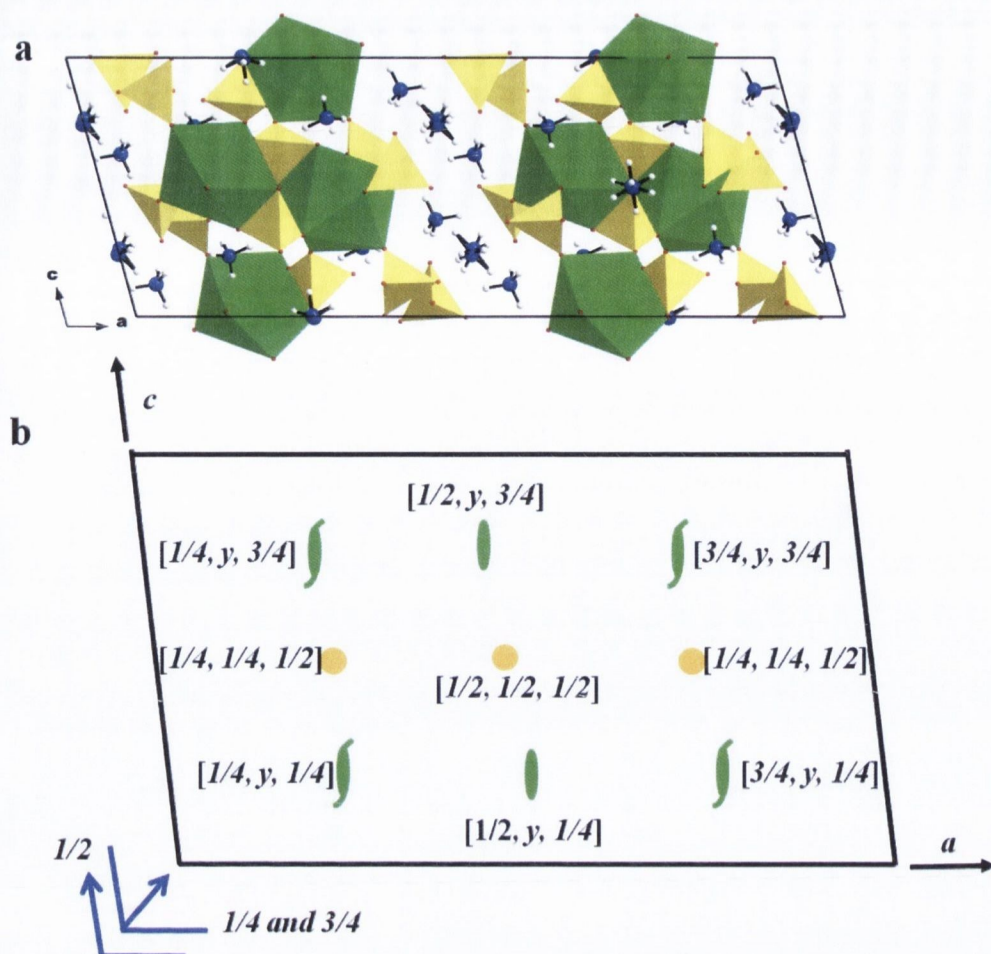


Figure 7.17: (a) Unit cell of **11** as viewed down the *b*-axis. (b) Diagram of symmetry elements required to generate all atoms within the unit cell of **11** as viewed down the *b*-axis.

To stabilise the negatively charged inorganic sheets, an extensive hydrogen bonding network exists between the sulphate oxygen atoms and the hydrogen atoms of the ammonium cations. The cations N(2) and N(3) are located within the corrugated voids of individual sheets resulting in intra-layer hydrogen bonding (**Figure 7.18**, red dashed bonds) with the oxygen donors of the sulphate moieties within a single layer. Further inter-layer hydrogen bonding (**Figure 7.18**, blue dashed bonds) occurs between adjacent stacked layers and the N(1) and N(4) cations that reside in the interlamellar space. The hydrogen bonds are weak with lengths that range between 2.798-3.154 Å (**Table 7.11**). The intra-layer hydrogen bonding can be viewed as stabilising the structure of individual layers whereas the inter-layer hydrogen bonding stabilises the stacking of adjacent layers. The resulting corrugated layers may be connected to two variables from the synthesis. In the synthesis of **10**, a larger Ln:SO₄ ratio was adopted compared to **9**. The larger, Ln:SO₄ ratio seems to be reflected by the increase of coordinated sulphate in the formula unit and as such, the structure changes to the corrugated nature to accommodate this. The templating effect of the cation through hydrogen bonding is important for this to remain stable, as observed with the location of ammonium cation in the corrugated layer void space. From the above observations, it is reasonable to see that the shape of the cation template is important where the relatively spherical

charge distribution of an ammonium cation may accommodate stabilisation of the small channels in the 3D network of **10** and also the corrugated void of **11**.

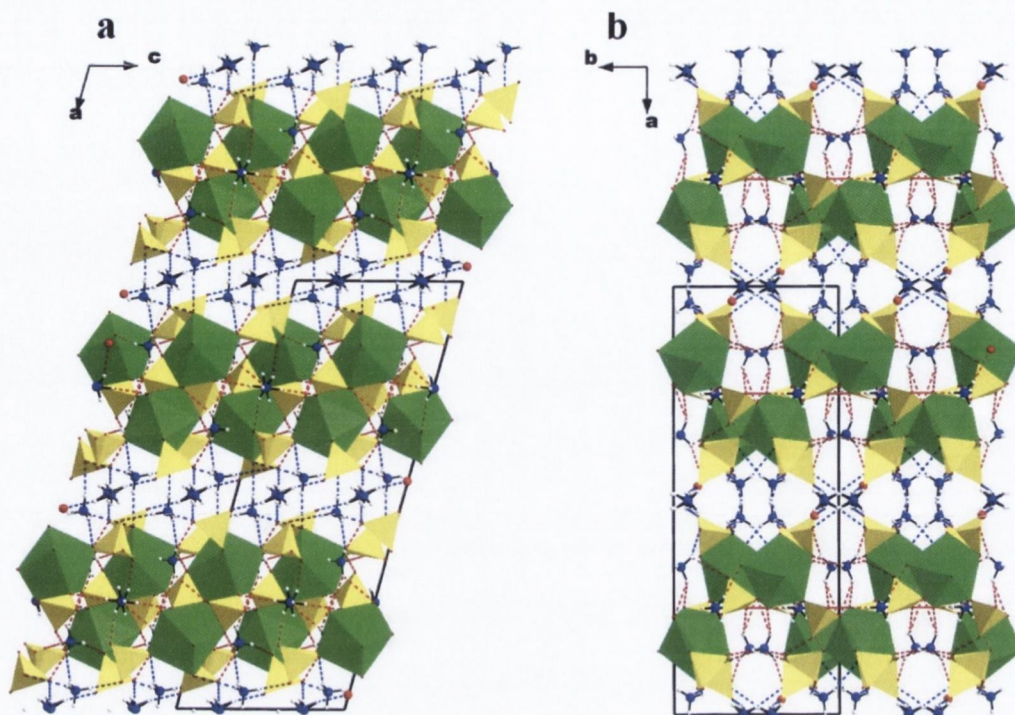


Figure 7.18: Hydrogen bonding network in **11** as viewed down the (a) *b*-axis and (b) *c*-axis. Inter-layer hydrogen bonds are denoted by blue-dashed line, intra-layer hydrogen bonds are denoted by red-dashed lines. Dy green polyhedra, S yellow polyhedra, O red, N blue and H white.

Table 7.11: Selected hydrogen bond distances in **11**.

	Donor-Acceptor Distance (Å)		Donor-Acceptor Distance (Å)
N(1)-H(1A)...O(5)#4	2.9674(14)	N(3)-H(3B)...O(3)	2.990(18)
N(1)-H(1C)...O(5)#1	3.1039(15)	N(3)-H(3C)...O(9)#8	3.053(19)
N(1)-H(1C)...O(7)#1	2.8390(14)	N(3)-H(3D)...O(1)#3	3.05(2)
N(1)-H(1B)...O(12A)#1	2.971(9)	N(4)-H(4B)...O(7)	2.891(6)
N(1)-H(1D)...O(10A)	2.848(9)	N(4)-H(4C)...O(8)#9	2.805(9)
N(2)-H(2A)...O(11A)	2.719(4)		
N(2)-H(2B)...O(2)#5	2.9779(15)		
N(2)-H(2B)...O(7)#5	2.7988(14)		
N(2)-H(2C)...O(1)#6	3.1540(15)		
N(2)-H(2C)...O(4)#7	3.0275(14)		
N(2)-H(2D)...O(6)#3	2.8443(14)		

Table 7.12: Crystal data and structure refinement for **11**.

Identification code	11	
Empirical formula	DyH ₁₂ N ₃ O ₁₂ S ₃	
Formula weight	504.81	
Temperature	100(2) K	
Wavelength	0.71073 Å	
Crystal system	Monoclinic	
Space group	C(1)2/c(1)	
Unit cell dimensions	a = 26.0627(6) Å	α = 90°.
	b = 9.7398(2) Å	β = 105.1570(10)°.
	c = 9.8635(2) Å	γ = 90°.
Volume	2416.70(9) Å ³	
Z	8	
Density (calculated)	2.775 Mg m ⁻³	
Absorption coefficient	6.770 mm ⁻¹	
F(000)	1944	
Crystal size	0.100 × 0.080 × 0.080 mm ³	
Theta range for data collection	1.619 to 36.429°.	
Index ranges	-43 ≤ h ≤ 43, -16 ≤ k ≤ 16, -16 ≤ l ≤ 16	
Reflections collected	100969	
Independent reflections	5903 [R(int) = 0.0182]	
Completeness to theta = 25.242°	99.9%	
Absorption correction	Semi-empirical from equivalents	
Max. and min. transmission	0.7471 and 0.6461	
Refinement method	Full-matrix least-squares on F ²	
Data / restraints / parameters	5903 / 12 / 236	
Goodness-of-fit on F ²	0.965	
Final R indices [I > 2σ(I)]	R1 = 0.0109, wR2 = 0.0284	
R indices (all data)	R1 = 0.0124, wR2 = 0.0289	
Extinction coefficient	n/a	
Largest diff. peak and hole	0.586 and -1.012 e.Å ⁻³	

7.6 Physicochemical characterisation of compounds 8-11

The PXRD patterns of the four different lanthanide sulphate materials were measured and compared against the calculated powder pattern for each respective structure model. **Figure 7.19** shows the PXRD patterns for **8-11** and the experimental patterns match with the strongest reflections from the model for all four materials. In some cases, the intensities vary slightly from the calculated model and may be explained due to the sample preparation using a stationary slide where preferred orientations of the crystallites can manifest in a change in reflection intensities. This could be avoided in the future by adopting a spinning capillary sample holder, however, this option is not available on the current in-house experimental set-up.

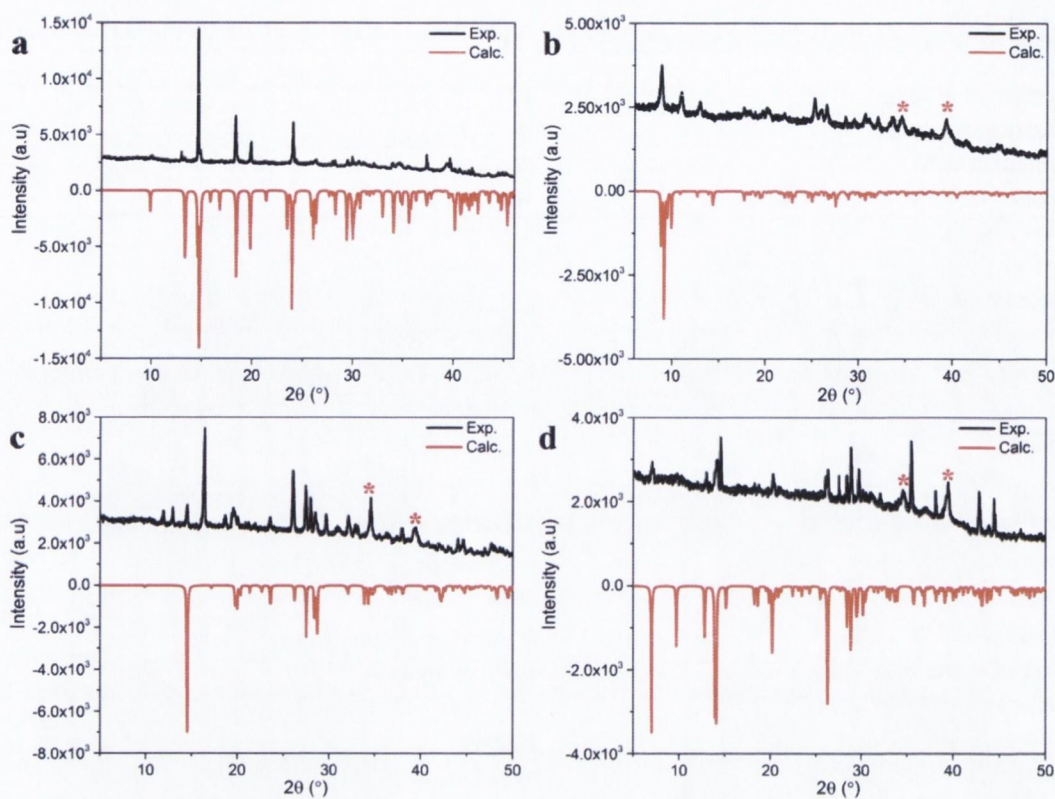


Figure 7.19: The experimental vs. calculated powder patterns for the lanthanide sulphates (a) $[\text{Nd}_2(\text{SO}_4)_3(\text{H}_2\text{O})_8]$, **8**, (b) $(\text{Me}_2\text{NH}_2)_9[\text{Nd}_5(\text{SO}_4)_{12}]$, **9**, (c) $(\text{NH}_4)[\text{Dy}(\text{SO}_4)_2(\text{H}_2\text{O})]$, **10** and (d) $(\text{NH}_4)_3[\text{Dy}(\text{SO}_4)_3]$, **11**. * indicate reflections from instrumental artefacts.

The FT-IR spectra for **8-11** in **Figure 7.20** are all similar, where bands arising from the sulphate group are identified. However, differences in the spectra arise from the different counter-ions and hydrogen bonding present within the structures. An uncoordinated sulphate group has T_d point group symmetry and has four fundamental normal modes of vibration, ν_{1-4} , of which ν_3 and ν_4 are IR active, while ν_{1-2} are all Raman active.²⁵ Through coordination of a sulphate to a metal centre, the symmetry is lowered and the ν_1 and ν_2 stretches may also be observed. In **8-11**, strong bands between $1050\text{-}1100\text{ cm}^{-1}$ are assigned to the ν_3 band of SO_4 . Weaker bands superimposed on this band at the lower energy range $950\text{-}1001\text{ cm}^{-1}$ are due to the ν_1 band. An absorption band down to 650 cm^{-1} appears to be growing before the experiment cut-off and has been assigned previously to the ν_4 band of the SO_4 group in other lanthanide sulphate materials.^{10, 12, 15} In **9-11**, there are also counter-ions (the organic template) present and these are assigned to bands around 1400 cm^{-1} arising from the $\nu_{\text{N-H}}$ stretches and in **9** a weaker band is also observed at 1594 cm^{-1} assigned to the $\nu_{\text{N-CH}_3}$ bending vibration. Extensive hydrogen bonding is observed between the counter-ions and sulphate oxygen centres in **9-11**. These are assigned to the sharper bands above 3000 cm^{-1} as has been noted in the literature.^{16, 26, 27}

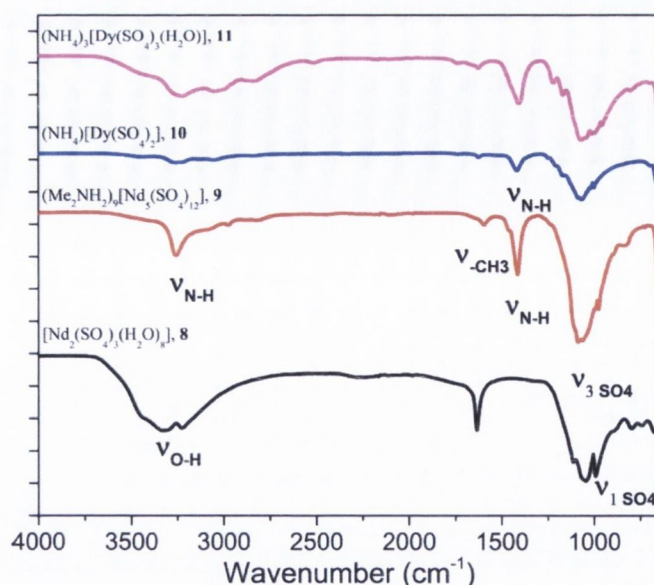


Figure 7.20: The FT-IR spectra for the lanthanide sulphates (a) $[\text{Nd}_2(\text{SO}_4)_3(\text{H}_2\text{O})_8]$, **8**, (black trace) (b) $(\text{Me}_2\text{NH}_2)_9[\text{Nd}_5(\text{SO}_4)_{12}]$, **9**, (red trace) (c) $(\text{NH}_4)[\text{Dy}(\text{SO}_4)_2(\text{H}_2\text{O})]$, **10**, (blue trace) and (d) $(\text{NH}_4)_3[\text{Dy}(\text{SO}_4)_3]$, **11**, (magenta trace).

The TGA of **8-11** was performed in air from 30-900 °C and is given in **Figure 7.21**. The stability of the materials is similar, consisting of two main decomposition paths. Up to a temperature of 300 °C, the decomposition involves the removal of water and the organic templates. In the range 300-900 °C the decomposition results in the evolution of SO_3 , as has been documented previously in lanthanide sulphates.^{15, 16}

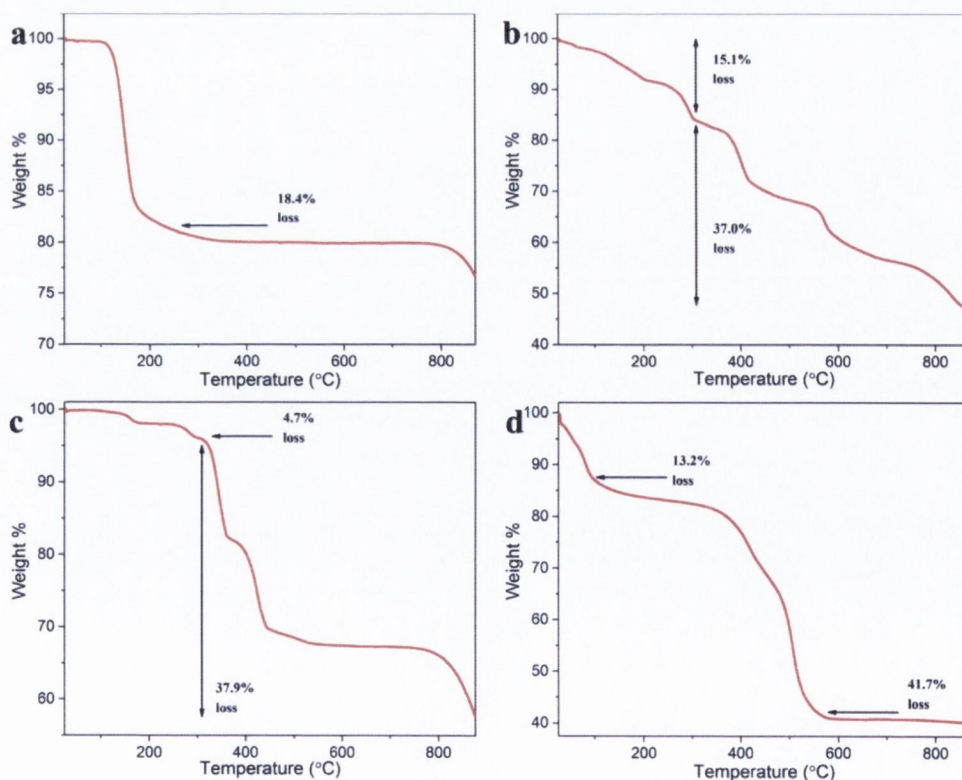


Figure 7.21: Thermograms for the lanthanide sulphates (a) $[\text{Nd}_2(\text{SO}_4)_3(\text{H}_2\text{O})_8]$, **8**, (b) $(\text{Me}_2\text{NH}_2)_9[\text{Nd}_5(\text{SO}_4)_{12}]$, **9**, (c) $(\text{NH}_4)[\text{Dy}(\text{SO}_4)_2(\text{H}_2\text{O})]$, **10**, and (d) $(\text{NH}_4)_3[\text{Dy}(\text{SO}_4)_3]$, **11**.

7.7 The effect of organic templates on the resulting structure

The introduction reviewed the current work on organic templating effects in the synthesis of lanthanide sulphates and in many of the structures of 2D and 3D nature, channels formed from 8-membered ring constructions were prevalent. The layered structure of **8** consists of “flat” neutral sheets that also display 8-membered rings. This indicates that there may be a preferential mechanism resulting in 8-membered rings, in both the absence of an organic template and in the templated examples discussed in the introduction. In the isolation of the 3D structure of $(\text{Me}_2\text{NH}_2)_9[\text{Nd}_5(\text{SO}_4)_{12}]$, **9**, we were able to create a structure with 10- and 20-membered ring channels. Perhaps of greater significance is that the organic template forms *in-situ* through the decomposition of dimethylformamide. The evolution of the organic template at elevated temperature and pressure will have a distinct effect on the changing pH with time. Although this is a difficult variable to quantify due to the nature of a sealed solvothermal reaction, we were able to further adapt this approach in synthesising **10** and **11** with the decomposition of diethylformamide into ammonium, NH_4^+ . It should be noted the initial intention was to produce diethylammonium cations *in-situ*, however, ammonium cations tended to evolve and this could be due to the stabilisation of the ethyl carbocation in the decomposition pathway. Nevertheless, the evolution of NH_4^+ cations results in the isolation of novel 2D and 3D lanthanide sulphates with ammonium counter-ions that differ from those currently known.²⁸ The importance of the hydrogen bonding in the templating effect can be highlighted by comparing the layers of the non-templated structure **8** and the templated corrugated waves of the layers in **11**. Through the presence of hydrogen bonding to the cation specifically, the layered structure is modified to that observed in **11**. In comparing the structures of **10** and **11**, one main difference in the reaction conditions is the quantity of sulphate present, where a smaller Ln:SO₄ ratio results in the 3D structure of **10**, and a higher ratio results in the 2D structure of **11**. It appears that this sulphate ratio may be reflected in the resulting molecular formula where **10** has one fewer sulphate moiety per unit formula. To conclude from this study, there is some growing evidence that *in-situ* evolution of the organic template is an effective strategy for unique lanthanide sulphate structures and with careful tuning of the Ln:SO₄ ratio can result in some control between 2D and 3D templated materials.

7.8 Conclusions and Outlook

The structures **9-11** discussed in this chapter differ from previous organically templated lanthanide sulphates in that the solvent also acts as the source of the organic template through *in-situ* decomposition. This route implies that the concentration of the template and the reaction pH will vary over time and have proven successful in the isolation of novel 2D and 3D structures, and as such provides a variable by which the pH is changed over the course of the reaction. Future objectives look to finding suitable solvents that may decompose to produce larger cations that could be exploited to template structures with larger channel voids. The gas absorption properties

of the 3D sulphate **10**, were probed but at present, removal of the organic template, $[\text{Me}_2\text{NH}_2]^+$ has not been successful. A similar problem has been observed with other porous lanthanide sulphates¹³ and future work will aim to find solutions that overcome this hurdle. The small nature of sulphate as a ligand ensures that Ln^{III}-Ln^{III} bond distances do not become too large and the different packing of lanthanide centres has us interested in understanding the magnetic properties and how the lanthanide centres couple. With this in mind, the magnetic properties of the Gd^{III}, Dy^{III} and Ho^{III}-analogues of **10** are currently under investigation, with a particular interest in possible magnetic cooling properties of **10-Gd**.

7.9 References

1. W. J. Roth, P. Nachtigall, R. E. Morris and J. Cejka, *Chem. Rev.*, 2014, **114**, 4807-4837.
2. P. B. Venuto, *Microporous Mater.*, 1994, **2**, 297-411.
3. R. Levanmao, N. T. Vu, S. Y. Xiao and A. Ramsaran, *J. Mater. Chem.*, 1994, **4**, 1143-1147.
4. G. Ferey, *Chem. Mater.*, 2001, **13**, 3084-3098.
5. G. Ferey, T. Loiseau, P. Lacorre and F. Taulelle, *J. Solid State Chem.*, 1993, **105**, 179-190.
6. T. Loiseau and G. Ferey, *J. Solid State Chem.*, 1994, **111**, 403-415.
7. C. Sassoie, T. Loiseau, F. Taulelle and G. Ferey, *Chem. Commun.*, 2000, 943-944.
8. T. Bataille and D. Louer, *J. Mater. Chem.*, 2002, **12**, 3487-3493.
9. T. Bataille and D. Louer, *J. Solid State Chem.*, 2004, **177**, 1235-1243.
10. M. Dan, J. N. Behera and C. N. R. Rao, *J. Mater. Chem.*, 2004, **14**, 1257-1265.
11. Y. L. Fu, Z. W. Xu and J. L. Ren, *J. Mol. Struct.*, 2006, **788**, 190-193.
12. J. Fu, L. Zheng, Y. Yuan, Y. Song and Y. Xu, *J. Chem. Crystallogr.*, 2011, **41**, 1737-1741.
13. L. Zheng, Z. B. Zhang, D. R. Zhu and Y. Xu, *Inorg. Chem. Commun.*, 2011, **14**, 258-260.
14. G. W. Ge, Z. Y. Qi, Z. G. Ni, Y. Z. Li, H. B. Du and X. Z. You, *Inorg. Chem. Commun.*, 2012, **20**, 228-233.
15. D. Zhang, Y. Lu, D. R. Zhu and Y. Xu, *Inorg. Chem.*, 2013, **52**, 3253-3258.
16. W. L. Zhou, X. R. Ding, Z. B. Zhang, L. Zheng, Y. Xu and D. R. Zhu, *Z. Anorg. Allg. Chem.*, 2010, **636**, 882-885.
17. W. L. Zhou, Q. Chen, D. R. Zhu and Y. Xu, *Z. Anorg. Allg. Chem.*, 2009, **635**, 572-576.
18. W. L. Zhou, Y. Xu, L. J. Han and D. R. Zhu, *Dalton Trans.*, 2010, **39**, 3681-3686.
19. Y. Xing, Y. L. Liu, Z. Shi, H. Meng and W. Q. Pang, *J. Solid State Chem.*, 2003, **174**, 381-385.
20. Y. L. Zhu, G. P. Zhou, Y. Xu, D. R. Zhu and X. F. Zheng, *Z. Anorg. Allg. Chem.*, 2008, **634**, 545-548.
21. X. M. Zhang and Y. F. Li, *Acta Crystallogr., Sect. E: Struct. Rep. Online*, 2010, **66**, M649-U518.
22. W. L. Zhou, Q. Chen, N. Jiang, X. Meng, D. R. Zhu and Y. Xu, *Inorg. Chim. Acta*, 2009, **362**, 3299-3302.
23. C. A. Murphy, T. S. Cameron, M. W. Cooke and M. A. S. Aquino, *Inorg. Chim. Acta*, 2000, **305**, 225-229.
24. E. Kahrovic, P. Orioli, B. Bruni, M. Di Vaira and L. Messori, *Inorg. Chim. Acta*, 2003, **355**, 420-423.
25. K. Nakamoto, *Infrared and Raman Spectra of Inorganic and Coordination Compounds*, Sixth edn., John Wiley & Sons, Inc., 2009.
26. A. Zecchina, L. Marchese, S. Bordiga, C. Paze and E. Gianotti, *J. Phys. Chem. B*, 1997, **101**, 10128-10135.
27. P. Sivagurunathan, K. Ramachandran and K. Dharmalingam, *Main Group Chem.*, 2006, **5**, 89-94.
28. M. S. Wickleder, *Chem. Rev.*, 2002, **102**, 2011-2087.

Chapter Eight



Conclusions and future work

This thesis has looked specifically at utilising phosphonic acids, iminodiacetic acid derivatives and the sulphate ion as new ligands for the synthesis and characterisation of new lanthanide-organic hybrid materials, with a focus towards 2D and 3D architectures that exploit the photoluminescence and magnetic properties of the lanthanide centre.

In **Chapter 3** the successful synthesis of three new lanthanide phosphonate materials was achieved using *tert*-butyl, 1-naphthalene- and 4-biphenyl phosphonic acid. The crystal structure of the **Ln-Bu^t** series was determined and shown to be a 1D coordination polymer that packs into a *pseudo*-2D material. Using a combination of PXRD, TGA and PL analysis the structures of **Ln-Naph** and **Ln-Biphen** were determined as 2D materials. The systematic variation of the ligand size and shape was used to investigate the crystal morphology and the PL properties. The morphologies vary between 1D nanorods to 2D plates. The number of lanthanide centres directly coordinated by the phosphonate group is an important factor in determining the crystal growth properties. When multiple Ln^{III} centres are bridged by the phosphonic along a certain direction, a concomitant anisotropic growth preference is manifested along a particular axis for the crystal growth. As the ligand became more hydrophobic, we saw the morphology of the crystal become more amorphous. With careful consideration, the Stark splitting of the Eu^{III} emission lines can aid characterisation of the structure in the solid-state with complementary data from PXRD and TGA. We have investigated ligand sensitisation in these materials and find **Biphen-PO₃H₂** to be an efficient sensitiser for both Eu^{III} and Tb^{III} centres with an improvement in the emission properties, while **Naph-PO₃H₂** is a more appropriate sensitiser for the Eu^{III} centre. We find that both ligands are suitable for sensitising NIR emission from Nd^{III} and Yb^{III} centres.

Future work looks to build on the studies of the **Ln-Biphen** series in particular and look into improving the photoluminescence quantum yields by reducing concentration quenching. We aim to investigate Eu^{III} and Tb^{III} co-doping into an La^{III} matrix whereby concentration quenching by energy transfer to nearest neighbour Eu^{III} and Tb^{III} sites is reduced from its dilution in the La^{III} matrix. By tuning the Eu^{III} and Tb^{III} ratios and using the efficient sensitisation of the biphenyl ligand we aim to identify white-light emitting materials. With the larger *d*-spacing and more amorphous nature of the crystal habit observed in **Ln-Biphen** we will further look into exfoliating these materials to produce thin-films to allow transfer into potential devices.

In **Chapter 4** we moved towards using H₃heidi as a ligand to stabilise the Ln^{III} ion in solution. In this regard, mononuclear and binuclear complexes were successfully isolated. In forming the binuclear complex we observe the formation of bridging μ_2 -hydroxo interactions. By studying the PL properties in the solid-state and solution we were able to identify that the mononuclear species is a stable species in solution which could be valuable in the synthesising new hybrid materials when used with a second organic ligand.

In the future, we intend to further study the Ln^{III}:H₃heidi reaction systems to try and tune the synthesis to favour larger clusters that may exhibit strong magnetic properties interaction

between Ln^{III} centres and intend to fully exploit the ligand in isolating novel structural topologies in conjunction with phosphonic acids and Ln^{III} ions together.

Chapter 5 looked into the chemistry of iminodiacetic acid substituted naphthols with lanthanide ions. The reaction of the ligand $\text{H}_4\text{C3hnida}$, results in two novel hybrid materials, **5**, which displays a chiral 3D architecture, and a 1D coordination polymer, **6**. The PL properties of Eu^{III} , Nd^{III} and Yb^{III} analogues of the 3D structure were measured and a weak PL is observed from **5-Eu**, while more promising PL is observed in the NIR from **5-Nd** and **5-Yb**. The structural features indicate a high density of the Ln^{III} ions and ligand in the chains along the *c*-direction. It has been shown in some Yb^{III} -MOF materials that this high density of ligand and Yb^{III} centres is advantageous for application in cell imaging.¹ In the reaction of $\text{H}_4\text{C6hnida}$, we isolated the structure of 5,5'-methylenebis(6-hydroxy-2-naphthoic acid), **4**, which comes from the decomposition of $\text{H}_4\text{C6hnida}$ and the two of the fragments reacting together. It is noted that this is an isomer of pamoic acid, a pharmaceutical agent for lowering the solubilities of products, as a result there is interest in understanding the solid-state packing of these compounds. We provide a contribution to this area with the identification of herring-bone packing of our isomer through directional hydrogen bonding that has not been currently observed in crystal structures of pamoic acid. We also provide a potential synthetic route to isolating a crystal structure for pamoic acid, where current crystal structures only exist with derivatives of lutidine.

The potential for this area of research is vast, and within the Schmitt group a large family of the iminodiacetic acid derived naphthols and phenols are known. We first aim to investigate more gentle synthetic conditions to react $\text{H}_4\text{C6hnida}$ directly with lanthanide ions and investigate the effect on network structure by the positional transfer of the additional carboxylate from the 3- to the 6-position. A naphthol derivative with no additional carboxylate on the backbone is known and we intend to reaction chemistry of this ligand with lanthanides. Additional structures isolated using these two ligands will help identify potential structure directing influences on the final structure, a necessity for synthesis of materials with a pre-determined structural feature. A large library of the iminodiacetic acid derived phenol ligands are known, where multiple side group substitutions in *ortho*- and *para*-position to the phenol exist. We plan to investigate the effect of side group substitutions on the lanthanide hybrid structure. The promising NIR emission of **5-Nd** and **5-Yb** will also be investigated collecting quantitative analysis in terms of the emission quantum yield and observed emission lifetimes to probe their potential for cell imaging applications.

The isolation of 3D chiral networks from the achiral ligand, benzoic acid, was characterised in **Chapter 6**. The chirality is manifested through four-fold screw axes that run along the *c*-axis and result in chiral chains of $\text{Ln}^{\text{III}}/\text{Na}^+$ polyhedra and a chiral arrangement of the benzoate ligand along a channel void. The optical activity of the material was investigated in the solid-state and characterised by an absorption band centred at 240 nm assigned to the $\pi^* \leftarrow \pi$ absorption in the ligand and indicates an excess of one enantiomer crystallising from solution. The

emission properties were investigated and the material had a high emission quantum yield $\Phi_{\text{PL}} = 23.8\%$

Future work aims to develop a synthesis that results in an enantio-pure material and preferably the isolation of both enantiomers. We are particularly interested in studying the CPL from these materials and, if successful, aim to expand the synthetic approach to consider the different ligands phenyl acetic acid, and 1- and 2-naphthoic acid. We foresee the potential of these materials as a new generation of chiral security tags.

The synthesis of high dimensional lanthanide sulphate materials was investigated in **Chapter 7**. Four different structures were isolated, an 2D array of $[\text{Nd}_2(\text{SO}_4)_3(\text{H}_2\text{O})_8]$, **8**, that forms in the absence of a templating agent to generate a neutral layered material. When organic cations are used as templates, three novel charged lanthanide sulphates were synthesised; the 3D networks of $(\text{Me}_2\text{NH}_2)_9[\text{Nd}_5(\text{SO}_4)_{12}]$, **9** and $\text{NH}_4[\text{Dy}(\text{SO}_4)_2(\text{H}_2\text{O})]$, **10**, while a higher Ln: SO_4^{2-} ratio yields the 2D $(\text{NH}_4)_3[\text{Dy}(\text{SO}_4)_3]$, **11**. To the best of our knowledge, our approach exploits the *in-situ* formation of the organic template from the decomposition of the solvent for the first time and at present we isolated two counter-ions by this method, the NH_4^+ and the dimethylammonium ions. We stress that by the *in-situ* formation of NH_4^+ ion we isolate novel structures that are different from those lanthanide sulphates currently known to form with the NH_4^+ ion.² We believe this could be due to the gradual change in pH over time as the counter-ion is formed.

The future goals from this body of work are to further investigate the potential of organic templating through *in-situ* decomposition and look for potential solvents that may generate larger counter-ions. We currently have a porous network in the structure of **9** and intend to isolate a routine to allow efficient evacuation of the channels with retention of the framework structure. We are currently investigating the magnetic properties of **9-Gd** and **9-Dy** and intend to probe the potential of **9-Gd** for magnetic cooling.

8.1 References

1. A. Foucault-Collet, K. A. Gogick, K. A. White, S. Villette, A. Pallier, G. Collet, C. Kieda, T. Li, S. J. Geib, N. L. Rosi and S. Petoud, *Proc. Natl. Acad. Sci. U.S.A.*, 2013, **110**, 17199-17204.
2. M. S. Wickleder, *Chem. Rev.*, 2002, **102**, 2011-2087.

Attached CD-ROM

This CD-ROM contains electronic versions of various files for the structures given in this thesis. There are 2 folders that contain these files.

The CIF folder contains all the crystallographic information files (*.cif).

The naming of each file corresponds to the structure as given in the thesis.

(e.g. 1 corresponds to compound 1).

CIFs can be viewed in the Mercury program which is a program available as a free download from the CCDC website (www.ccdc.cam.ac.uk)

The PDF folder contains a PDF type file of this entire thesis, should the reader require an electronic copy. PDF files can be viewed in the Adobe Acrobat Reader program, which is available as a free download from the Adobe website (www.adobe.com/products/acrobat/reader.html).